JOURNAL OF APPLIED PHYSICS

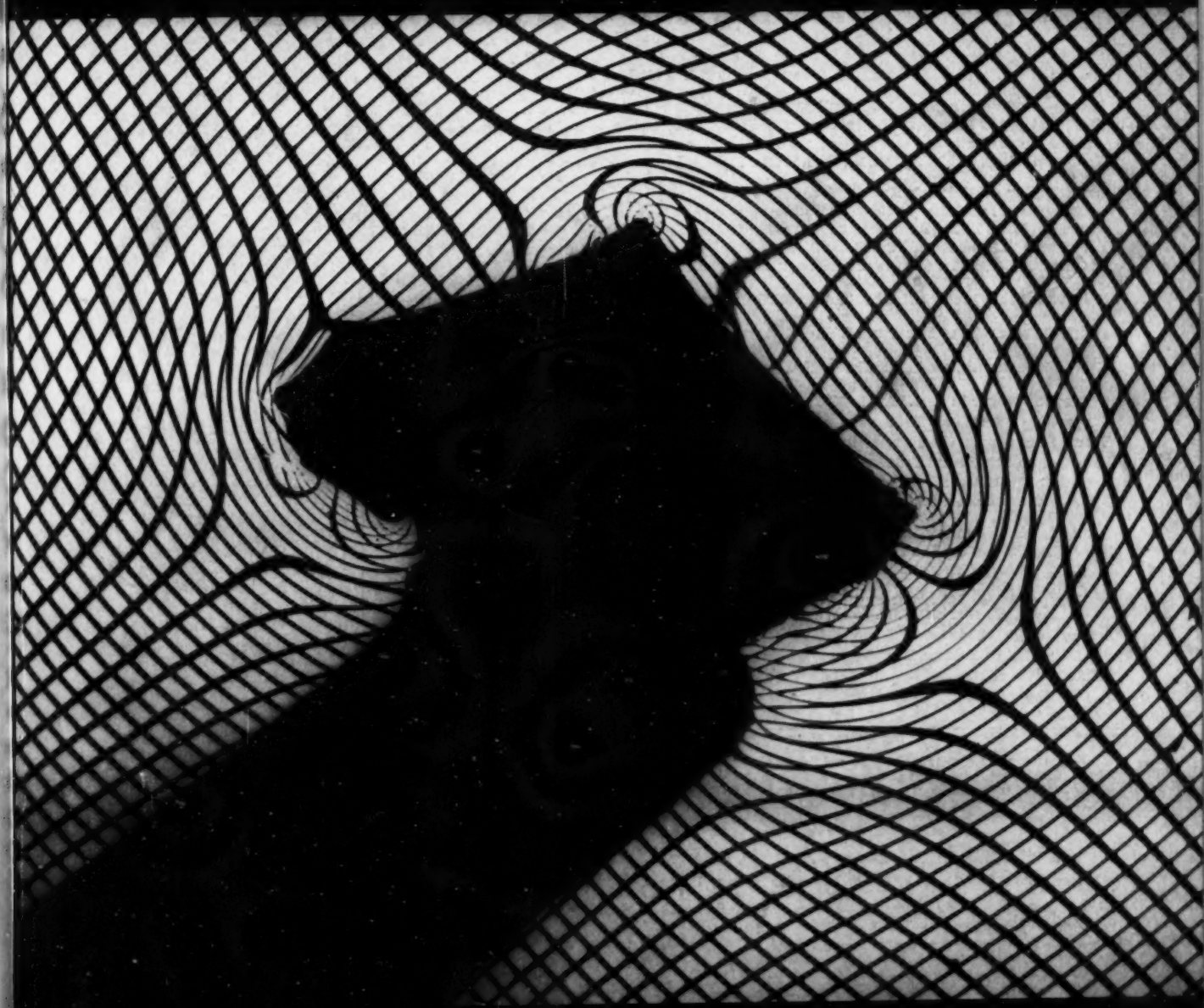

JOURNAL OF APPLIED PHYSICS

Vol. 20, No. 12 DECEMBER, 1949

In This Issue

		Page
Influence of Atomic Order on Magnetic Properties	J. E. Goldman	1131
Contributed Original Research		
Induced Fibration of Suspensions	W. M. Winslow	1137
Calculation of X-Ray Mass Absorption Coefficients	John A. Victoreen	1141
Electron Transit Time in Space-Charge Limited Current between Coaxial Cylinders	Paul L. Copeland and Delbert N. Eggenberger	1148
Bending of a Thin Circular Plate of an Aeolotropic Material under Uniform Lateral Load (Supported Edge)	H. Ōkubo	1151
On the Torsion of a Prismatic Cylinder with a Star-Shaped Section	H. Ōkubo	1155
Method for Studying the Distribution and Sign of Static Charges on Solid Materials	Harry H. Hull	1157
Study of the Sintering of Glass	G. C. Kuczynski	1160
On the Magnitude of the Mechanical Component of Solid Friction	C. D. Strang and C. R. Lewis	1164
Properties of Gold Deposited at Liquid Air Temperature	P. G. Wilkinson and L. S. Birks	1168
Electron Optical Mapping of Electromagnetic Fields	L. Marton and S. H. Lachenbruch	1171
Attenuation of Neutrons of Various Energies in Water	C. E. Falk and E. Creutz	1183
Note on the Role of Rifting in Cold-Work and a Possible Measure of Plastic Deformation	Donald P. Smith	1186
Investigation of Dielectric Rod as Wave Guide	C. H. Chandler	1188
Attenuation in a Dielectric Circular Rod	Walter M. Elsasser	1193
Traveling-Wave Tube (Discussion of Waves for Large Amplitudes)	L. Brillouin	1196
Distribution of Phases in Two-Phase Solids	Leonard D. Jaffe	1206
Aluminum-Beryllium Alloy for Substrate and Replica Preparations in Electron Microscopy	Wilbur Kaye	1209
Method for the Quantitative Evaluation of X-Ray Patterns from Mixed Powders	J. C. M. Brentano	1215
Physical Properties of Titanium. I. Emissivity and Resistivity of the Commercial Metal	Walter C. Michels and Sally Wilford	1223
Grain Boundary Relaxation and the Mechanism of Embrittlement of Copper by Bismuth	T'ing-Sui Kê	1226
Collimation Error in Small Angle X-Ray Scattering	K. L. Yudowitch	1232
Magnetite Concrete for Radiation Shielding	E. Creutz and K. Downes	1236
Volume Changes in the Plastic Stages of Simple Compression	P. W. Bridgman	1241
Impedance of Resonant Transmission Lines and Wave Guides	W. W. Harman	1252
Letters to the Editor:		
Application of Galerkin's Method to Compressible Fluid Flow Problems	Chi-Teh Wang and R. F. Brodsky	1255
Activation Phenomena with Thoria Cathodes	O. A. Weinreich	1256
X-Ray Diffraction Line Broadening and Strain Hardening	D. Rosenthal	1257
Orientation of Single-Crystal Rods of Copper Grown from the Melt	A. A. Petrauskas and F. Gaudry	1257
Fringe Fields of Ferromagnetic Domains	L. Marton, S. H. Lachenbruch, John A. Simpson, and A. Van Bronkhorst	1258
Author Index to Volume 20		1259
Subject Index to Volume 20		1264
Index to Advertisers		xxxiv

BOARD OF EDITORS

Elmer Hutchisson, *Editor*

Associate Editors

R. Bowling Barnes
Otto Beeck
W. James Lyons
Philip Morrison
Paul E. Sabine
Raymond J. Seeger
Frederick Seitz
Charles S. Smith
J. R. Townsend

Publication of the American Institute of Physics

OFFICERS

George R. Harrison, *Chairman*
George B. Pegram, *Treasurer*
John T. Tate, *Adviser on Publications*

GOVERNING BOARD

Luis W. Alvarez
J. W. Beams
Wallace R. Brode
E. U. Condon
W. F. Fair, Jr.
Harvey Fletcher
George R. Harrison
W. V. Houston
Paul Kirkpatrick
Paul E. Klopsteg
F. W. Loomis
Philip M. Morse
J. R. Oppenheimer
George B. Pegram
Harold K. Schilling
John T. Tate
Wallace Waterfall
M. W. White
A. G. Worthing

Consultant on Printing

Melvin Loos

ADMINISTRATIVE STAFF

Henry A. Barton, *Director*
Wallace Waterfall, *Executive Secretary*
Theodore Vorburger, *Business Manager*
Ruth F. Bryans, *Publication Manager*
Betty Hofstadter, *Office Manager*
Eileen B. Neuberger, *Circulation Manager*

The Journal of Applied Physics, published monthly at Prince and Lemon Sts., Lancaster, Pa., is devoted to physics in its role as the science basic to other natural sciences and to the arts and industries. Previous to 1937 this publication was known as Physics. The Journal of Applied Physics publishes editorials, news of physicists, and reviews, as well as technical papers of applied physics. Articles appearing in it are indexed regularly, according to their field, by Physics Abstracts, Chemical Abstracts, Engineering Index, Inc., Industrial Arts Index, etc.

Manuscripts should be submitted to Elmer Hutchisson, Editor, Case Institute of Technology, Cleveland 6, Ohio. The authors' institutions are requested to pay a **publication charge** of $4 per page which, if honored, entitles them to 100 free reprints. Instructions will be sent with galley proofs.

Subscriptions and orders for back numbers should be addressed to Prince and Lemon Streets, Lancaster, Pa. or to the American Institute of Physics, 57 East 55 Street, New York 22, N. Y.

Subscription Price	U.S. and Canada	Elsewhere
To members and associate members of the American Institute of Physics	$7.00	$ 8.00
To all others	9.00	10.00

Back Number Prices

Complete set: Vol. 1, July, 1931–Vol. 19, 1948—$140.00
Yearly back number rate: $10.00
Single copies: $1.00 each.

Changes of address should be sent to the Business Manager, American Institute of Physics; **corrected proofs** should be sent to the Publication Manager, American Institute of Physics.

Advertising rates supplied on request. Orders, advertising copy, and cuts should be sent to the American Institute of Physics.

Entered as second class matter January 22, 1937, at the Post Office at Lancaster, Pennsylvania, under the Act of March 3, 1879. Accepted for mailing at the special rate of postage provided for in the Act of February 28, 1925, authorized May 2, 1932.

Copyright 1949, by the American Institute of Physics.

Journal
of
Applied Physics

Volume 20, Number 12 December, 1949

The Influence of Atomic Order on Magnetic Properties*

J. E. GOLDMAN

Westinghouse Research Laboratories, East Pittsburgh, Pennsylvania

MANY unusual magnetic properties of alloys are associated with composition ranges in which an order-disorder transformation is found to exist. Many of these changes can be directly attributed to the transformation and there is sufficient evidence to indicate that the correlation is not fortuitous. The purpose of this paper is to review the various effects on magnetic properties resulting from the order-disorder transformations and show the manner in which some of the recent theories and experimental findings in this field can make possible a clearer understanding of several hitherto unexplained magnetic phenomena. The paper is divided into three parts. The first part is a review of recent data on the effect on the magnetic properties of the order-disorder transformation. The second part is devoted to the extension of a recently developed theory of the influence of order on the saturation moment to cases such as Ni_3Mn and the Heusler alloy, where there is as yet no theoretical explanation for the influence of order on the moment. The final part is somewhat speculative and consists essentially of a new approach in interpreting the structure-sensitive magnetic properties, notably permeability and coercive force, based on some of the consequences of order-disorder transformations.

I. EXPERIMENTAL SUMMARY

For the purposes of this discussion, we shall, in the usual manner, divide the magnetic properties into two classes: the intrinsic structure-insensitive "volume" properties which depend only upon the composition of the material and its crystalline character; and the structure sensitive properties, those which depend upon treatment, thermal and mechanical history, impurities, etc. In the first category belong the saturation moment, Curie temperature, anisotropy, and spontaneous magnetostriction.** The latter classification includes the permeability, coercive force and, in general, the magnetization process below saturation.

1. The Intrinsic Volume Properties

a. *Saturation Moment*

Perhaps the most remarkable observed influence of an order-disorder transformation upon a magnetic property is the case of the alloy Ni_3Mn. This is a face centered cubic alloy of the Cu_3Au structure and is strongly ferromagnetic in the ordered state but very weakly ferromagnetic when disordered. In Fig. 1, the intrinsic induction ($4\pi I$) is plotted against percent manganese for the quenched and annealed alloys in the Ni-Mn system.[1] It is seen that the quenched alloys which are known to be disordered are either paramagnetic or very weakly ferromagnetic while the annealed alloys are ferromagnetic. At 25 atomic percent manganese which is the composition where perfect order may obtain, the intrinsic moment is 44 percent greater than that of pure nickel.

In the iron-cobalt system at the ordering composition of 50 atomic percent, a less pronounced but nevertheless

* Based on a lecture delivered as part of a Symposium on Solid State Physics at the Cleveland meeting of the American Physical Society, March, 1949.

** This is what Becker refers to as the spontaneous distortion of the lattice due to the magnetization as distinct from the macroscopically measured longitudinal magnetostriction at saturation which is dependent upon the domain distribution and is, therefore, structure sensitive.

[1] S. Kaya and A. Kussman, Zeits. f. Physik 72, 293 (1931).

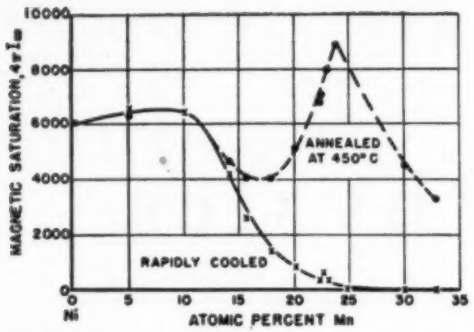

FIG. 1. Magnetic saturation ($4\pi I$) as a function of manganese content for annealed and rapidly cooled iron-manganese alloys.

measurable increase in moment takes place;[2] the saturation moment increases by approximately 4 percent on ordering. The theory of the effect in that alloy has been treated and forms the basis of Part II of this article. An increase in moment of almost 6 percent on ordering has also been observed in the case of the Fe-Ni system in the Permalloy region (75 atomic percent nickel).

Discontinuities in the saturation moment *vs.* percent alloying element curve for various alloys of iron at compositions usually associated with the appearance of an ordered lattice have been attributed by Fallot to ordering. His data on Fe-Si are presented in Fig. 2.[3] Similar discontinuities appear in other alloy systems and are attributed by Fallot to superlattice formation.

b. *Curie Point*

A pronounced discontinuity in the Curie point *vs.* composition curve is found at 12.5 atomic percent silicon. This is the composition at which superlattice lines first appear in x-ray diffraction photographs.[4] It is interesting to note that a discontinuity in θ is also observed at 6.25 percent atomic percent although this has not been confirmed. There is metallurgical evidence for the beginning of a superstructure at that composition[5] although no superlattice lines are observed. The magnetic data appear to support this view.

c. *Crystalline Anisotropy*

It has been shown by Grabbe[6] that associated with the order-disorder transformation in the permalloy region of the Fe-Ni system is a marked change in the crystalline anisotropy. In the disordered quenched alloy the anisotropy is equal to zero at the composition $FeNi_3$. On ordering the anisotropy becomes quite pronounced and is similar to that of nickel, i.e., the [111] direction is the direction of easy magnetization and the [100] is the most difficult. The magnetization curves for the two cases are shown in Fig. 3. The anisotropy constants in the ordered case are respectively (in the conventional notation) $K_1 = -2.30\times10^4$ ergs/cc and $K_2 = -1.65\times10^4$ ergs/cc. In the disordered state both are equal to zero. The discontinuity in the crystal anisotropy *vs.* composition curve that is observed in Fe-Si at 9.5 atomic percent silicon has similarly been attributed by Tarasov[7] to a sharp change in the character of the silicon superlattice.

d. *Magnetostriction*

Goldman and Smoluchowski[8] have shown that the saturation magnetostriction of a 50 percent Fe-Co alloy increases on ordering. Their results are shown in Table I. The magnitude of the observed increase is of the order of 40 percent and can be explained theoretically on the basis of the Becker dipole interaction theory. A similar increase has also been observed recently in the case of Permalloy and iron-aluminum.[9] In the case of the former the magnetostriction changes by a factor greater than two. It is with the pronounced change in the anisotropy and magnetostriction upon ordering and its effect on the structure sensitive properties that the latter portion of this article is concerned.

2. Structure Sensitive Properties

The effect of the order-disorder transformation on the structure sensitive properties is even more marked than the changes in volume, *i.e.* structure insensitive, properties. Although no exact relation between the permeability or coercive force and the state of order has been established, the existence of some interdependence between the two is clear. One can say with certainty that

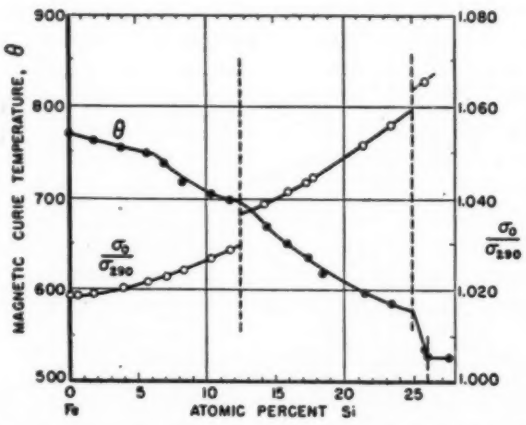

FIG. 2. Magnetic Curie temperature and the ratio of the saturation moment at absolute zero to that at room temperature plotted as a function of atomic percent silicon for a series of Fe-Si alloys (after Fallot).

[2] J. E. Goldman and R. Smoluchowski, Phys. Rev. **75**, 310 (1949).
[3] M. Fallot, Ann. de physique **6**, 305 (1936).
[4] E. R. Jette and E. S. Greiner, Trans. A.I.M.E., Iron and Steel Division, February 1933.
[5] E. R. Jette and E. S. Greiner, see reference 4; see also Greiner, Marsh, and Stoughton, *Alloys of Iron and Silicon* (McGraw-Hill Book Company, Inc., New York, 1933).
[6] E. M. Grabbe, Phys. Rev. **57**, 728 (1940).
[7] L. P. Tarasov, Phys. Rev. **56**, 1231 (1939).
[8] J. E. Goldman and R. Smoluchowski, Phys. Rev. **75**, 140 (1949).
[9] J. E. Goldman, Phys. Rev. **76**, 471 (1949).

pronounced order of magnitude changes are known to occur at compositions where ordering takes place, and the treatment employed to bring out the desired property is similar to the one which will inhibit or accelerate ordering as the case may be. We shall discuss this in greater detail below and consider its interpretation in Part III.

a. *Permeability*

The highest obtainable initial and maximum permeabilities are to be found in the iron-nickel system in the range of the order-disorder composition $FeNi_3$. Moreover, the treatment is such as to indicate the desirability of suppressing the transformation from disorder to order. The initial permeability for annealed and quenched alloys is shown in Fig. 4.[10] A similar, although not as pronounced, effect is found at the 50 percent nickel composition where the presence of an order-disorder transformation is suspected and in the iron-cobalt alloys in the 50 percent range.

b. *Coercive Force*

In recent years, materials have been discovered with extremely high coercive force, orders of magnitude larger than the old permanent magnet steels. The iron-platinum and cobalt-platinum alloys are two examples and in both cases the state of high coercive force appears to be associated with the order-disorder transformation. The former alloy has been studied quite extensively by Lipson and his collaborators in England; the latter at Carnegie Institute of Technology by Smoluchowski and his students.[11]

Another such alloy is a Heusler alloy containing silver, manganese, and aluminum which was shown by Potter[12] to have an anomalously high coercive force and is currently marketed in this country under the name Silmanal. Here, too, the extremely high coercivity appears to be associated with the order-disorder transformation known to exist in this composition range. In the Alnico alloys, as well, the atomic arrangement is known to play an important role in making possible the state of high coercive force.[13]

II. THE "VOLUME" PROPERTIES AND THE ROLE OF THE ELECTRON DENSITY

We shall now examine in somewhat greater detail and from a more theoretical point of view some of the volume property changes. Until recently very little has been done by way of attempting to describe these effects on theoretical grounds. This is particularly striking in the case of the changes in moment and Curie temperature. The effect on anisotropy has already been treated theoretically by McKeehan and the magnetostriction by Goldman and Smoluchowski.[14] In this section, the recent theory developed by the latter authors which predicts the proper increase in saturation moment on ordering in a 50 percent iron-cobalt alloy will be briefly described and extended to the case of Ni_3Mn where a semi-quantitative interpretation of the pronounced effect of ordering on the moment can be obtained. The salient feature of this theory is the emphasis placed on the fluctuations in local electron density at each lattice point which depends on the character of the neighbors.

If our attention is confined for the moment to nearest neighbors alone, then the difference between the ordered and disordered states can easily be calculated by statistical means. In a body-centered cubic structure in the ordered state of composition AB, such as Fe-Co, this means that the nearest neighbor of an A atom is always

TABLE I.

	Quenched	Annealed
Saturation magnetostriction	6.5×10^{-6}	9.2×10^{-6}
Electrical resistivity (micro-ohm-cm)	24.2	18.82
Neutron diffraction	Slightly ordered	Well ordered

Saturation magnetostriction for ordered and disordered samples of a 50 percent iron-cobalt alloy. The degree of order is determined from neutron diffraction experiments.

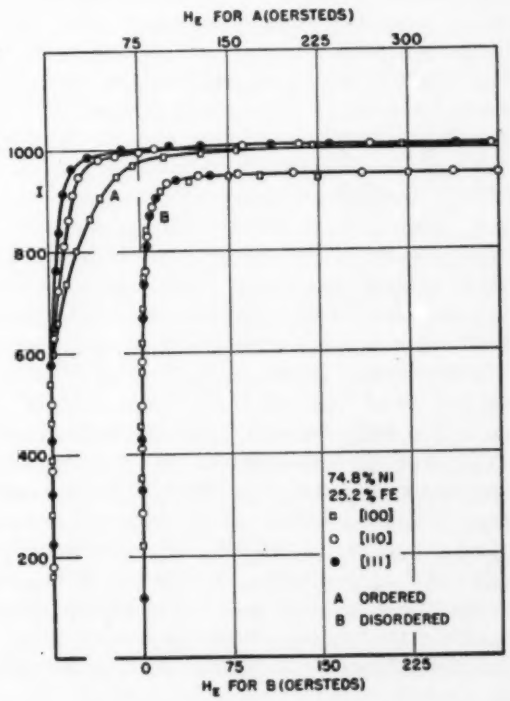

FIG. 3. Magnetization curves for the three principle crystalline directions of ordered and disordered Ni_3Fe. The three curves coincide for the case of the disordered alloy (after Grabbe).

[10] R. M. Bozorth, Rev. Mod. Phys. **19**, 29 (1947).
[11] H. Lipson, D. Schoenberg, and G. V. Stupart, J. Inst. Metals **67**, 333 (1941). C. B. Newkirk and R. Smoluchowski, Phys. Rev. **76**, 471 (1949).
[12] H. H. Potter, Phil. Mag. Ser VII **12**, 255 (1931).
[13] W. Sucksmith Proc. Roy. Soc. **171A**, 525 (1939).
[14] L. W. McKeehan, Phys. Rev. **52**, 18 (1937); J. E. Goldman and R. Smoluchowski, see reference 7.

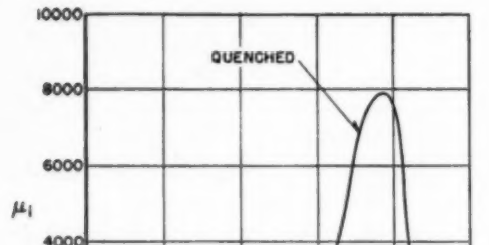

FIG. 4. Initial permeability as a function of composition for the iron-nickel system. The solid curve is for rapidly cooled alloys and probably corresponds to the disordered state. The dashed curve represents furnace cooling followed by a low temperature bake which treatment presumably orders the lattice (after Elmen).

a B atom and for a B atom the nearest neighbor is an A atom. This permits us to define uniquely the local electron density of each atom since we know with certainty the character of its eight surrounding nearest neighbors. On the other hand, in the completely disordered state, the probability that each A atom will be surrounded by eight A atoms, by seven A atoms and one B atom, by six A atoms and two B atoms, etc. is finite for any distribution and can be readily calculated statistically. Associated with each such distribution of neighbors is a *local* electron density and a magnetic moment characteristic of an atom having that density which can be found from the Pauling-Shockley curve of the saturation moment as a function of the average electron density per atom reproduced in Fig. 5.[15] By statistically weighting the contributions to the total moment of each such distribution an average total macroscopic moment is obtained for the ordered and the disordered states respectively. It may be argued that this is not in conformity with band theory. However, this has been a simple averaging of the fluctuations in local electron density which is, in effect, all that can be said about a band approach to $3d$ shells; moreover, it is the only type of approximation that has yielded a satisfactory explanation of magnetostriction and the effect of ordering on the moment. Applied to iron-cobalt, such a treatment yields good theoretical results; its success in extending its application to explain the ordering anomaly in Ni_3Mn and a qualitative explanation of the ferromagnetism and saturation moment of Heusler alloy in the ordered state further justifies its employment.

Consider first the case of Ni_3Mn. In the ordered state the distribution of the respective atoms in the face centered cubic lattice is as shown in Fig. 6. Each Mn atom has as its nearest neighbors twelve nickel atoms while each Ni atom is surrounded by eight nickel atoms and four manganese atoms in the twelve available nearest neighbor sites. In order to ascertain whether the $3d$ electrons in the Mn atoms will contribute to the magnetic moment, one must first of all apply the Néel criterion for positive molecular field[16] (similar to the exchange integral in Slater's theory) to the Mn atom in a neighborhood characteristic of its position in the ordered lattice. Since this consists entirely of Ni atoms, one may treat it as a simple Mn-Ni pair and use the d-shell radii calculated by Slater[17] for these atoms and originally employed by him in his theory of ferromagnetism.*** Combining this with the experimental value for the interatomic distance as given by Valentiner and Becker[18] we obtain a value of 1.04 for the difference which when fitted into Néel's curve (Fig. 7) indicates that the molecular field is probably negative and, therefore, can not produce ferromagnetism. We conclude, therefore, that the Mn atoms do not contribute to the ferromagnetism. On the other hand, the nickel atoms are ferromagnetic in their surroundings and possess an average local electron density of 9.5. On Pauling's curve (Fig. 5) this implies an average magnetic moment per nickel atom of approximately 1.2 Bohr magnetons. Since only three-fourths of the total number of atoms are nickel atoms, the volume moment is of the order of 0.9 Bohr magnetons per atom. A more exact calculation yields a saturation induction ($4\pi I_s$) of 8700 gauss in good agreement with the experimental value.

In the disordered state, the situation is somewhat more complicated. As before, none of the Mn atoms contribute to the magnetism, for, as we have seen before even in the most favorable case of a Mn atom surrounded completely by Ni atoms the criterion for

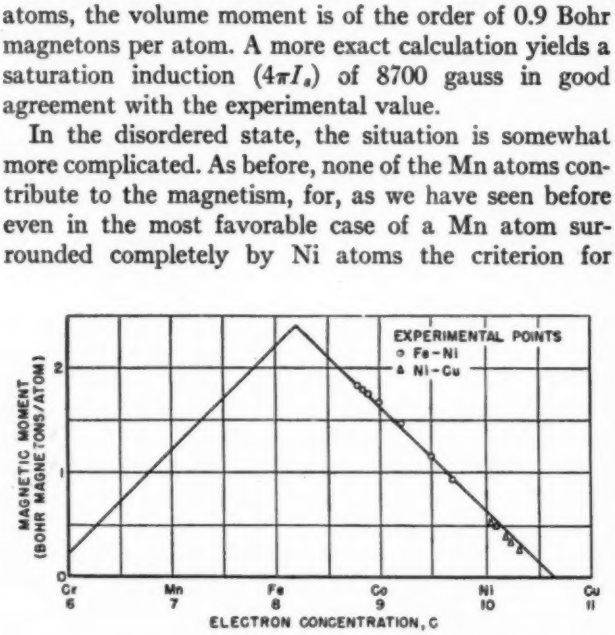

FIG. 5. Saturation moment of ferromagnetic alloys plotted against number of electrons per atom outside the highest filled band (schematic). Experimental points are included for two alloys with face-centered cubic lattices (after Pauling, Shockley).

[15] L. Pauling, Phys. Rev. **54**, 899 (1938); W. Shockley, Bell Sys. Tech. J. **18**, 645 (1939); F. Seitz, *Physics of Metals* (McGraw-Hill, Book Company, Inc., New York, 1943).

[16] L. Néel, Reports on the Paris Conference on Magnetism (1940).

[17] J. C. Slater, Phys. Rev. **36**, 57 (1930).

*** The Slater-Bethe theory relates the exchange energy to the ratio of the interatomic distance to the radius of the $3d$ "shell"; in Néel's theory it is the difference between these two quantities rather than this ratio. It appears that the latter theory is more quantitative and has, therefore, been employed here.

[18] Valentiner and Becker, Zeits. f. Physik **93**, 795 (1935).

ferromagnetism is not satisfied. And any replacement of some or all of the nickel neighbors by manganese make the conditions for ferromagnetism even less favorable. On the other hand, where formerly all the Ni atoms were magnetic, now those nickel atoms that find themselves in cells in which a preponderance of the nearest neighbors are Mn atoms will not be magnetic using the above criterion. The lattice now ceases to be a simple three-dimensional chain of dipoles. In this state, presumably, a sufficiently large number of cells will have negative contributions to the molecular field which may render the entire material antiferromagnetic. A relatively straightforward statistical treatment shows the alloy to be at most weakly ferromagnetic.

A qualitative extension of these ideas to the case of the Heusler alloy is now possible. In the ordered state, the manganese atoms are always completely surrounded by copper atoms as their nearest neighbors. The manganese atoms at the equilibrium lattice constant of ordered Heusler alloy can be shown by the methods of Slater and Néel to satisfy their respective criteria for ferromagnetism. By calculating the electron density based on the contribution of 4*s* electrons from the copper to the 3*d* shells of the manganese atoms, one again obtains a value for the saturation moment that agrees well with the experimental value.

III. THEORY OF THE STRUCTURE SENSITIVE PROPERTIES

Turning from the "volume" properties to the so-called structure sensitive properties we consider now the role of order in causing the pronounced changes described previously. The magnetic changes produced by ordering are, indeed, very much more marked than the changes produced in other structure sensitive properties. Mechanical hardness and other mechanical properties, e.g., yield stress, brittleness, are affected in some alloys by ordering but to only a minor extent as compared to the changes in magnetic permeability and coercive force where order of magnitude increments are observed. It is difficult to reconcile these large changes produced in the magnetic properties on ordering with the usual view of attributing these changes to variations in what Becker calls the internal strain parameter, σ_i. Various investigators have explicitly attributed the unusually high coercivity in some ordered alloys or the phenomenal changes in permalloy to the straining of the lattice on ordering due to a slight tendency toward tetragonality in an ordered cubic lattice. It is questionable though whether this accounts completely for such high values of the coercive force.

To emphasize the importance of the volume property changes on ordering in influencing those properties which are customarily known as structure-sensitive, let us review the factors affecting μ_0 and H_c, the permeability and coercive force. Becker has related the coercive force and initial permeability to the internal strain, saturation magnetization and magnetostriction through the following relations:

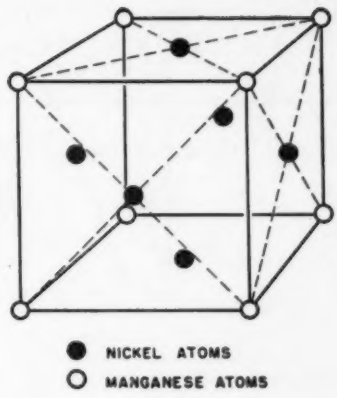

FIG. 6. Ordered lattice of Ni_2Mn showing the respective positions of the nickel and manganese atoms.

$$H_c = p_c \frac{\lambda_s \sigma_i}{J_s} \qquad \mu_0 = 1 + \frac{K J_s^2}{\lambda_s \sigma_i}.$$

λ_s is the saturation magnetostriction, J_s is the saturation magnetization and p_c is a parameter which depends on the effective length of a strained region and the width of a Bloch wall. Since the relation between μ_0, and H_c is virtually an inverse one, i.e., $H_c \sim (K' J_s/\mu_0)$ we can, for the remainder of this discussion, concern ourselves only with the coercive force. The dependence of the coercive force on structure and its variation from material to material has generally been attributed to its critical dependence upon the internal strain parameter σ_i.

It now appears, however, in view of the significant changes that occur in some of the more basic structure insensitive volume properties on ordering that one must consider more than just the internal strain. The unusual changes that occur on ordering are attributable to significant changes in magnetostriction and anisotropy which when coupled with ordinary changes in internal strain result in the large variations that are, in fact, observed on ordering. This interpretation has been approached quantitatively in the case of the soft magnetic materials and experiments are in progress designed to investigate its applicability to very high coercive materials.

In Permalloy, for example, we can now see that there should be an order of magnitude difference in the coercive force between the quenched and annealed states. The constant p_c in the above expression for the coercive force has been related by Becker to the ratio l/δ when l is the average linear length of the strained region in the lattice and δ is the thickness of the Bloch wall.[19] When the crystalline anisotropy is very small as it is in the case of Permalloy, the Bloch wall thickness becomes large and the ratio p_c is small. The magnitude of δ in Permalloy has recently been discussed by Bozorth[20] and supports this view. On ordering, the

[19] Becker-Doring, *Ferromagnetismus* (Berlin, 1939), p. 207.
[20] R. M. Bozorth, Zeits. f. Physik 124, 519 (1948).

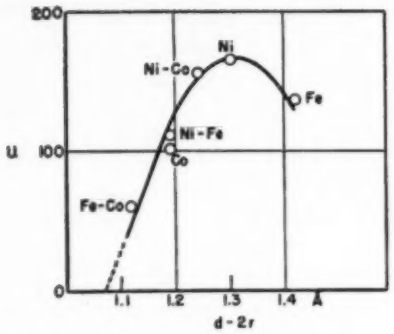

FIG. 7. Neel's curve showing the dependence of the molecular field on the difference between the interatomic distance and twice the average radius of the 3*d* "shell."

anisotropy increases with an accompanying increase in p_c. There is a simultaneous increase in the value of the magnetostriction and an inevitable rise in σ_i, the internal strain arising from the very small tetragonality of the ordered lattice. Thus, we can account for the large magnitude of the change in coercive force (and in initial permeability) in Permalloy on ordering in spite of the fact that measurements of hardness do not reflect too significant a change in the degree of internal strain. In the 50 percent iron-cobalt alloy, the situation is very similar. The observed increase in magnetostriction on ordering suggests that rapid cooling should bring about a proportional decrease in coercive force which, as we have shown above, is confirmed experimentally.

That these principles can be applied to the case of permanent magnets has already been pointed out for certain specific cases. In the case of cobalt magnet steel it has been shown[21] that the large coercive force can be traced directly to the abnormally high magnetostriction in this alloy. It is quite probable that the much higher coercivities found in some of the ordered alloys can be similarly correlated with basic changes in the volume properties. Quantitiative data on this is the subject of a current investigation.

IV. SUMMARY

The observed effects of order-disorder transformations on the structure insensitive and structure sensitive magnetic properties of ferromagnetic alloys have been reviewed. The properties affected include the saturation moment, Curie temperature, crystalline anisotropy, saturation magnetostriction, permeability and coercive force. The theory advanced to explain the increase in saturation moment of iron-cobalt on ordering has been described and extended to the case of nickel-manganese where the anomalous behavior of the saturation moment as a function of order had hitherto not been quantitatively understood. The macroscopic moment is considered as arising from a summation of pseudo-atomic moments which depend upon the local electron density. The large observed variations in permeability and coercive force on ordering have been ascribed to changes not only in the degree of internal strain but in the anisotropy and magnetostriction as well. The author is indebted to Professor Smoluchowski for stimulating discussions on various phases of this subject and many valuable suggestions, and to Dr. Sidney Siegel and Dr. T. D. Yensen for critical comments on the paper.

[21] J. E. Goldman, Trans. A.S.M. 37, 212 (1946).

Contributed Original Research

Induced Fibration of Suspensions

W. M. Winslow
Wheatridge, Colorado
(Received February 23, 1949)

This paper describes some of the phenomena found to have their origin in electrically induced fibration of small particles in fluid liquid suspension. Particular attention is given to induced shear resistances found in layers of the fluid (0.01 to 0.15 cm) when bounded by potentialized electrode surfaces. Ingredients and manner of compounding concentrated fluids capable of reversible shear resistance up to several hundred grams per cm² are described. Dynamic induced shear resistance or the corresponding induced bulk viscosity are shown to be a parabolic function of field strength wherein parameters dependent on surface conditions of the particles are involved. Various properties of these fluids are discussed with regard to the mechanism of induced fibration, its application in slip clutches and other hydraulic devices, and some of the factors for best results. Consideration is given to the analogous magnetically induced fibration of ferromagnetic particles in fluid suspension. It is found that the observed values of induced shear resistance approximate those predictable from the well-known formulas for tractive force in both the electric and magnetic cases. Mention is also made of fluid suspensions of ferrite powders which respond to both electric and magnetic fields.

A SERIES of experiments begun in 1939 has established that certain kinds of particles suspended in low viscosity oils tend to form an oil-occluding fibrous mass when acted upon by an electric field. The fibers form in the general direction of the field and in such a manner that the electrodes are mechanically linked together.[1] The effect has been found intrinsically reversible under action of shear or, in the case of very fluid suspensions, by action of kinetic agitation alone.

Particles found most suitable have been semiconductive solids of high dielectric constant. Particularly good results have been obtained with slightly moist hydrophile adsorbent materials of about one micron particle diameter, such as activated silica gel powders, which have been worked into a kerosene fraction to a concentration of about 50 percent by volume. This is accomplished with addition of suitable dispersing agents such as metallic soaps, sorbitol fatty acid esters, etc., and by prolonged circulation through a screw pump.

In general, concentrated suspensions with particle volume exceeding 38 percent, and with viscosity of the oil below 20 c.p. at 25°C, yield the best results as determined by rotational electro-viscometer tests using the instrument of Fig. 1. With such high concentration, migration due to cataphoresis is a neglible factor and the dynamic induced shear resistance of thin films reaches several hundred grams per sq. cm for over-all field strength of 30,000 volts per cm.

In all types of fluids, maximum ratio of induced viscosity to normal viscosity requires the use of a low viscosity vehicle in the range of 2 to 20 c.p. at 25°C in order to hold the normal viscosity to a minimum. Such vehicles for practical uses should have minimum vapor pressure times viscosity to avoid also difficulties caused by thickening as a result of volatilization. Diester liquids such as dibutyl sebacate may be used for the vehicle.

The observed increase in bulk viscosity of the fluid is apparently due to those components of force along the fluid film arising from tension of inclined fibers. At high concentrations an additional component is added, apparently caused by compression or jamming of closely packed particles.

The induced shear resistance, S, i.e., the increase above that for the de-energized fluid, is found to be nearly a parabolic function of applied potential, V,

$$S \pm S_0 = K(V \pm V_0)^2. \qquad (1)$$

The supplemental potential, V_0, the supplemental shear resistance, S_0, and the factor, K, appear to be associated with the particle surfaces, depending upon the type and amount of dispersing agent used. The applied potential, V, may be either alternating or direct. With 60-cycle supply the viscometer produces a 120-cycle hum.

Typical curves obtained with the viscometer of Fig. 1 are illustrated in Fig. 2 and show Eq. (1) to be valid for a range of voltages up to over half of the breakdown value. The curves shown are from data taken at a slip speed of 65 cm per second with a spacing of 0.025 cm.

Although the described fibration is impeded by high viscosity of the oil phase, it is desirable that ingredients such as stearate soaps be added to impart gelcosity or thixotropy. Otherwise settling and phase separation in bulk may occur. A further requirement of practical importance is stability of the particle surface under the rubbing action occurring at high concentration. Stability can be achieved initially by the pumping operation mentioned.

The resistivity of the most effective fluids lies in the range of 10^8 to 10^{10} ohm cm, and depends, among other

[1] Willis M. Winslow, U. S. Patent 2,417,850 (March 25, 1947).

factors, on the amount of water or like substance of high dielectric constant imbibed by the particles. Tests on slipping clutches in which appreciable heat is generated have shown that resistivity decreases with temperature, being at 25°C several times that at 80°C.

The power factor depends upon the kind of ingredients, the field strength, and the temperature. In general the silica gel type mix gives, for 60-cycle supply, power factors down to about 0.5 by holding the water content to a minimum; for higher water content, temperature, and field strength the power factor increases to about 0.7. For frequencies of higher order such as used in tests on audiofrequency response, the power factor of silica gel mixes is low and compares favorably with electrolytic condensers. Power factor measurements were made by a comparison of currents flowing through the field responsive fluid, and a parallel resistor.

$$pf = 1-(I_1+I_2+I_3)(I_1+I_2-I_3)/2I_1I_2, \qquad (2)$$

where I_1 is the current drawn by the electric fluid sample under test, I_2 the current drawn by the parallel resistor, and I_3 the total current drawn by the paralleled sample and resistor. Such measurements are made with the electric fluid contained between the flat plates of Fig. 3 or the electro-viscometer of Fig. 1.

Efficiencies in terms of induced shear resistances and input have reached 25 kg shear per watt. The upper limit is still a matter of conjecture. Undoubtedly, it is determined by barriers at the surface of the particles which in turn determine the over-all breakdown strength of the fluid. The highest bulk breakdown value measured in the viscometer experiments was 40,000 volts per cm for a film 0.01 cm thick. It is apparent that the surface active agents used should be chosen relative to insulating qualities since most of the potential drop is between contacting particles.

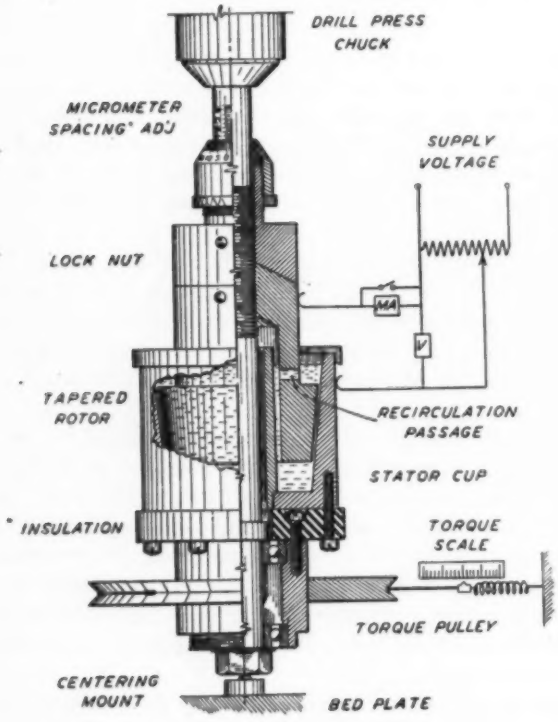

FIG. 1. Electro-viscometer.

A dilute film of zinc hydroxide suspension between microscope slides and potentialized by foil electrodes in the plane of the film enables one to see separate fibers. Formation of long and straight fibers is achieved by shearing at right angles to the field.

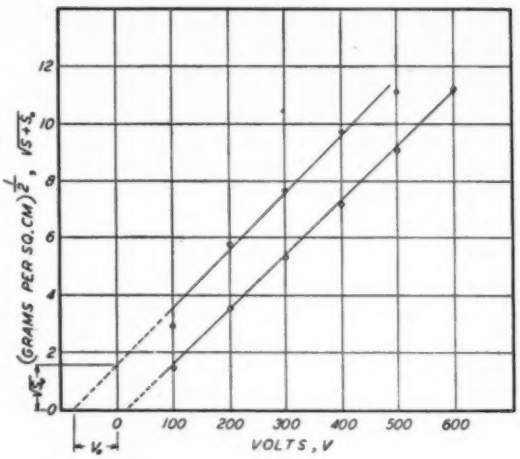

FIG. 2. Correlation of experimental shear-voltage data.

The fluids when confined have been found to exhibit some electro-striction. Also, it is found that on stopping the viscometer the dial returns rapidly to a minimum and then moves slowly upward a short distance indicative of a tightening or shortening of the inclined fibers.

The trailing edge of a plate potentialized with 60-cycle voltage and slid over a film of electro-viscous fluid will produce an oscillographic deposition of the film. Contour-like lines are obtained, caused by intermittent migration of particles at the edge region by reason of higher field intensity. This effect is shown in Fig. 3.

About ten grams of concentrated electro-viscous fluid can be lifted from a beaker between probes at 10,000 volts a.c., thus illustrating electrically induced fibration. Pictures of this experiment are shown in Fig. 4.

The response to audio frequencies can also be demonstrated with the plates of Fig. 3. With the modulated output of a small radio applied to the plates a reproduction of music and voice is had on sliding one plate relative to another.

The pumped flow of an electro-viscous fluid through a narrow passage can be regulated or blocked by an electric field normal to the direction of flow. In this manner a fluid pressure can be built up which has a parabolic dependence on the applied voltage. The valve used in experiments of this nature is shown in Fig. 5(A).

A screw-type viscosity pump containing electro-viscous fluid will develop a higher pressure and pump

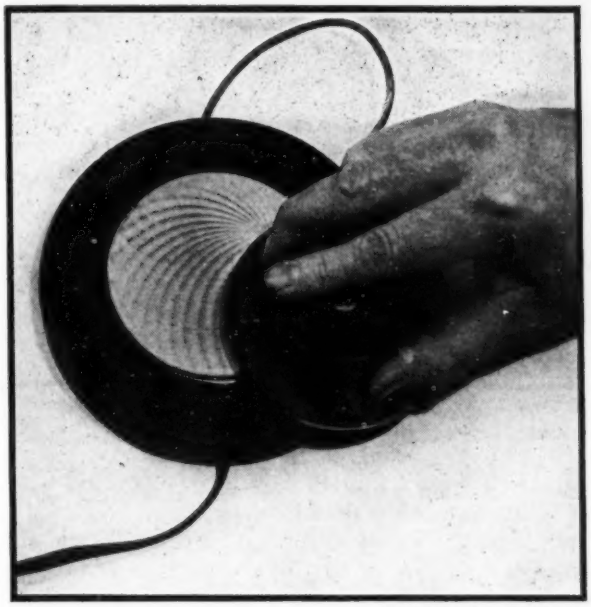

Photo by Ernest Galway.

FIG. 3. Flat metal plates showing trailing edge contours.

more efficiently when an electric field is impressed across the working space.

Induced fibration and the marked increase in bulk or averaged viscosity associated with it is to be distinguished from the induced viscosity of dilute colloids reported by Bjornstahl and Snellman.[2] In their work orientation occurs and the important factors are the nematic form and polar character of the elementary particles. In contrast, induced fibration will occur when the particles are spherical and depends basically on minute lateral migrations of particles to regions of high field intensity between gaps of incomplete chains followed by mutual attraction thereafter. By the present effect it is possible to produce a greater relative change in bulk viscosity and the induced resistance to shear is many times larger in absolute value.

A study of magnetically induced fibration of concentrated iron suspensions has recently been undertaken at the National Bureau of Standards.[3] The behavior of magnetic fluids is very similar to electric fluids, differing mainly in that magnetic saturation rather than dielectric strength is the limiting factor. The N. B. S. experiments have shown it possible to exceed the above efficiency of electric fluids by the use of an efficient magnetic circuit. On the other hand, the electric effect is favored by small over-all weight of the equipment and its limitations have not yet been reached.

The shearing resistance, on theoretical grounds, is the tractive force normal to supposedly flat parallel particles multiplied by a factor A to account for the actualities of reduced particle contact area and the effective inclination of fibers. The tractive force in dynes per cm^2 between flat parallel particles is

$$F = kE^2/8\pi \tag{3}$$

for the electric effect, and

$$F = B^2/8\pi \tag{4}$$

for the magnetic effect, where E is the field intensity *between particles* in abvolts per cm, and B is the magnetic induction *between iron particles* in maxwells. A value for A of about 0.05 gives approximate agreement between calculated and observed shear resistance in the two cases. The factor k applicable in Eq. (3) to

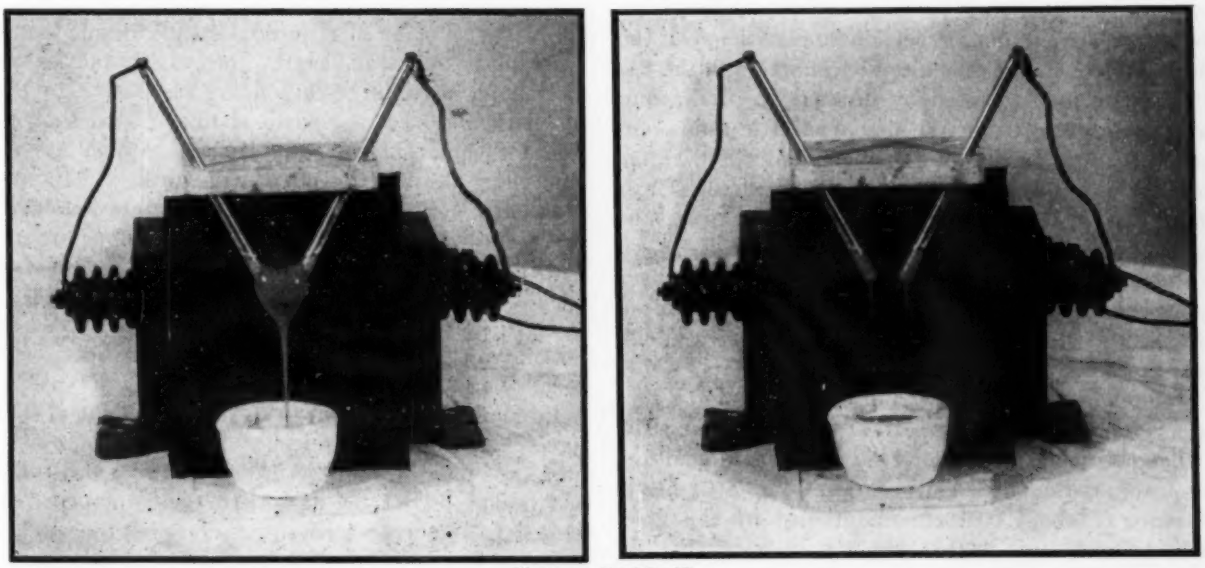

Photos by Paul Saville.

(A) (B)

FIG. 4. Electrically induced fibration between probes. (A) voltage=10,000; (B) voltage=0.0.

[2] Von Y. Bjornstahl and K. O. Snellman, Kolloid Zeits. 79, 259 (1937).
[3] "Magnetic fluid clutch," News Bull. J. Research Bur. Stand. 32, 54–60 (May, 1948).

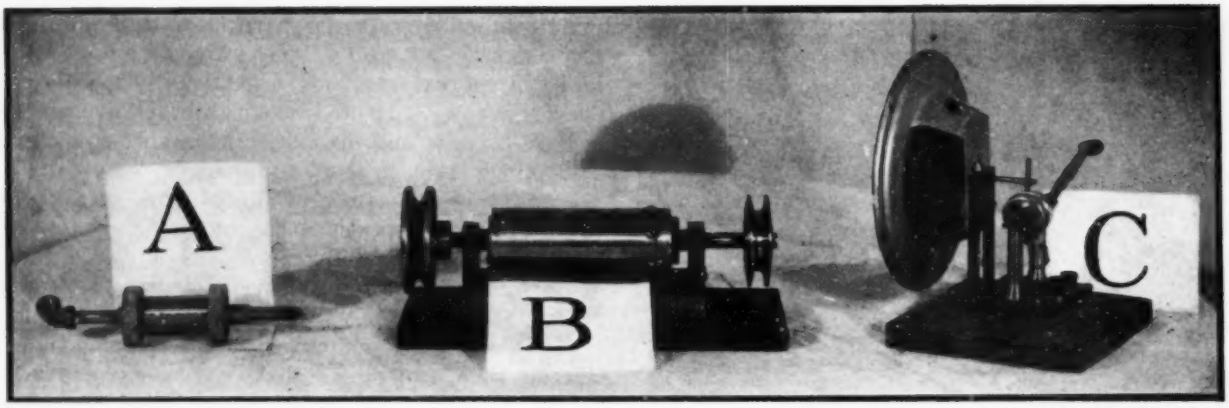

Photo by Paul Saville.

FIG. 5. Electrically controlled valve with no moving parts (A); clutch or brake (B); clutch-driven loudspeaker (C).

the electro-fibration effect is the dielectric constant of the boundary layers between adjoining particles.

It is also apparent that the bulk dielectric constant for the electric fluids in the direction of the field is about 0.05 of that for a pile of sheet conductors of individual thickness equal to the mean particle diameter and separated by films of thickness equal to the films between the particles in contact. Likewise, for magnetic fluids in the presence of a field, the bulk permeability in the direction of the field is about 0.05 what it would be if the fluid were replaced by a similar pile of ferromagnetic material of the same composition as the particles. The factor 0.05 is representative of those found for intense fields and varies to some extent with the shape of the particles. A lower factor is obtained for fluids having particle volume lower than 50 percent, and for low field strengths.

The rate of response and release for electric fluids is found to be higher than for magnetic fluids. This is an important advantage for certain applications of the effect. Moreover, the difficulties encountered in the use of magnetic fluids, caused by residual magnetization, have no counterpart in the use of electric fluids. On the other hand purity of the ingredients used is far more important for electric than magnetic fluids. Thus, while soaps or other surface agents are used to advantage in both types of fluids to render them thixotropic and non-settling, and to preclude agglomeration which causes unstable torque during operation at high shear stresses, such agents in the case of the electric fluids must be chosen for minimum conductivity.

Maintenance of proper clearance between clutch surfaces is inherently more important for the electric than the magnetic type but is found to present no difficulties. For example, the small clutch unit of Fig. 5(C) has a clearance of about 0.01 cm maintained by the fluid itself, being in this respect like the plates of Fig. 3. The unit of Fig. 5(C) operates on a modulated bias of about 100 volts which is about one-third of the breakdown value. A similar unit having fluid-maintained spacing and connected to drive a switch was operated in a recycling circuit for 18 days (200,000 cycles) without breakdown of the fluid film.

While oil-like vehicles are used for both electric and magnetic fluids, in the first of necessity to sustain the electric field and in the second to lubricate and reduce eddy current losses, it is possible to use conductive vehicles in case of magnetic fluids. For example, a magnetic fluid of iron powder and mercury similar to one patented by Lucas[4] shows high values of induced shear resistance in a viscometer when subject to magnetic fields produced by direct or low frequency current.

Finely ground precipitates of magnetic oxides, that is, Fe_3O_4 and composite oxides or so-called ferrites of the type described by Snoek,[5] when dispersed in a low viscosity oil, have been found responsive to both magnetic and electric fields, either separately or simultaneously applied, to produce induced shear resistances many times the normal shear resistance of the fluid. Apparently, for best results, the internal resistance of the particles of an electric fluid should be moderately high and possessed of electron trapping properties. The viscometer used in testing fluids responsive to both magnetic and electric fields is similar to that shown in Fig. 1 except that the rotor has five annular grooves containing alternately wound magnetizing coils.

Relative to ultimate possibilities of fibration effects, it is a curious fact that the tractive force for pure iron, when subject to maximum magnetic induction of about 22,000 maxwells, is substantially the same as the tractive force for thin dielectric, when subject to maximum electric field strength, the latter being of the order of 4 to 15×10^6 volts per cm.[6]

In general, both phenomena have been found quite forceful, depending, of course, on the area of the working film, thus pointing to practical applications in clutches and brakes, Fig. 5(B), and hydraulic equipment, Fig. 5(A), using concentrated suspensions for the working fluid, these devices lending themselves to smooth regulation through electrical control of the applied fields.

[4] Ralph Lucas, U. S. Patent 2,149,782 (March 7, 1939).
[5] J. L. Snoek, U. S. Patents 2,452,529 to 31 (October 26, 1948).
[6] A. E. Austin and S. Whitehead, Proc. Roy. Soc. 176,33 (1940).

The Calculation of X-Ray Mass Absorption Coefficients

JOHN A. VICTOREEN
Radiation Laboratory, The Victoreen Instrument Company, Cleveland, Ohio
(Received March 17, 1949)

An empirical method of calculating mass absorption coefficients is given. Complete tables of constants are presented for calculating μ/ρ for all elements and for wave-lengths less than the K critical absorption wave-length. Partial tables give constants for wave-lengths between the L_1 and M_1 critical wave-lengths. Calculated mass absorption coefficients are given for the common elements.

INTRODUCTION

SPECTROSCOPISTS, since the discovery of the various series of spectral emission lines, have contributed much to the knowledge of atomic structure. Spectroscopic methods yield data of almost unbelievable accuracy which in turn lead to precise evaluation of the electronic energy states within an atom. There is, therefore, available much practical data pertaining to the emission of radiation by atoms.

Comparatively, little work has been done on the absorption of x-radiation by atoms. Methods of determining absorption coefficients do not even remotely approach the accuracy of spectroscopic methods and this has apparently discouraged investigation of the subject. Such data as are available are widely scattered in the literature and disagreement between observers is sufficiently great as to make any single observed value doubtful. There is great practical need for reasonably accurate values of the mass absorption coefficients of the elements.

It is the purpose of this paper to present an empirical method of calculating the values of the x-ray mass absorption coefficients for practical purposes. The accuracy appears to be of the order of one percent depending upon the constants selected as representing experimental values.

EQUATIONS

The absorption of radiation is related to the emission of radiation by the quantized structure of the atom. It has been found[1] that much of the mathematical treatment of the emission of radiation may be empirically employed in the calculation of mass absorption coefficients.

It is convenient here, as in spectroscopy, to use wave numbers instead of wave-lengths or frequencies. Thus, for present purposes we have

$$1/\lambda=(E_2/hc)-(E_1/hc)=\text{wave number}, \qquad (1)$$

where h is Planck's constant, 6.624×10^{-27} erg sec., λ is wave-length in cm, c is the velocity of light in cm/sec., and E_1 and E_2 are the energies in ergs of two quantum states within the atom.

It is possible to calculate the atomic energy states of Eq. (1) by means of the expression

$$\frac{E}{hc}=R\left\{\frac{(Z-s)^2}{n^2}+\left[\frac{\alpha^2(Z-s)^4}{n^4}\left(\frac{n}{k}-\frac{3}{4}\right)+\cdots\right]\right\}, \qquad (2)$$

where R is Rydberg's constant in reciprocal centimeters, Z is atomic number, s is a small screening constant, and n is the principal quantum number of the particular orbit. In calculating absorption coefficients, it has been assumed that $n/k=1$: where k is determined by angular momentum, spin moment, etc., and has been assumed to be equal to n, which may or may not be justifiable. The bracketed term is the relativity correction which must be carried to the higher powers of α^2 until the contribution of all the following terms may be neglected. $\alpha=2\pi e^2/ch$ is Sommerfeld's fine structure constant.

Expanding Sommerfeld's equation,[2] partly given by

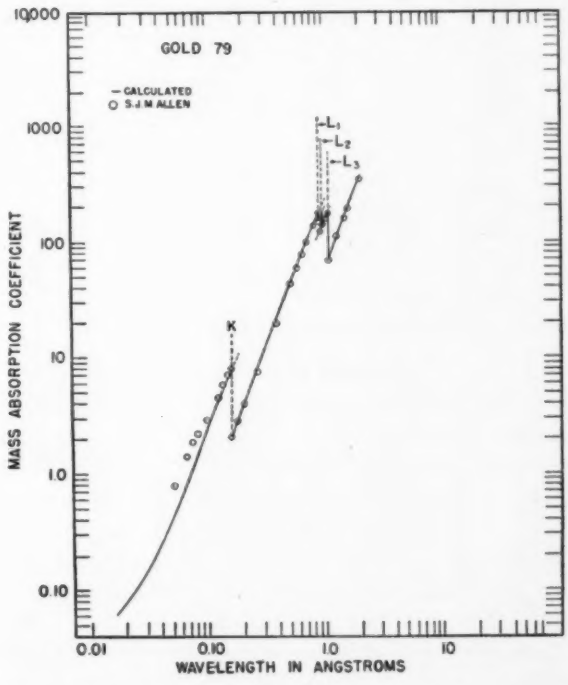

FIG. 1. Mass absorption coefficient of gold showing typical disagreement with Allen's tables at short wave-lengths. The calculated values are supported by other observers. (See reference 8.)

[1] J. A. Victoreen, J. App. Phys. **19**, 855 (1948).

[2] A. Sommerfeld, *Atomic Structure and Spectral Lines* (Methuen and Company, Ltd., London), third edition, p. 257 (1934).

TABLE I. Values of C, D, Z/A, and λ_3 for the elements (wave-length in angstroms).

Z	C	D	Z/A	Limit λ_3
1	0.01274	4.661×10^{-6}	0.9922	
2	0.05135	75.17×10^{-6}	0.4997	504.2
3	0.1499	493.7×10^{-6}	0.4322	
4	0.3647	2134.0×10^{-6}	0.4434	
5	0.6088	0.00451	0.4621	64.3
6	1.224	0.01421	0.5000	43.5
7	2.048	0.03167	0.4997	31.1
8	3.178	0.06544	0.5000	23.5
9	4.420	0.1169	0.4736	
10	6.497	0.2147	0.4954	
11	8.513	0.3438	0.4783	
12	11.59	0.5616	0.4934	9.496
13	14.60	0.8362	0.4820	7.935
14	18.47	1.144	0.4989	6.731
15	22.52	1.618	0.4835	5.774
16	28.70	2.368	0.4990	5.008
17	33.62	3.159	0.4794	4.383
18	38.08	4.040	0.4506	3.865
19	48.94	5.825	0.4859	3.431
20	59.32	7.871	0.4990	3.064
21	64.80	9.531	0.4656	2.751
22	74.25	12.04	0.4592	2.491
23	84.19	15.00	0.4514	2.263
24	98.63	19.21	0.4614	2.065
25	110.8	23.54	0.4551	1.891
26	128.5	29.63	0.4656	1.739
27	142.7	35.61	0.4580	1.604
28	166.9	44.95	0.4770	1.483
29	178.5	51.73	0.4561	1.377
30	200.0	62.24	0.4588	1.280
31	215.2	71.72	0.4446	1.190
32	236.0	84.05	0.4407	1.116
33	260.2	98.81	0.4405	1.042
34	279.6	113.0	0.4305	0.9777
35	312.0	134.0	0.4379	0.9180
36	335.1	152.7	0.4301	0.8637
37	368.1	177.9	0.4330	0.8141
38	401.5	204.8	0.4336	0.7683
39	441.2	237.6	0.4385	0.7255
40	478.2	271.6	0.4385	0.6873
41	520.8	311.5	0.4394	0.6515
42	557.9	351.0	0.4375	0.6184
43	596.9	394.6	0.4396	
44	640.1	444.0	0.4326	0.5584
45	695.8	506.4	0.4372	0.5330
46	735.7	560.4	0.4311	0.5079
47	796.6	634.9	0.4356	0.4844
48	835.5	696.1	0.4270	0.4631
49	892.9	777.0	0.4269	0.4429
50	940.2	853.8	0.4212	0.4239
51	996.7	943.9	0.4188	0.4060
52	1032	1018	0.4074	0.3892
53	1125	1156	0.4175	0.3734
54	1178	1259	0.4112	0.3577
55	1258	1398	0.4140	0.3440
56	1314	1518	0.4076	0.3307
57	1402	1681	0.4103	0.3181
58	1337	1665	0.4139	0.3062
59	1431	1847	0.4186	0.2951
60	1503	2047	0.4158	0.2845
61	1584	2196	0.4178	
62	1660	2384	0.4121	0.2644
63	1761	2617	0.4144	0.2548
64	1826	2808	0.4068	0.2462
65	1925	3062	0.4082	0.2376
66	2033	3341	0.4062	0.2301
67	2121	3602	0.4097	0.2226
68	2233	3916	0.4116	
69	2349	4254	0.4073	0.2085
70	2450	4578	0.4045	0.2016
71	2579	4972	0.4057	0.1951
72	2688	5343	0.4031	0.1901
73	2822	5782	0.4024	0.1836
74	2948	6225	0.4021	0.1782
75	3090	6721	0.4025	0.1735
76	3212	7194	0.3968	0.1675
77	3355	7737	0.3987	0.1620
78	3517	8347	0.3995	0.1577
79	3687	9006	0.4006	0.1532
80	3838	9642	0.3987	0.1489
81	3986	10298	0.3963	0.1444
82	4158	11045	0.3957	0.1404
83	4357	11899	0.3971	0.1367
84	4544	12752	0.4565	
85	4817	13887	0.4009	
86	4833	14314	0.3873	
87	5077	15443	0.3901	
88	5283	16501	0.3911	
89	5547	17785	0.3886	
90	4685	15337	0.3877	0.1127
91	4964	16764	0.3888	
92	5077	17593	0.3863	0.1065
93	5370	19090	0.392	
94	5610	20454	0.393	
95	5858	21907	0.394	
96	6142	23553	0.396	

TABLE II. K series.

Z	s	λ_1 n_1	n_2	λ_2 n_3	n_4	λ_3 n_5	n_6
1, 2, 3, 4	0	1	2	1	3	1	∞
5 to 13	½	1	3	1	4	1	∞
14 to 57	1	1	4	1	∞	1	∞
58 to 89	1	1	3	1	4	1	∞
90 to 96	1	1	2	1	3	1	∞

TABLE III. L series.

Z	s L_1	L_2	L_3	λ_1 n_1	n_2	λ_2 n_3	n_4	λ_3 n_5	n_6
6	2½			1	3	2	3	2	∞
13, 29, 35, 38	4			1	3	2	3	2	∞
42, 47, 50, 56	4			1	2	2	4	2	∞
73, 74, 78, 79, 82, 90	4	8	16	1	2	2	5	2	∞

Eq. (2), with $n/k=1$, we have:

$$\frac{E}{hc}=R\left\{\frac{(Z-s)^2}{n^2}+\left[\frac{1}{4}\frac{\alpha^2(Z-s)^4}{n^4}+\frac{1}{8}\frac{\alpha^4(Z-s)^6}{n^6}+\frac{1}{12.8}\frac{\alpha^6(Z-s)^8}{n^8}+\frac{1}{18.28}\frac{\alpha^8(Z-s)^{10}}{n^{10}}+\frac{1}{24.35}\frac{\alpha^{10}(Z-s)^{12}}{n^{12}}+\cdots\right]\right\}. \quad (3)$$

It has been shown[1] that the true atomic absorption coefficient is given within experimental error by the expression:

$$\tau_a=\left\{\left[3-\frac{\lambda}{\lambda_3}\right]\lambda\frac{\lambda}{\lambda_1}\frac{\lambda}{\lambda_2}\right\}\pi\frac{e^2}{mc^2}, \quad (4)$$

TABLE IV. Calculated mass absorption coefficients, K series.

λ	H 1	He 2	Li 3	Be 4	B 5	C 6	N 7
0.010	0.1134	0.0571	0.0494	0.0506	0.0528	0.0571	0.0571
0.012	0.1240	0.0624	0.0540	0.0554	0.0577	0.0624	0.0624
0.015	0.1388	0.0699	0.0605	0.0620	0.0646	0.0699	0.0699
0.020	0.1577	0.0794	0.0687	0.0705	0.0734	0.0794	0.0794
0.025	0.1736	0.0874	0.0756	0.0776	0.0808	0.0874	0.0874
0.030	0.1870	0.0939	0.0814	0.0835	0.0871	0.0941	0.0941
0.040	0.2083	0.1049	0.0910	0.0933	0.0973	0.1052	0.1053
0.050	0.2252	0.1134	0.0981	0.1006	0.1048	0.1135	0.1136
0.060	0.2407	0.1212	0.1049	0.1076	0.1122	0.1215	0.1217
0.080	0.2628	0.1325	0.1147	0.1176	0.1228	0.1331	0.1335
0.100	0.2794	0.1407	0.1219	0.1252	0.1307	0.1419	0.1428
0.12	0.2926	0.1474	0.1277	0.1314	0.1373	0.1494	0.1509
0.15	0.3081	0.1553	0.1347	0.1389	0.1455	0.1592	0.1621
0.20	0.3263	0.1647	0.1433	0.1487	0.1568	0.1741	0.1807
0.25	0.3366	0.1702	0.1489	0.1560	0.1662	0.1884	0.2013
0.3	0.3498	0.1773	0.1563	0.1660	0.1792	0.2089	0.2310
0.4	0.3599	0.1841	0.1660	0.1838	0.2061	0.2588	0.3111
0.5	0.3660	0.1899	0.1773	0.2083	0.2455	0.3357	0.4376
0.6	0.3736	0.1978	0.1939	0.2443	0.3037	0.4494	0.6252
0.8	0.3854	0.2171	0.2417	0.3552	0.4864	0.8119	1.226
1.0	0.3939	0.2433	0.3156	0.5330	0.7819	1.402	2.208
1.2	0.4069	0.2824	0.4258	0.7978	1.222	2.280	3.668
1.5	0.4318	0.3687	0.6731	1.393	2.213	4.256	6.949
2.0	0.4927	0.6064	1.362	3.058	4.980	9.765	16.07
2.5	0.5916	0.9970	2.494	5.789	9.517	18.76	30.95
3.0	0.7375	1.578	4.181	9.851	16.25	32.10	52.94
4.0	1.208	3.465	9.644	22.97	37.99	74.92	123.1
5.0	1.984	6.570	18.61	44.43	73.47	144.3	236.4
6.0	3.142	11.19	31.92	76.19	125.8	246.2	401.6
8.0	6.902	26.18	74.93	178.1	293.4	568.9	919.2
10	13.09	50.80	145.2	343.5	563.9	1082	1731
12	22.32	87.37	249.0	586.1	958.7	1821	2883
15	43.17	169.7	481.3	1122	1826	3413	5310
20	101.6	398.9	1120	2576	4149	7522	11320
25	197.6	772.9	2149	4863	7748	13574	19267
30	340.7	1325	3649	8118	12784	21549	29656
40	804.0	3094	8334	17878	27420	41983	
50	1564	5949					

λ	O 8	F 9	Ne 10	Na 11	Mg 12	Al 13	Si 14
0.010	0.0571	0.0541	0.0566	0.0546	0.0563	0.0551	0.0570
0.012	0.0625	0.0592	0.0619	0.0597	0.0616	0.0602	0.0623
0.015	0.0700	0.0663	0.0693	0.0669	0.0690	0.0675	0.0698
0.020	0.0795	0.0753	0.0788	0.0760	0.0784	0.0767	0.0794
0.025	0.0875	0.0829	0.0868	0.0838	0.0865	0.0845	0.0876
0.030	0.0943	0.0891	0.0935	0.0903	0.0933	0.0910	0.0945
0.040	0.1055	0.1000	0.1047	0.1012	0.1046	0.1024	0.1062
0.050	0.1138	0.1080	0.1132	0.1096	0.1134	0.1112	0.1155
0.060	0.1220	0.1159	0.1216	0.1179	0.1222	0.1201	0.1250
0.080	0.1342	0.1278	0.1347	0.1312	0.1367	0.1353	0.1417
0.100	0.1440	0.1378	0.1460	0.1432	0.1505	0.1502	0.1588
0.12	0.1529	0.1473	0.1573	0.1558	0.1654	0.1672	0.1788
0.15	0.1659	0.1619	0.1757	0.1771	0.1920	0.1985	0.2167
0.20	0.1897	0.1909	0.2145	0.2248	0.2541	0.2740	0.3100
0.25	0.2189	0.2292	0.2686	0.2938	0.3461	0.3882	0.4532
0.3	0.2614	0.2852	0.3482	0.3955	0.4822	0.5573	0.6652
0.4	0.3827	0.4513	0.5896	0.7092	0.9060	1.087	1.333
0.5	0.5769	0.7192	0.9807	1.218	1.594	1.950	2.420
0.6	0.8649	1.116	1.560	1.973	2.615	3.226	4.028
0.8	1.791	2.396	3.428	4.400	5.893	7.318	9.179
1.0	3.305	4.485	6.476	8.353	11.21	13.95	17.51
1.2	5.550	7.580	10.97	14.18	19.05	23.68	29.74
1.5	10.59	14.51	21.03	27.18	36.46	45.24	56.74
2.0	24.57	33.67	48.73	62.79	83.93	103.6	129.6
2.5	47.28	64.66	93.29	119.7	159.3	195.6	244.0
3.0	80.71	110.0	158.2	202.2	267.6	326.7	406.2
4.0	186.8	253.1	361.0	457.0	598.2	720.7	889.4
5.0	356.5	479.6	678.1	849.5	1097	1304	1591
6.0	601.9	803.5	1125	1393	1775	2072	2507
8.0	1359	1784	2447	2950	3634		
10	2524	3251	4350	5075			
12	4135	5215	6775				
15	7414	9000					
20	14957						

TABLE IV.—*Continued.*

λ	P 15	S 16	Cl 17	A 18	K 19	Ca 20	Ti 22
0.010	0.0553	0.0570	0.0548	0.0515	0.0555	0.0570	0.0525
0.012	0.0605	0.0623	0.0599	0.0563	0.0607	0.0624	0.0575
0.015	0.0677	0.0698	0.0672	0.0632	0.0682	0.0700	0.0645
0.020	0.0771	0.0795	0.0765	0.0719	0.0776	0.0798	0.0736
0.025	0.0882	0.0877	0.0844	0.0794	0.0858	0.0882	0.0815
0.030	0.0918	0.0948	0.0912	0.0859	0.0929	0.0956	0.0885
0.040	0.1034	0.1069	0.1031	0.0973	0.1054	0.1088	0.1014
0.050	0.1127	0.1168	0.1130	0.1070	0.1164	0.1206	0.1134
0.060	0.1223	0.1273	0.1236	0.1175	0.1285	0.1338	0.1273
0.080	0.1399	0.1470	0.1442	0.1388	0.1537	0.1623	0.1593
0.100	0.1587	0.1690	0.1683	0.1646	0.1852	0.1990	0.2024
0.12	0.1814	0.1963	0.1988	0.1978	0.2267	0.2480	0.2612
0.15	0.2255	0.2506	0.2607	0.2664	0.3131	0.3512	0.3871
0.20	0.3368	0.3899	0.4216	0.4463	0.5420	0.6261	0.7257
0.25	0.5096	0.6082	0.6754	0.7318	0.9065	1.065	1.268
0.3	0.7655	0.9315	1.051	1.154	1.445	1.713	2.068
0.4	1.572	1.956	2.244	2.496	3.159	3.775	4.609
0.5	2.891	3.622	4.181	4.673	5.932	7.107	8.697
0.6	4.835	6.078	7.033	7.870	9.998	11.98	14.64
0.8	11.05	13.91	16.10	18.01	22.85	27.34	33.25
1.0	21.08	26.52	30.65	34.21	43.30	51.64	62.37
1.2	35.75	44.87	51.74	57.60	72.68	86.38	103.5
1.5	68.00	85.06	97.67	108.2	135.8	160.5	189.7
2.0	154.4	191.8	218.6	240.1	298.5	348.8	401.4
2.5	288.7	355.9	402.0	437.1	537.1	619.4	
3.0	477.1	583.2	654.2	702.6	851.4	964.4	
4.0	1037	1230	1343				
5.0	1803	2107					

λ	Cr 24	Fe 26	Ni 28	Cu 29	Zn 30	Ge 32	Se 34
0.010	0.0528	0.0533	0.0546	0.0523	0.0526	0.0506	0.0494
0.012	0.0578	0.0584	0.0599	0.0573	0.0577	0.0555	0.0543
0.015	0.0649	0.0656	0.0673	0.0644	0.0649	0.0625	0.0612
0.020	0.0741	0.0750	0.0771	0.0739	0.7455	0.0719	0.0706
0.025	0.0822	0.0834	0.0860	0.0826	0.0833	0.0807	0.0796
0.030	0.0896	0.0911	0.0943	0.0907	0.0918	0.0893	0.0886
0.040	0.1034	0.1061	0.1110	0.1073	0.1092	0.1077	0.1082
0.050	0.1169	0.1215	0.1288	0.1255	0.1287	0.1290	0.1319
0.060	0.1330	0.1403	0.1512	0.1486	0.1537	0.1568	0.1634
0.080	0.1720	0.1880	0.2101	0.2102	0.2215	0.2342	0.2527
0.100	0.2266	0.2567	0.2968	0.3018	0.3230	0.3517	0.3896
0.12	0.3025	0.3533	0.4198	0.4323	0.4681	0.5204	0.5868
0.15	0.4664	0.5634	0.6888	0.7180	0.7862	0.8909	1.020
0.20	0.9100	1.134	1.420	1.495	1.651	1.898	2.198
0.25	1.622	2.050	2.593	2.741	3.037	3.507	4.073
0.3	2.669	3.395	4.311	4.561	5.059	5.847	6.787
0.4	5.987	7.637	9.706	10.26	11.37	13.11	15.16
0.5	11.29	14.38	18.23	19.25	21.28	24.41	28.05
0.6	18.98	24.10	30.41	32.02	35.31	40.25	45.92
0.8	42.80	53.86	67.24	70.38	77.11	86.58	97.05
1.0	79.59	99.10	122.1	126.9	138.0	152.1	
1.2	130.7	160.8	195.4	201.4	216.8		
1.5	235.7	284.0					
2.0	481.7						

where λ is incident wave-length in cm, e is electronic charge, m is electronic mass, c is the velocity of light, and τ is assumed to be the sum of the photoelectric absorption coefficient and the true absorption coefficient associated with scattering. λ_1, λ_2, and λ_3 are critical wave-lengths characteristic of the particular atom. It will be observed that $1/\lambda_1$, $1/\lambda_2$, $1/\lambda_3$ may be considered as wave numbers as given by Eq. (1) and that their values may be calculated from atomic energy states as given by Eq. (3).

The term e^2/mc^2 has a dimension of length and if, for the moment, we consider this as a fundamental unit of length l_0, we may assume the relation:[3]

$$e^2/mc^2 = l_0 = \lambda_0 = 2.8197 \times 10^{-13} \text{ cm}. \qquad (5)$$

If we multiply Eq. (4) by l_0 and divide by $\lambda_0 = l_0$, the bracketed term becomes dimensionless and we obtain

$$\tau_a = \left\{\left[3 - \frac{\lambda}{\lambda_3}\right]\frac{\lambda}{\lambda_0}\frac{\lambda}{\lambda_1}\frac{\lambda}{\lambda_2}\right\}\pi l_0^2, \qquad (6)$$

where λ_0 is assumed to be unit wave-length, l_0 is assumed

[3] A. H. Compton, *X-Rays and Electrons* (D. Van Nostrand Company, Inc., New York, 1926), p. 56.

TABLE IV.—*Continued.*

λ	Br 35	Kr 36	Rb 37	Sr 38	Mo 42	Pd 46	Ag 47
0.010	0.0503	0.0494	0.0498	0.0499	0.0505	0.0500	0.0505
0.012	0.0552	0.0543	0.0547	0.0548	0.0556	0.0551	0.0558
0.015	0.0641	0.0613	0.0618	0.0620	0.0631	0.0628	0.0636
0.020	0.0721	0.0710	0.0717	0.0721	0.0740	0.0743	0.0755
0.025	0.0814	0.0804	0.0814	0.0820	0.0851	0.0867	0.0884
0.030	0.0986	0.0899	0.0913	0.0924	0.0972	0.1006	0.1031
0.040	0.1118	0.1116	0.1142	0.1164	0.1269	0.1364	0.1411
0.050	0.1375	0.1385	0.1431	0.1473	0.1669	0.1863	0.1945
0.060	0.1719	0.1748	0.1822	0.1893	0.2221	0.2562	0.2695
0.080	0.2703	0.2794	0.2959	0.3121	0.3873	0.4680	0.4971
0.100	0.4219	0.4410	0.4722	0.5031	0.6461	0.8010	0.8558
0.12	0.6405	0.6744	0.7268	0.7792	1.020	1.282	1.353
0.15	1.121	1.187	1.286	1.382	1.841	2.333	2.502
0.20	2.425	2.578	2.802	3.026	4.045	5.130	5.500
0.25	4.498	4.785	5.201	5.618	7.492	9.448	10.11
0.3	7.492	7.964	8.630	9.333	12.37	15.47	16.51
0.4	16.69	17.69	19.16	20.60	26.87	32.89	34.88
0.5	30.78	32.51	35.05	37.54	47.96	57.09	
0.6	50.18	52.77	56.61	60.34	75.17		
0.8	105.0	109.2	115.7				

λ	Sn 50	Te 52	I 53	Xe 54	Ba 56	Ce 58	Nd 60
0.010	0.0490	0.0475	0.0488	0.0481	0.0478	0.0486	0.0490
0.012	0.0542	0.0526	0.0541	0.0534	0.0532	0.0540	0.0545
0.015	0.0620	0.0604	0.0622	0.0614	0.0614	0.0633	0.0631
0.020	0.0743	0.0728	0.0752	0.0746	0.0750	0.0762	0.0778
0.025	0.0880	0.0870	0.0902	0.0898	0.0912	0.0926	0.0954
0.030	0.1040	0.1038	0.1081	0.1083	0.1111	0.1140	0.1173
0.040	0.1466	0.1492	0.1570	0.1587	0.1661	0.1685	0.1785
0.050	0.2078	0.2152	0.2282	0.2327	0.2473	0.2507	0.2694
0.060	0.2942	0.3087	0.3295	0.3379	0.3632	0.3678	0.3990
0.080	0.5581	0.5950	0.6397	0.6606	0.7190	0.7332	0.7959
0.100	0.9733	1.045	1.127	1.167	1.277	1.293	1.415
0.12	1.571	1.693	1.828	1.895	2.077	2.095	2.295
0.15	2.871	3.095	3.343	3.466	3.795	3.808	4.165
0.20	6.324	6.764	7.292	7.544	8.221	8.177	8.884
0.25	11.49	12.28	13.20	13.62	14.74	14.53	15.62
0.30	18.61	19.77	21.17	21.75	23.34		
0.4	38.46						

λ	Tb 65	Ta 73	W 74	Pt 78	Au 79	Hg 80	Pb 82
0.010	0.0485	0.0488	0.0488	0.0490	0.0493	0.0493	0.0492
0.012	0.0543	0.0552	0.0552	0.0558	0.0562	0.0562	0.0563
0.015	0.0635	0.0657	0.0659	0.0673	0.0680	0.0682	0.0688
0.020	0.0798	0.0858	0.0865	0.0903	0.0917	0.0925	0.0944
0.025	0.1003	0.1124	0.1140	0.1215	0.1241	0.1259	0.1298
0.030	0.1264	0.1475	0.1504	0.1635	0.1677	0.1709	0.1778
0.040	0.2013	0.2508	0.2575	0.2878	0.2973	0.3049	0.3210
0.050	0.3142	0.4082	0.4210	0.4781	0.4955	0.5100	0.5403
0.060	0.4753	0.6326	0.6538	0.7484	0.7770	0.8008	0.8507
0.080	0.9689	1.315	1.361	1.564	1.625	1.675	1.780
0.100	1.734	2.357	2.439	2.794	2.899	2.986	3.163
0.12	2.813	3.797	3.923	4.464	4.623	4.751	5.010
0.15	5.076	6.723	6.925	7.767	8.010		
0.20	10.64						

to be unit radius, defining an area πl_0^2, and λ is incident wave-length in centimeters.

The scattering coefficient per electron σ_e is given by the Klein-Nishina[4] formula:

$$\sigma_e=\frac{8}{3}\frac{\pi e^4}{m^2c^4}\cdot\frac{3}{4}\left[\frac{1+\alpha_0}{\alpha_0^2}\left(\frac{2[1+\alpha_0]}{1+2\alpha_0}-\frac{1}{\alpha}\log[1+2\alpha_0]\right)+\frac{1}{2\alpha_0}\log[1+2\alpha_0]-\frac{1+3\alpha_0}{(1+2\alpha_0)^2}\right], \quad (7)$$

where $\alpha_0=h\nu/mc^2$ and ν is incident frequency.

[4] O. Klein and Y. Nishina, Zeits. f. Physik **52**, 853 (1928).

By rearrangement we obtain from Eqs. (5) and (7):

$$\sigma_e=\sigma_0\pi l_0^2=\pi l_0^2\left[\frac{2+2\alpha_0}{\alpha_0^2}\left(\frac{2[1+\alpha_0]}{1+2\alpha}-\frac{1}{\alpha}\log[1+2\alpha_0]\right)+\frac{1}{\alpha_0}\log[1+2\alpha_0]-2\frac{1+3\alpha_0}{(1+2\alpha_0)^2}\right], \quad (8)$$

where σ_0 represents the bracketed term which is the

TABLE IV.—*Continued.*

λ	Bi 83	Th 90	U 92
0.010	0.0496	0.0488	0.0490
0.012	0.0569	0.0562	0.0567
0.015	0.0696	0.0692	0.0703
0.020	0.0961	0.0964	0.0992
0.025	0.1329	0.1346	0.1400
0.03	0.1828	0.1865	0.1956
0.04	0.3320	0.3406	0.3612
0.05	0.5605	0.5747	0.6124
0.06	0.8834	0.9020	0.9624
0.08	1.849	1.860	1.981
0.10	3.279	3.236	3.426
0.12	5.180		

λ	Air	Water	Nylon	Polyethylene	Polystyrene
0.010	0.05700	0.0634	0.0624	0.0651	0.0614
0.012	0.0623	0.0693	0.0683	0.0712	0.0672
0.015	0.0698	0.0777	0.0762	0.0789	0.0752
0.020	0.0793	0.0882	0.0869	0.0906	0.0854
0.025	0.0873	0.0971	0.0956	0.0998	0.0941
0.030	0.0941	0.1046	0.1030	0.1075	0.1013
0.040	0.1052	0.1170	0.1151	0.1201	0.1133
0.050	0.1136	0.1263	0.1242	0.1295	0.1221
0.060	0.1217	0.1353	0.1330	0.1386	0.1307
0.080	0.1337	0.1486	0.1457	0.1517	0.1431
0.100	0.1433	0.1591	0.1554	0.1617	0.1526
0.12	0.1520	0.1686	0.1638	0.1700	0.1605
0.15	0.1643	0.1819	0.1747	0.1806	0.1708
0.20	0.1862	0.2050	0.1916	0.1959	0.1858
0.25	0.2123	0.2321	0.2084	0.2097	0.1999
0.30	0.2501	0.2713	0.2323	0.2291	0.2198
0.40	0.3561	0.3801	0.2921	0.2733	0.2666
0.50	0.5250	0.5533	0.3845	0.3406	0.3380
0.60	0.7750	0.8099	0.5212	0.4385	0.4435
0.80	1.575	1.634	0.9573	0.7506	0.7788
1.00	2.879	2.979	1.667	1.257	1.324
1.2	4.805	4.974	2.723	2.010	2.134
1.5	9.110	9.454	5.096	3.706	3.995
2.0	20.96	21.88	11.79	8.432	9.046
2.5	40.02	42.06	22.46	16.15	17.35
3.0	67.80	71.76	38.37	27.59	29.67
4.0		166.0	89.24	64.33	69.20
5.0		316.9	171.3	123.9	133.3
6.0		534.9	291.0	211.3	227.4
8.0		1208	667.0	488.1	525.3
10		2243	1258	928.8	999.5

dimensionless part of the electronic scattering coefficient σ_e.

The atomic scattering coefficient σ_a is obtained by multiplying Eq. (8) by Z, the number of electrons per atom, and we then have

$$\sigma_a = \sigma_0 Z \pi l_0^2. \tag{9}$$

Combining Eqs. (6) and (9) and multiplying by N_0/A the number of atoms per gram, we have for the mass absorption coefficient μ/ρ:

$$\frac{\mu}{\rho} = \frac{\tau}{\rho} + \frac{\sigma}{\rho} = \left\{\left[\frac{3\lambda^3}{\lambda_0\lambda_1\lambda_2} - \frac{\lambda^4}{\lambda_0\lambda_1\lambda_2\lambda_3}\right] + \sigma_0 Z\right\} \pi l_0^2 \frac{N_0}{A}, \tag{10}$$

where λ is the incident wave-length in centimeters.

Calculated values agree well with experimentally observed values, as given in Allen's tables[5] for all elements. Any obvious deviations appear to result from experimental error, which is substantiated by reference to other observers. A typical example is the deviation below 0.2A observed in Fig. 1. Allen's generally excellent tables contain a wave-length error for most elements below 0.2A which in some cases appears as an error in the observed value of μ/ρ amounting to over 60 percent.

CALCULATION

For purposes of tabulation, Eq. (10) may be rearranged to minimize computation. Substituting and collecting numerical values for the physical constants, we have

$$\left(\frac{\mu}{\rho}\right)_Z = C\lambda^3 - D\lambda^4 + \sigma_e N_0 \frac{Z}{A}. \tag{11}$$

A graph showing the variation of μ/ρ with λ for gold is given in Fig. 1. Values of μ/ρ were calculated from Eq. (11) using the values of C and D as given in Table I.

[5] A. H. Compton and S. K. Allison, *X-Rays in Theory and Experiment* (D. Van Nostrand Company, Inc., New York, 1935), S. J. M. Allen's Tables, pp. 800–806.

For wave-lengths other than those given in Table V, it is necessary to calculate values of $\sigma_0\pi l_0^2 N_0$ from the Klein-Nishina formula, Eq. (8).

For wave-lengths greater than λ_k it is necessary to assign values to s and n as given in Table III, for the L series, and to calculate values of C and D for the particular wave-length region. This work has not been completed.

TABLES

Table I gives values of C and D for Eq. (11). Values of Z/A are given as well as λ_k which defines the limiting wave-length for which Eq. (11) is valid without change in constants. All wave-lengths are in angstroms.

Tables II and III give values of the constants for Eq. (3) which have been found to give good agreement with experimentally observed values[6] of μ/ρ when μ/ρ is calculated from Eq. (10) or (11).

For present purposes the apparently arbitrary assignment of values to s and n is consistent and systematic, with appropriate change for the K, L_1, L_2, L_3, etc., absorption regions, and atomic number groups.

The physical constants used in calculation are those suggested by Birge.[7]

Table IV gives values of μ/ρ, for various elements, calculated from Eqs. (10) or (11).

Table V gives values of $\sigma_0\pi l_0^2 N_0$ for Eq. (10) or (11).

SUMMARY

Equation (6) expediently assumes a unit of length $l_0=e^2/mc^2$. It is possible to obtain a slightly different interpretation of this by rearranging Eq. (6), thus

$$\tau_a=\left\{1-\frac{1}{3}\frac{\lambda}{\lambda_3}\right\}\frac{3}{4\pi}\frac{\lambda}{\lambda_0}\frac{\lambda}{\lambda_1}\frac{\lambda}{\lambda_2}\cdot\left(\frac{2\pi e^2}{mc^2}\right)^2, \qquad (12)$$

in which case the term $3/4\pi\lambda_0$ becomes $1/\lambda_m=3mc^2/4\pi e^2$ where λ_m has been previously suggested[3] as a limiting minimum wave-length.

The obvious experimental error of observed mass absorption coefficients available in the literature makes it difficult to determine the value of the screening constant s in Eq. (2). The values of 0, $\frac{1}{2}$, and 1 for the K level appear satisfactory and have been used solely because of agreement with experimental data. One may speculate that the quantum conditions which obtain at the instant of quantum ejection may not be the same as those existing at the instant of quantum absorption, but lead to values of about the same magnitude.

The term $n/k=1$ in Eq. (2) has also been used because of agreement with experimental data. Unlike the screening constant s, k normally changes over values which would be readily detectable in the value of μ/ρ and it would appear that only the one condition, $n/k=1$, is satisfactory for this purpose.

Term values given are not assumed to be correct, but satisfactory, until more accurate values can be established. It is believed that the values of μ/ρ obtained from them are more accurate, however, over a wide range of wave-lengths and atomic numbers than those obtained from any single observer.

In Eq. (10), λ_3 differs from λ_k by about 20 percent for elements of low atomic number and approaches equality at high atomic numbers. Substitution of λ_k for λ_3, however, does not produce satisfactory agreement.

The value of R for infinite nuclear mass has been used without correction for finite values. The correction would be negligible for present purposes.

For each series of discontinuities such as the L_1, L_2, and L_3, the value of n in Eq. (3) appears to remain unchanged, while s may be 4, 8, 16 (for $Z=79$) for the $K-L_1$, L_1-L_2, L_2-L_3 regions.

All data given for the L series in the tables are tentative, due to small number of published observed values and wider experimental error in this region.

A discussion of the errors encountered in published values of mass absorption coefficients has been given elsewhere.[8]

Calculations have all been carried to five significant figures, although this should not be taken as indicative of the absolute value. The transitions given by the values of n_1, n_2, etc. on Tables II and III are probably not actual but approximate the sum of a series of such transitions which accompany the event of absorption.

TABLE V. Maximum value 0.4011, wave-length in angstroms.

λ	$\sigma_0\pi l_0^2 N_0$	λ	$\sigma_0\pi l_0^2 N_0$	λ	$\sigma_0\pi l_0^2 N_0$	λ	$\sigma_0\pi l_0^2 N_0$
0.0010	0.0262	0.010	0.114	0.10	0.282	1.0	0.384
0.0012	0.0300	0.012	0.125	0.12	0.295	1.2	0.388
0.0015	0.0350	0.015	0.140	0.15	0.310	1.5	0.392
0.0020	0.0431	0.020	0.159	0.20	0.329	2.0	0.394
0.0025	0.0502	0.025	0.175	0.25	0.339	2.5	0.396
0.0030	0.0566	0.030	0.188	0.30	0.352	3.0	0.397
0.0040	0.0680	0.040	0.210	0.40	0.362	4.0	0.397
0.0050	0.0778	0.050	0.227	0.50	0.367	5.0	0.398
0.0060	0.0866	0.060	0.243	0.60	0.374	6.0	0.399
0.0080	0.101	0.080	0.265	0.80	0.382	8.0	0.400

[6] See reference 5, pp. 792–793.

[7] R. T. Birge, Rev. Mod. Phys. **13**, 233 (1941). Also see reference 3.

[8] J. A. Victoreen, J. App. Phys. **14**, 95 (1943).

Electron Transit Time in Space-Charge Limited Current between Coaxial Cylinders

PAUL L. COPELAND AND DELBERT N. EGGENBERGER*
Department of Physics, Illinois Institute of Technology, Chicago, Illinois
(Received March 31, 1949)

From information about space-charge-limited currents, the transit time of electrons between a cylindrical cathode and an external coaxial anode has been computed. Taylor's series expansions of the functions useful in the calculations are given. These together with the tabulated values permit rapid calculation of electron transit times with an accuracy of 0.1 percent.

ALTHOUGH the large ratio of the charge to the mass of electrons makes them highly mobile, so that for many purposes it is unnecessary to consider the transit time in thermionic vacuum tubes, it has become important to determine the transit time in tubes that are used at very high frequencies. It must be obvious that the operation of ordinary grid-controlled tubes, depending as it does on the space-charge limitation of thermionic emission, is dependent on finite electron transit time. The space charge is set up by swarms of electrons in space, and for a given current it is proportional to the time that each electron spends in passing from cathode to anode. It is hence natural to use the well-known relationships for space-charge-limited current as a means of obtaining information concerning electron transit times. Ferris[1] has used these principles for comparing the transit time of electrons between coaxial cylinders with that between parallel planes of the same separation, and he has given a graph for the factor k which, when multiplied by the electrode separation and divided by the electron velocity at the anode, gives the transit time of the electrons. Practical use of the graph given by Ferris for the calculation of transit times is limited by uncertainties of about one percent. In the present paper functions convenient for the accurate calculation of transit time are developed.

BASIS OF THE COMPUTATION

The most elementary treatment of space-charge flow involves certain idealizations of the physical situation which simplify the mathematical analysis. The electrons are assumed to be emitted from an equipotential cathode with negligible initial velocities. Hence, each electron has an energy that is determined by the potential difference between its position in space and the cathode. These simplifying assumptions make the transit-time problem definite, and they will be used as the basis of the calculations presented in this paper.

Combination of Poisson's equation with the current density relation, $J=\rho v$, results in the equation

$$1/v=-\nabla^2V/4\pi J, \tag{1}$$

where V is the potential in statvolts relative to the cathode, J is the current-density in statamperes/cm², and v is the velocity of the electron in cm/sec. Transit times may then be computed from the differential equation

$$dt=ds/v=-ds\nabla^2V/4\pi J, \tag{2}$$

where ds is the displacement of the electron in cm during the time dt sec. The expression for the element of time gives a positive result, because the current density and the Laplacian operating on the potential differ in sign. For coaxial cylinders with the Laplacian operator reduced to dependence on the radius r only, Eq. (2) becomes

$$dt=-dr\nabla^2V/4\pi J=-dr\frac{d\left(r\frac{dV}{dr}\right)}{dr}\Big/4\pi Jr. \tag{3}$$

Let $J'=2\pi Jr$ be the current between the cylinders per centimeter of axial length, which is a constant for the problem considered. Equation (3) contains only perfect differentials, and the integration gives

$$t_2-t_1=-\frac{1}{2J'}\left[r_2\left(\frac{dV}{dr}\right)_2-r_1\left(\frac{dV}{dr}\right)_1\right]. \tag{4}$$

The negative of the quantity in brackets divided by the factor 2 is just the total charge per unit of length contained between the cylinder of radius r_2 and the cylinder of radius r_1. Thus, the transit time between any two cylinders coaxial with the cathode is the space charge between them divided by the current between them. The result that has just been derived is subject only to the conditions implied in the fundamental relationships for energy, current density, and potential. In particular, since the equation for current density accounts only for the conduction current and neglects the Maxwell displacement current, the result is restricted to those cases in which the displacement current is truly negligible. If the transit time turns out to be a small fraction of the period of any a.c. component that is applied to the coaxial cylinders, the transit time may be computed from the instantaneous potential differences. Equation (4) is not restricted to the case of space-charge-limited current, nor is it restricted in applicability to the electrode cylinders alone.

The present discussion will be concerned with the space-charge-limited current between a cylindrical

* Now at Armour and Company.
[1] W. R. Ferris, Proc. I.R.E. 24, 82 (1936).

cathode and a coaxial external cylindrical anode. In accordance with the conventions for the treatment neglecting the initial velocities of the electrons, the potential gradient is assumed to be zero at the cathode. Hence Eq. (4) reduces to

$$t=-r_p\left(\frac{dV}{dr}\right)_p\Big/2J', \tag{5}$$

where t is the time of transit from cathode to anode, and the subscript p is attached to quantities evaluated at the anode.

As a result of theoretical studies by Langmuir and Blodgett,[2] the potential distribution between coaxial cylinders carrying space-charge-limited current may be written as

$$V=\left[\frac{9}{4}J'\left(\frac{2m}{e}\right)^{\frac{1}{2}}\right]^{\frac{2}{3}}[r\beta^2]^{\frac{1}{3}}, \tag{6}$$

where β satisfies the differential equation

$$3\beta\frac{d^2\beta}{du^2}+\left(\frac{d\beta}{du}\right)^2+4\beta\frac{d\beta}{du}+\beta^2=1, \tag{7}$$

and $u=\ln r/a$, a being the radius of the cathode. The use of these expressions in the equation for the transit time gives

$$t=\frac{3\sqrt{2}}{4}\left(\frac{m}{eV_p}\right)^{\frac{1}{2}}r_p\beta\left(\beta+2r_p\frac{d\beta}{dr}\right), \tag{8}$$

and the transit time may be determined from information concerning geometry and potential difference if both β and $r(d\beta/dr)=d\beta/du$ are assumed to be known.

SPACE-CHARGE-LIMITED CURRENTS BETWEEN COAXIAL CYLINDERS

Langmuir and Blodgett[2] have given the solution of Eq. (7) in the form of a power series in u, and they have calculated the coefficients of the first fourteen terms. While this series is entirely satisfactory for small values of u, the calculations become very tedious when u is larger than 5. The situation is even worse when an attempt is made to evaluate the derivative of β with respect to u.

Recently Page and Adams[3] have succeeded in eliminating the first of these difficulties by developing a power series the coefficients of which contain trigonometric functions of the ratio of the radii. This series converges very rapidly when the ratio of the radii is large. The calculations of β^2 tabulated by Page and Adams show a general agreement with those given by Langmuir and Blodgett. There are differences in detail. Furthermore, the series given by Page and Adams does not lend itself to a convenient calculation of $d\beta/du$.

[2] I. Langmuir and K. B. Blodgett, Phys. Rev. 22, 347 (1923)
[3] L. Page and N. I. Adams, Phys. Rev. 68, 126 (1945).

For use in the calculation of transit times by Eq. (8), it is important to have β and $d\beta/du$ expressed as rapidly converging power series in u. Taylor's series expansions in the variable $(u-u_i)$ may be obtained for various convenient values u_i of the variable u which are distributed throughout the range within which the behavior of the function is of interest. Assume that the solution of the differential equation in the form of the series given by Langmuir and Blodgett and its derivative obtained through a term by term differentiation may be used to calculate the values of β and $d\beta/du$ at u_1, which is the first of the values about which β is to be expanded in a Taylor's series. These values β_1 and $(d\beta/du)_1$ enter the new power series expansion as the two arbitrary constants which are required for adjusting a solution of the second-order differential equation to the boundary conditions. It is not feasible to obtain the higher order derivatives through successive differentiations of the series given by Langmuir and Blodgett, but the differential equation itself may be used for this purpose. Equation (7) gives directly

$$\frac{d^2\beta}{du^2}=\left[1-\beta^2-4\beta\frac{d\beta}{du}-\left(\frac{d\beta}{du}\right)^2\right]\Big/3\beta.$$

A single differentiation of Eq. (7) gives

$$\frac{d^3\beta}{du^3}=\left[-5\frac{d^2\beta}{du^2}\frac{d\beta}{du}-4\left(\frac{d\beta}{du}\right)^2-4\beta\frac{d^2\beta}{du^2}-2\beta\frac{d\beta}{du}\right]\Big/3\beta. \tag{9}$$

A second differentiation of Eq. 7 gives

$$\beta^4=[-8\beta^3\beta^1-5(\beta^2)^2-12\beta^1\beta^2-4\beta\beta^3-2(\beta^1)^2-2\beta\beta^2]/3\beta, \tag{10}$$

where, because the only power of β appearing is the first, exponents need not be reserved for expressing powers of β, and they may be used for expressing the order of the derivative of β with respect to u. In more conventional notation when numbers are used thus, they are enclosed in parentheses or written as Roman numerals. The conventional notation is not necessary in this problem if it is recognized that β is not the same as β^1, and that the exponents applied to parentheses are used to denote powers rather than derivatives. A third differentiation, expressed in this notation, gives

$$\beta^5=[-11\beta^4\beta^1-18\beta^3\beta^2-16\beta^3\beta^1-4\beta\beta^4-12(\beta^2)^2-6\beta^2\beta^1-2\beta\beta^3]/3\beta. \tag{11}$$

The writing of these expressions may be simplified somewhat when $\beta=1$, and expansions may be made about the values of u for which β becomes unity. Particularly simple expressions are obtained when β attains a maximum or a minimum value, which may be denoted by β_m. Then all terms containing $d\beta/du$ may be dropped from the final expressions.

$$d^2\beta/du^2=(1-\beta_m^2)/3\beta_m, \tag{12a}$$

TABLE I. Data for calculation of transit time.

u	r/a	β	$d\beta/du$	$\beta\left(\beta+2\frac{d\beta}{du}\right)$
0	1	0	1	0
2.4147	11.186	1	0.0907	1.1814
3.7265	41.53	1.04267	0	1.09471
9.151	9426	1	−0.001034	0.99793
10.458	34,807	0.99947	0	0.99894
0.00995	1.010	0.00991	0.99207	0.01976
0.100	1.105	0.09608	0.9227	0.1865
0.300	1.3499	0.26636	0.7833	0.4882
1.000	2.718	0.67896	0.42554	1.0388
1.900	6.686	0.93415	0.17117	1.19242
2.000	7.389	0.95033	0.15263	1.19322
2.100	8.166	0.96473	0.13559	1.19231
2.30259	10.0	0.9890	0.10526	1.1864
3.000	20.086	1.0353	0.03505	1.1444
4.6052	100.0	1.0384	−0.01440	1.0484
6.000	403.43	1.0178	−0.01263	1.0103
6.908	1000.0	1.0085	−0.00793	0.9926
8.000	2981.0	1.0024	−0.00353	0.9978
9.210	10,000	1.0008	−0.00143	0.9986

$$d^3\beta/du^3=-4(d^2\beta/du^2)/3, \tag{12b}$$

$$\beta^4\equiv d^4\beta/du^4=[-5(\beta^2)^2-4\beta_m\beta^3-2\beta_m\beta^2]/3\beta_m, \tag{12c}$$

$$\beta^5=[-18\beta^3\beta^2-4\beta_m\beta^4-12(\beta^2)^2-2\beta_m\beta^3]/3\beta_m, \tag{12d}$$

$$\beta^6=[-29\beta^4\beta^2-18(\beta^3)^2-40\beta^3\beta^2-4\beta_m\beta^5-2\beta_m\beta^4-6(\beta^2)^2]/3\beta_m, \tag{12e}$$

$$\beta^7=[-43\beta^5\beta^2-65\beta^3\beta^4-40(\beta^3)^2-60\beta^4\beta^2-4\beta_m\beta^6-20\beta^3\beta^2-2\beta_m\beta^5]/3\beta_m. \tag{12f}$$

If $1-\beta^2\ll\beta_m$ as is the case for maxima and minima higher than the first, for $n\geqslant 4$

$$\beta^n\simeq(-4\beta^{n-1}-2\beta^{n-2})/3. \tag{12g}$$

SERIES USEFUL IN THE CALCULATION OF TRANSIT TIME

Because the series for β, which has been given by Langmuir and Blodgett,[2] is entirely satisfactory as a basis for the calculation of transit time for low values of u, the quantity $\beta[\beta+2(d\beta/du)]$ has been evaluated through term by term operations with this series. The result which we have obtained may be expressed in the form

$$\beta[\beta+2(d\beta/du)]=20U-140U^2+573.33333U^3-1657.5774U^4+3711.341U^5-6783.556U^6+10475.13U^7-14006.97U^8+16516.7U^9-17416.7U^{10}+16612.5U^{11}-14465U^{12}+11460U^{13}-8310U^{14}+\cdots, \tag{13}$$

where $U\equiv u/10$. Calculations of transit time by Eq. (13) for values of u as high as 3 have been checked against other independent calculations of transit time for the same values of u, and it is believed that throughout this range the errors involved in using Eq. (13) are less than 0.1 percent. The Taylor's series expansions discussed previously are most important at higher values of u.

Our own calculations based on the series of Langmuir and Blodgett show that the first maximum of β occurs at $r/a=41.53$ or $u=3.7265$. These values have been checked by the use of the series of Page and Adams. At the first maximum we have found that the value of β given by the series of Langmuir and Blodgett is 1.04626, whereas the corresponding value calculated from the series of Page and Adams is 1.04628. At the first maximum, therefore, our estimate of β is 1.04627. Hence the relationships (12) give for the power series expansion about the first maximum

$$\beta=1.04627-1.5081(\Delta U)^2+6.7021(\Delta U)^3-14.566(\Delta U)^4+19.4(\Delta U)^5-18(\Delta U)^6+15(\Delta U)^7-13(\Delta U)^8+\cdots, \tag{14}$$

where $\Delta U\equiv(u-3.7265)/10$. Differentiation with respect to u gives

$$d\beta/du=-0.30162\Delta U+2.0106(\Delta U)^2-5.826(\Delta U)^3+9.70(\Delta U)^4-10.8(\Delta U)^5+10.5(\Delta U)^6-10.5(\Delta U)^7+\cdots. \tag{15}$$

Although the behavior of β at values of u greater than that corresponding to the first maximum is quite simple and is fairly well known, an expansion about the second unity of the function β is useful for calculations. The second unity occurs at a value of $r/a=9426$ or $u=9.151$, and at this point $d\beta/du=-0.001034$. The higher derivatives calculated from Eqs. (7), (9), (10), and (11) are used in the coefficients of the Taylor's series.

$$\beta=1.00000-0.01034(\Delta U)+0.06892(\Delta U)^2-0.1912(\Delta U)^3+0.254(\Delta U)^4-0.039(\Delta U)^5+\cdots. \tag{16}$$

$$d\beta/du=-0.001034+0.01378\Delta U-0.0574(\Delta U)^2+0.102(\Delta U)^3-0.2(\Delta U)^4+\cdots, \tag{17}$$

where here $\Delta U\equiv(u-9.151)/10$. The Taylor's series expansions about all of the higher maxima and minima are easily obtained from the corresponding values of β_m.

TABULATION OF RESULTS

The primary points about which expansions have been made are those values of u for which either β becomes unity or $d\beta/du$ vanishes. Langmuir and Compton[4] have tabulated these values, without, however, extending them to the computation of transit time, and our values, listed in the first part of Table I, cover the range in which discrepancies[5] between their calculations and ours would lead to significant differences when the results are applied to the calculation of transit time.

[4] I. Langmuir and K. T. Compton, Rev. Mod. Phys. 3, 247 (1931).

[5] Compton and Langmuir give the position of the first maximum as $r/a=44.05$ or $u=3.7827$. Our calculations show that the maximum occurs when $r/a=41.53$ or $u=3.7265$. The difference in the calculated transit time is roughly 4 percent in the vicinity of the first maximum.

VARIATION OF TRANSIT TIME WITH CATHODE RADIUS

If the outer or anode cylinder is of fixed radius and the inner or cathode cylinder is imagined to shrink in size with the potential difference maintained constant, the transit time varies both on account of the change in path length and on account of the change in the electrostatic field distribution. If the difference between the radii of the cylinders is small, the transit time is relatively small because of the short path. As the cathode radius is made smaller, the transit time first increases because the distance to be traversed increases. The concentration of the field in the neighborhood of the cathode, of course, acts to accelerate the electrons more rapidly as the cathode radius is decreased, and when the ratio of the radii is about 6.7, the transit time approaches a maximum. It then decreases and oscillates about a value which is just half that for electrons between parallel planes with the same potential difference and a separation equal to the radius of the anode cylinder.

Bending of a Thin Circular Plate of an Aeolotropic Material under Uniform Lateral Load (Supported Edge)

H. ŌKUBO
Institute of High Speed Mechanics, Tōhoku University, Sendai, Japan
(Received March 30, 1949)

The bending problem is solved mathematically for a thin circular plate subjected to a uniform load. The material of the plate is assumed to have three symmetrical planes with respect to its elastic properties. The solution is carried out in the case when the edge is simply supported, and it involves some numerical calculations. An empirical formula for the deflection is also given in a simpler form.

IN this paper, the bending problem of a thin circular plate with supported edge subjected to uniform lateral load is treated. It is well known from early times that the problem is solved for the case of a plate of an isotropic material. In the case of the aeolotropy, the mathematical analysis is quite similar with the case of the isotropy when the edge is clamped. But when the edge is supported, the analysis is quite different from that of the isotropy.

Let us assume that the material of the plate has three planes of symmetry with respect to its elastic properties. Taking these planes as coordinate planes, the relations between the stress and strain components for the case of plane stress can be represented by

$$\left.\begin{aligned} e_{xx}&=S_{11}X_x+S_{12}Y_y,\\ e_{yy}&=S_{22}Y_y+S_{12}X_x,\\ e_{xy}&=S_{66}X_y. \end{aligned}\right\} \tag{1}$$

The plate is assumed to be of uniform thickness h, and we take x, y axes in the plane of the plate before bending. If we denote the deflection at any point of the plate by w, then we have[1]

$$D_1\frac{\partial^4 w}{\partial x^4}+2(D_2+D_4)\frac{\partial^4 w}{\partial x^2\partial y^2}+D_3\frac{\partial^4 w}{\partial y^4}=q, \tag{2}$$

where q is the intensity of the load and

$$D_1=\frac{h^3S_{22}}{12(S_{11}S_{22}-S_{12}^2)},\quad D_3=\frac{h^3S_{11}}{12(S_{11}S_{22}-S_{12}^2)},$$

$$D_2=-\frac{h^3S_{12}}{12(S_{11}S_{22}-S_{12}^2)},\quad D_4=\frac{h^3}{6S_{66}}.$$

[1] S. Timoshenko, *Theory of Plates and Shells* (McGraw-Hill Book Company, Inc., 1940), p. 189.

Equation (2) can be transformed into

$$\left(\frac{\partial^2}{\partial x^2}+\frac{1}{k_1^2}\frac{\partial^2}{\partial y^2}\right)\left(\frac{\partial^2}{\partial x^2}+\frac{1}{k_2^2}\frac{\partial^2}{\partial y^2}\right)w=\frac{q}{D_1}, \tag{3}$$

in which

$$k_1=\frac{D_1^{\frac{1}{2}}}{(D_2+D_4+\{(D_2+D_4)^2-D_1D_3\}^{\frac{1}{2}})^{\frac{1}{2}}},$$

$$k_2=\frac{D_1^{\frac{1}{2}}}{(D_2+D_4-\{(D_2+D_4)^2-D_1D_3\}^{\frac{1}{2}})^{\frac{1}{2}}}.$$

If we denote the particular solution of the differential equation (3) by w_0, then the general solution can be expressed by

$$w=w_0+R[f_1(x+ik_1y)+f_2(x+ik_2y)], \tag{4}$$

where f_1 and f_2 are arbitrary functions and R denotes the real part of the complex function.

We consider a circular plate with radius unity and transform the Cartesian coordinates into the following curvilinear coordinates

$$\left.\begin{aligned} x+iy&=e^{\alpha+i\beta}\\ x+ik_1y&=c'\cosh(\alpha'+i\beta'),\\ x+ik_2y&=c''\cosh(\alpha''+i\beta''), \end{aligned}\right\} \tag{5}$$

provided with

$$c'\cosh a'=1,\quad c'\sinh a'=k_1,$$
$$c''\cosh a''=1,\quad c''\sinh a''=k_2.$$

The bounding circle of the plate is expressed by $\alpha=0$, $\alpha'=a'$ and $\alpha''=a''$ respectively. By virtue of the transformation (5), at the boundary we find

$$\beta=\beta'=\beta''. \tag{6}$$

Now, putting

$$w=R[f_1(x+ik_1y)+f_2(x+ik_2y)]+C_1x^4+C_2x^2y^2+C_3y^4+C_4x^2+C_5y^2+C_6, \quad (7)$$

and

$$\left.\begin{aligned} f_1''(x+ik_1y)&=\sum_{n=2}^{\infty}A_n\cosh 2n(\alpha'+i\beta'),\\ f_2''(x+ik_2y)&=\sum_{n=2}^{\infty}B_n\cosh 2n(\alpha''+i\beta''),\end{aligned}\right\} \quad (8)$$

we have

$$\begin{aligned} w=&\frac{c'^2}{4}\sum_{n=2}^{\infty}A_n\left\{\frac{\cosh(2n+2)\alpha'}{(2n+2)(2n+1)}\cos(2n+2)\beta'\right.\\ &-\left[\frac{1}{(2n+1)2n}+\frac{1}{2n(2n-1)}\right]\cosh 2n\alpha'\cos 2n\beta'\\ &\left.+\frac{\cosh(2n-2)\alpha'}{(2n-1)(2n-2)}\cos(2n-2)\beta'\right\}\\ &+\frac{c''^2}{4}\sum_{n=2}^{\infty}B_n\left\{\frac{\cosh(2n+2)\alpha''}{(2n+2)(2n+1)}\cos(2n+2)\beta''\right.\\ &-\left[\frac{1}{(2n+1)2n}+\frac{1}{2n(2n-1)}\right]\cosh 2n\alpha''\cos 2n\beta''\\ &\left.+\frac{\cosh(2n-2)\alpha''}{(2n-1)(2n-2)}\cos(2n-2)\beta''\right\}\\ &+C_1x^4+C_2x^2y^2+C_3y^4+C_4x^2+C_5y^2+C_6. \end{aligned} \quad (9)$$

To satisfy the differential Eq. (3)

$$3D_1C_1+(D_2+D_4)C_2+3D_3C_3=\frac{q}{8}. \quad (10)$$

From the condition that w vanishes at the edge, we obtain

$$\left.\begin{aligned} &3C_1+C_2+3C_3+4C_4+4C_5+8C_6=0,\\ &C_1-C_3+C_4-C_5+\frac{A_2}{2}c'^2\cosh 2a'\\ &\qquad+\frac{B_2}{12}c''^2\cosh 2a''=0,\\ &\frac{C_1}{8}-\frac{C_2}{8}+\frac{C_3}{8}-\frac{A_2}{30}c'^2\cosh 4a'-\frac{B_2}{30}c''^2\cosh 4a''\\ &\qquad+\frac{A_3}{80}c'^2\cosh 4a'+\frac{B_3}{80}c''^2\cosh 4a''=0,\\ &\qquad\vdots\\ &\left\{\frac{A_{n-1}}{2n-1}-\left(\frac{1}{2n+1}+\frac{1}{2n-1}\right)A_n+\frac{A_{n+1}}{2n+1}\right\}\\ &\qquad\times c'^2\cosh 2na'+\left\{\frac{B_{n-1}}{2n-1}-\left(\frac{1}{2n+1}\right.\right.\\ &\qquad\left.\left.+\frac{1}{2n-1}\right)B_n+\frac{B_{n+1}}{2n+1}\right\}c''^2\cosh 2na''=0.\\ &\qquad\vdots \end{aligned}\right\} \quad (11)$$

(Equation (11) continued on next column)

From the condition that the bending moment M_α vanishes at the edge, we have

$$\{D_1+D_2+(D_1-D_2)\cos 2\beta\}\frac{\partial^2 w}{\partial x^2}+\{D_2+D_3+(D_2-D_3)\cos 2\beta\}\frac{\partial^2 w}{\partial y^2}+2D_4\sin 2\beta\frac{\partial^2 w}{\partial x\partial y}=0,$$

where

$$\begin{aligned} \frac{\partial^2 w}{\partial x^2}&=\sum_{n=2}^{\infty}(A_n\cosh 2na'+B_n\cosh 2na'')\cos 2n\beta\\ &\quad+6C_1+C_2+2C_4+(6C_1-C_2)\cos 2\beta,\\ \frac{\partial^2 w}{\partial y^2}&=-\sum_{n=2}^{\infty}(A_nk_1^2\cosh 2na'+B_nk_2^2\cosh 2na'')\cos 2n\beta\\ &\quad+6C_3+C_2+2C_5-(6C_3-C_2)\cos 2\beta,\\ \frac{\partial^2 w}{\partial x\partial y}&=-\sum_{n=2}^{\infty}(A_nk_1\sinh 2na'+B_nk_2\sinh 2na'')\\ &\quad\times\sin 2n\beta+2C_2\sin 2\beta, \end{aligned}$$

or

$$\left.\begin{aligned} &3(3D_1+D_2)C_1+\left(\frac{D_1}{2}+3D_2+2D_4+\frac{D_3}{2}\right)C_2\\ &\quad+3(3D_3+D_2)C_3+2(D_1+D_2)C_4\\ &\quad+2(D_2+D_3)C_5=0,\\ &12D_1C_1-12D_3C_3+2(D_1-D_2)C_4\\ &+2(D_2-D_3)C_5+\{\tfrac{1}{2}(D_1-D_2)\cosh 4a'\\ &-\tfrac{1}{2}(D_2-D_3)k_1^2\cosh 4a'\\ &-D_4k_1\sinh 4a'\}A_2+\{\tfrac{1}{2}(D_1-D_2)\cosh 4a''\\ &-\tfrac{1}{2}(D_2-D_3)k_2^2\cosh 4a''-D_4k_2\sinh 4a''\}B_2=0, \end{aligned}\right\}$$

(Equation (12) continued on next page)

$$
\begin{aligned}
&3(D_1-D_2)C_1-\left(\frac{D_1+D_3}{2}-D_2+2D_4\right)C_2\\
&+3(D_3-D_2)C_3+A_2\{D_1+D_2\\
&-(D_2+D_3)k_1^2\}\cosh 4a'+B_2\{D_1+D_2\\
&-(D_2+D_3)k_2^2\}\cosh 4a''+A_3\{\tfrac{1}{2}(D_1-D_2)\\
&\times\cosh 6a'-\tfrac{1}{2}(D_2-D_3)k_1^2\cosh 6a'\\
&-D_4k_1\sinh 6a'\}+B_3\{\tfrac{1}{2}(D_1-D_2)\cosh 6a''\\
&-\tfrac{1}{2}(D_2-D_3)k_2^2\cosh 6a''-D_4k_2\sinh 6a''\}=0,\\
&\vdots\\
&A_{n+1}\left\{\frac{(D_1-D_2)}{2}\cosh(2n+2)a'-\frac{(D_2-D_3)}{2}\right.\\
&\left.\times k_1^2\cosh(2n+2)a'-D_4k_1\sinh(2n+2)a'\right\}\\
&+A_n\{D_1+D_2-(D_2+D_3)k_1^2\}\cosh 2na'\\
&+A_{n-1}\left\{\frac{(D_1-D_2)}{2}\cosh(2n-2)a'\right.\\
&-\frac{(D_2-D_3)}{2}k_1^2\cosh(2n-2)a'\\
&\left.+D_4k_1\sinh(2n-2)a'\right\}\\
&+B_{n+1}\left\{\frac{(D_1-D_2)}{2}\cosh(2n+2)a''\right.\\
&-\frac{(D_2-D_3)}{2}k_2^2\cosh(2n+2)a''\\
&\left.-D_4k_2\sinh(2n+2)a''\right\}\\
&+B_n\{D_1+D_2-(D_2+D_3)k_2^2\}\cosh 2na''\\
&+B_{n-1}\left\{\frac{(D_1-D_2)}{2}\cosh(2n-2)a''\right.\\
&-\frac{(D_2-D_3)}{2}k_2^2\cosh(2n-2)a''\\
&\left.+D_4k_2\sinh(2n-2)a''\right\}=0.\\
&\vdots
\end{aligned}
\qquad (12)
$$

If we determine the arbitrary constants $C_1, C_2, \cdots, C_6, A_2, B_2, A_3, B_3, \cdots$ to satisfy Eqs. (10), (11) and (12), then the edge condition is fully satisfied under the restriction that the functions f_1 and f_2 converge. There are mathematical difficulties to find the constants which satisfy these conditions in general form, so we shall find an approximate solution by a method shown in the following example.

In the case of an oak plate cut parallel to the grain of wood

$$k_1^2=0.3428-0.2279i, \quad k_2^2=0.3428+0.2279i.$$

Let us take a plate of thickness unity and as the first approximation, assuming

$$A_2=B_2=A_3=B_3=\cdots=0,$$

we find from Eqs. (10), (11) and (12)

$$
\begin{aligned}
&C_1=0.000768, \quad C_4=-0.003229,\\
&C_2=0.001311, \quad C_5=-0.003004,\\
&C_3=0.000543, \quad C_6=0.002461, \qquad \text{(unit } q\text{)}.
\end{aligned}
$$

At the edge, w vanishes but M_α does not vanish and the edge condition is not fully satisfied. The residual bending moment at the edge is

$$
\begin{aligned}
M_\alpha&=-\tfrac{1}{2}\left\{3(D_1-D_2)C_1-\left(\frac{D_1+D_3}{2}-D_2+2D_4\right)C_2\right.\\
&\qquad\left.+3(D_3-D_2)C_3\right\}\cos 4\beta\\
&=-0.00896q\cos 4\beta,
\end{aligned}
$$

which is about 4.3 percent of the maximum bending moment at the center of the plate.

As the second approximation, assuming

$$A_3=B_3=A_4=B_4=\cdots=0,$$

we find

$$
\begin{aligned}
&C_1=0.000738, \quad C_3=0.000539, \quad C_5=-0.003019,\\
&C_2=0.001393, \quad C_4=-0.003201, \quad C_6=0.002457,\\
&A_2=-0.0000798+0.0000176i,\\
&B_2=-0.0000798-0.0000176i, \quad \text{(unit } q\text{)}.
\end{aligned}
$$

The residual bending moment at the edge is

$$
\begin{aligned}
M_\alpha=-\tfrac{1}{2}\Bigg[&A_2\left\{\frac{(D_1-D_2)}{2}\cosh 4a'\right.\\
&\left.-\frac{(D_2-D_3)}{2}k_1^2\cosh 4a'+D_4k_1\sinh 4a'\right\}\\
&+B_2\left\{\frac{(D_1-D_2)}{2}\cosh 4a''-\frac{(D_2-D_3)}{2}k_2^2\cosh 4a''\right.\\
&\left.+D_4k_2\sinh 4a''\right\}\Bigg]\cos 6\beta\\
=&-0.00199\cos 6\beta.
\end{aligned}
$$

The residual bending moment of the second approximation is only 22 percent of that of the first approximation.

TABLE I.

x or y	0	0.2	0.4	0.6	0.8	1
$w_{y=0}$	0.2467	0.2349	0.1964	0.1396	0.0709	0
$w_{x=0}$	0.2467	0.2355	0.2001	0.1457	0.0767	0

In this way, if we take few terms of the series we can find an approximate solution with sufficient accuracy.

We shall find the deflections on the axes of x and y, using the solution of the second approximation. On the axis of x, we have

$$w=\frac{4}{15}\left(\frac{A_2}{c'^4}+\frac{B_2}{c''^4}\right)x^6+\left\{C_1-\frac{2}{3}\left(\frac{A_2}{c'^2}+\frac{B_2}{c''^2}\right)\right\}x^4 +\{C_4+\tfrac{1}{2}(A_2+B_2)\}x^2+C_6-\tfrac{1}{2}(c'^2A_2+c''^2B_2),$$

on the axis of y, we obtain

$$w=-\frac{4}{15}\left(\frac{A_2k_1^6}{c'^4}+\frac{B_2k_2^6}{c''^4}\right)y^6 +\left\{C_3-\frac{2}{3}\left(\frac{A_2k_1^4}{c'^2}+\frac{B_2k_2^4}{c''^2}\right)\right\}y^4 +\{C_5-\tfrac{1}{2}(A_2k_1^2+B_2k_2^2)\}y^2+C_6-\tfrac{1}{2}(c'^2A_2+c''^2B_2).$$

Values of w calculated from the above equations are tabulated in Table I (unit $q\times10^{-2}$):

There is no considerable discrepancy between the deflections on the axes of x and y as is shown in the above table. From this fact we shall propose an empirical formula in a simpler form:

$$w=\frac{q}{64D^*}(1-r^2)(C^*-r^2), \tag{13}$$

where

$$D^*=\tfrac{1}{8}(3D_1+2D_2+2D_4+3D_3),$$

$$C^*=\frac{7D_1+10D_2+6D_4+7D_3}{2(D_1+2D_2+D_3)}.$$

Putting $D_1=D_3=D$, $D_2=\sigma D$, $D_4=(1-\sigma)D$ in Eq. (13), we have

$$w=\frac{q}{64D}(1-r^2)\left(\frac{5+\sigma}{1+\sigma}-r^2\right),$$

which coincides with the exact solution of the isotropy.

We shall further obtain the bending moment at the center of the plate by using the solution of the second approximation:

$$M_\alpha=-\tfrac{1}{2}(2C_4+A_2+B_2)\{D_1+D_2+(D_1-D_2)\cos2\beta\} +\tfrac{1}{2}(k_1^2A_2+k_2^2B_2-2C_5)\times\{D_2+D_3+(D_2-D_3)\cos2\beta\} =(0.2071-0.1248\cos2\beta)q,$$

$$M_{\alpha\beta}=-\tfrac{1}{2}\{(2C_4+A_2+B_2)(D_1-D_2) -(k_1^2A_2+k_2^2B_2-2C_5)(D_2-D_3)\}\sin2\beta =-0.1248q\sin2\beta,$$

and the maximum bending moment at the centre is

$$[M_\alpha]_{\max}=0.2071q.$$

The bending moment at the centre derived from Eq. (13) is

$$M_\alpha=\frac{3D^*+D_2}{16D^*}\left(1-\frac{D_3-D_1}{D_1+2D_2+D_3}\cos2\beta\right)q =(0.1977-0.1225\cos2\beta)q,$$

$$M_{\alpha\beta}=-\frac{(3D^*+D_2)(D_3-D_1)}{16D^*(D_1+2D_2+D_3)}q\sin2\beta=-0.1225q\sin2\beta,$$

which is in rather good agreement with the result obtained by using the exact solution (second approximation).

In the case of an elliptic plate, the transformation (5) is replaced by

$$\left.\begin{aligned} x+iy&=c\cosh(\alpha+i\beta),\\ x+ik_1y&=c'\cosh(\alpha'+i\beta'),\\ x+ik_2y&=c''\cosh(\alpha''+i\beta''),\end{aligned}\right\} \tag{14}$$

provided with

$$c\cosh a=c'\cosh a'=c''\cosh a'',\quad k_1c\sinh a=c'\sinh a',$$

$$k_2c\sinh a=c''\sinh a''.$$

If $\alpha=a$ represents the periphery of the elliptic plate, then at the boundary

$$\beta=\beta'=\beta'',$$

and the further analysis is quite similar with that of a circular plate.

On the Torsion of a Prismatic Cylinder with a Star-Shaped Section

H. ŌKUBO
Institute of High Speed Mechanics, Tōhoku University, Sendai, Japan
(Received March 30, 1949)

The torsion problem is theoretically treated for a prismatic cylinder with a star-shaped section. To simplify the calculation, the bounding curve is assumed to be composed of logarithmic spirals. In one example the stress distributions on the boundary and on the symmetrical radial lines, and the torque are calculated. The result is confirmed by an experiment.

IN this paper the torsion problem of a prismatic cylinder with sharp notches in the direction of the axis is treated. The problem is directly connected with the torsion problem of a serrated shaft which is widely in practical use at the present time. So far as the writer is aware, such a problem has not yet been treated theoretically. Moreover, it is difficult to obtain an accurate result experimentally, since the shaft has a number of small notches.

Taking the generators of the surface of the cylinder to be parallel to the axis of z, the stress components that do not vanish are

$$X_z=\mu\tau\left(\frac{\partial\phi}{\partial y}-y\right),\quad Y_z=-\mu\tau\left(\frac{\partial\phi}{\partial x}-x\right),\qquad(1)$$

provided with

$$(\partial^2\phi/\partial x^2)+(\partial^2\phi/\partial y^2)=0,\qquad(2)$$

where μ is the modulus of rigidity and τ is the twist. Since the bounding surface is free from traction, the function ϕ must satisfy the boundary condition:

$$\phi-\tfrac{1}{2}r^2=\text{const.}\qquad(3)$$

In the case of a cylinder with p notches, we shall take the function ϕ given by the expression

$$\phi=R[\sum_{n=1}^{\infty}A_n\phi_n(w)],\qquad(4)$$

where

$$\phi_1=\log\left(1+\frac{e^{pw}}{a^p}\right),\quad \phi_2=p\int\phi_1dw,$$

$$\phi_3=p\int\phi_2dw,\quad\cdots.$$

$x+iy=e^w$, $w=\alpha+i\theta$, $r=e^\alpha$ and R denotes the real part of the complex variable.

Except the points $r=a$, $\theta=n\pi/p$, $n=1, 3, \cdots, 2p-1$, the right side of Eq. (4) is expanded in the series:

$$\left.\begin{aligned}\phi=&-A_1p\log a+A_1\{p\alpha+(a/r)^p\cos p\theta-\tfrac{1}{2}(a/r)^{2p}\cos 2p\theta+\cdots\}\\&+A_2\{p^2/2(\alpha^2-\theta^2)-p^2\alpha\log a-(a/r)^p\cos p\theta+1/2^2(a/r)^{2p}\cos 2p\theta+\cdots\}\\&+A_3\{p^3/6(\alpha^3-3\alpha\theta^2)-p^3/2(\alpha^2-\theta^2)\log a+(a/r)^p\cos p\theta-1/2^3(a/r)^{2p}\cos 2p\theta+\cdots\}\\&+\cdots\qquad\qquad r\geqq a,\\ \phi=&A_1\{(r/a)^p\cos p\theta-\tfrac{1}{2}(r/a)^{2p}\cos 2p\theta+\cdots\}\\&+A_2\{(r/a)^p\cos p\theta-1/2^2(r/a)^{2p}\cos 2p\theta+\cdots\}\\&+A_3\{(r/a)^p\cos p\theta-1/2^3(r/a)^{2p}\cos 2p\theta+\cdots\}\\&+\cdots\qquad\qquad r\leqq a,\end{aligned}\right\}\qquad(5)$$

where $a=e^{-k\pi/p}$.

As is shown in Fig. 1, when the bounding curve of the cross section is given by

$$\left.\begin{aligned}r&=e^{-k\theta},\quad \pi/p\geqq\theta\geqq 0,\\ r&=e^{k\theta},\quad 0\geqq\theta\geqq-\pi/p,\end{aligned}\right\}\qquad(6)$$

at the boundary, we find

$$\phi=\sum_{n=1}^{\infty}\sum_{m=1}^{\infty}A_na_{nm}\cos mp\theta+\text{const.},$$

and

$$\tfrac{1}{2}r^2=\sum_{m=0}^{\infty}C_m\cos mp\theta,$$

and to satisfy the boundary condition (3), we have the simultaneous equations of A_m:

$$\sum_{n=1}^{\infty}a_{nm}A_n=C_m,\quad m=1, 2, 3,\quad\cdots,\qquad(7)$$

where

$$C_m=\frac{2kp\{1+(-1)^{m+1}e^{-2k\pi/p}\}}{\pi(4k^2+m^2p^2)},$$

$$a_{1m}=\frac{2k}{\pi m^2}\{1+(-1)^{m+1}\}+\frac{k}{\pi}\sum_{n=1}^{\infty}C_{nm},$$

$$a_{2m}=\frac{2(k^2-1)(-1)^m}{m^2}-\frac{2pk\log a}{\pi m^2}\{1+(-1)^{m+1}\}-\frac{k}{\pi}\sum_{n=1}^{\infty}\frac{C_{nm}}{n},$$

TABLE I.

m	$\sum_{n=1}^{5} a_{nm}A_n$	C_m	Error $= \sum_{n=1}^{5} a_{nm} - C_m$
1	0.0727	0.0727	0
2	0.0041	0.0041	0
3	0.0082	0.0082	0
4	0.0006	0.0010	−0.0004
5	0.0032	0.0030	0.0002
6	−0.0000	0.0005	−0.0005
7	0.0019	0.0015	0.0004
8	−0.0003	0.0003	−0.0006
9	0.0014	0.0010	0.0004
10	−0.0003	0.0002	−0.0005
11	0.0011	0.0006	0.0005
12	−0.0004	0.0001	−0.0005

$$a_{3m}=\frac{(3k-k^3)}{\pi}\left\{\frac{\pi(-1)^m}{m^2}+\frac{2\{1+(-1)^{m+1}\}}{m^4}\right\}$$

$$-2p(k^2-1)\log a\cdot\frac{(-1)^m}{m^2}+\frac{k}{\pi}\sum_{n=1}^{\infty}\frac{C_{nm}}{n^2},$$

$$\cdots$$

$$C_{nm}=\{(-1)^{m+1}+(-1)^n e^{-n\pi k}\}$$

$$\times\left\{\frac{1}{n^2k^2+(m+n)^2}+\frac{1}{n^2k^2+(m-n)^2}\right\}.$$

If we find the arbitrary constants A_m by solving the simultaneous Eqs. (7), we can obtain ϕ from Eq. (4).

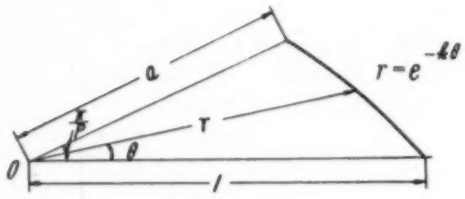

FIG. 1.

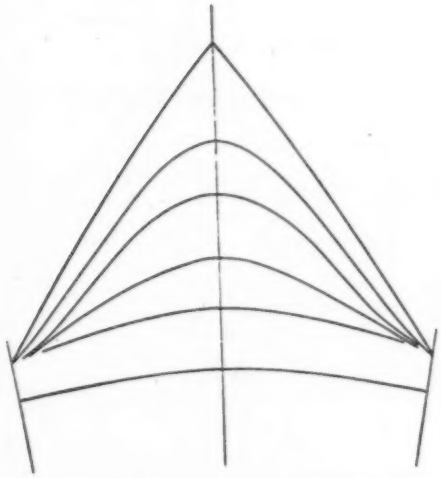

FIG. 2. Lines of shearing stress around the notch.

As an example, we shall make a numerical calculation for the case of a cylinder with the diameter 2 of the circumscribed circle of the cross section and $p=18$, $a=0.8$. In this case, $k=1.2785$.

To simplify the calculation, we shall take the first 3 terms of the series in Eq. (4), by putting

$$A_4=A_5=\cdots=0,$$

then we have from Eq. (7),

$$A_1=0.00550,\quad A_2=0.01207,\quad A_3=-0.00021.$$

The error of ϕ at the bounding surface due to the neglect of the terms of higher infinitesimal is rather small as is shown in Table I.

Figure 2 shows the lines of shearing stress around the notch. From the figure it may be seen that the stress concentrates considerably at the bottom of the notch. The lines of shearing stress coincide approximately with concentric circles at the points where r is smaller than a and, therefore, the result obtained here can be used with sufficient accuracy as an approximate solution of a hollow shaft.

From Eq. (1), the shearing stress along the bounding curve of the cross section is

$$\tau_s=-\frac{\mu\tau}{(1+k^2)^{\frac{1}{2}}}\left\{\frac{\partial\phi}{\partial r}-r+\frac{k}{r}\frac{\partial\phi}{\partial\theta}\right\},\tag{8}$$

and on the radii $\theta=0°$ and $\theta=10°$ is

$$\tau_0 \text{ or } \tau_{10}=-\mu\tau\left(\frac{\partial\phi}{\partial r}-r\right)_{\theta=0°\text{ or }10°}.\tag{9}$$

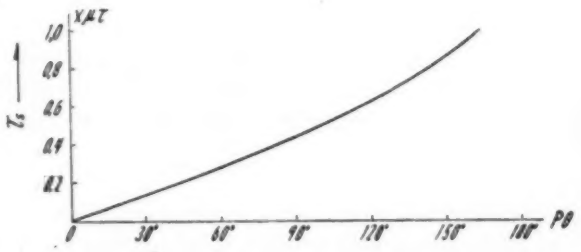

FIG. 3. Stress distribution on the bounding curve.

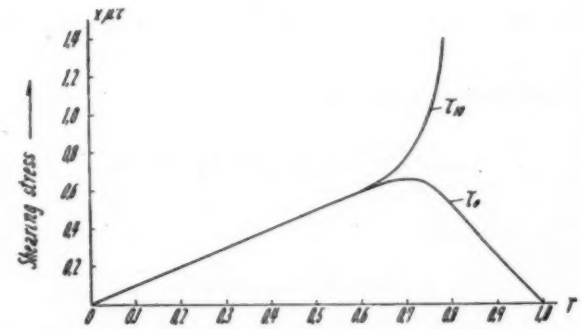

FIG. 4. Stress distributions on the radii $\theta=0°$ and $\theta=10°$.

The values of shearing stress calculated from Eqs. (8) and (9) are plotted in Figs. 3 and 4.

The torque acting on the cylinder is

$$T=0.805\mu\tau,$$

then the stiffness ratio[1] of this case is 0.512, and it is shown that the stiffness of the shaft is considerably diminished by notches. The stiffness ratio of a serrated shaft when $p=30$ was obtained experimentally by Griffith and Taylor.[2] From the result obtained by them, the stiffness ratio for the serrated shaft with sharp notches is estimated about 0.56.

The case obtained by them is not the same as that treated here, regarding the number and the shape of notches. Upon this, we made the torsion test using test pieces shown in Fig. 5. The experimental result is

$$T=0.783\mu\tau.$$

Accordingly, the experimental and the theoretical results are rather in good agreement.

In conclusion, the writer wishes to express his thanks to the financial aid of the Natural Science Subsidy of the Education Ministry of Japan.

FIG. 5. Test piece.

[1] The ratio of the stiffness of a shaft to the stiffness of a circular shaft without a notch.

[2] A. A. Griffith and G. I. Taylor, Tech. Report Adv. Comm. Aeronautics (1918), p. 944.

A Method for Studying the Distribution and Sign of Static Charges on Solid Materials

HARRY H. HULL
R. R. Donnelley and Sons Company, Chicago, Illinois

(Received May 6, 1949)

A special powder is used to show how static electricity is distributed on materials such as paper. Red particles of this powder are attracted to positively charged areas and blue particles are attracted to negatively charged areas. Paper from heat-set printing presses shows streaks of static electricity generated by idling rollers and shifting patterns of static electricity generated in the folder, often with opposite charges on the same sheet of paper.

PAPER processors, printers, and others who must handle sheet materials are constantly confronted with the problem of handling these materials when they contain electrical charges which cause the sheets to cling together and hinder their separation and jogging. The printer particularly finds himself in impossible situations when printed sheets or "signatures" cling together so that they cannot be jogged for stacking, or handled in the bindery, and the result is unduly long delays for which no solution is immediately apparent.

A common conception of the formation of static electricity is that it results from the rubbing of one material with another and that a positive charge is generated on one material and on the other a negative charge results. If the charges formed in a printing press are produced by paper rubbing on another substance, all the paper should have one charge sign and the sheets should repel each other. Since the sheets cling together they cannot all be charged the same.

In the course of studies with static eliminators on a web-fed rotary printing press, using heat-drying inks and delivering folded signatures, it became desirable to develop a better means for studying the behavior of static electricity on paper. Strachan[1] has stated that adjacent sheets of paper from the cutter in a paper mill may have opposite charges and that when two identical sheets of dielectric are pressed together (100 to 120 lb. per sq. in.) and separated, the surfaces are charged. They sometimes show patches of one charge surrounded by charges of opposite sign. Bürker[2] and Kundt[3] made use of selected powdered materials to show distribution of plus and minus pyroelectricity on crystals. The two powders are such that one develops a negative charge of static electricity and the other a positive charge. These charges are developed either by friction between the particles or by friction of the individual particles with air. Studies of static charges on insecticide dusts have been made by MacLeod and Smith.[4]

The powder mixtures appeared to have possible application to the current problem, so several were tried. The mixture used by Bürker, of carmine, sulfur, and lycopodium powder was satisfactory except that the negatively charged areas did not show plainly as the attracted particles were approximately the same color as

[1] James Strachan, "Static electricity in paper manufacture," Paper Maker 93, TS 81–82 (1937).

[2] K. Bürker, "Über ein dreipulvergemisch zur darstellung elektrischer staubfiguren," Ann. d. Physik 1, 474 (1900).

[3] W. Voigt, *Lehrbuch der Kristallphysik* (B. G. Teubner, Leipzig, Germany, 1910), p. 230.

[4] G. F. MacLeod and Leslie M. Smith, "Deposits of insecticidal dusts and diluents on charged plates," J. Agr. Research 66, 87–95 (1943).

the paper. Bürker says the particles attracted to this area are yellow. However, microscopic examination shows that they are largely lycopodium powder. Accordingly the lycopodium powder was dyed blue and a very satisfactory definition of the negative areas was obtained.

The mixture was prepared as follows. One part by volume of carmine was ground with five parts of flowers of sulfur. This was then mixed with three parts of lycopodium powder dyed blue. The lycopodium powder was dyed blue by adding approximately 70 grams to 100 cc of a two percent solution of methyl violet in alcohol and allowing the mixture to dry thoroughly in the air.

When this powder is dusted near the poles of an electrostatic generator, the plus pole attracts the red portion of the powder while the minus pole attracts the blue portion. A glass rod rubbed with silk and then placed in contact with the powder attracts the red material and the blue remains behind. When a glass rod was used to write upon Cellophane and the latter dusted, the writing outline was left covered with a blue powder and other portions of the same sheet sometimes showed areas which attracted the red powder (apparently from friction with the desk top).

In the study of signatures from a printing press the powder mixture was dusted between the pages as they were separated. This is necessary, for the static charges rapidly leak off the separated pages. When the sheets are in close proximity they act as condensers and the voltages are small (as shown by the equation $V=4\pi qd/kA$.* When the sheets are separated, the voltages increase in the same way that the voltage on charged condenser plates increases as they are separated. With dusting, the high voltages produced on separating the pages attract the oppositely charged particles of static powder and the pattern of the static charges is shown in color according to the charge.

The powder shows that positive and negative charges are often on the same sheet of paper with only a small neutral space between them. The charges at times follow the outline of the printed matter on the other side. However, they often shift and an area which is positive on one sheet will be negative on a subsequent sheet. Tracks of rubber rollers across the paper will show up as a streak of electrically charged surface. A photograph of such a track is shown in Fig. 1. Figure 2 shows the areas of positive and negative charge. These tracks are primarily of one charge but star-shaped patterns of the opposite charge occur frequently in the track. On one press the charges did not follow the printing pattern but the left half of the opened book was positive and the right half negative.

The most effective method of preventing static electricity is the maintenance of a sufficiently high humidity in the atmosphere so that the materials involved absorb water and become conductive. This is commonly used in the textile mills and is practised where possible in certain printing processes. In rotogravure printing the ink is dried by passing the paper over steam-heated cylinders and in high speed letterpress printing the ink is often dried by passing the paper under radiant gas burners. This removes moisture from the paper so that it is a very effective insulator. If the dried paper sheets or "signatures" are stacked so that air does not circulate freely

FIG. 1. A photograph of the track of an idling roller on a printing press across the paper surface (approximately 2.4×).

* q is the plate charge, d is the distance between the plates, A is the plate area, and k is the dielectric constant.

FIG. 2. A diagram of Fig. 1 showing charge distribution. The red or positive areas are outlined. The blue or negative areas are solid. The rest of the area is a light blue.

among them, or are stored in an atmosphere of low humidity, the charge will remain on them for several days. The charge will be readily dissipated as soon as the paper is sufficiently conductive, or when the sheets are separated.

A common method of neutralizing static in the printing plant is the use of grounded Christmas tree tinsel in virtual contact with the paper. Other methods utilize the ionization of the air in the vicinity of the paper either by radioactive material, high voltage discharge, or even by an open flame. These are effective, but where large amounts of static electricity are generated, sufficient ions must be formed to conduct the static charge to ground or to an oppositely charged area. They are also subject to the difficulty that a static eliminator may be required where there is no space to place it, or where its effects are required in the interior of a folded book or "signature."

The "static powder" described may be used in determining the qualitative efficiencies of these various static eliminators and in determining their proper placement. An electroscope or electrostatic voltmeter can be used in conjunction with the powder in determining the source of static electricity. For example, in the heater-equipped printing presses there are large quantities of electricity generated as the paper passes over the impression cylinder; but, immediately following are the radiant gas burners and as the hot gasses are ionized the static charge is neutralized. This is best shown by the electroscope, as the powder cannot be used effectively on a moving web. The electrically neutral paper then contacts idling rollers (rubber-covered) and these generate a static path across the paper. These paths can be shown by the electroscope, but they are shown more clearly by dusting the static powder on the web just after the press has stopped. A streak of static is shown starting at each roller and leading into the folder. However, the powder shows clearly that the major portion of the charges is generated in the folder on most presses. During folding, rubbing of the ink-covered paper probably produces a different charge than the rubbing of the plain paper, and this may account for the outlining of the printing but would not explain the shift in sign in the same area of subsequent sheets. Frictional contacts, pressure, piezoelectric effects as suggested by Strachan,[5] or induced charges may contribute substantially to the effects observed. The peculiar star-shaped designs encountered in the idling roller tracks appear to be caused by discharges onto the paper.

The powder described here furnishes a sensitive method of determining sign and charge distribution of static electricity on paper or other objects. It is useful in explaining the behavior of static electricity in many problems, and for the location of troublesome sources of static generation.

The writer wishes to thank Dr. M. Rogers for his help in preparing this paper, and the management of R. R. Donnelley and Sons Company for permission to publish the results of these investigations.

[5] James Strachan, "Static electricity in paper-making and paper-using," Paper Market 45, 47 (February 1948); 67, 69 (March 1948).

Study of the Sintering of Glass*

G. C. Kuczynski
Sylvania Electric Products, Inc., Bayside, New York
(Received May 9, 1949)

It has been shown experimentally that the mechanism of sintering of spherical glass particles is that of viscous flow. The viscosities of the investigated glass were determined for a range of temperatures from 575°C to 744°C. These viscosities remain in good agreement with those obtained by other methods.

It has been shown by the author of this paper[1] that metallic particles bond together by a diffusion mechanism. It was also pointed out that other mechanisms such as evaporation-condensation and viscous flow can bring about similar results when conditions are opportune for their occurrence. These mechanisms can be distinguished by the particular relationship of the radius of the "neck" x found between two particles (Fig. 1) and sintering time t. These relationships are:

viscous flow	$x^2 \sim t$
evaporation-condensation	$x^3 \sim t$
volume diffusion	$x^5 \sim t$
surface diffusion	$x^7 \sim t$.

(1)

The evaporation-condensation mechanism was discussed in the above-mentioned paper.[1] It would involve the evaporation of the atoms from the convex parts of the system and condensation on the concave areas, or in the "neck." This process may take place if the vapor pressure of the material is high.

There is a distinct difference between the mechanism of viscous flow and that of volume diffusion although the former may also be caused by diffusion. The definition of viscous flow is contained in the equation:

$$f = \eta \dot{\epsilon}, \tag{2}$$

where $\dot{\epsilon}$ is the strain rate, f the acting stress, and η viscosity coefficient. For the occurrence of viscous flow, then, stress is needed. In our case this stress may be produced by surface tension. On the other hand, in the case of volume diffusion flow such a stress is not necessary. This point is best illustrated in Fig. 2. If we assume that diffusion takes place by atoms moving to the neighboring holes, then in the case of viscous flow (Fig. 2(a)) the atoms will jump preferably in the direction of the acting stress. The average concentration of the vacancies in the body remains constant. In the case of self-diffusion flow (without acting force), there must be a gradient of vacancies (Fig. 2(b)) which causes atoms to move in that direction.

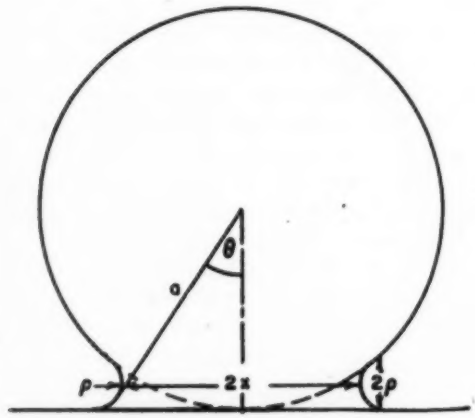

FIG. 1. Schematic representation of the cross section of a spherical particle sintered to a glass block.

In the case of metals, viscous flow has not been observed except perhaps in the grain boundaries.[2] It is, therefore, highly improbable that this mechanism may be responsible for the bonding together of two particles. Besides, it can be shown that the rate of sintering of copper particles by the mechanism of viscous flow would be very much slower than that by volume diffusion. In the case of glass, at higher temperatures when viscosity is low the rate of sintering due to viscous flow should be much faster after a small neck has been built up by a simple diffusion process.

Frenkel[3] has shown that if the bonding of particles occurs by viscous flow, the following relationship between x and t will be obeyed

$$(x/a)^2 = (3/2)(\sigma' t/a\eta), \tag{3}$$

where σ' is the surface energy of the material and a the original radius of the bonded particles. This relationship can be checked by direct measurements of x and a as described in the next section.

MATERIALS AND METHODS

For the experiments some small spherical particles of glass (about 0.05 cm in diameter) were used. They were furnished by the courtesy of Dr. M. Steinberg of Horizons, Incorporated, Cleveland. These beads were sintered to glass plates of approximately the same composition as can be ascertained from Table I.

The spherical particles were spread on the glass plates and heated in air at temperatures ranging from 575°C to 743°C for various periods of time. After heating, the samples were cooled rapidly, mounted in

* This work was done on a research program sponsored by the AEC Contract AT-30-1-GEN 367.
[1] G. C. Kuczynski, J. Metals, 169 (February 1949).
[2] T'ing-Sui Kê, J. App. Phys. **20**, 274 (1949).
[3] J. Frenkel, J. Phys. U.S.S.R. **9** (5), 385 (1945).

Bakelite, cut, polished and etched with $HF+HNO_3$ and examined under the microscope. Some of the cross sections as viewed under the microscope are represented in Figs. 3 and 4. The radii of these particles as well as the radii of the junctions formed between the beads and plates were readily measured with a micrometer eyepiece. It was found profitable to do the measurements under polarized light (Fig. 4) because of the better contrast.

RESULTS

In Table II the measured values of x (radius of the neck) and a (radius of the particles) are listed along with $(x/a)^2$ and viscosity η evaluated from Eq. (3). It has been assumed that the average surface energy of the glasses used is 300 erg/cm².[4] The plot of (x^2/a) *versus* t for 676°, 713°, and 743°C are represented in Fig. 5. There is an obvious linear relationship between x^2 and time t, indicating that viscous flow is the mechanism of bonding in this case. The logarithms of the viscosity values, η, as calculated from Eq. (3), are plotted against T°C in Fig. 6. The plot is similar to those obtained by Lillie[5] and other authors.[4]

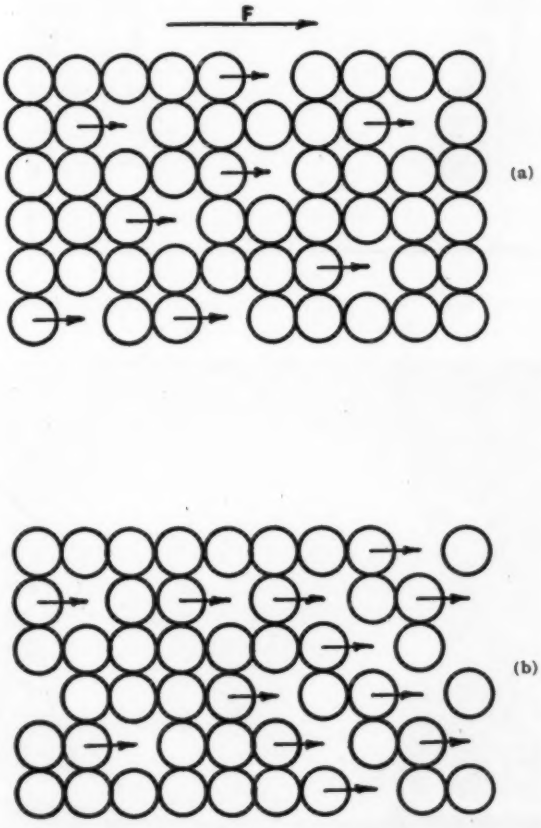

FIG. 2. (a) Schematic representation of the movement of atoms in case of viscous flow. The concentration of vacancies is constant throughout the body of the material. (b) Schematic representation of the diffusion flow. Atoms move preferably in the direction of the greater concentration of vacancies.

TABLE I. The composition of glass in percent.

Component	Beads	Plates
SiO_2	69.20	71.20
CaO	6.06	9.46
MgO	4.59	4.23
R_2O_3	0.79	0.94
PbO	0.27	—
MnO	0.16	—
B_2O_3	0.57	—
Na_2O (by difference)	18.36	14.17

TABLE II. Radii of the junctions and viscosities of glass.

T°C	t(min.)	$x\times10^{-4}$ cm	$a\times10^{-4}$ cm	$(x/a)^2$	η(poises)
575	6.70×10^3	1.92	2.60	0.005	1.27×10^{13}
620	3.70×10^3	2.20	2.42	0.008	5.90×10^{10}
	1.44×10^4	4.15	2.65	0.246	
676	30	4.00	2.42	0.027	1.22×10^9
	60	4.90	2.25	0.047	
	90	6.55	2.40	0.075	
	120	7.60	2.40	0.100	
	150	8.50	2.50	0.120	
713	10	6.00	2.41	0.063	1.94×10^8
	15	6.80	2.35	0.084	
	20	8.90	2.61	0.116	
	25	9.60	2.52	0.114	
	30	9.20	2.20	0.117	
	40	11.90	2.47	0.230	
743	5	6.50	2.31	0.082	7.00×10^7
	10	8.30	2.40	0.132	
	15	12.90	2.60	0.250	
	20	14.00	2.45	0.325	

The above method, then, can be used for quick estimations of viscosity, in the neighborhood of annealing temperatures. Its limitations are obvious. It cannot be used at very high temperatures due to the great speed of reaction nor at very low temperatures due to the prohibitively long periods of time required for sintering.

The heat of activation of viscosity varies with temperature according to the equation:

$$\eta = A \exp(E/RT), \tag{4}$$

where E is the energy of activation of viscosity and A a constant. It was found, however, that both A and E vary considerably with temperature.[6] In our case:

$$\eta = 4.1\times10^{-19} \exp(121{,}000/RT)$$

for temperatures less than 700°C and

$$\eta = 2.8\times10^{-7} \exp(67{,}000/RT)$$

for temperatures higher than 700°C. Using the formula for viscosity established by Eyring,[7]

$$\eta = (h/\delta^3) \exp(E/RT), \tag{5}$$

[4] G. W. Morey, *The Properties of Glass* (Reinhold Publishing Corporation, New York, 1938).

[5] H. R. Lillie, J. Am. Ceram. Soc. 14, 502 (1931).

[6] R. C. L. Bosworth, Trans. Faraday Soc. 44, 308 (1948).

[7] Glasstone, Laidler, and Eyring, *The Theory of Rate Processes* (McGraw-Hill Book Company, Inc., New York, 1941).

where h is the Planck's constant and δ the length of unit flow, Seddon[8] explains the decrease of E with temperature accompanied with increase of A, by the decrease of the unit flow δ with temperature. According to him, the structure of glass may break down into a collection of large groups. The bonding within each of these groups is complete. The size of the group identified with unit flow, decreases steadily with increasing temperature. This mechanism then would account for the increase of A and decrease of E with temperature. If this were true, however, the unit of flow should decrease from 250,000A at low temperatures to about 28A at high temperatures in our case. Stanworth[9] rightly points out that such considerable changes are not feasible, since for flow units which are too large, viscosity would be dependent on the acting force and, consequently, flow would not be Newtonian, and this was never observed in glasses.

It is, therefore, more plausible to accept Stanworth's[8] point of view according to which the unit of flow δ does not change appreciably with temperature. If E is replaced by ΔF, free energy of activation $\Delta F = E' - T\Delta S$ (4) would take the form:

$$\eta = [(h/\delta^3) \exp(-\Delta S/R)] \exp(E'/RT),$$

where ΔS is the entropy of activation whose marked variations with temperature cause the variations in A. E' is now the observed energy of activation of viscous

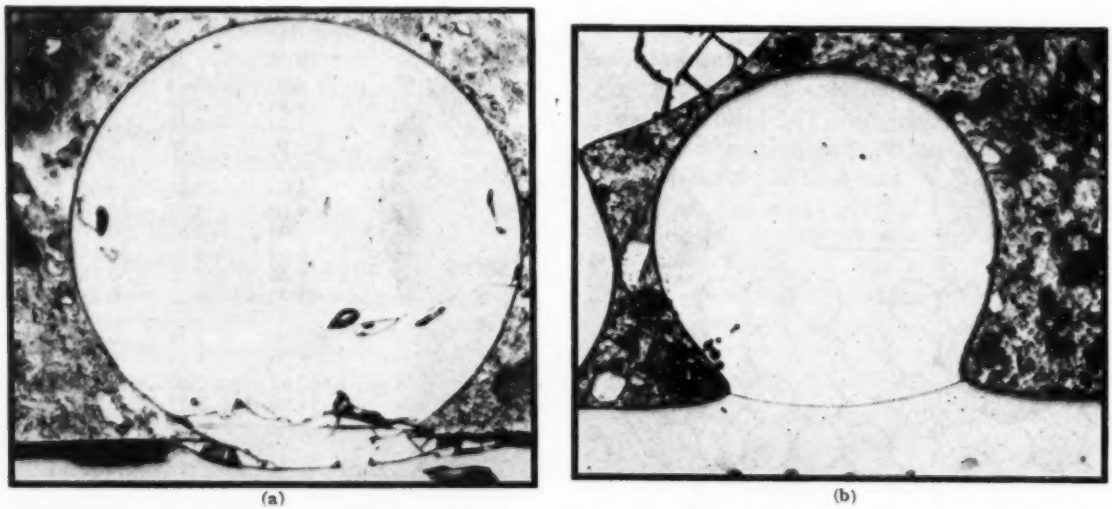

(a) (b)

FIG. 3. Glass particles sintered to glass block. (a) At 712°C for 30 min.—mag. 150×. (b) At 700°C for 10 min.—mag. 150×.

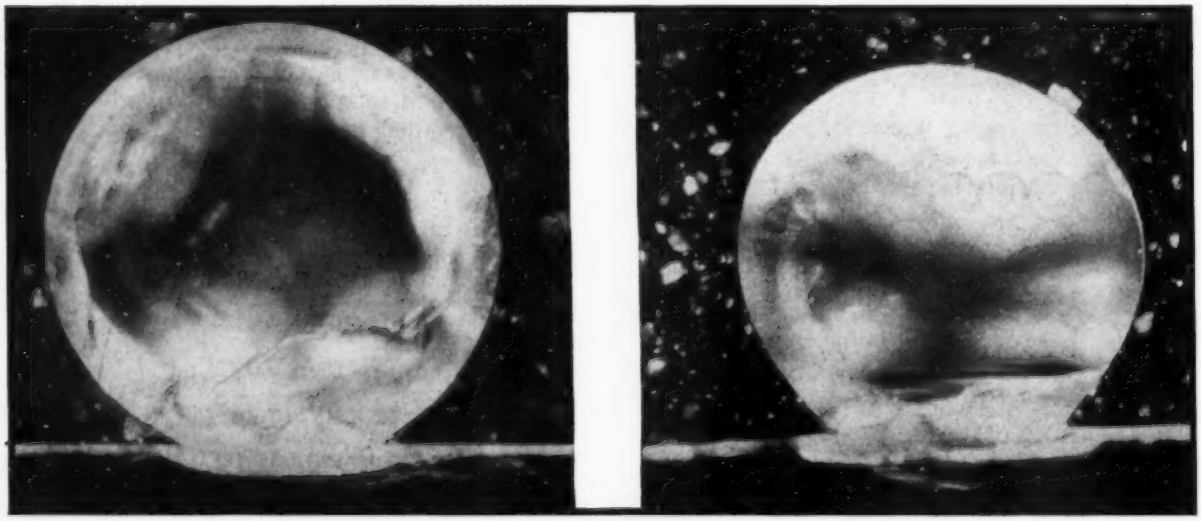

(a) (b)

FIG. 4. Glass particles sintered to glass block at 712°C. Photo-micrographs taken under polarized light. (a) For 30 min.—mag. 150×. (b) For 40 min.—mag. 150×.

[8] E. Seddon, J. Soc. Glass Tech. (Trans.) 23, 36 (1939).
[9] J. E. Stanworth, J. Soc. Glass Tech. 32, 20–31 (T) (February 1948).

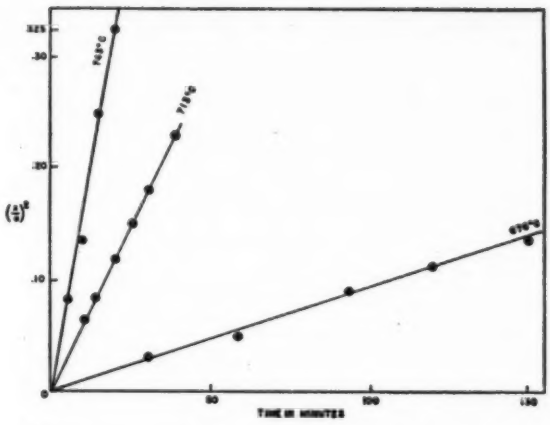

FIG. 5. $(x/a)^2$ *versus* t plots for glass spheres bonded to glass plates.

flow. This energy can be written in the following way:

$$E' = E_0 + \Delta E,$$

where E_0 is the energy required for the formation of a vacancy of volume comparable with δ^3 and should be of the order of magnitude of the heat of vaporization of the diffusing molecule. ΔE is the energy needed for transfer of a molecule from its original position to the adjacent hole. According to Stanworth,[8] E_0 will take its full value in the flow activation energy when the free volume is very small, namely at low temperatures. At higher temperatures the free volume of molecules is so great that E_0 becomes zero. Keeping this in mind, the difference between the two activation energies at very low and very high temperatures should be of the same order of magnitude as the heat of vaporization of the glass components. In our case, this difference is 54,000 cal./mole and at still higher temperatures it will most probably be greater. It should be noted that the

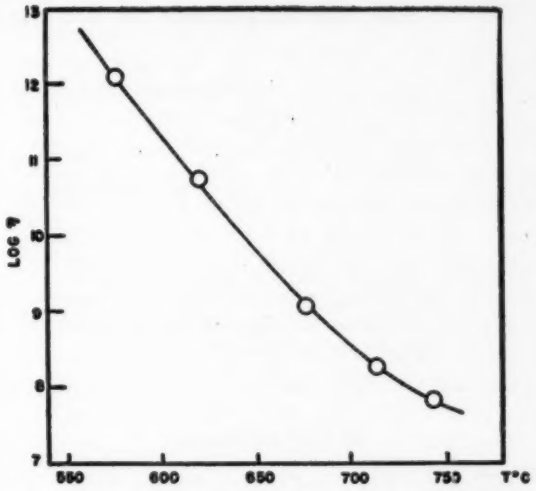

FIG. 6. Logarithm of viscosity *versus* temperature curve.

heats of vaporization of Na_2O, 36,000 cal./mole, CaO, 78,000 cal./mole, and SiO_2, 65,000 cal./mole, as estimated from Trouton's rule, are fairly close to the observed difference.

It is, therefore, possible that the diffusion of these molecules is responsible for the viscous flow of glass. The results, however, are not detailed enough to permit further discussion.

ACKNOWLEDGMENT

The author wishes to express his gratitude to Mr. W. E. Kingston, Manager of Metallurgical Laboratories, for supporting this work. Thanks are also due H. Lipson and J. Black for their help in various phases of this work and Mrs. L. Roth for metallographic preparation of the specimens.

On the Magnitude of the Mechanical Component of Solid Friction

C. D. STRANG*
Massachusetts Institute of Technology, Cambridge, Massachusetts.

AND

C. R. LEWIS**
Chrysler Corporation, Highland Park, Detroit, Michigan

(Received May 9, 1949)

An experiment was performed in order to determine the magnitude of that portion of dry, kinetic friction which is contributed by Coulomb friction, or the mechanical interlocking of surface irregularities. The results indicate that the work of the mechanical component of friction accounts for only a few percent of the work of total measured friction.

INTRODUCTION

THE oldest and most widely known theory of friction is due to Coulomb[1] who postulated that the work of friction is expended in lifting the irregularities of one sliding surface over those of the other. This concept is still defended by some workers[2] although other authorities prefer to explain friction phenomena in terms of electrostatic attraction,[3,4] molecular attraction,[5,6] and local welding and ploughing[7,8] of the surfaces. It is probable that several of these mechanisms are present and their effects add, to yield the commonly observed values of total friction force.

This report describes a simple experiment which was performed in order to determine the magnitude of the mechanical or Coulomb component of dry kinetic friction, and its relation to the value of total kinetic friction. This was done by sliding a relatively flat friction specimen over the surface of a similar specimen and recording the vertical motion of the upper member as its surface asperities climbed over those of the lower specimen. The work of mechanical friction was computed from the recorded values of vertical motion and the weight of the upper sliding specimen and was then compared with the work of total friction as obtained from the measured value of total friction force.

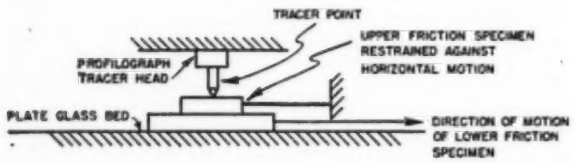
TRACER POINT
UPPER FRICTION SPECIMEN RESTRAINED AGAINST HORIZONTAL MOTION
PROFILOGRAPH TRACER HEAD
PLATE GLASS BED
DIRECTION OF MOTION OF LOWER FRICTION SPECIMEN

FIG. 1. Diagrammatic sketch of apparatus for measuring vertical motion of friction specimen.

EXPERIMENTAL PROCEDURE

Figure 1 is a diagrammatic sketch of the apparatus employed in the experiment. Horizontal relative motion between the friction specimens was obtained by towing the lower specimen with a fine lead-screw arrangement, at a velocity of 0.0062 in./min., while the upper specimen was restrained from moving horizontally, but was permitted to move vertically. The polished under side of the lower block slid on a sheet of polished plate glass to minimize any vertical movements from this source. The vertical motion of the upper specimen was detected by the tracer point of a Proficorder,[9] electronically amplified by a factor of 2500 and recorded on a moving strip chart. The tracer point bore upon the upper specimen at the center of its upper surface. Hence, even if the specimen were to tilt while being lifted by the action of the interlocking asperities, the tracer point would still record the vertical motion of the center of gravity of the specimen, which is the quantity needed for computing the mechanical work of friction.

The horizontal restraint for the upper specimen was supplied by a horizontal steel rod touching one end of the upper specimen. Except for friction, the smooth end of the specimen was free to slide vertically with respect to the rod. It can easily be shown that this latter friction force opposing the vertical motion between the rod and the specimen cannot exceed the product of the specimen weight and the square of the friction coefficient for the material employed for the specimens and restraining rod. In this experiment, therefore, the parasitic force opposing the vertical motion between rod and specimen was approximately six percent of the specimen weight and thus offered little resistance to vertical motion.

The force of total friction was obtained by removing the tracer point, holding the lower specimen stationary, and towing the upper specimen over the lower. The towing or friction forces were measured with a steel dynamometer ring on which was mounted a Wheatstone bridge of resistance wire strain gauges. A force measuring instrument of this type combines high sensi-

* Research Associate in Mechanical Engineering.
** Staff Research Engineer.
[1] Coulomb, Mem. Math. Phys. Acad. Roy. Sci., 161, (1785).
[2] J. J. Bikerman, Lubrication Engineering 4, 208 (1948).
[3] R. Schnurmann and E. Warlow-Davies, Proc. Phys. Soc. 54, 14 (1942).
[4] P. E. Shaw, Phil. Mag. 9, 628 (1930).
[5] W. B. Hardy, *Collected Works* (Cambridge University Press, London, 1936).
[6] G. A. Tomlinson, Phil. Mag. 905, (1929).
[7] Bowden, Moore, and Tabor, J. App. Phys. 14, 80 (1943).
[8] F. P. Bowden, Proc. Roy. Soc. N.S.W. 78, 187 (1945).
[9] E. J. Abbott and E. Rupke, Trans. A.S.M.E. 70, 263 (1948).

tivity with rigidity and is useful in minimizing relaxation oscillations in friction measurements at low velocities.

The specimens were made of mild steel and prepared with fairly coarse surface finishes to favor the mechanical component of friction. The test surface of the lower specimen was prepared by machining with a single point tool in a shaper while the upper specimen surface was formed by rubbing the surface on a coarse single cut file, the rubbing motion parallel to the teeth. Profilometer readings for the surfaces of the upper and lower surfaces were 140–150 microinches R.M.S. and 350–400 microinches R.M.S., respectively. The apparent area of contact between the specimens was one square inch. Figure 2 shows representative surface profile traces of the two test surfaces, taken at right angles to the lay of the surface finish. The finish was found to be essentially uniform over the surface of each specimen. In Fig. 2 the traces are arranged to indicate the relative positions of the specimens as used in the friction experiments, that is, the lower trace is that for the lower specimen and has its asperities projecting upward while the upper trace is that for the upper specimen and has its asperities projecting downward. It should be noted that the vertical magnification of these traces is 2500 while the horizontal magnification is only 242. Therefore, in visualizing the interlocking of the asperities, one should mentally expand the horizontal scale.

Figure 3 shows photomicrographs of the two test surfaces. It will be seen that the surface finish marks are parallel on the lower friction specimen and are essentially parallel on the upper specimen although exhibiting some criss-crossing.

Figure 4 indicates the orientation of the surface finish marks in the two tests which were run. In Case *A*, the finish marks are parallel and would therefore, be expected to result in greater vertical motion of the upper specimen than in Case *B*, where the surface finishes were arranged at right-angles to each other. This was found to be true, as shown in the traces of Fig. 5. These traces, obtained with the apparatus of Fig. 1, represent the vertical motion of the upper specimen as the lower member is moved horizontally. It will be seen that the vertical motion is considerably greater in Case *A* than in Case *B*. The traces shown are for only a short portion of the horizontal travel but are fully representative of several traces obtained over relatively long lengths of travel at different points on the specimens.

The coefficients of total friction were then measured and found to be 0.25 for both Case *A* and Case *B*. The coefficients were obtained first with a load of 34 grams (the weight of the top specimen and the tracer point), then with an additional load of 500 grams, and were found to be constant with load for this range. Moving the small upper specimen to new locations on the lower specimen failed to result in any significant change in the values of the friction coefficients, which were reproducible to within a few percent. Except for washing and drying with purified benzene and acetone, the specimens were used in the as-machined condition. It is probable that a thin layer of invisible oxides and air-

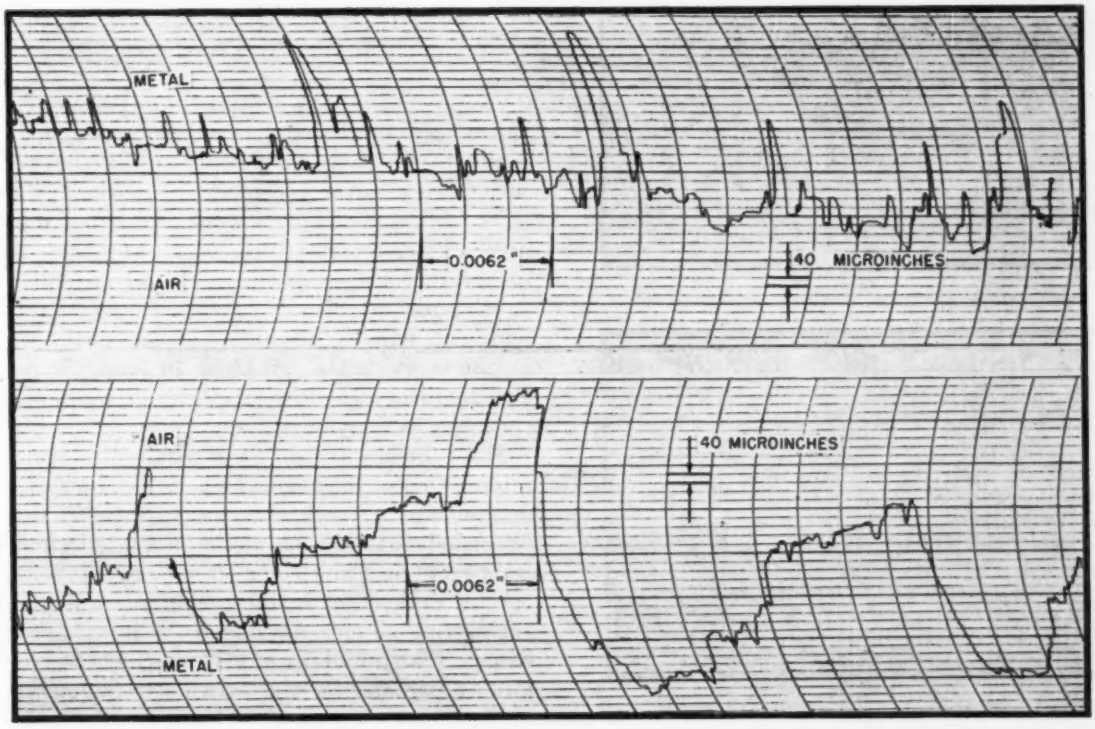

FIG. 2. Representative surface profile traces of the upper and lower friction specimens.

TABLE I.

	Case *A*	Case *B*
Sum of vertical displacements of upper specimen during horizontal sliding distance of 0.062 inch. (Taken from traces of Fig. 5.)	0.00302 cm	0.00102 cm
Weight of upper specimen and tracer point.	34 g	34 g
Mechanical work to lift upper specimen.	34(0.00302) = 0.102 g cm	34(0.00102) = 0.35 g cm
Measured coefficient of friction.	0.25	0.25
Frictional work to move upper specimen through izontal distance of 0.062 inch.	34(0.062)(0.25) (2.54) = 1.34 g cm	34(0.062)(0.25) (2.54) = 1.34 g cm
Percent mechanical lifting work of total frictional work.	$\frac{0.102}{1.34}(100) = 7.6\%$	$\frac{0.035}{1.34}(100) = 2.5\%$

borne contamination was present on the surfaces during the experiments. This should not affect the results of the experiment in any way other than reducing the absolute values of the friction coefficients.

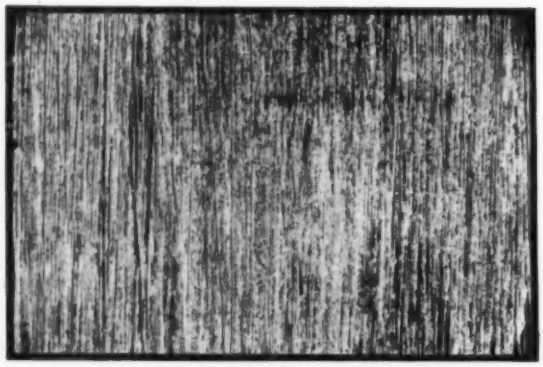

(a)

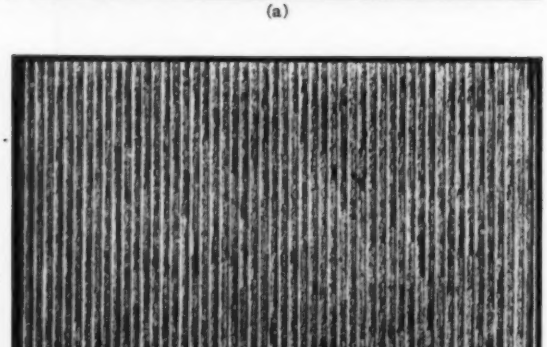

(b)

FIG. 3. Photomicrographs of the surfaces of the friction specimens. 10×.

RESULTS AND DISCUSSION

In computing the work of lifting the upper friction specimen over the asperities of the lower specimen it was assumed that no energy was recovered when the upper specimen moved downward. This assumption will make the computed value of mechanical work be somewhat greater than its true value as there is probably some energy recovery in the downward motion. The sum of all the individual vertical displacements of the upper specimen, which occurred while the specimens were rubbed through a horizontal sliding distance of 0.062 inch, was obtained from the large original of each trace of Fig. 5. The mechanical work of lifting the upper specimen was found by taking the product of this sum of the vertical rises and the combined weight of the upper friction specimen and the profile recorder tracer point. The results of these measurements are given in Table I.

It will be seen that the work of mechanical friction is only a few percent of the total friction work as calculated from the measured values of friction coefficient.

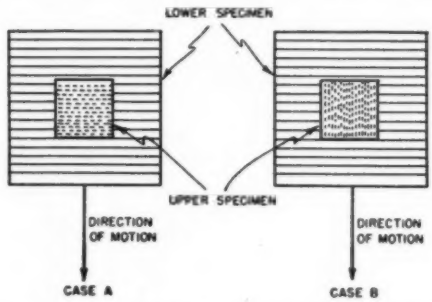

FIG. 4. Orientation of the surface finish marks in the two cases which were investigated.

This procedure was repeated for two other sets of traces (not shown) and the three sets of values were found to be in good agreement, with the mechanical lifting work never exceeding 10 percent of the total work of friction. Thus, it would seem that the measurable surface irregularities, which comprise the usual engineering surface finish, have only a small part in causing resistance to dry sliding. Apparently there is a sufficient number of widely-spaced peaks of similar height in contact at all times to limit the magnitude and frequency of the vertical movements of the test specimen to very low values.

Since the mechanical work required to overcome the interlocking of the engineering surface finishes does not account for the work of measured total friction, it can be argued that the whole mechanical interlocking process is repeated on a much smaller scale to satisfy the difference in work. That is, the irregularities of the gross or engineering surface finish may in turn have on their surface a large number of very much smaller asperities, formed perhaps by the occasional fragmenting of a metallic grain. Presumably, these smaller order irregularities might then interlock to lift and drop the upper

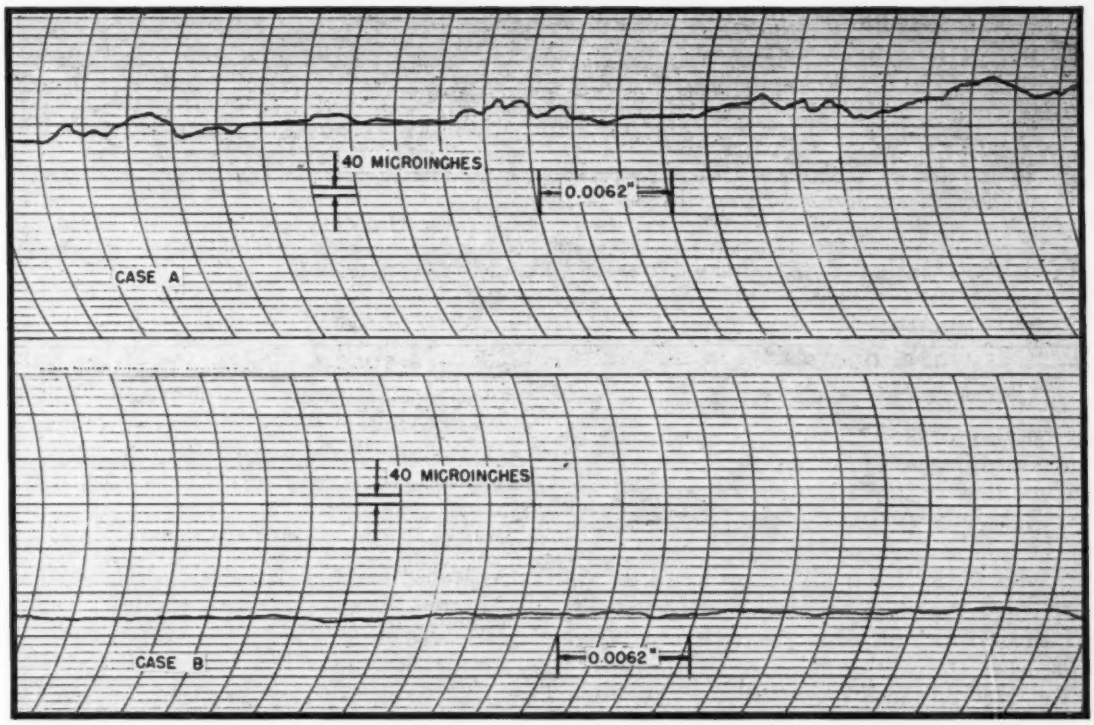

FIG. 5. Representative traces showing the vertical motion of the upper specimen as the lower member is moved horizontally.

friction specimen through a very small distance but at a high frequency, so requiring enough mechanical work to explain the measured work of total friction. The movements of the specimen produced by these irregularities would not be detected by the present instrumentation. However, if we extend the interlocking asperities picture to this "asperity's asperities" scale, it also seems reasonable to extend the explanation for the mechanism which prevented the gross irregularities of the engineering surface finish from being responsible for resistance to sliding. That is, if the measurable machined irregularities failed to result in appreciable vertical motion of the specimens at a frequency high enough to explain the work of total friction, it seems likely that a similar condition would exist in the case of the smaller order asperities—there would be a sufficient number of peaks of similar height in contact at all times to reduce both the magnitude and frequency of the vertical movements of the specimen to values incapable of explaining the work of total friction.

CONCLUSIONS

Unfortunately, much of the foregoing argument is supposition and because of the possibility of the existence of smaller order asperities, the experiment described herein cannot be fully conclusive in evaluating the role played by the mechanical component of friction. However, the following conclusions have been drawn from the experimental results of this investigation:

1. The work of mechanical friction is only a few percent of the total friction work, as calculated from the data of this experiment.
2. It would seem that the measurable surface irregularities which comprise the engineering surface finish have only a small part in causing resistance to dry sliding.
3. The coefficient of dry kinetic friction is essentially independent of the surface roughnesses that constitute the ordinary engineering surface finish, as indicated by the measured values obtained for Case *A* and Case *B*.
4. If lifting of the specimens by the interlocking of asperities is to contribute more than a small part of the total friction or resistance to sliding, it must be accomplished with high frequency vertical motions of less than a few microinches, that is, motions below the detectable limit of the tracer system used in this experiment.
5. If the resistance to sliding is considered to be due to the interlocking of extremely small asperities on the surfaces of the larger irregularities which constitute the ordinary surface finish, the process by which the very small asperities are formed must be such as to leave a non-directional distribution of these small asperities. This would be necessary if the friction is to be similar in several directions as was found in Case *A* and Case *B*.

The authors are indebted to Mr. James Lunan of the Chrysler Research Laboratories for his contributions to the experimental technique and to Professor John T. Burwell, Jr. of Massachusetts Institute of Technology for many helpful discussions.

This work was made possible through the generosity of the Chrysler Corporation.

Properties of Gold Deposited at Liquid Air Temperature

P. G. Wilkinson and L. S. Birks
U. S. Naval Research Laboratory, Washington, D. C.
(Received May 12, 1949)

Gold deposited in vacuum at liquid air temperature contained defects and strain. The number of defects and their characteristic decay energy increased rapidly with increasing rate of deposit in the range from 1 to 5 micrograms/cm²/min. The defects decayed with rising temperature but the relief of strain did not occur until after most of the defects had disappeared. Electron micrographs showed that the gold film was made up of aggregations of discreet particles rather than a smooth continuous film.

INTRODUCTION

MUCH work has been done in the past on the electrical, optical, and structural properties of thin, evaporated metal films.[1] In particular, Vand[2] deposited the films at liquid air temperature and observed an irreversible decrease in electrical resistance on aging the film or heating it to room temperature. He developed a theory for this decrease based on the assumption that the metallic lattice, as deposited, contained defects which increased the resistance. When the film was heated, according to his theory, the defects decayed and the resistance decreased. By measuring the rate of change of resistance he was able to set up a distribution function for the energy of decay of the lattice defects.

The purpose of this paper is to relate the decay energy distribution to the rate of deposit and correlate findings with electron microscopy and x-ray diffraction.

EXPERIMENTAL PROCEDURE

For the resistivity measurements, gold was evaporated from a conical tungsten filament in an all glass system at 10^{-6}-mm pressure. It was collected on glass or quartz at liquid air temperature. The resistance was measured continuously during deposition and after deposition as the temperature rose slowly and linearly with time to room temperature. Spectrographic analysis showed that no tungsten was deposited with the gold. After the resistance measurements were made on a specimen, the thickness was determined by dissolving the gold and making a colorimetric chemical analysis.[3]

Electron microscope specimens were collected in the same system on Formvar substrates. They were necessarily thinner than the resistance specimens and could not, of course, be observed at liquid air temperature. By placing a metal strip almost touching the Formvar, a shadow edge of finite width was obtained which showed a variation in the thickness of gold corresponding to a variation in the rate of deposit.

The x-ray diffraction studies were made in the apparatus described by Birks and Friedman[4] except that provision was made for cooling the specimen to liquid air temperature rather than heating it. The gold was evaporated inside the apparatus onto either glass or quartz at liquid air temperature, and new resistance measurements made along with the x-ray patterns.

ELECTRICAL RESISTANCE MEASUREMENTS

As is well known, the resistivity, ρ, of a metal may be expressed as the sum

$$\rho=\rho_T+\rho_B+\rho_i, \tag{1}$$

where ρ_T is due to scattering of electrons by the thermal oscillations of the atoms in the lattice and is reversible with temperature; ρ_B is due to scattering of electrons by the boundary of the film and is approximately constant for a given specimen; ρ_i is due to scattering of the electrons by lattice defects and impurities and is irreversible as the defects decay. It is assumed that the defects are sufficiently dilute so that they scatter the electrons independently.

Vand assumed that defects occur in the lattice of vacuum deposited metals. These defects were what he called combined type where lattice deficiencies and excesses existed close enough together so that only a small amount of energy was needed to combine them and form a more perfect lattice. When metal was deposited at liquid air temperature and then raised at a uniform rate to room temperature, he observed an irreversible resistance change corresponding to the change in ρ_i caused by the decay of the lattice defects. If the contribution to the resistivity by one defect per unit volume of characteristic decay energy ϵ is $r(\epsilon)$, and $N(\epsilon, t)$ is the number of defects of decay energy ϵ per unit volume at time t, ρ_i may be expressed approximately as

$$\rho_i=\int_{-\infty}^{+\infty} r(\epsilon)\cdot N(\epsilon, t)d\epsilon. \tag{2}$$

The determination of $N(\epsilon, t)$ at $t=0$ is desirable. However $r(\epsilon)$ is unknown and therefore only the product $r(\epsilon)\cdot N(\epsilon, 0)\equiv F_0(\epsilon)$ can be determined. Vand's mathematical development will not be repeated here, but for a uniformly rising temperature he arrived at the following result:

$$F_0(\epsilon)=-(1/kU)\cdot(d\rho_i/dT), \tag{3}$$

[1] Conference on the conduction of electricity in solids at Bristol, Proc. Phys. Soc. **49**, 151 (1937).
[2] V. Vand, Proc. Phys. Soc. **55**, 222 (1943).
[3] W. S. Clabaugh, J. Res. Nat. Bur. Stand. **36**, 119 (1946).
[4] L. S. Birks and H. Friedman, Rev. Sci. Inst. **19**, 323 (1948).

where k is the Boltzman constant, T is the temperature in degrees Kelvin and U is a function of the energy ϵ and the temperature T by the following equations:

$$u+\log u=\log 4nft, \tag{4}$$

$$U=u(u+2)/u+1, \tag{5}$$

and

$$\epsilon=ukT. \tag{6}$$

In Eqs. (4), (5), and (6), ϵ is the characteristic decay energy in ergs, n is the number of atoms which can initiate the decay of a defect and is estimated by Vand to be approximately 10 atoms per defect. f is the maximum Debye frequency of the lattice and has a value of $3.55\cdot10^{12}$/sec. for gold; u merely serves to relate ϵ and T to U in Eq. (3). The introduction of the Debye frequency f raises the calculated values of decay energy to the same order of magnitude as the binding energy of the lattice. To obtain values of $F_0(\epsilon)$ as a function of ϵ it is necessary to determine $d\rho_i/dT$ and U at various values of T and relate them to $F_0(\epsilon)$ and ϵ.

Figure 1 is a typical resistance curve for gold and shows a drop in resistance from 10,000 ohms at 220°K to less than 100 ohms at 290°K. To obtain the distribution function $F_0(\epsilon)$ it is only necessary to measure the slope of this curve at successive values of temperature T and correct the slope to resistivity rather than resistance and also correct for ρ_T. The temperature time relation is known so U may be determined from Eqs. (4) and (5) and the value of ϵ from Eq. (6). The distribution function $F_0(\epsilon)$ is plotted against energy in Fig. 2 and the peak ϵ_{max}, corresponds approximately to the mean energy of decay of the lattice defects. The peak is shifted to greater energy and greater amplitude with increased rate of deposit. Figure 3 for gold on quartz is similar to Fig. 2 except that the peak amplitudes $F_0(\epsilon)$ differ by several orders of magnitude. If $r(\epsilon)$ may be assumed constant for different substrates, there must be about 500 times as many defects in gold on glass as in gold on quartz. By varying the rate of deposit it was possible to establish the relation of the peak position ϵ_{max} and the peak amplitude $F_{0\,max}$ to the rate of deposit as shown in Fig. 4. As the deposit rate decreased, the peak energy became a minimum and the amplitude representing the number of defects appeared to approach zero. This means that for slow deposition, few defects are formed and these are of small decay energy. This is confirmed by plotting the resistance value itself immediately after deposit as a function of the rate of deposit (Fig. 5). The initial resistance is related to the sum of all the defects by the integral in Eq. (2). As the rate of deposit decreased, the initial resistance approached that of bulk gold. Separate experiments showed that ϵ_{max} and F_0 max were independent of film thickness in the range between 100 and 900 A.U. for a constant rate of deposit. Vand stated that ϵ_{max} increased with film thickness; however the data he reported did not take account of the rate of deposit and this probably explains the discrepancy.

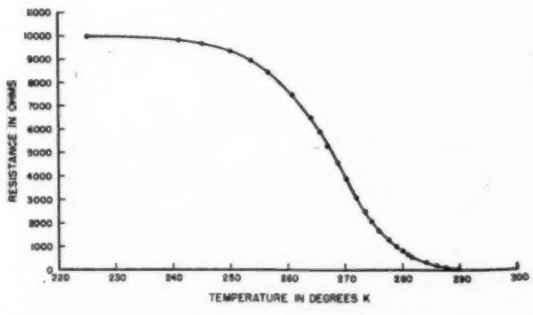

FIG. 1. Irreversible decrease in resistance of gold on glass as the film was heated to room temperature.

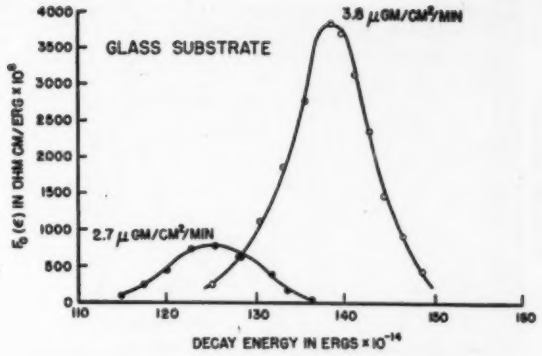

FIG. 2. The function $F_0(\epsilon)\equiv r(\epsilon)\cdot N(\epsilon)$ for glass substrate and two different rates of deposit.

X-RAY DIFFRACTION

If the lattice defects caused strain in the crystal lattice, they would be detectable by x-ray line broadening measurements. For bulk gold with our apparatus, the (111) line has a breadth at half maximum of about 0.5 degree. The gold film deposited on either glass or quartz showed a breadth of 1.3 degrees, Fig. 6, curve A. The deposit showed a strong preferred orientation with the (111) planes parallel to the substrate. As the temperature rose and the resistance decreased in its usual manner, the line breadth remained almost constant, contrary to what was expected since relief of strain is usually accompanied by narrowing of the x-ray lines. Suddenly when the specimen was almost to room temperature and the resistance approached its minimum value, the line width decreased rapidly to about 1 degree, curve B. The preferred orientation still existed. No further change took place on standing at room temperature. However, when the specimen was heated to 300°C for two hours, the breadth further decreased to 0.56 degree, curve C, or about that of bulk gold. The above data is typical of nine such x-ray experiments. The x-ray specimens had to be two or three times as thick as those described in the previous section in order to obtain a reasonable intensity of diffracted radiation; however, the resistance measurements made on them showed the same typical decrease indicating that the

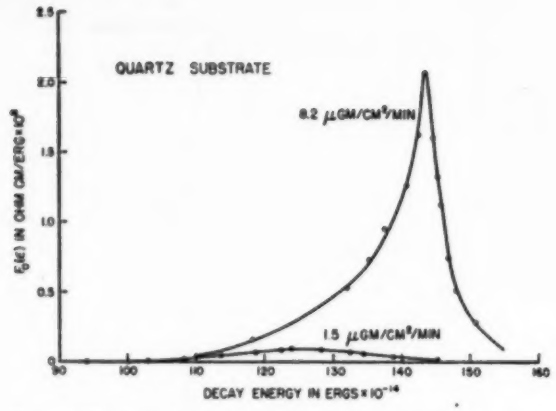

FIG. 3. The function $F_0(\epsilon) \equiv r(\epsilon) \cdot N(\epsilon)$ for quartz substrate and two different rates of deposit.

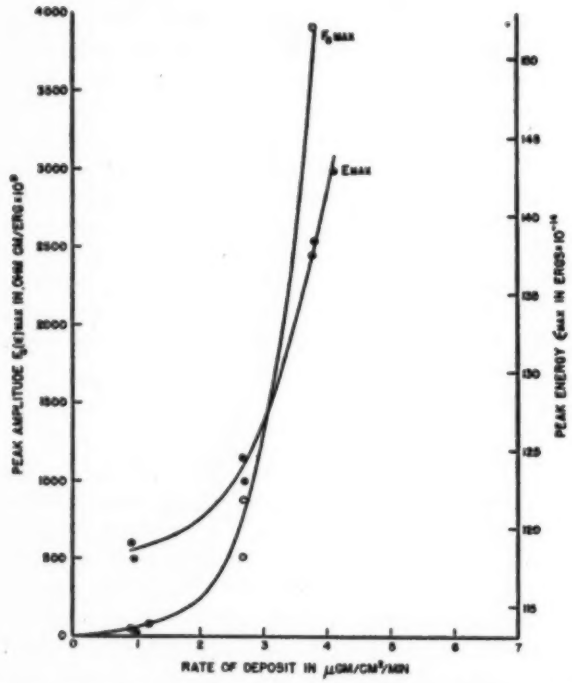

FIG. 4. The peak value of the $F_0(\epsilon)$ curve and the corresponding decay energy as functions of the rate of deposit.

increased thickness had not changed the properties of the deposit. Although the decrease in breadth from room temperature to 300° might be due to recrystallization and increase in particle size, it seems reasonable to assume that the sudden decrease in breadth below room temperature was caused by a sudden decrease in strain. More work is necessary before it will be possible to explain why the decrease in strain as indicated by x-ray diffraction does not seem to accompany the decay of lattice defects as indicated by change of electrical resistance.

ELECTRON MICROSCOPY

By using a metal strip to give a shadow edge on the microscope specimen it was possible to obtain a range of rates of deposit in one field. As Fig. 7 shows, there was a variation in particle size in going across the shadow edge, the particles being larger for the faster rates of deposit. This discreet particle type of structure is typical of gold evaporated at less than 10^{-4}-mm pressure if the deposit does not show tungsten spectrographically.[5] Where the gold was thick away from the shadow edge it appeared to be made up of aggregations of particles similar to the larger ones in Fig. 7. These discrete particles were definitely not the result of granulation in the microscope. From the micrographs, it was possible to say that although gold strikes the substrate as atoms, it has enough energy and mobility to collect

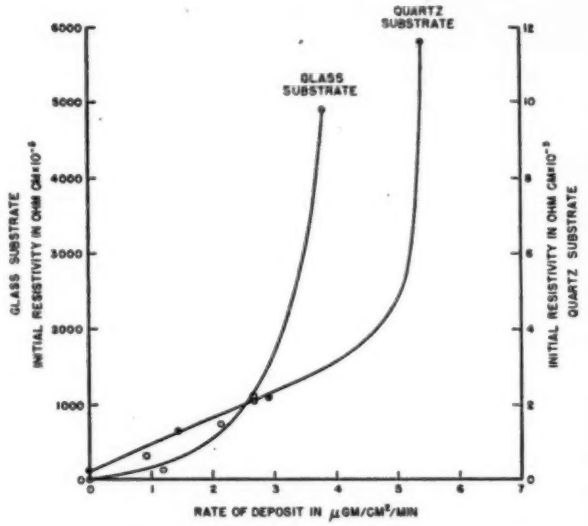

FIG. 5. Initial resistivity of gold on glass and on quartz as functions of the rate of deposit.

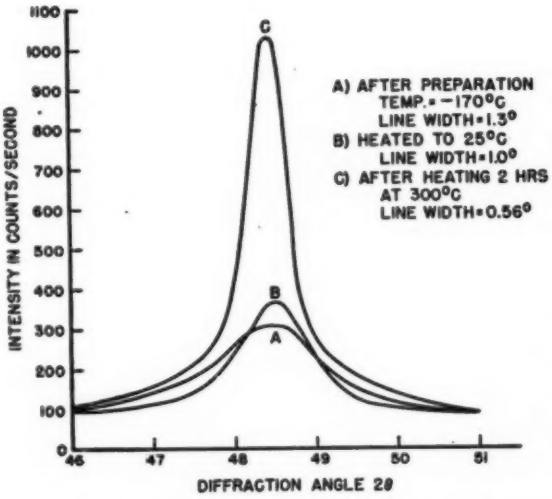

FIG. 6. X-ray line broadening of gold on glass.

[5] P. G. Wilkinson and L. S. Birks, NRL Report 3443, "Tungsten oxide shadowing of electron micrographs."

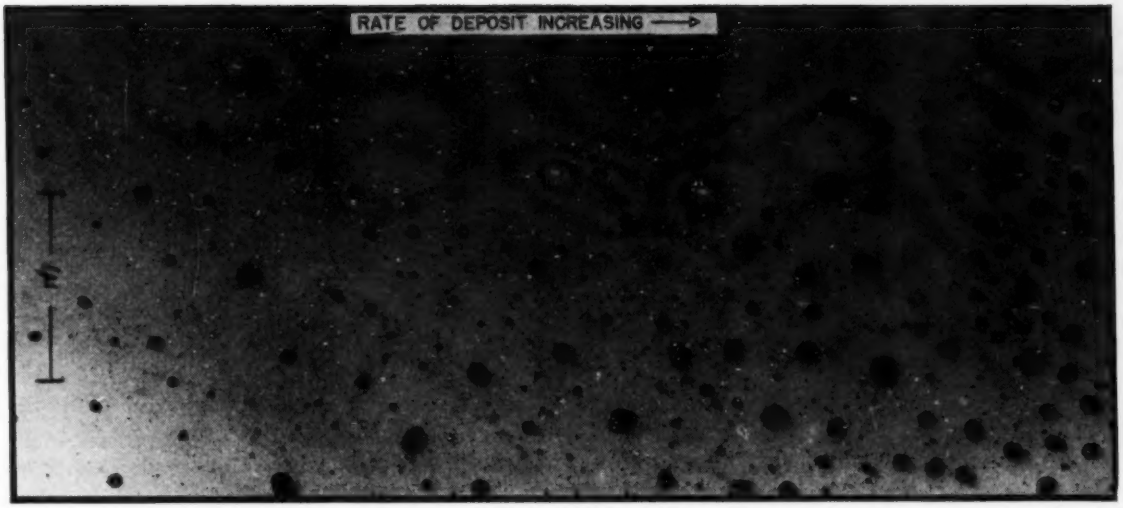

FIG. 7. Gold deposited on Formvar at liquid air temperature at about 10^{-6}-mm pressure. The Formvar was partially covered by a metal strip to produce a shadow edge corresponding to a changing rate of deposit.

into small crystalline particles. With increased rate of deposit, the growth is more rapid and more defects occur in the lattice.

ACKNOWLEDGMENT

We wish to thank Mr. R. T. Seal for his assistance in obtaining the experimental data.

Electron Optical Mapping of Electromagnetic Fields

L. MARTON AND S. H. LACHENBRUCH
National Bureau of Standards, Washington, D. C.
(Received May 16, 1949)

Two techniques have been devised for the exploration of electrostatic and magnetic fields where conventional methods fail. Both use electron lens systems to magnify the deflecting effect of the fields on electron beams. One technique is the electron optical analog of the "Schlieren" method; the other involves deformed shadows of a thin obstruction.

For several reasons the "Schlieren" patterns obtained experimentally thus far have been interpreted only qualitatively. The patterns obtained by the shadow method, however, have been used for quantitative evaluation of field strengths. Experimental patterns of both types, produced by the fields of magnetized recording wires, are shown.

The shadow method is theoretically applicable to the quantitative evaluation of a wide variety of electric and magnetic fields. It utilizes formulas based on relations between field distribution and electron deflection, and between the latter and the geometrical parameters of a focusing system. Such formulas are derived and applied to several simple types of field.

An application of the theory to the magnetized wires used in the experiments yields relations from which each field distribution is evaluated by fitting a line to experimentally determined points. The theory also predicts the geometrical properties of the experimental patterns.

The agreement between theory and experiment is sufficiently good to justify the underlying theoretical assumptions and approximations.

1. INTRODUCTION

IN a short communication[1] it was pointed out that, in close analogy to the light optical "Schlieren" effect, by means of which small variations of optical density can be observed,[2] an electron optical "Schlieren" effect can be produced and used for the observation of electrostatic and magnetic fields of minute extent.

A subsequent communication[3] contained a brief description of a second method of exploring such fields. This method is a direct outgrowth of the "Schlieren" experiments, and utilizes approximately the same apparatus, but involves measurements on deformed shadows against a bright background, as contrasted with the dark-field "Schlieren" intensity patterns.

An extensive analytical study of the experimental results obtained by this bright-field shadow method has since indicated that it lends itself especially well to the quantitative evaluation of field distributions, whereas the "Schlieren" method, in its present experimental stage, appears to be of value primarily as a tool for qualitative investigations.

[1] L. Marton, J. App. Phys. **19**, 687 (1948).
[2] See for example H. Schardin, *Toepler's Schlieren Method* (Translation 156, David W. Taylor Model Basin, U. S. Navy, July, 1947).
[3] L. Marton, J. App. Phys. **19**, 863 (1948).

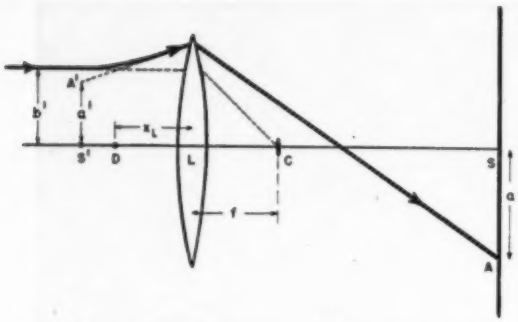

FIG. 1. Electron optical diagram of "Schlieren" method.

After brief descriptions of the experiments on the "Schlieren" and shadow methods, and a presentation of the experimental patterns obtained, this paper treats in detail the theory underlying the shadow method as a technique by which a wide variety of electromagnetic fields may be evaluated. The theory is then applied to the field used in the experiments. The experimental results are compared with predictions; and finally, theoretical formulas are applied to experimental data, for an evaluation of the field distribution and for a partial check on the validity of the underlying theoretical assumptions.

The experiments described deal with the observation of the magnetic field surrounding a magnetized recording wire, which was found to be an especially appropriate test object for bright-field shadow analysis. Such wires can be magnetized by short pulses of current by means of the conventionally built magnetic recording heads. Although such recording wires have been used for several years for practical purposes, there was very little information available on the extent of the magnetized regions and on the intensity of the magnetic field produced. As far as the extent of the magnetization is concerned, it can be determined experimentally by means of either the "Schlieren" effect or a powder pattern produced by extremely fine iron dust or a ferromagnetic colloid.[4] As regards the value of the field strength, its determination by means of the conventional methods seems to be highly impractical because of the very small dimensions of the magnetized regions. Under these conditions the best approach to the problem seems to be the use of electrons for the exploration of the fringe field extending from each magnetized region.

The consistency of the results obtained by the shadow method on this fringe field indicates the appropriateness of the method for such investigations and suggests its use in numerous other applications.

2. EXPERIMENTAL OBSERVATION OF A FIELD DISTRIBUTION

2.1. "Schlieren" Experiments

In its simplest form the electron optical "Schlieren" effect can be observed by using an electron source, the image of which is projected on a conveniently placed stop by means of an electron optical lens or lens system. This stop blocks all direct rays. In the absence of any scattering object or deflecting field in the space between source and lens, there is no radiation reaching the space beyond the stop. If, however, in the space between source and lens there exists a variation of the electromagnetic index of refraction (or there is some material present which scatters the electrons), the rays will be deflected from their normal pattern and will form a (dark-field) image in the image space beyond the stop. This image is obviously a pictorial representation of the deflections in the plane conjugate to the image plane with respect to the lens.

The electron optical arrangement used for obtaining "Schlieren" images of inhomogeneities produced by a deflecting field is shown schematically in simplified form in Fig. 1. The object (field) is placed in the vicinity of the point D, and for simplicity is assumed so oriented that trajectories incident in the plane of the figure remain in that plane after deflection. A converging lens L

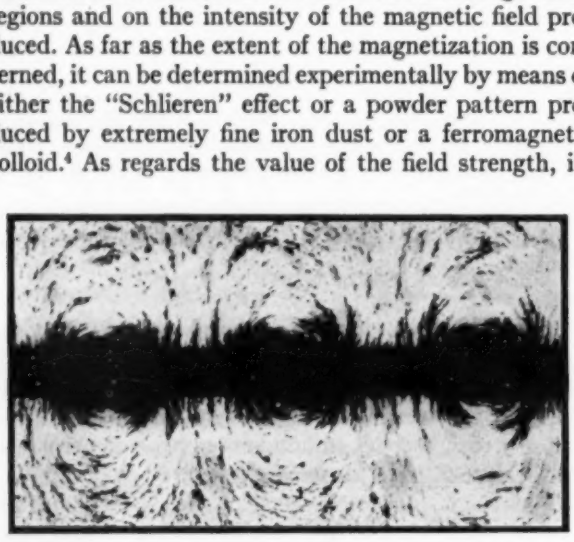

FIG. 2. Powder pattern identifying magnetized regions of experimental object; total magnification about 50×. (Courtesy of Irvin L. Cooter.)

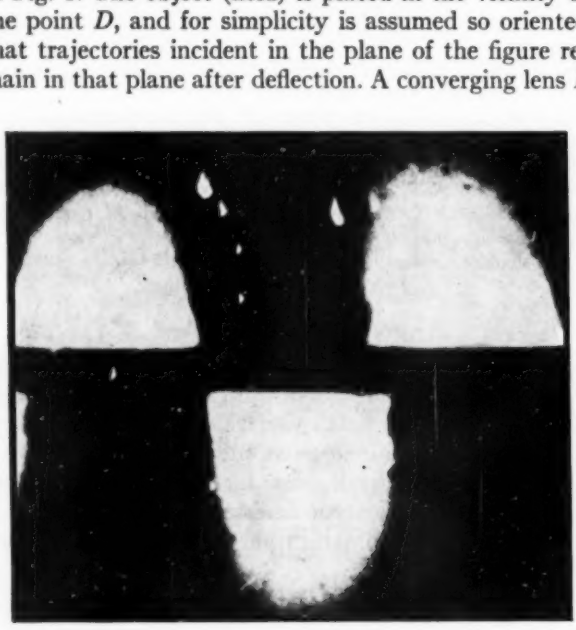

FIG. 3. A typical "Schlieren" pattern; total magnification of wire about 50×.

[4] I. L. Cooter, Paper No. 48–237, presented at Middle Eastern District No. 4 Technical Meeting of A.I.E.E., October, 1948.

is placed at a distance x_L from D, outside the field of the object. In the absence of such a field, a parallel[5] beam of electrons will be blocked by the center stop C placed at the lens focus; whereas rays deflected sufficiently by the field pass the stop and are collected on a fluorescent screen S.

The point A at which the electron path impinges upon the screen S is an optical image of the *virtual* object point A' at which the asymptote of the ray emerging from the deflecting field intersects the plane S' conjugate to S. Thus the distribution of electrons on the screen S is an image of the virtual distribution formed in the conjugate plane S' by the extended final asymptotes of the deflected rays.

The first "Schlieren" experiments conducted in this laboratory used as object a sample of cobalt-nickel-

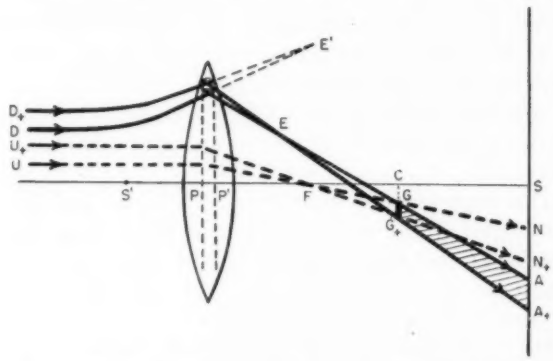

FIG. 4. Electron optical diagram of system used in shadow method. Displacement CG is adjustable.

plated brass recording wire, 0.117 mm in diameter, which was magnetized by short current pulses spaced at about 0.43 mm distance and alternating in sign. Thus the wire consists of a series of magnetized portions of approximately equal strength, size, and separation. Neighboring poles of successive magnets are of the same kind and result in repelling forces. Figure 2 is a powder pattern[4] showing the extent of the magnetized regions of the wire. The wire is placed normal to the plane[6] of Fig. 1 at D.

The experiments were carried out by means of a somewhat converted electron microscope. This electron microscope, of horizontal design, consists of an electron gun, three magnetic lenses and a fluorescent screen. The electron gun, for the purpose of these experiments, has been operated at 40 kv. The lenses are of the conventional ironclad design, without internal polepieces. In most experiments only one lens of the instrument was used for producing the "Schlieren" image, and the other two lenses were not connected at all. The lens most used for the experiments is the projector lens of the electron microscope, thus reducing the whole instrument to the simplest instrumentation as described above. In some experiments, however, the condenser lens of the instrument was switched on for the purpose of obtaining increased intensity of the image. As the condenser lens was used as a weak lens, it did not influence the essential optical arrangement, although it enhanced the available intensity.

The object was placed at distances varying from 20 to 50 mm from the lens center. The center stop at the lens focus consisted of a 1-mm diameter copper disk supported by two very fine metallic crosswires (0.033 mm diameter). The fluorescent screen for the observation of the image was placed at a distance of about 300 mm from the lens center.

A typical "Schlieren" image from the magnetized wire is shown in Fig. 3. The dark shadow of the wire is easily recognized in the image, surrounded by the bright "Schlieren" images. Such an image gives immediately a good qualitative picture of the extent of the magnetic field, and allows judgment about the extent of the magnetization along the wire axis. A comparison with the powder pattern of Fig. 2 permits an easy identification of the magnetized regions.

For actual quantitative field determinations, however, the potentialities of the direct "Schlieren" method have not been sufficiently explored. A quantitative application which suggests itself consists in assuming a simple analytical form for the field, and solving numerically for the parameters involved by equating some dimension of the actual "Schlieren" pattern to that predicted by theory. But ordinarily such a measurable dimension involves pattern boundaries determined by such limitations as beam thickness, lens aperture, and the size of the center stop. The causes of the actual pattern limitations measured must be positively identified experimentally before quantitative investigations may be

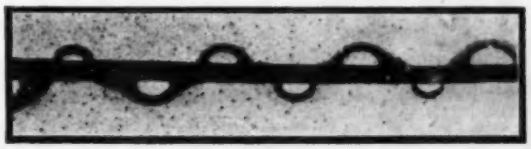

FIG. 5. Shadow pattern produced by thin, straight wire obstruction due to field of magnetized wire, whose image is the straight dark band. Photographic magnification of screen about 2.5×. Experimental parameters: $\mu=7$, $\nu=27$, $f=40$ mm, $V=4\times10^4$ volts. Obstruction approximately centered on optical axis.

FIG. 6. Shadow pattern similar to Fig. 5 but with obstruction appreciably off axis.

[5] Replacement of the parallel beam by a convergent or divergent beam requires only simple modification of the theoretical analysis.

[6] When, as in these experiments, the lens is of the magnetic type, the rays in image space and object space are generally in different planes. The plane of a schematic diagram will be understood to be that of its object space; that of its image space is obtainable by rotation about the optical axis.

undertaken. In addition, the patterns must be sufficiently well defined to permit quantitative measurements thereon.

2.2. Bright-Field Shadow Experiments

The bright-field shadow method,[3] while closely related to the "Schlieren" method, is free from the difficulties inherent in quantitative measurement of intensity patterns. Extensive experiments with this method, again using a magnetized wire as object, have indicated that it lends itself especially well to quantitative work. Insertion of a series of easily obtained experimental measurements into theoretically derived formulas has yielded fairly consistent values for the field strength, and close agreement with theory. The method has since been extended with some success to the measurement of fields of other forms than that of the magnetized wire.

Figure 4 is a symbolic diagram of the general arrangement used in the shadow method. In the absence of the deflecting field to be investigated (dashed rays U, U_+ in Fig. 4), a parallel[5] incident beam of electrons will converge to the focus F of the lens, whose principal planes are at P', P, and then diverge past the thin obstruction GG_+, which will cast a shadow NN_+ on the fluorescent screen S.

When a deflecting field is placed in the midst of the incident beam, a different pair of rays (solid rays D, D_+ in Fig. 4) will determine the shadow boundary. The cross-over point will be displaced from F, to some point E, and the resulting displacement of the shadow NN_+ to the position AA_+ may then be measured and substituted into theoretical formulas to obtain an estimate of the field strength. If a series of independent estimates is so obtained, for different values of the experimental parameters (such as the electron energy and the distances FC, CG), the degree of consistency with which they follow predicted laws serves as a measure of the applicability of the theoretical assumptions.

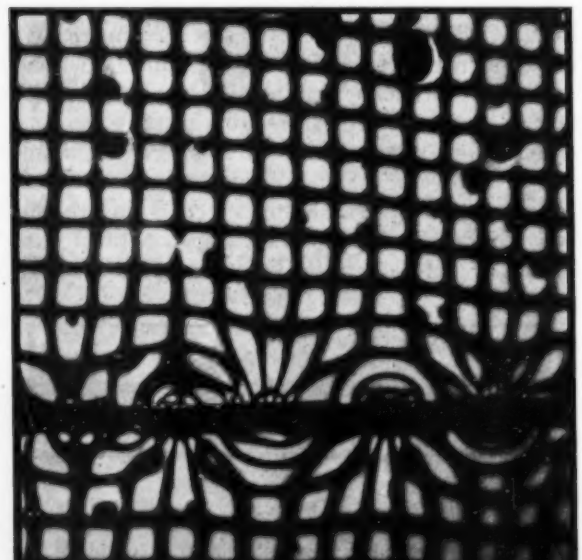

FIG. 7. Shadow pattern produced by wire mesh obstruction due to field of magnetized wire, whose image is the straight dark band. Photographic magnification of screen about 2.5×. Experimental parameters: $\mu=12.5$, $\nu=22$, $f=52$ mm, $V=1.2\times10^4$ volts.

Magnetized wire samples of the type described in Section 2.1 proved to be excellent test objects for quantitative study by the shadow method. The wire is placed normal to the plane[6] of Fig. 4, with its axis intersecting that plane at the point S' conjugate to S. Since the fields in the equatorial planes of any two adjacent magnetized regions of the wire are opposite in sign, the deflections of the beam in such planes, and the consequent displacements of the shadow NN_+, must be in opposite directions. This fact accounts for the zigzag shape of the shadow of the thin silver wire used as obstruction.

This long filiform obstruction is oriented parallel to the image of the magnetized wire. Since that image rotates as the magnification of the magnetic lens is varied, mechanical means must be provided for the alignment of the two images.

The apparatus used in the shadow method experiments is essentially the same as the "Schlieren" apparatus described in Section 2.1. The latter, together with the above remarks describing the rearrangement, should constitute a sufficient description of the experimental procedure involved.

Figures 5 and 6 are photographs of the configurations on the fluorescent screen for two different positions of the obstruction GG_+. The wide dark band is the image of the magnetized wire, while the thinner, distorted band is the shadow image of the obstruction. In Fig. 5 the obstruction is approximately centered about the optical axis, while in Fig. 6 it is at an appreciable distance therefrom. As the obstruction is moved still further from the central position, its shadow straightens out. The turning points, i.e., points of maximum and minimum deflection of the shadow, correspond to the equatorial planes of the magnetized regions.

Instead of varying the distance GC, as in these photographs, one may substitute for the single obstruction a fine wire mesh, thus obtaining an entire series of measurements simultaneously from a single shadow pattern on the screen. Figure 7 is a photograph[7] obtained using a wire mesh having 91 wires per cm in two perpendicular directions, one of which is made approximately parallel to the image of the magnetized wire. Each of the mesh wires in this parallel direction produces a shadow approximately equivalent to that produced by

[7] Experiments conducted by Mr. D. L. Reverdin.

a single obstruction in a given position. The object used in Fig. 7 is not identical with that used for the other photographs, but has the same geometrical dimensions.

The peculiarities and significance of these shadow patterns, and the quantitative data which they yield, are discussed in Section 5 after a general theoretical analysis.

3. THEORY OF SHADOW METHOD

3.1. First-Order Optics of Method

Mathematical formulas will now be derived for the quantitative evaluation of electric and magnetic fields from patterns obtained by the bright-field shadow

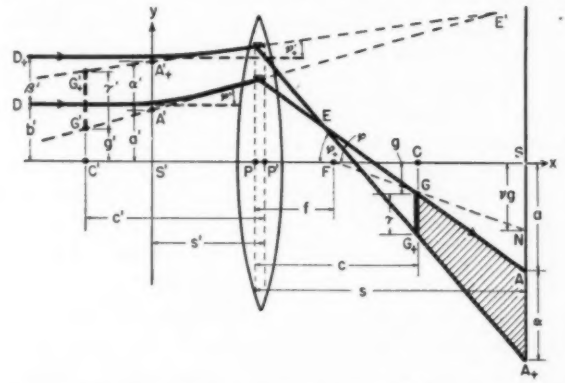

FIG. 8. Detailed electron optical diagram of shadow method, defining notation.

method. We shall limit the general analysis to systems having the following properties:

(a) The trajectories lie entirely in one plane[6] (i.e., the plane of Fig. 4).

(b) All lateral distances and angles (measured from the optical axis)—at least for those rays which determine shadow measurements—are sufficiently small to make geometrical aberrations negligible, so that Gaussian dioptrics is applicable.

(c) The distance between deflecting field and lens field is sufficiently great so that the interaction between the two fields may be neglected.

(d) The electron energy V involved is in the non-relativistic range.

These conditions place limitations on the form of the electromagnetic field, as well as its position and orientation. Thus condition (a) requires that planes exist in which the field produces only plane deflections; and condition (b) requires that these deflections be small in general.

Figure 8 is similar to Fig. 4 but contains sufficient additional detail to define the symbols to be used in the analysis. The two rays drawn[6] represent the paths of the limiting electrons which, after deflection by the field, just pass the obstruction at its edges G and G_+ and thus form the boundaries of the displaced shadow AA_+. The dashed lines $G'A'E'$, $G_+'A_+'E'$ are the asymptotes of these trajectories on the emergent side of the field. *Primed* points, distances, and angles represent *conjugates* of corresponding unprimed symbols with respect to the

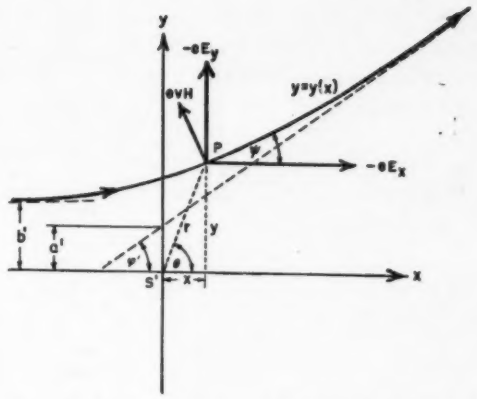

FIG. 9. Coordinate diagram of typical plane electron trajectory in deflecting field.

lens; points such as C', G', A', A_+', and distances such as γ', g', α', c', are thus defined.

All labeled distances and angles are defined as positive when as in Fig. 8, and negative when in the opposite sense. Without loss of generality it is always possible, and often convenient, to specify that

$$g \geqslant 0. \tag{1}$$

A diagram in which g is negative (i.e., in which G is above C) may always be reflected with respect to the optical axis to produce an equivalent diagram which satisfies (1) and in which all distances normal to the optical axis have changed sign.

The location of the deflecting field in the system must satisfy condition (c) above but is otherwise somewhat arbitrary. As will be shown in Section 4.1, it is often advantageous to center the field about S', the point conjugate to the screen center.

By conditions (b) and (c) above, the rays EA_+ and EA (Fig. 8) are straight lines and are conjugate to the asymptotes $E'A_+'$ and $E'A'$ with respect to the lens. Thus the effect of the field and distant source is equivalent to that of a virtual source at E', defined as the point of intersection of these asymptotes. The resulting one-to-one correspondence reduces the analysis to a study of the geometry in the object space to the left of the lens, and in particular along the line $S'A'A_+'$. The geometry of the image is then obtained directly through the introduction of magnification factors.

We define four such magnification factors:

$\mu = s/s' =$ magnification, on screen, of object on line $S'A'A_+'$; (2)

$\nu = (s-f)/(c-f) = NN_+/GG_+$ (Fig. 4)
= magnification of obstruction GG_+ as determined by its shadow on screen *in absence of deflecting field;* (3)

$n = \alpha/\gamma = EA/EG =$ shadow magnification similar to ν but *in presence of field;* (4)

$\omega = c/c' = \gamma/\gamma' = g/g'$
= magnification associated with obstruction plane CGG_+ and its conjugate plane $C'G'G_+'$. (5)

Ordinarily only μ and ν will be known experimentally, the others being derivable therefrom, as will be shown.

From (2), (5), and the image formula $1/s+1/s'=1/c+1/c'=1/f$, we obtain

$$c=f(1+\omega), \quad s=f(1+\mu), \tag{6}$$

whence (3) yields a simple formula for ω in terms of μ and ν:

$$\omega=\mu/\nu. \tag{7}$$

Equations (2)–(7) and Fig. 8 yield the following relations between quantities in object and image spaces:

$$\left.\begin{array}{llll} a'=a/\mu, & a_+'=a_+/\mu, & \alpha'=\alpha/\mu; \\ g'=g/\omega=g\nu/\mu, & g_+'=g_+\nu/\mu, & \gamma'=\gamma\nu/\mu; \\ s'=s/\mu=f(1+1/\mu); & c'=c/\omega=f(1+\nu/\mu). \end{array}\right\} \tag{8}$$

Finally, condition (b) and the geometry of Fig. 8 yield a relation involving the deflection angle ϕ' for the ray $DG'GA$:

$$a'-g'-\phi'(c'-s')=0. \tag{9}$$

The general key equation for the determination of field strength is now obtained at once by transforming (9) into image space by means of (8):

$$a-\nu g-(\nu-1)f\phi'=0. \tag{10}$$

The following considerations should clarify the meaning of Eq. (10). In it ν, g, and f, are known parameters of the optical system; a is the experimentally measurable shadow distance SA (Fig. 8) on the fluorescent screen; and ϕ' is the angular deflection of the ray considered. In general, ϕ' and a', which together completely describe the asymptote $G'A'E'$ of this ray, are functions of the field distribution, the electron energy, and the initial distance parameter b' which identifies the ray in the incident parallel beam. On eliminating b' between these two relations, one obtains ϕ' as a function of field, energy, and $a'=a/\mu$, μ being another known optical parameter. Hence on substitution of such a function for ϕ', one obtains from (10) an implicit relation among the unknown parameters of the field distribution, the known parameters of the apparatus, and the experimentally measurable distance a on the screen. Thus, if the field distribution is assumed to have any specified analytical form, involving, say, N parameters, these parameters may in general be evaluated through the application of (10) to each of N independent measurements.

A relation exactly similar to (10) applies for the second ray $D_+G_+'G_+A_+$:

$$a_+-\nu g_+-(\nu-1)f\phi_+'=0, \tag{11}$$

where

$$a_+=a+\alpha, \quad g_+=g+\gamma. \tag{12}$$

Hence in the general case the two screen measurements $SA=a$ and $SA_+=a_+$ may themselves yield two independent relations from a single screen image, provided the difference between these measured distances is not too small.

3.2. Relation between Field and Deflection

In order to use Eq. (10) one must first express the deflection ϕ' in terms of the field distribution parameters. In this section the equations required to obtain such an expression are derived for the very general case of an arbitrary field distribution subject only to the restrictions that its electrostatic and magnetic components separately satisfy the conditions of Section 3.1.

Figure 9, which shows a typical electron path $y=y(x)$ through the deflecting field to be studied, defines a coordinate system in the object space. The optical axis of the system is taken as x-axis, while the point S' of Fig. 8, usually taken at or near the field center, is chosen as origin. As the incident asymptote is parallel to the x-axis, the initial ordinate $b'=y(-\infty)$ serves as a parameter identifying the ray. The emergent asymptote is characterized by a slope $\tan\phi'=y'(+\infty)$ and y-intercept a' which are functions of b', the field parameters, and the energy V. The notation of Fig. 9 corresponds to that used for the ray D of Fig. 8, and requires simple and obvious modification by means of subscripts for the second ray D_+. Polar (r, θ) and rectangular (x, y) coordinates will be used interchangeably.

In the plane of Fig. 9, let $E_x(x, y)$, $E_y(x, y)$ be the x- and y-components of the electric field, and $H(x, y)$ the magnetic field directed normal to this plane. The other components of both fields must be zero, in accordance with our limitation that condition (a) (Section 3.1) be satisfied by both fields separately. If the sense of H is defined as positive when directed upward from the plane of the figure, then the normal force $F(x, y)$ on the electron at any point (x, y) of the trajectory is (Fig. 9)

$$F(x, y)=e(E_x\sin\psi-E_y\cos\psi+vH), \tag{13}$$

where e, m, and $v(x, y)$ are the charge, mass, and speed of the electron, and

$$\tan\psi(x, y)=dy/dx, \tag{14}$$

the slope of the trajectory. The sign of $F(x, y)$ in (13) is that of its y-component.

If $V(x, y)$ is the potential at (x, y), referred to that at the cathode of the electron gun, and condition (d) (Section 3.1) is taken into account, then

$$E_x=-\partial V/\partial x, \quad E_y=-\partial V/\partial y, \quad v=(2eV/m)^{\frac{1}{2}}. \tag{15}$$

One may now equate two expressions for the curvature $1/R$ of the electron path at the point (x, y):

$$(d^2y/dx^2)[1+(dy/dx)^2]^{-\frac{1}{2}} = 1/R(x, y)=F(x, y)/mv^2. \tag{16}$$

On substituting (13), (14), and (15) into (16), one obtains directly the differential equation of the trajectory $y=y(x)$:

$$(d^2y/dx^2)[1+(dy/dx)^2]^{-\frac{1}{2}}-(e/2mV)^{\frac{1}{2}}H +[(\partial V/\partial x)dy/dx -\partial V/\partial y][1+(dy/dx)^2]^{-\frac{1}{2}}/2V=0. \tag{17}$$

But condition (b) (Section 3.1) implies

$$dy/dx\ll 1, \tag{18}$$

so that (17) simplifies approximately to

$$y''(x)+[(\partial V/\partial x)/2V]y'(x) -[(\partial V/\partial y)/2V+(e/2mV)^{\frac{1}{2}}H]=0. \quad (19)$$

When specific analytical expressions are substituted for $V(x, y)$ and $H(x, y)$, differential Eq. (19) and the boundary conditions

$$y(-\infty)=b', \quad y'(-\infty)=0 \quad (20)$$

determine the form of the trajectory $y(x)$, implicitly at least. The total angular deflection ϕ', which must be substituted into (10), is then determined from the definition

$$\phi' \approx \tan\phi' = y'(+\infty), \quad (21)$$

the approximation being justified by (18).

Each of the examples in the next section involves an electrostatic or magnetic field sufficiently simple in analytical form so that the differential Eq. (19) may be solved explicitly. For the case of a magnetic field alone, V and v are constants.

3.3. Application to Special Field Types

The formulas (19), (20), (21), (10) are now applied to three specific types of field distribution, to obtain analytical relations between the parameters of such distributions and the known or measurable experimental parameters. In Section 4.1 the analysis is extended to the field of the magnetized wire used in the experiments.

3.3.1. Uniform Magnetic Field

One of the simplest magnetic field distribution forms is given by[8]

$$H(x, y)=\begin{cases} H_0=\text{constant} & \text{when } |x|<x_0 \\ 0 & \text{when } |x|>x_0 \end{cases} \quad \text{(all values of } y\text{)}, \quad (22)$$

where H_0 and x_0 may, in general, be considered as unknown parameters.

For this case one integration of (19), when combined with (20), yields for the deflection angle

$$\phi'=y'(+\infty)=(e/2mV)^{\frac{1}{2}}\int_{-x_0}^{x_0} H_0 dx = x_0 H_0 (2e/mV)^{\frac{1}{2}}. \quad (23)$$

On substituting this expression for ϕ' in the key formula (10), one obtains the relation

$$x_0 H_0=(mV/2e)^{\frac{1}{2}}(a-vg)/(v-1)f=K(a-vg). \quad (24)$$

Here K and v are known constants of the optical system and electron beam, while g in general is known but variable, and the corresponding a is measurable. Equation (24) thus implies that $(a-vg)$ is theoretically a fixed quantity, identical for all rays and all values of g, and proportional to the product x_0H_0. The degree to which this constancy is approximated experimentally serves as a test of the hypothetical distribution form (22), while if either x_0 or H_0 is measurable, the other parameter may be evaluated.

[8] The Laplace equation rules out the exact realization of this case, which, however, serves as a good first approximation for several types of fields.

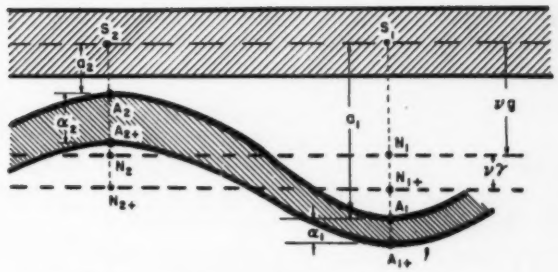

FIG. 10. Diagram of a typical shadow pattern produced by wire obstruction due to field of magnetized wire. Dashed lines represent position of shadow in absence of field. Straight solid band is image of magnetized wire.

3.3.2. Uniform Electrostatic Field

A simple electrostatic example is that of the deflecting field of two parallel plates, separated by a distance $2D$, and at potentials $V_0+\Delta V$, $V_0-\Delta V$, where V_0 is the potential corresponding to the initial energy of the electron beam. The plates are placed parallel to the optical (x-) axis (Fig. 9), with the origin S' at the field center, their x-dimension being $2x_0$. We limit ourselves to the case in which ΔV is sufficiently small in comparison with V_0 so that the field is approximately uniform ($\partial V/\partial y \equiv \Delta V/D$, $\partial V/\partial x \equiv 0$) between the plates ($|x|<x_0$) and zero elsewhere.

The expression for the angle of deflection of an electron incident parallel to such plates is well known, and is easily verified by means of Eqs. (19), (20):

$$\phi'=y'(+\infty)=x_0\Delta V/V_0 D. \quad (25)$$

Substitution of (25) into the key formula (10) yields

$$x_0\Delta V/D=V_0(a-vg)/(v-1)f. \quad (26)$$

The quantities on the right are known or measurable parameters of the optical system, while ΔV, x_0, D are characteristics of the electrostatic field. It is seen that the constancy and interdependence of these quantities, as predicted by (26), are quite analogous to those predicted by (24) for the magnetic case. Thus the degree of accuracy of the approximations in any particular case may be tested experimentally by the shadow method, while if either x_0 or the field $\Delta V/D$ is known the other may be evaluated.

3.3.3. Pair of Point Poles

If the field is that of a magnet perpendicular to the plane of Fig. 8, having its center at S', and consisting of point poles of strengths $+p$ and $-p$ at distances λ below and above the plane of the figure, respectively,

then that plane is the equatorial plane of the magnet, so that condition (a) (Section 3.1) is satisfied. The field in that plane is well known to be

$$H(x, y)=2p\lambda/(x^2+y^2+\lambda^2)^{\frac{3}{2}}=M/(r^2+\lambda^2)^{\frac{3}{2}}, \quad (27)$$

M being the magnetic moment.[9] (If λ is allowed to approach zero, M remaining finite, this field reduces to that of an ideal dipole.)

Condition (b) (Section 3.1) limits the analysis to rays which are only slightly deflected by the field H. We shall therefore be here concerned only with trajectories sufficiently distant from the magnet poles so that, in the region of appreciable field, y does not differ from its initial value b' by more than an amount

$$\Delta y \ll (b'^2+\lambda^2)^{\frac{1}{2}}, \quad (28)$$

and therefore, by (27), to very close approximation along the trajectory,

$$H(x, y)=H(x, b')=M/(x^2+b'^2+\lambda^2)^{\frac{3}{2}}. \quad (29)$$

Furthermore, since the deflection angle is small, the line of symmetry of the trajectory, which must obviously pass through S' (Fig. 9) and intersect the trajectory orthogonally, almost coincides with the y-axis. Hence the two asymptotes intersect approximately at the point ($x=0$, $y=b'$). The y-intercept, a', of the final asymptote is therefore very closely approximated by

$$a'=b'. \quad (30)$$

In fact, it can be shown that the difference between a' and b' is small even in comparison with the small quantity Δy of (28), and it is this property which is utilized experimentally as an aid to focusing (end of Section 4.1).

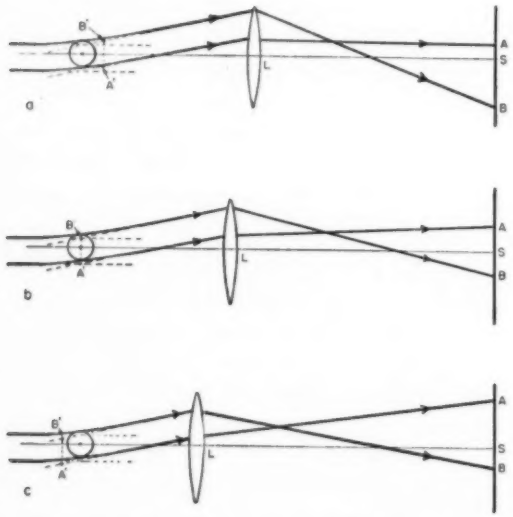

FIG. 11. Optical diagram in an equatorial plane of magnetized wire, showing method of focusing wire on screen.

(a) Object too far from lens, image AB not centered.
(b) Object in focus, image AB approximately centered.
(c) Object too close to lens, image AB not centered.

[9] The permeability factor, being unity for a vacuum when e.m.u. are used, is omitted from (27).

On substituting (29) into (19), integrating once, and using (20), (21), (30), and (8), one obtains for the total angular deflection in this case

$$\phi'=y'(+\infty)=(e/2mV)^{\frac{1}{2}}\int_{-\infty}^{+\infty} Mdx/(x^2+b'^2+\lambda^2)^{\frac{3}{2}}$$

$$=2B/(b'^2+\lambda^2)=2B/(a'^2+\lambda^2)$$

$$=2\mu^2B/(a^2+\mu^2\lambda^2), \quad (31)$$

where

$$B=M(e/2mV)^{\frac{1}{2}}=Me/mv. \quad (32)$$

The key formula (10) thus takes the form

$$B-\lambda^2 u=w, \quad (33)$$

where

$$u=(a-\nu g)/2(\nu-1)f, \quad w=a^2(a-\nu g)/2\mu^2(\nu-1)f. \quad (34)$$

Here B and λ^2 are constants of the field distribution (the electron energy V being fixed), while a, g, ν, μ, and f, and therefore u and w, are in general experimentally known or measurable quantities. Hence any two sets of values of these quantities yield a pair of equations from which B, λ, and therefore $H(x, y)$ can be evaluated; while the replacement of a and g by a_+ and g_+ in (34) redefines u and w to yield an equally satisfactory relation (33) based on the other shadow edge.

4. THEORETICAL BASIS OF THE SHADOW EXPERIMENTS

4.1. Extension of Theory to Experimental Object

A modification of the results of Section 3.3.3 yields theoretical relations which, when applied to measurements on the photographs of Figs. 5–7, yield an evaluation of the fields surrounding the magnetized wires described in Section 2.1.

The wire is placed normal to the plane[6] of Fig. 8, with its axis intersecting that plane at S'; and the separation of the magnetized regions is sufficiently small compared with the object-to-lens distance s' so that all their equatorial planes may be considered as passing through the lens center. Thus Fig. 8 may be considered as lying in any one of the equatorial planes, condition (a) (Section 3.1) being satisfied to close approximation in every such plane.

For purposes of analysis it is assumed that, outside the wire surface, the field in each equatorial plane is equivalent to that of a pair of point poles, of unknown moment M, and separated by an unknown distance 2λ. The field distribution in each such plane is therefore of form (27) (Section 3.3.3), M and λ being field parameters to be determined experimentally. In accordance with the sign conventions described in Section 3.2, the equatorial fields are

$$H_1=H_1(x, y)=H_1(r)=M/(r^2+\lambda^2)^{\frac{3}{2}} \quad (35a)$$

for one set of alternate magnets, and

$$H_2=-H_1=-M/(r^2+\lambda^2)^{\frac{1}{2}} \tag{35b}$$

for the other set of alternate magnets. When it is specified that

$$M>0, \tag{36}$$

then H_1 pertains to the magnets whose fields are directed upward from the plane of Fig. 8.

When the wire is placed as described in the optical system of Fig. 8, the resulting shadow AA_+ of the obstruction GG_+ on the screen S traces a zigzag pattern in the plane normal to the figure. Figure 10 shows the approximate shape of such a pattern for a particular position g of the obstruction. The points S_1, N_1, A_1, etc., and S_2, N_2, A_2, etc. represent the positions of the points S, N, A, etc., of Figs. 4 and 8 in two consecutive equatorial planes, corresponding to the fields H_1 and H_2 respectively, and define distances such as a_1, α_1, a_2, α_2.

An adaptation of (33) to the fields (35) yields equations of the form

$$B-\lambda^2 u=w, \tag{37}$$

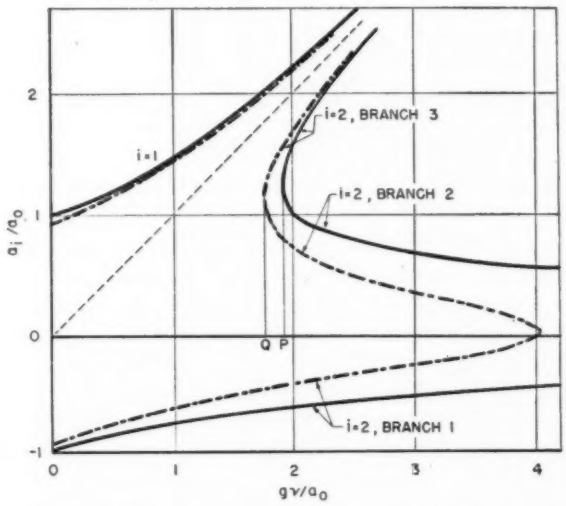

FIG. 12. Theoretical distances a_i (normalized) of shadow edge from optical axis, in equatorial planes of magnetized wire image, as functions of distance g (normalized) of corresponding edge of obstruction itself from optic axis. Solid curves are for $\lambda=0$ (ideal dipole), dot-dashed curves are for $\lambda=0.5a_0/\mu$.

where B, defined by (32), is >0 by convention (36), and

$$\left.\begin{aligned} u&=(-1)^i(\nu g-a_i)/2(\nu-1)f, \\ w&=(-1)^i a_i^2(\nu g-a_i)/2\mu^2(\nu-1)f, \end{aligned}\right\}(i=1,2). \tag{38}$$

On each shadow pattern, in general, each of the measurements a_1, a_2, as well as a_{1+}, a_{2+} for the other edge of the shadow, determines a pair[10] of values (u, w), which may be plotted on a linear scale to form a scatter diagram, when the parameters μ, ν, f, g of the optical system are known. According to (37), theory predicts that all these points will fall on a straight line of slope $(-\lambda^2)$ and w-intercept B. It follows that the field parameters B and λ may be evaluated by fitting a line to the experimental points, while the deviation of these points from the line serves as a test of the hypotheses.

Finally, the field strengths H_1 and H_2 at any specified distance r from the wire axis may be obtained from the following expressions, derived from (35) and (32):

$$\begin{aligned} H_1=-H_2&=(2mV/e)^{\frac{1}{2}}B/(r^2+\lambda^2)^{\frac{1}{2}} \\ &=33.7BV^{\frac{1}{2}}/(r^2+\lambda^2)^{\frac{1}{2}}. \end{aligned} \tag{39}$$

(The last form gives H_i in oersteds for B in mm^2, r and λ in mm, and the electron energy V in electron volts.)

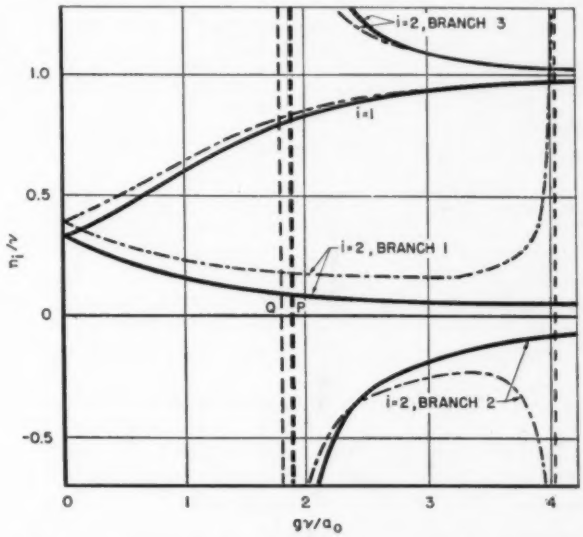

FIG. 13. Theoretical magnifications n_i (normalized) of thin shadow, in equatorial planes of magnetized wire image, as functions of obstruction distance g (normalized). Solid curves are for $\lambda=0$ (ideal dipole), dot-dashed curves are for $\lambda=0.5a_0/\mu$.

The measurement of the a's is somewhat facilitated by the presence of the image of the magnetized wire itself, which appears as a straight dark band across the pattern (Fig. 10). The axis of the band is easy to construct on a photograph, and serves as an origin for the measurement of the shadow distances in the equatorial planes.

The same band may be utilized as an aid to focusing. At the voltages used in the experiments, even the boundary rays from the edges of the wire (object) suffer only small deflections, as may be verified from Section 5.2. According to (30) the two asymptotes of any such trajectory intersect approximately in the object plane, i.e., the plane through the wire axis and normal to the optical axis. Hence the electrons entering the lens from the wire boundaries appear to have emerged from approximately the same point in this object plane as would the same electrons in the absence of the deflecting field. When, as in Fig. 11(b), this plane is in focus on the screen S of Fig. 8, therefore, the location of the images of the rays from different parts of the wire boundary is practically independent of the field, and therefore an approximately true image AB of the wire appears on the screen S when the wire axis is in the conjugate plane S'. Figures 11(a), 11(c), on the other hand, represent out-of-focus objects. It will be noted that the slight curvature of the trajectory produces a slightly off-

[10] In some cases a single edge of the obstruction casts a double or triple shadow, yielding additional values of (u, w), as shown in Sections 4.2 and 5.1.

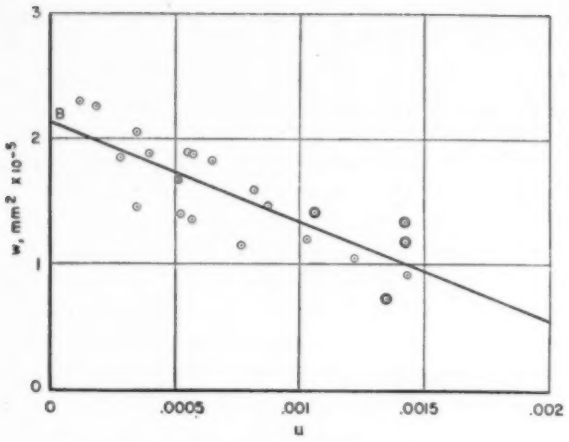

FIG. 14. Experimental scatter diagram obtained from measurements on Figs. 5 and 6, and fitted theoretical line, determining parameters B and λ required to evaluate field strength of first magnetized wire. Points in double circles were given double weight in fitting the line.

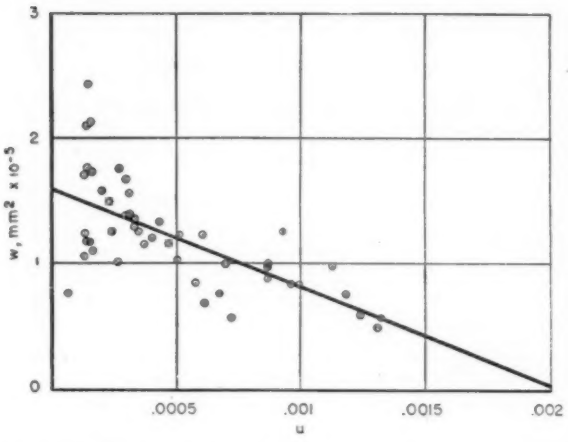

FIG. 15. Experimental scatter diagram obtained from measurements on Fig. 7, and fitted theoretical line, for evaluation of field strength of second magnetized wire. (Converted to same beam energy as Fig. 14.)

center image even in Fig. 11(b), since the virtual object $A'B'$ does not quite coincide with a diameter of the wire; but under the existing experimental conditions this error has been found to be negligible. The adjustment of the lens for a straight image of the wire therefore constitutes a simple criterion for the best possible focus. It is possible, furthermore, that this effect may itself serve as a method for the quantitative evaluation of the field strength.

4.2. Theoretical Form of Shadow Pattern

With the magnetized wire as object, theoretical expressions and curves are now obtained to describe the functional dependence of a and α on g, i.e., the manner in which the shadow moves along the fluorescent screen, and in which its thickness varies, as the obstruction casting the shadow is moved in toward the optical axis. Certain recognizable peculiarities in the shadow behavior afford a qualitative check between experimental conditions and theoretical assumptions, while additional quantitative predictions are also obtained.

As in Figs. 8 and 10, suppose the rim G of the obstruction to be displaced a distance g from the optical axis, with resulting shadow-rim displacements $a_1=a_1(g)$, $a_2=a_2(g)$, at points corresponding to alternate equatorial planes. Then by (37) and (38),

$$(a_1^2+\mu^2\lambda^2)(a_1-\nu g)=(a_2^2+\mu^2\lambda^2)(\nu g-a_2)$$
$$=2\mu^2(\nu-1)fB=\text{constant},$$

or

$$\left.\begin{aligned}\nu g/a_0&=a_1/a_0-1/[(a_1/a_0)^2+(\mu\lambda/a_0)^2],\\ \nu g/a_0&=a_2/a_0+1/[(a_2/a_0)^2+(\mu\lambda/a_0)^2],\end{aligned}\right\}\quad(40)$$

where

$$a_0=[2\mu^2(\nu-1)fB]^{\frac{1}{3}}=\text{constant}.\quad(41)$$

(a_0 is the common value of a_1 and $-a_2$ when $g=0$ and $\lambda=0$.) Thus g is related to both a_1 and a_2 by cubic equations, which if solved may be expected to make the a_i triple-valued functions of g in some intervals, and single-valued functions elsewhere.

Figure 12, based on (40), is a plot of the distances a_i (in normalized form a_i/a_0) as functions of g (in normalized form $\nu g/a_0$). The solid curves are for an ideal dipole field ($\lambda=0$), while dot-dashed curves are for that of a magnet of half-length λ given by $\mu\lambda/a_0=0.5$, which approximates the experimental conditions of Figs. 5 and 6. This graph predicts theoretically the shape of the shadow of an obstruction edge placed at any given distance g from the optical axis. With this g as abscissa,[11] the ordinates on the appropriate curves of Fig. 12 give the values of the a_i ($i=1, 2$) of Fig. 10. (The distances $a_{i+}=a_i+\alpha_i$ of the other shadow edge are given by corresponding ordinates with $g_+=g+\gamma$ as abscissa.) The curves are discussed further in the next section.

There remains the analysis of shadow *thickness* and magnification. For a *thick* shadow, the thicknesses α_i (Fig. 10) are obtained from Fig. 12 as differences Δa_i between ordinates corresponding to abscissa differences $\Delta g=\gamma$, $|\gamma|$ being the obstruction diameter; and the corresponding shadow magnifications $n_i=\alpha_i/\gamma$, as defined by (4), are proportional to these thicknesses. In fact, the magnification ratio n_i/ν, expressing the shadow magnification in the presence of the field in units of that obtained with zero field, is obtained directly (and in proper units) as the slope of the chord joining the two relevant points on the appropriate curve of Fig. 12. For such a slope is of the form

$$\Delta(a_i/a_0)/\Delta(\nu g/a_0)=\alpha_i/\nu\gamma=n_i/\nu.\quad(42)$$

For a shadow so thin, however, that γ and α are of differential magnitude, the two points implied by (42) are so close together that a good approximation of n_i/ν is given by the instantaneous slope of the curve at the abscissa g or g_+. This slope, as obtained by differentia-

[11] Although the curves appear to be plotted for positive g only, those for negative g (seldom needed—see Eq. (1)) are obtained by changing the signs of *both* coordinates while interchanging the labels "$i=1$" and "$i=2$."

tion of, and combination with, Eqs. (40), takes the form

$$n_1/\nu=\alpha_1/\nu\gamma=1/\{1+2(a_1/a_0)[(a_1/a_0)^2+(\mu\lambda/a_0)^2]^{-2}\},$$
$$n_2/\nu=\alpha_2/\nu\gamma=1/\{1-2(a_2/a_0)[(a_2/a_0)^2+(\mu\lambda/a_0)^2]^{-2}\}. \quad (43)$$

Equations (43) and (40) together are the parametric equations (with a_i/a_0 as parameter) giving n_1 and n_2 (also α_1 and α_2) as functions of g for a thin shadow. Figure 13, based on these equations, is a plot of het shadow magnifications n_i or thicknesses α_i (in normalized form n_i/ν) *versus* g (in normalized form $\nu g/a_0$). It is essentially a plot of the derivatives of the functions of Fig. 12. In Fig. 13, as in Fig. 12, the solid curves correspond to the dipole field ($\lambda=0$), while the dot-dashed curves correspond to the case $\mu\lambda/a_0=0.5$ of Figs. 5 and 6.

Although Fig. 13 pertains to infinitesimally thin shadows, the magnification of a shadow of any thickness is, in general, a mean of the two values obtained from the figure with g and g_+ taken in turn as abscissas, and hence may be determined approximately from the figure.

The curves are discussed further in the next section.

5. COMPARISON OF THEORY AND EXPERIMENT

5.1. Qualitative Comparison

The shadow photographs of Figs. 5–7 show good qualitative agreement with the theoretical curves derived in the preceding section. Each of Figs. 5 and 6, and each roughly horizontal mesh-wire shadow in Fig. 7, corresponds to a particular abscissa g on the graphs of Figs. 12 and 13, or more precisely, to two abscissas g and g_+ for the two edges of the obstruction element involved. The following properties of the experimental patterns are seen to follow the theoretical predictions regarding displacement (Fig. 12) and thickness (Fig. 13) of the shadow:

(a) When (Fig. 5) the obstruction is approximately centered on the optical axis ($g\approx-g_+\approx0$), then the deflections at the two equatorial planes are in opposite directions but approximately equal in magnitude ($a_2\approx-a_1$, etc.), and the corresponding shadow thicknesses are of the order of one-third to one-half of that for distant shadows in the region of negligible field.

(b) As g departs from this central value (Figs. 5, 7), the shadows in the two equatorial planes move in the same direction, and the shadow which recedes from the central image expands while that nearing that image shrinks; i.e., when the shadow bulges out on both sides of the central image it is thicker on the side which shows the greater bulges.

(c) As g reaches a critical value, indicated by the point P or Q in Figs. 12 and 13, two new and very thick shadows (Branches 2 and 3 of the curves) appear in the "$i=2$" equatorial plane, and a_2 becomes triple-valued, so that the fields H_2 then actually produce *three* shadows of the same edge of the obstruction, yielding additional values of a_2 for independent points on the scatter diagram. Of the two new shadows, the one nearer the central image (Branch 2) is inverted ($n_2<0$). The phenomenon is most clearly exhibited in the extreme left-hand portion of Fig. 6. Here the two new shadows appear below the central image, while a very slight but distinct bulging above the central image is the remaining visible portion of the first shadow (Branch 1 of the curves of Fig. 12). In other parts of Figs. 6 and 7, the two new shadows run together, due to the fact that only one edge of the obstruction is beyond the critical position in those planes.

(d) As g increases further, these "$i=2$" shadows shrink rapidly, and all but the outermost (Branch 3 of Figs. 12, 13) disappear behind the wire image, whose half-thickness is of the order of $0.4a_0$ in these experiments (Fig. 7).

(e) Finally, as g becomes large, the entire shadow straightens out as a_1 and a_2 approach the common value νg (indicated by the broken line of unit slope in Fig. 12), while its thickness in all equatorial planes approaches that in the absence of the field (Fig. 7).

This apparent qualitative agreement of theory and experiment may be interpreted as tentative verification of the theoretical assumptions. More positive results are obtained in the next section, in which the quantitative data are analyzed.

5.2. Quantitative Results

Figure 14 shows a plot[12] of 22 experimental points (u, w) calculated from (38) from shadow-edge displacement measurements in different portions of Figs. 5

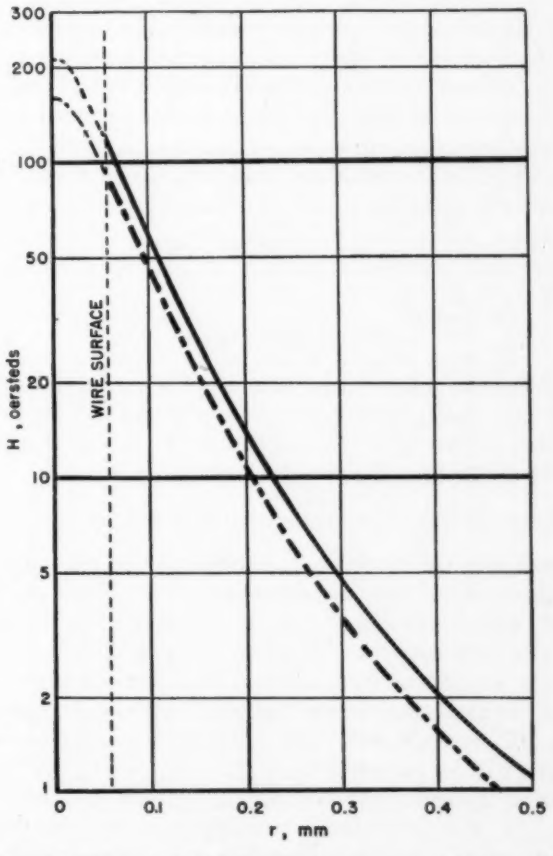

FIG. 16. Theoretical field distribution in equatorial planes of the first (solid curve) and second (dot-dashed curve) magnetized wires, based on data in Figs. 14 and 15. (r=distance from wire axis.) Curves are meaningless for r less than wire radius.

[12] Calculations by Mr. A. A. Nargizian.

TABLE I.

Fig. No.	i	Magnification ratio (n_i/ν) Theoretical	Measured
5 (averaged)	1	0.432	0.400
5 (averaged)	2	0.344	0.370
6	1	0.832	0.841
2 of ref. 3	1	0.814	0.818
3 of ref. 3	1	0.492	0.515
3 of ref. 3	2	0.447	0.435

and 6, and in two similar photographs[12] for which the same object was used. In each case g was determined by equating the values of $(\lambda^2 u+w)$ of (37) at two values of a_i, so that the two points so obtained are not entirely independent of each other, and each is given only half weight in all averaging. The 18 singly encircled points in Fig. 14 form 9 such pairs, while each of the 4 doubly encircled points represents an entirely independent measurement; the 22 points are thus equivalent to 13 independent measurements.

Figure 15 is a similar scatter diagram[12] based on Fig. 7 and two other wire mesh photographs, for all of which a second magnetized wire sample with somewhat different parameters was used. The 47 experimental points in Fig. 15 were obtained from independent measurements, g having been determined for each measurement by linear graphical interpolation between the two sets of straight, evenly spaced shadows at a large distance on either side of the central image.

In Fig. 14 the solid line, fitted to the points by least squares in accordance with (37), has a slope

$$-\lambda^2=-0.00790 \text{ mm}^2, \tag{44}$$

and a w-intercept

$$B=2.14\times10^{-5} \text{ mm}^2. \tag{45}$$

These are therefore the parameter values, for the sample of Figs. 5 and 6, obtained on the hypothesis that the field is that of two point poles separated by a distance 2λ. From (44), this *equivalent pole separation* is

$$2\lambda=0.178 \text{ mm}=1.5 \text{ magnetized wire diameters.} \tag{46}$$

This agrees well with Fig. 2, showing actual elementary magnets about two diameters long, and hence places each equivalent point pole about one-fourth of the way in from extremity to center of the magnet.

The experiments on the two wire samples did not involve the same beam energy V. Before plotting Fig. 15, however, the data on which it is based were converted, by means of a constant factor $(V_2/V_1)^{\frac{1}{2}}$, to their equivalents at the energy V_1 corresponding to Fig. 14. The properties of the two wire samples may therefore be compared through a direct comparison of the fitted lines of Figs. 14 and 15. Thus a comparison of their slopes and w-intercepts indicates that the magnetized regions of the second sample have about the same length (2λ) as those of the first, but are about 25 percent weaker.

From (45) and (39) one obtains a magnetic field (in oersteds)

$$H=0.144/(r^2+0.0079)^{\frac{1}{2}} \quad (r \text{ in mm}). \tag{47}$$

This distribution is plotted in Fig. 16 (solid curve). At 0.1 mm from the wire axis, or about 0.04 mm from the wire surface, it has a value of 60 oersteds.

The results of a similar analysis of the second wire sample, as obtained from Fig. 15, are also plotted in Fig. 16 (dot-dashed curve).

Further verification of the hypothesis is provided by a comparison of the actual shadow thickness with that predicted by (43), as shown in Table I.

6. CONCLUSION

While the experiments described herein pertain to a very special application of the electron optical "Schlieren" and bright-field shadow methods, these methods are capable of wide application to the observation and measurement of electric and magnetic fields not susceptible to investigation by established techniques.[1,3] Other examples, in some of which preliminary experiments have been undertaken or planned, are space charge fields, standing electromagnetic waves, time-varying fields, and ferromagnetic domains.

Essentially, the methods introduce a new category of objects to observation by means of electron optical systems. In the past, electron optics has been used to observe or to form images of two types of "objects":

(1) Objects emitting electrons, whereby the image is used for the study of surface properties and emission phenomena.
(2) Observation by scattered electrons, in which case the image formation shows differences in the scattering properties of different parts of the object and is therefore confined to observations of "transparent" or "translucent" objects.

To these two categories we now add a third category of objects: electromagnetic fields. The methods here described are essentially methods designed to form visible images of field distributions and to interpret them.

7. ACKNOWLEDGMENTS

The authors gratefully acknowledge the assistance of Mr. Irvin L. Cooter, who prepared the wire samples and furnished important information on their properties; Messrs. Daniel L. Reverdin and John A. Simpson, who conducted additional experiments to provide supplementary data; and Mr. Andrew A. Nargizian, who carried out the extensive photographic measurements and numerical calculations leading to the set of final results.

[12] Figures 2 and 3 of reference 3.

The Attenuation of Neutrons of Various Energies in Water

C. E. Falk and E. Creutz
Department of Physics, Carnegie Institute of Technology, Pittsburgh, Pennsylvania
(Received May 17, 1949)

Threshold detectors (In^{115}, Ag^{107}, and C^{12}) were used to determine the relative intensities of neutrons at various distances inside a large water tank. Neutrons with energies up to 30 Mev were produced by (d, n) reactions. At distances in the water >20 cm the "half-thickness" of water was found to be almost independent of neutron energy (about 8 cm).

A KNOWLEDGE of the attenuation of neutrons by passage through matter is useful for the designing of shields for nuclear particle accelerators. For these experiments neutrons ranging from 1.4 ev to greater than 21 Mev were studied with the University of Pittsburgh cyclotron, by bombarding various targets with deuterons of approximately 16 Mev energy. Threshold detectors were used to measure the density of various energy groups throughout a water tank, as indicated in Table I.

One difficulty in medium scale attenuation experiments is brought about by the desirability of establishing conditions which approach those of an attenuation medium of infinite extent. The water in these experiments was in a $2'\times2'\times4'$ brass tank, the square front of which was 60 cm from the neutron source (see Fig. 1). The attenuation was measured along the central axis. Due to the great number of room-scattered neutrons, it was important to shield the sides of the tank. This was accomplished by surrounding the tank by a 2-in. thick mixture of paraffin and B_2O_3. Next to this were placed water cans filled with $Na_2B_4O_7\cdot10H_2O$ solution, and in addition to this cement blocks which had been soaked in paraffin. The tank was placed lengthwise along the forward direction of the neutron beam (see Fig. 1). The indium detectors were foils 1 cm $\times$1 cm $\times$0.005 inches thick. These were wedged between cadmium plates and into slits in a hollow aluminum tube (1 cm diameter) which was held in position along the central line of the parallelopiped of water by means of a light aluminum framework.

The silver and carbon detectors were made in the form of hollow cylinders. Such detectors could be slipped over the Geiger-Mueller tubes used in detecting the various activities. This helped considerably in obtaining fairly high counting rates. The cylinders were 1 inch in outside diameter and 2 inches in length. During bombardment they were surrounded by cadmium cylinders in order to cut down the intensity of reactions induced by thermal neutrons. The cylinders were suspended by thin wires from a thin brass bar placed over the top of the tank.

A thick Be target was used for all experiments, except those involving neutrons of 21 Mev and above. In the latter case $LiBO_2$ was fused onto a copper cup which was then used as a rotating target. Due to the tendency of lithium-containing targets to sputter, it was not

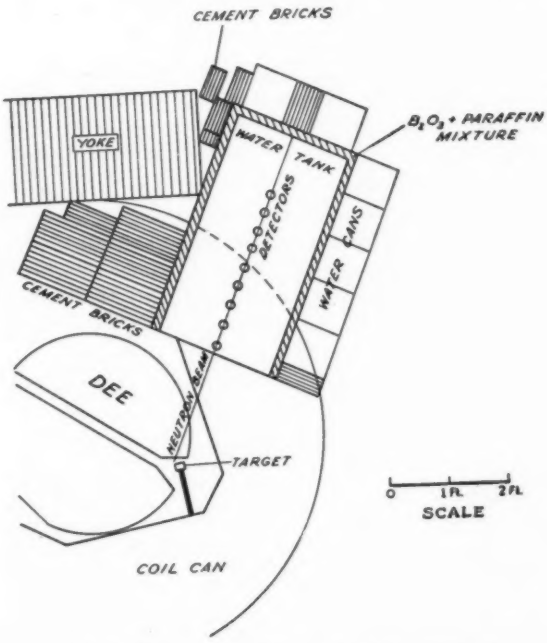

FIG. 1. Plan view of experimental arrangement.

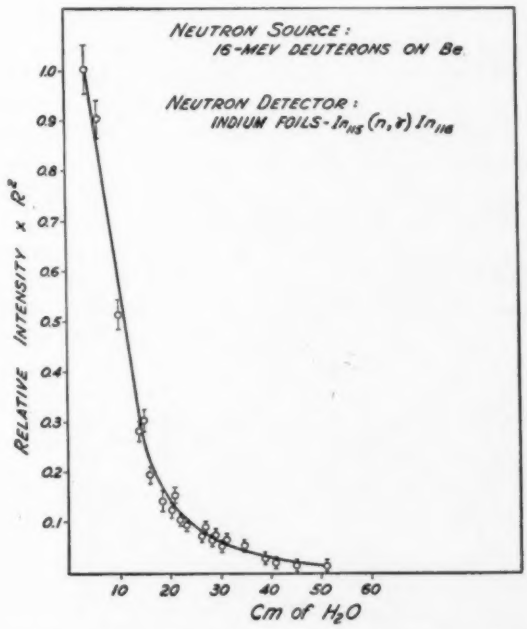

FIG. 2. Spatial distribution of indium resonance (1.4 volt) neutrons in water.

TABLE I.

Detector	Energy	Reaction	Half-life
In	1.4 ev (resonance)	$In^{115}(n, \gamma)In^{116}$	54 min.
Ag	6 Mev (threshold)	$Ag^{107}(n, 2n)Ag^{106}$	24.5 min.
C	20.5 Mev (threshold)	$C^{12}(n, 2n)C^{11}$	20.5 min.

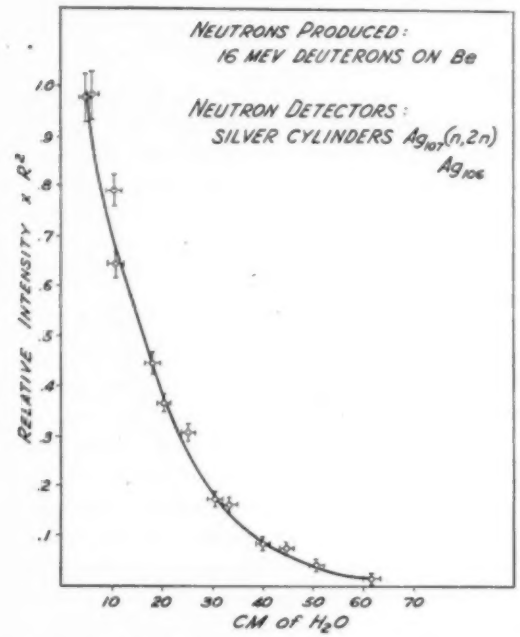

FIG. 3. Spatial distribution of neutrons of energies greater than 6 Mev in water. Spatial experimental uncertainties are due to cylindrical shape of detectors.

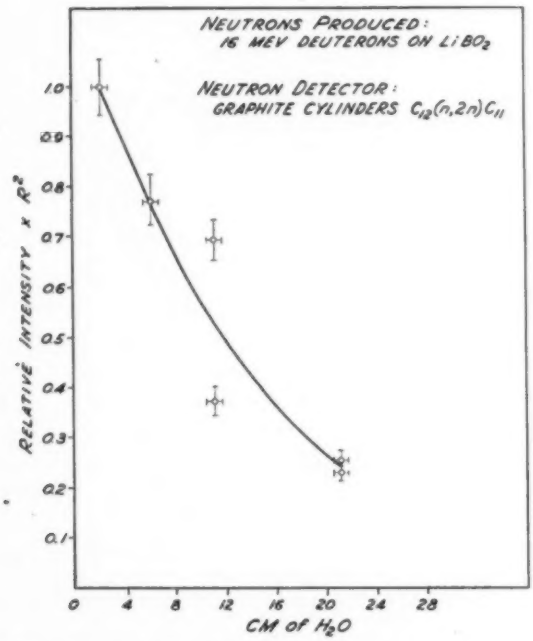

FIG. 4. Spatial distribution of neutrons of energies greater than 20.5 Mev. Spatial experimental uncertainties are due to cylindrical shape of detectors.

possible to use the full strength of the deuteron beam (about 200 microamperes). As a result the high energy neutron flux was comparatively weak, and the attenuation could be measured only over a short distance and with low accuracy.

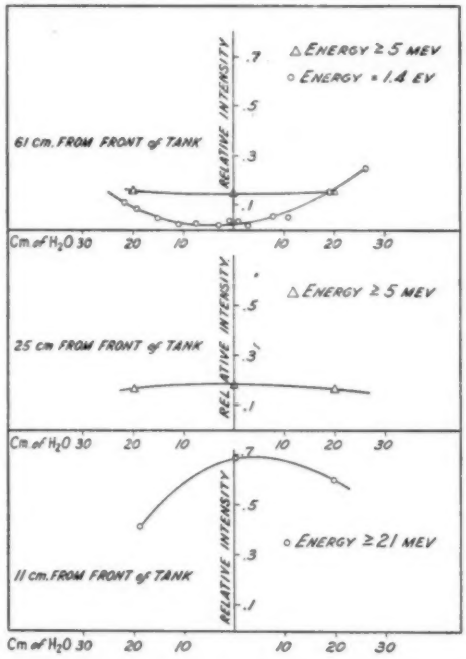
△ ENERGY ≥ 5 MEV
○ ENERGY = 1.4 EV
61 cm. FROM FRONT of TANK
RELATIVE INTENSITY
Cm of H_2O
△ ENERGY ≥ 5 MEV
25 cm FROM FRONT of TANK
○ ENERGY ≥ 21 MEV
11 cm. FROM FRONT of TANK

FIG. 5. Transverse spatial distributions of various energy neutrons at several distances from the front of the tank.

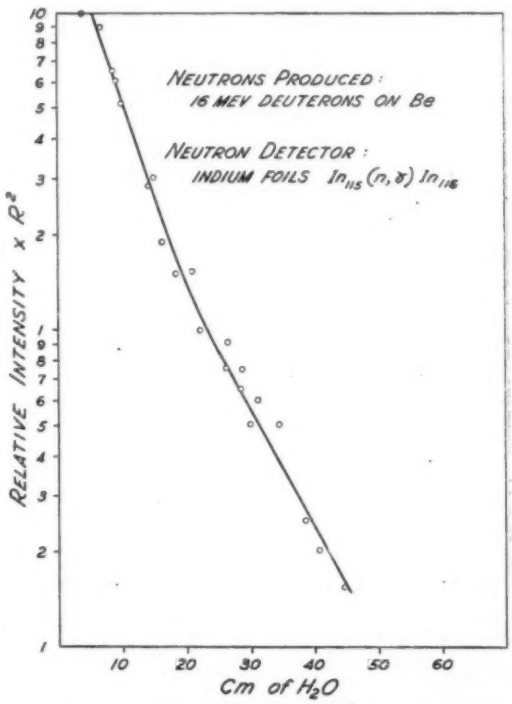

FIG. 6. Semilogarithmic plot of spatial distribution of indium resonance neutrons in water. Change of slope shows that characteristic length λ_0 increases with distance.

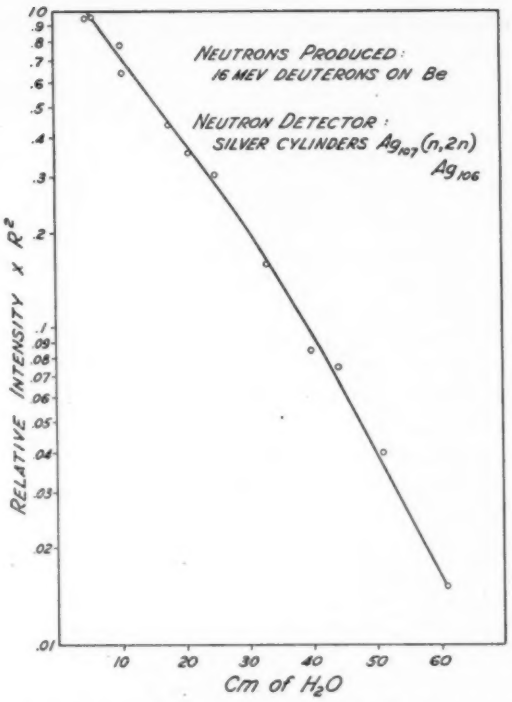

FIG. 7. Semilogarithmic plot of spatial distribution of neutrons of energies greater than 6 Mev. Change of slope shows decrease of characteristic length λ_0 with distance.

Figures 2–4 show the experimental curves obtained. Transverse distribution measurements were also made for each target (Fig. 5). As can be seen, there is no neutron influx from the sides of the tank for energies of 5 Mev or greater. However, the side shielding is much less satisfactory for the very large slow neutron room background, as seen from Fig. 5.

The above data is replotted on a semi-logarithmic scale in Figs. 6, 7, and 8. If the points followed a straight line, the expression $IR^2=C\exp[-x/\lambda_0]$ would be correct and would indicate a characteristic length λ_0. Here I is the intensity, R the distance from the target, and x the distance in water. ($R=x+60$ cm.) It is seen that for neutrons of 5–30 Mev and 21–30 Mev λ_0 becomes slightly smaller with increasing distance in the water, while for 1.4-ev neutrons it increases with distance.

Since the tank is far from the source, there is an essentially plane neutron wave with a continuous energy spectrum incident upon the water, and neutrons are

TABLE II.

Neutron energy group	Thickness of water to reduce neutron intensity to one-half	
	$x<20$ cm	$x>20$ cm
Indium resonance (1.4 ev)	4.5±0.5 cm	8.0±0.5 cm
6 Mev to 30 Mev	10.5±0.5 cm	8.0±1 cm
20.5 Mev to 30 Mev	10 ±1 cm	

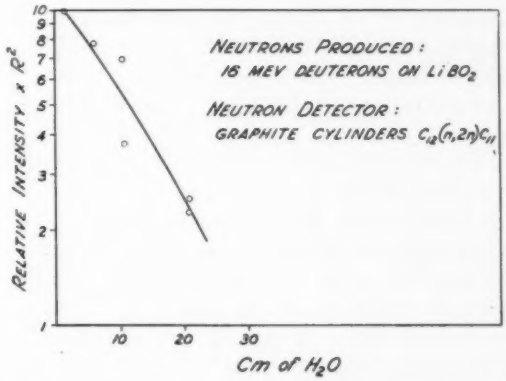

FIG. 8. Semilogarithmic plot of spatial distribution of neutrons of energies greater than 20.5 Mev. Change of slope suggests decrease of characteristic length λ_0 with distance.

continually being slowed down. Upon their first collision in the tank the fast neutrons lose a considerable part of their energy. Slow neutrons then diffuse out from the region of this collision. The slow neutron density should therefore follow about the same spatial pattern as that of the fast. This can be observed in Figs. 6 and 7 beyond 20 cm of H_2O. However, at values of x less than about 20 cm the principle source of low energy neutrons is directly from the target. The half-thickness of water at small distances then is smaller, corresponding to the larger scattering cross section for these lower energy neutrons.

The decrease of penetrating power for the fast neutrons at large distances in the water (Fig. 7) is probably due to the "softening" of the spectrum after most of the neutrons have made several small angle collisions with hydrogen.

The measured "half-thickness" of water for each energy group is shown in Table II.

We wish to thank Professor A. J. Allen of the University of Pittsburgh for his helpful cooperation and for the use of the cyclotron.

Note on the Role of Rifting in Cold-Work and a Possible Measure of Plastic Deformation

DONALD P. SMITH
Frick Chemical Laboratory, Princeton University, Princeton, New Jersey
(Received May 19, 1949)

MANY indications are to be found to the effect that plastic deformation of crystalline metallic bodies is accompanied by opening of lattice structure, and various such evidences of rifting, afforded by the behavior of metals with hydrogen, have recently been discussed at length.[1] The present note is concerned with some probable connections between rifting and deformation.

The first of these has to do with the incipience of plastic deformation.

During the elastic distortion which under ordinary conditions precedes plastic deformation, the successive displacements of atoms, and the resultant interatomic repulsions, must build up to high values in certain regions of the lattice, attaining maxima in places which depend upon the lattice symmetry and upon the manner and direction in which the stress is applied.

So long as the distortion proceeds in such a way that the components of the compressive forces acting upon any atom, and those of the forces opposed to them, differ from one another only infinitesimally, the process is reversible. Under such conditions, work is done solely in overcoming interatomic repulsions or their equivalents, no energy is dissipated, and the distortion continues to be elastic.

If the initial state of the lattice was perfect, and the increase of stress was entirely uniform and gradual, it is conceivable that elastic compression might continue indefinitely. In such ideal compression, if f_n represents the vector sum of the forces acting upon an atom A_n in the direction of displacement, and $\bar{f}_n$ the sum of forces opposing, it would at all times be true that $f_n - \bar{f}_n = 0$; and a very small displacement of A_n would cause only such changes in the forces as consist with this equality.

The "forward" force f_n is however made up in part of repulsions from atoms "behind": ϕ_1, ϕ_2, etc.; and it is probable that each such repulsion increases very rapidly upon near approach of the atoms concerned. Merely to clarify our discussion, we will suppose these repulsions to be representable with fair approximation by some such function as $\phi = a \cdot e^{b/l}$, where l is the distance between atom centers, and a and b are constants, the latter of considerable magnitude. In such case there must come a time in the compressive process when a very slight diminution of l will cause an enormous rise in ϕ—as will be clearly evident if a few curves of the family are plotted. This critical condition must sometimes be reached simultaneously by several of the component ϕ's, and hence in still greater degree by their resultant f_n; and it must even happen that such a state occurs coincidently for several neighboring atoms of the compression front.

Merely upon the basis of probability it would therefore appear that a local condition must now and again arise in which any further minute compression would cause an exceedingly large increase in the forward impulsion exerted on part of a sheet of atoms—which in some instances may lie upon a plane of weakness of the lattice.

Even when all of the conditions just indicated concur, only renewed elastic compression will result, provided that everything proceeds with perfect smoothness and regularity. But such perfection of operation is highly improbable. In the first place there are the inhomogeneities, both chemical and physical, present in any piece of metal, which may make the transmission of stress uneven and the increase of f_n irregular. Any abrupt increment in this force would destroy the balance and cause a sudden irreversible advance of part of an atom-sheet—in other words, rift-formation. The same is perhaps true of inequalities of temperature. Finally, there are the rapid changes of internal condition to which individual atoms are subject; and these may result in fluctuations of the forces which they exert.

It seems, then, that continued severe compression must somewhere cease to be elastic; that this departure from balanced conditions must be highly localized; and that the first consequence must be a lasting alteration of atomic spacing—also localized, and in all probability originating upon one of the low index planes of the lattice. When once such riftings have taken place in considerable numbers, and the lattice strength has been diminished in many places, there comes about a situation in which some low index plane, on which the resolved stress is large, passes through many of the weakened spots. Upon this plane—in general not identical with the plane(s) of rifting—there then occurs a major relative displacement of different parts of the lattice, translational slip.

From the considerations just roughly outlined it seems likely that *the minor deformations which constitute local rifting of a metallic lattice are the first irreversible events to occur* during compression by an outer stress; and that *their occurrence induces the more readily observable and greater disturbance, plastic deformation.* That the latter in turn may produce further riftings, or may enlarge those from which it resulted, is also probable.

The second matter to be considered is the well-established fact of the formation of rifts in metals which are permeable to hydrogen, merely by the intrusion of this element. Here the hydrogen or its ionization product exerts upon the containing metal

[1] D. P. Smith, *Hydrogen In Metals* (University of Chicago Press, Chicago, 1948).

something nearly equivalent to a uniform outward pressure—uniform however only if the volume units considered are not too small. This last is evident since entry of hydrogen increases the volume available to itself, the occlusive capacity, but does *not* enlarge the over-all volume of the metal. In this we have evidence of local displacements of atoms, with production of internal spaces, but without effect on general lattice dimensions—behavior which is confirmed by pronounced broadening of the lines of the x-ray diffraction spectrum, unaccompanied by influence upon the lattice parameters of such metals as iron or nickel. (With palladium and other exothermically absorbing metals, the case is different owing to formation of hydrides or other complexes.)

It is further significant that, although the facts just mentioned, and others as well, indicate an entire absence of penetration of hydrogen into the normal lattice, as distinguished from its locally widened spacings, or rifts, yet at given temperature and hydrogen-pressure the metal has its own solubility for hydrogen. This can apparently be accounted for only if the rifts open in a manner which is peculiar to the particular metal, and at given hydrogen-pressure expand to a fixed degree.

This may be otherwise expressed by saying that *the rift-system of a given metallic lattice is not determined by accidental flaws but is something as fully defined as the lattice itself.* Just as the crystal may be imperfectly developed, so also may its rift-system; yet for each there is a definite perfect or ideal state, which is more or less closely approached according to circumstances. The ideal state of the fully annealed metallic crystal is one in which rifts are wholly absent. The ideal state of the cold-worked metal may equally well be regarded as one in which rifting is complete and the rift-system continuous.

The third connection between rifting and plastic deformation is one upon which present information is deficient, but with regard to which some interesting possibilities suggest themselves.

Merely as the obverse of what has just been said we may state that for a given metal, at temperatures *not below* the recovery range, occlusive capacity for hydrogen constitutes criterion of the extent to which the rift-system has been opened; but the degree of the opening is determined by the intruding hydrogen, or properly by the pressure of this. Here rifting and recovery (rift-healing) are the opposed reactions of a reversible process, and equilibrium is maintained with the expansive force of the intruding element.

At lower temperatures this is not the case, and a solubility equilibrium between hydrogen and metal is unattainable. Of this there is ample empirical evidence in the literature of iron-hydrogen, nickel-hydrogen and other well-studied pairs, although the temperature at which reversibility gives place to irreversibility is in no case clearly definable, and is doubtless much influenced by purity and other factors. The lower or irreversible temperature range is co-extensive with that of "cold-working."

In this region the occlusive capacity of the metal is highly dependent upon the degree and manner of foregoing plastic deformation, but is *not further affected by the intruding hydrogen itself*, as is indicated by the fact just mentioned that no solubility equilibrium can be reached. There is also evidence[2] that the occluded hydrogen can be withdrawn at moderate temperature without altering the worked state of the metal.

The facts and indications mentioned make it likely that their occlusive capacities for hydrogen, at room temperature, may be made to serve as quantitative measures of the degree of plastic deformation of the mechanically important metals—all of these being among the endothermic occluders. Such a measure would be of service in the study of plastic deformation and its mechanical effects, where at present we seem to have only such rough measures as degree of reduction or of elongation.

That the matter is not yet entirely certain and simple is evident, however, from results of several investigators. Thus, while occlusive capacity is usually increased by plastic deformation,[3] the latter has sometimes the opposite effect, at least for certain conditions of working, or for particular metals.[4]

Further study of the relations between the degree *and manner* of deformation, and the resulting occlusive capacity and permeability for hydrogen, are therefore needed before such a measure of cold-work can safely be employed, or its possibilities can be estimated. Yet there is already good ground for the expectation that the results of such studies might have an importance extending much beyond mere questions of the absorption of hydrogen.

---

[2] Moreau, Chaudron, and Portevin, Comptes Rendus **201**, 212 (1935); Portevin, Chaudron, and Moreau, Sci. Repts. Tôhoku Imp. Univ., Honda Anniv. Vol., 933 (1936); Chaudron, Portevin, and Moreau, Comptes Rendus **207**, 235 (1938); E. Schmid and H. D. Graf von Schweinitz, Aluminium **21**, 772 (1939).

[3] Holt, Edgar, and Firth, Zeits. f. physik. Chemie **82**, 513 (1913); G. Tammann and J. Schneider, Zeits. f. anorg. allgem. Chemie **172**, 43 (1928); Alexejew, Afanassjew, and Ostroumow, Zeits. f. Elektrochemie **40**, 92 (1934); K. Moers, Metallwirtschaft **13**, 640 (1934); D. P. Smith and G. Derge, J. Am. Chem. Soc. **56**, 2513 (1934); G. A. Moore and D. P. Smith, Trans. A.I.M.E. **135**, 255 (1939).

[4] G. Tammann and J. Schneider, see reference 3; P. Bardenheuer and H. Ploum, Mitt. K-W. Inst. Eisenforschung **16**, 129 (1934); D. P. Smith and G. Derge, see reference 3; J. E. Burke and C. S. Smith, J. Am. Chem. Soc. **69**, 2500 (1947).

An Investigation of Dielectric Rod as Wave Guide*

C. H. CHANDLER
RCA Laboratories Division, Radio Corporation of America, Princeton, New Jersey
(Received May 25, 1949)

An experimental investigation of dielectric rod as wave guide indicates that the guiding effect is retained even when the rod is only a fraction of a wave-length in diameter. The greater part of the guided energy is then outside the dielectric, so that a very low loss wave guide results. Measurements of performance made at 1.25 cm indicate attenuations down to 0.004 decibel per meter in polystyrene rod, and show good agreement with theoretical predictions. A resonator utilizing the dielectric-rod wave guide is described, in which a maximum Q of approximately 53,000 was observed.

I. INTRODUCTION

THE use of dielectric materials for refracting and guiding very short radio waves is well known;[1-5] but even the best available dielectrics are too lossy to compete with metal wave guides for the latter function, in the case for which the electromagnetic energy is substantially confined within the dielectric material. However, experiments made by H. A. Iams at RCA Laboratories in 1947 indicated that a form of dielectric wave guide having exceptionally low losses might be made by using a thin dielectric rod or "wire." In this case, most of the electromagnetic energy, while guided by the dielectric, would be outside the material and hence not subject to its losses.

A theoretical study of the problem, made by W. M. Elsasser,[6] is shown to be in substantial agreement with the experimental work. Elsasser examined the three lowest modes of propagation: a transverse electric and a transverse magnetic ($n=0$), and a so-called "dipole" ($n=1$) mode. It is the last of these with which the present work is concerned.

II. PROPERTIES OF DIPOLE MODE

These are fully described in the companion article;[6] but for the sake of continuity they may be briefly mentioned here. The dipole mode in dielectric-rod wave guide propagates as a hybrid wave, having longitudinal components of both electric and magnetic fields. It has no cut-off, but exists for arbitrarily thin rods or long wave-lengths. As the rod is made thinner, or as the length of the guided waves is increased, a greater and greater fraction of the energy is found outside the rod. This is the reason for the low losses. There is, however, no radiation of energy if the rod is perfectly straight.

III. EQUIPMENT

A. General

Microwave power at 1.25 cm was supplied by a 2K33 reflex klystron oscillator, which could be operated continuously, on-off keyed at audiofrequencies up to 5 kc, or recurrently swept in frequency by means of a 60-cycle "saw-tooth" voltage applied to the reflecting electrode.

Signals traversing the wave guide system were detected by a 1N26 crystal in a standard holder. The rectified signal envelope was amplified in an audio amplifier having adequate band width for a precise display of the pass characteristics of the wave guide system by a cathode-ray oscilloscope, upon the screen of which the form of the envelope was viewed and measured. Other items of equipment included standard K band components: wave guide, attenuators, directional couplers, and a high Q circular-mode cavity wave meter. For the dielectric wave guide, cylindrical polystyrene rod was used, in a number of commerically available diameters from $\frac{1}{16}$ inch to $\frac{1}{2}$ inch (0.125λ to 1.01λ).

The method of transferring microwave energy from an ordinary metal wave guide into the polystyrene rod was quite straightforward. Since a rectangular metal guide operating in the dominant mode has an electric field whose configuration is roughly similar to the transverse component of the electric field in the dipole mode of the dielectric guide, the transfer could be made simply by inserting the polystyrene rod longitudinally into the metal guide for a short distance. Somewhat better transfer resulted when the rectangular metal guide carrying the $TE_{1,0}$ mode was modified by a transition to circular guide, changing the mode to $TE_{1,1}$, and the dielectric rod, tapering from a point to minimize reflection, was inserted to fill the open end of the circular guide. After emerging from the metal guide, the rod could be further tapered to whatever diameter was required for a given test. This was the method used throughout the present work; a typical transition of this type is shown in Fig. 1(A). Two other typical transition structures, less convenient for experimental work but affording somewhat better coupling from the metal to the dielectric wave guide, are indicated in Fig. 1(B).

* A report on this work was presented at a Joint Meeting of the U.R.S.I. and I.R.E. in Washington, D. C. (May 4, 1948).

[1] Lord Rayleigh, Phil. Mag. **43**, 125 (1897).

[2] G. C. Southworth, "Hyper-frequency wave guides—general considerations and experimental results," Bell Sys. Tech. J. **15**, 284 (1936).

[3] R. D. Richtmeyer, "Dielectric resonators," J. App. Phys. **10**, 391 (1939).

[4] R. B. Watson and C. W. Horton, "Radiation patterns of dielectric rods—experiment and theory," J. App. Phys. **19**, 7 (1948).

[5] R. M. Whitmer, "Fields in non-metallic waveguides," Proc. I.R.E. **36**, 1105 (1948).

[6] W. M. Elsasser, "Attenuation in a dielectric circular rod," J. App. Phys. **20**, 1193 (1949).

B. Dielectric-Rod Resonator

Direct measurements of such low attenuation as is encountered in the smaller diameters of dielectric wave guide would, for even fair accuracy, require extreme and physically unwieldy lengths of guide. Consideration was accordingly given to the use of reflecting terminations as a means of utilizing a convenient length of dielectric rod for more than one traversal by the guided waves. The device eventually developed consisted of a length of dielectric-rod wave guide, used as a transmission line, placed between and extending through two plane parallel reflectors to form a simple resonator. A cross section of the structure is shown in Fig. 2(A). Transmission through the line section took place when the resonator length was an integral number of half-waves. The sharpness of the transmission peaks, that is, the "Q" of the resonator, provided the information necessary for calculating the attenuation of the line.

Since the resonator was many wave-lengths long, a number of resonances occurred at discrete intervals within the available range of signal frequency. For the purposes of the present work, such behavior was satisfactory; but other applications of the device might require means of obtaining a resonance at any arbitrarily chosen frequency. It would be possible to tune the resonator continuously by changing its length; but such a method would pose mechanical design problems of some magnitude. It is possible, however, to change the electrical length of the dielectric wave guide within the resonator, by changing the effective cross section of the guide over a portion of its length. The tuning action results from the dependence of the wave-length in the dielectric wave guide upon the cross section of the guide. A possible structure for the tuning device, employing a movable dielectric tuning element, is shown in Fig. 2(B). The design of Fig. 2(C), while mechanically simpler, has the disadvantage of greatly increased coupling from the resonator to the external system as compared to the method of Fig. 2(B).

The resonator described differs from most microwave resonators in that resonant frequencies are uniformly spaced, showing that the significant mode of propagation involves only waves traveling longitudinally in the resonator. This is true as long as substantially all the microwave energy surrounding the dielectric rod is intercepted by the reflecting plates. Thus, for $\frac{1}{8}$-in. diameter polystyrene rod the six-foot resonator exhibited resonances at regular intervals of approximately 85 megacycles throughout the accessible frequency range. However, in the case of $\frac{1}{16}$-in. diameter rod, the increased spread of energy outside the rod allowed transverse reflections from the edges of the reflecting plates and possibly other uncontrolled reflections from extraneous surfaces, so that irregularities in the frequency characteristic of the resonator were observed.

Defining

$$Q \equiv f/\Delta f,$$

where f is the frequency of resonance and Δf is the total half-power band width, the relation between Q and the losses in the resonator may be found. The complete expression is

$$Q=\frac{2\pi}{\alpha\lambda}\left\{\frac{\alpha L}{\sinh[\alpha L+2\log(1/R)]}\right\},$$

in which L is the length of the resonator in centimeters, α is the power attenuation of the line in nepers per centimeter, R is the reflection coefficient (including coupling loading) at either end of the resonator, and λ is the wave-length in the dielectric guide, in centimeters. For small α, and R near unity, the relation may be approximated by

$$Q=\frac{2\pi}{\lambda[\alpha+2(1-R)/L]}.$$

In the application of the formula, measurements were made for two or more resonator lengths, and R found and used, or eliminated between them.

The resonator and associated equipment are shown in block-diagram form in Fig. 3, while a photograph appears in Fig. 4. The reflectors were plate-glass sheets, three feet square and $\frac{3}{8}$ inch thick, heavily silver-plated on the reflecting surfaces and having $\frac{1}{4}$-inch diameter holes in their centers through which the dielectric-rod wave guide passed. They were aligned as accurately as

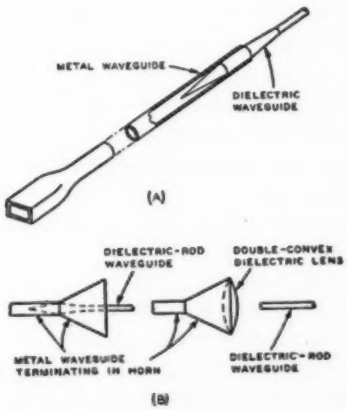

FIG. 1. Transitions from metal to dielectric wave guide.

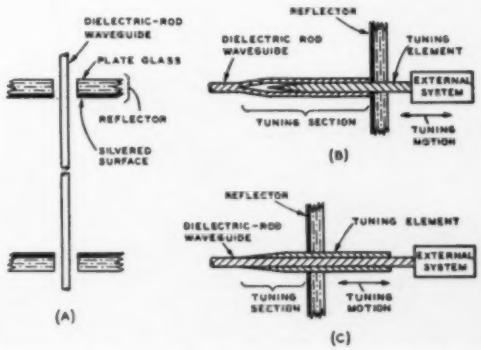

FIG. 2. Dielectric-rod resonator and methods of tuning.

possible to be parallel to each other and perpendicular to the rod. A wooden frame held the reflectors, which were so disposed that the dielectric rod was vertical; in this way any curvature of the rod due to its own weight was avoided.

The maximum length of the resonator was approximately six feet. Lengths of two feet and six inches were obtained by supporting the upper reflector on spacers accurately machined from heavy Bakelite tubing.

The degree of coupling from the external dielectric wave guide system into the resonator is determined, in part, by the diameter of the holes through the reflectors. Although the coupling did not appear to be sensitive to slight lateral movements of the wave guide, tapered plugs of solid or expanded polystyrene were used to center the dielectric rod in the holes. This precaution was taken to insure, insofar as possible, that R remained constant when the resonator length was changed.

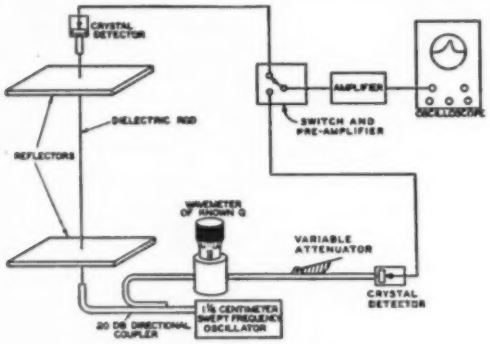

FIG. 3. Apparatus for comparing Q's.

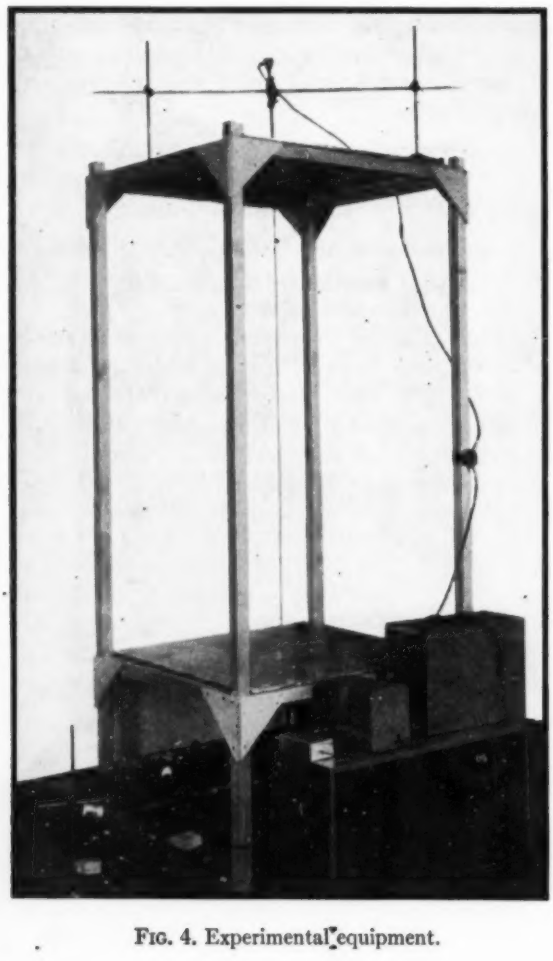

FIG. 4. Experimental equipment.

IV. MEASUREMENTS

A. Procedure

While the wave-length in the dielectric-rod wave guide could be computed from the frequency interval between adjacent transmission peaks in the resonator, a simpler method, applicable to all rod diameters with equal facility, was actually used. In this method a probe, such as the open end of a metal wave guide, was moved along the rod in contact with it, and the signal picked up was mixed with a reference signal of fixed phase. The distances between successive points of signal reinforcement and cancellation were observed and averaged over a number of wave-lengths. Results of these measurements, together with a curve plotted from the theoretical predictions of Elsasser,[6] are shown in Fig. 5. While the lower ($n=0$) modes are not of primary concern in the present work, such measurements as were made on these are included in the figure in order to supplement their treatment in the companion paper.

Early measurements of the attenuation along the rod were made with a probe similar to that mentioned above. Power picked up was detected with a bolometer, amplified, and indicated by a suitable meter. The decline in power with increasing distance from the source was easily measured in this way for thick rods with high attenuation. For lower values of attenuation, however, the errors in such a method far exceeded the quantities to be measured, and the resonator technique was developed.

The experimental system, set up as shown in Fig. 3, was used for measurements in the following manner. With a swept-frequency signal supplied by the klystron oscillator, the amplifier system was first switched to the signal passing through the dielectric-rod resonator, and the coarse frequency control on the klystron adjusted to bring a resonance peak on the oscilloscope screen. Vertical and horizontal position and amplitude controls were used to provide a convenient scale for the resonance curve, and their settings were left unchanged during the remainder of the measurement. The amplifier was then switched to the signal passing through the wave meter, which was tuned to bring its transmission peak to the same portion of the oscilloscope sweep as was previously occupied by that from the resonator. The magnitude of the wave meter resonance curve was adjusted by means of the wave guide attenuator to the same value as the previously set signal from the dielectric-rod resonator.

These adjustments served to bring two resonance curves of equal heights but generally differing band widths to the screen of the oscilloscope. Either could be viewed merely by operating a switch, without changing other settings, and their widths could be compared at any convenient level or levels.

Inasmuch as the measurement of Q was made with reference to a wave meter, the manner of determining the latter's Q may appropriately be described here. A "frequency standard" was obtained by use of the microwave absorption spectrum of ammonia gas at low pressure, in which the (3,3) line occurs at a frequency of 23,870.13 megacycles, flanked by two pairs of satellite lines 1.72 and 2.34 megacycles above and below the center frequency. The absorption lines and the wave meter pass characteristic were displayed on an oscilloscope in such a manner that the frequency markers from the ammonia absorption line provided a scale by which the half-power band width of the wave meter could be measured. In this way the Q of the wave meter was found to be 16,000.

Figure 6 is a composite photograph of oscillographic traces illustrating the comparison between the wave meter resonance curve and that for the dielectric-rod resonator operating with a Q of approximately 40,000.

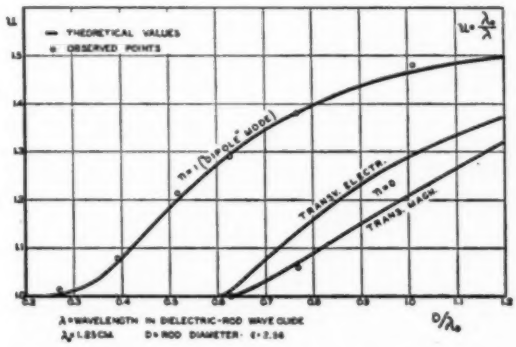

FIG. 5. Wave-length in dielectric-rod wave guide as a function of rod diameter.

B. Results

Average results for a typical set of measurements are given in Table I. Values of attenuation in the dielectric-rod wave guide show good agreement with the theoretical predictions,[6] being asymptotic to a maximum of 3.5 decibels per meter for thick rods, becoming about equal to good metal wave guide (0.4 decibel per meter) when the rod diameter is on the order of three-tenths of the free-space wave-length, and decreasing very rapidly for smaller diameters. The lowest attenuation measured was 0.004 decibel per meter, in the case of $\frac{3}{32}$-inch (0.187λ) polystyrene rod. The highest Q observed in the dielectric-rod resonator was approximately 53,000. The attenuation measurements correspond well to a loss factor of 0.001 in the polystyrene, a value which is

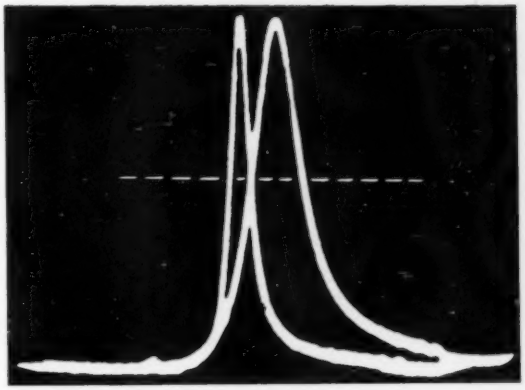

FIG. 6. Resonance curves of wave meter and dielectric-rod resonator.

in good agreement with independently published measurements made at longer wave-lengths.[7,8] Measured values of attenuation are plotted, together with the theoretical curve, in Fig. 7.

The entries in Table I for the two smallest rod diameters provide a good illustration of the behavior of the dipole mode in dielectric-rod wave guide with respect to the spread of energy outside the dielectric material. It will be noted that the lower reflection coefficient is associated with the thicker rod. For these two cases the holes through the resonator reflectors were the same diameter. Since other factors were equal, a greater fraction of the guided energy was concentrated within a given radius from the axis of the thicker rod, so that a greater fraction of the energy was enabled to pass through the aperture when guided by the thicker rod. The reflection coefficient was thus lower in that case because of the greater coupling to the external system.

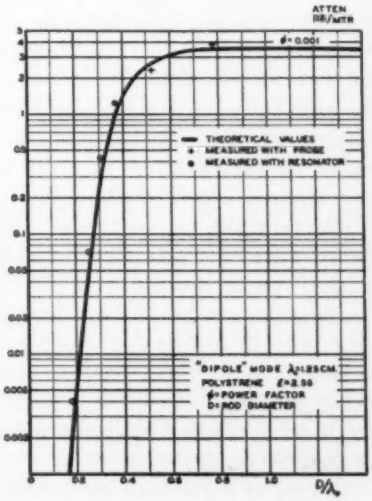

FIG. 7. Attenuation of dielectric-rod wave guide as a function of rod diameter.

[7] Sperry Gyroscope Company, "Microwave transmission design data," Publication No. 23-80, p. 179 (1944).

[8] C. G. Montgomery, *Technique of Microwave Measurements* (McGraw-Hill Book Company, Inc., New York, 1947), p. 666 (Radiation Laboratory Series No. 11).

TABLE I.*

D/λ_0	L(cm)	Q	R	α(db/meter)
0.77		Measured with probe		3.8
0.52		Measured with probe		2.3
0.37	60	2050	substantially 1	1.06
0.31	60	5000	substantially 1	0.44
0.25	180	5000	0.92	0.048
	60	1800		
0.18	180	53,600	approx. 0.993	0.0036
	60	19,000		

* D = rod diameter; L = length of resonator; R = reflection coefficient; α = attenuation of dielectric-rod wave guide; $\lambda_0 = 1.25$ cm.

V. CONCLUSION

Measurements have indicated that dielectric rod of sufficiently small diameter, excited in the appropriate mode, may provide a wave guide having much lower attenuation than the best metal wave guide at K band frequency. In addition, a resonant structure utilizing such wave guide has been shown to be possible and to give values of Q which are very good in view of the frequency used. Generally good adherence to theoretically predicted trends has been found.

Some comment is in order regarding the qualitative behavior of the dielectric-rod wave guide. As the rod diameter is decreased, the stability of transmission is affected by slight bends in the rod and by surrounding objects to an increasing degree, depending on the extent of the electromagnetic fields outside the rod. When the rod is bent, power is lost by radiation along the tangent to the curve. No quantitative description has been attempted; but in the course of working with the dielectric-rod wave guide it was noted that for a given rod the loss increases with increasing curvature, and for a given curvature it increases with decreasing thickness of the rod. Consequently the amount of curvature, or proximity of extraneous objects, which may be tolerated in a transmission line using such rod becomes small for very low loss guide. With due precautions in this regard, however, the dielectric-rod wave guide might be made to offer some advantages over conventional types for suitable applications. Suggested uses, aside from its service as a subject in the present investigation, are as follows: low loss transmission line, especially in a case for which no metallic connection between the ends is desired; an element in a resonator or other frequency-sensitive device; a mode-selector or mode-reinforcer in a microwave device having a number of possible modes.

In view of the sensitivity to curvature just mentioned, the dielectric-rod wave guide would appear to have rather limited convenience as a transmission line. However, means have been found for making bends in the dielectric guide. As shown in Fig. 8(A), a reflector appropriately placed causes the reflected image of one section of the wave guide to appear as a continuation of the other. The plane containing the guide axes is normal to that of the reflector. In Fig. 8(B), the guide is bent and an external reflector is used. The distance D from the reflector to the rod affects the transmission around the bend and may be adjusted to bring such transmission to a maximum.

In connection with the dielectric-rod resonator measurements a matter which should not be overlooked is the fact that, in the case of the smallest rod diameters, a very small attenuation loss is being measured in the presence of a relatively large reflection loss. Under such circumstances the accuracy of the determination of α is adversely affected. It seems worth while therefore to consider how the dielectric-rod resonator might be improved, and its usefulness enhanced, by a more refined mechanical design than was feasible under the conditions of the present investigation. In general, improvements should take the form of insuring flatness and rigidity of the plane reflectors, provision for fine and stable adjustments for the alignment of the reflectors, and provision for continuous control of the coupling into the resonator. While an operable resonator is readily obtained with $\lambda/16$ variation in flatness or parallelism of the reflectors in the region within which appreciable energy is intercepted, there is evidence that the tolerances should be closer for optimum results.

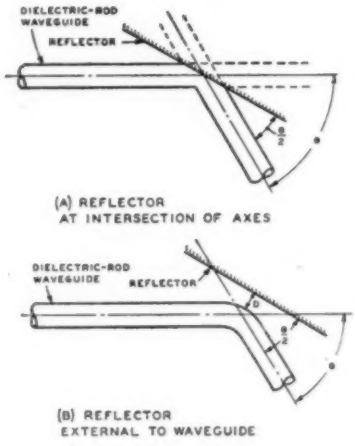

FIG. 8. Bends in dielectric-rod wave guide.

VI. ACKNOWLEDGMENT

Any account of this investigation would be incomplete without specific acknowledgment of the preliminary experiments of Harley Iams, which initiated the present work. Contributions to the method of coupling from metal to dielectric-rod wave guide were made by W. C. Wilkinson. Finally, it is my privilege to express appreciation of the consistent encouragement and many valuable suggestions received from W. D. Hershberger, to whom I am in particular indebted for the derivation of the expression for the Q of the dielectric-rod resonator.

Attenuation in a Dielectric Circular Rod

WALTER M. ELSASSER*
Randal Morgan Laboratory of Physics, University of Pennsylvania, Philadelphia, Pennsylvania
(Received May 25, 1949)

Analysis of the non-radiative modes propagated along a circular dielectric rod is accompanied by a discussion of dielectric loss. The attenuation for the three lowest modes in polystyrene is computed and agrees with the experimental data of Chandler given in the preceding paper.

IT is known that a dielectric circular rod possesses electromagnetic modes that propagate along the rod without radiative attenuation if the rod is perfectly straight. If such a rod is used as a wave guide, losses occur owing to three principal causes: There is in general radiation and reflection at transitions caused by imperfect matching; there is radiative loss if the rod is curved; finally there is dielectric loss in the material of the rod if the latter is not a perfect dielectric. Only the last effect is dealt with in the present note.

The problem was first treated early in this century.[1] With the advent of microwave techniques the problem was reinvestigated[2] and the formal solution of the field equations in terms of cylinder functions is given in Schelkunoff's well-known book.[3] The present paper originated in an attempt to interpret experimental results obtained by H. A. Iams and C. H. Chandler. The agreement between the theory and the experiments is excellent; comparisons may be found in the preceding paper.[4]

Earlier work on the subject was largely concerned with the solutions of rotational symmetry. These are circularly polarized and often less useful than the "dipole" mode in which the dielectric is polarized in a direction perpendicular to the axis of the rod. The experiments of Iams and Chandler showed very soon that it is easy to excite the dipole mode by inserting the rod into a rectangular wave guide. This mode, which is discussed here in some detail, does not possess a finite cut-off frequency, but that feature turns out to be less of a practical advantage than one might think.

ANALYSIS

We shall follow the notation of Schelkunoff with only slight changes. The radius of the rod will be a. With a cylindrical coordinate system ρ, ϕ, z having its z axis in the axis of the rod, the longitudinal components of the field vectors are, inside the rod,

$$\left.\begin{aligned} E_z &= AJ_n(p\rho/a)\cos n\phi e^{-i\beta z+i\omega t} \\ H_z &= BJ_n(p\rho/a)\sin n\phi e^{-i\beta z+i\omega t} \end{aligned}\right\} \quad (1)$$

and outside the rod,

$$\left.\begin{aligned} E_z &= CK_n(q\rho/a)\cos n\phi e^{-i\beta z+i\omega t} \\ H_z &= DK_n(q\rho/a)\sin n\phi e^{-i\beta z+i\omega t} \end{aligned}\right\} \quad (2)$$

where J_n is a Bessel function; K_n is, apart from a constant factor, the Hankel function of the second kind and of imaginary argument. K_n decreases exponentially for large values of ρ. The other field components are obtained from (1) and (2) by differentiations and are given by Schelkunoff. The following relations hold:

$$\left.\begin{aligned} \delta^2+p^2/a^2 &= \omega^2\mu\epsilon_1 \\ \delta^2-q^2/a^2 &= \omega^2\mu\epsilon_2 \end{aligned}\right\} \quad (3)$$

where ϵ_1 and ϵ_2 refer to the inside and outside, respectively. We assume the outside to be air or vacuum and set for the relative dielectric constant

$$\epsilon=\epsilon_1/\epsilon_2.$$

The free-space wave-length is

$$\lambda_0=2\pi/\omega(\mu\epsilon_2)^{\frac{1}{2}},$$

and from (3) we obtain on eliminating δ:

$$\frac{2\pi a}{\lambda_0}=\left(\frac{p^2+q^2}{\epsilon-1}\right)^{\frac{1}{2}}. \quad (4)$$

The relations (3) and (4) are obtained directly from Maxwell's equations; a second relation between the parameters p and q is found by fulfilling the boundary conditions; this yields the secular equation,

$$(\epsilon f+g)(f+g)-n^2(\epsilon/p^2+1/q^2)(1/p^2+1/q^2)=0, \quad (5)$$

where the following abbreviations have been used

$$f=\frac{J_n'(p)}{pJ_n(p)}, \quad g=\frac{K_n'(q)}{qK_n(q)}, \quad (6)$$

the primes denoting differentiation. For given values of ω, n and ϵ the Eqs. (4) and (5) yield a pair of values p, q, defining a mode propagated along the rod. It is furthermore convenient to introduce two more abbreviations,

$$U\equiv\left[\frac{(\epsilon/p^2+1/q^2)}{(1/p^2+1/q^2)}\right]^{\frac{1}{2}}. \quad (7)$$

$$V\equiv[(\epsilon f+g)/(f+g)]^{\frac{1}{2}}. \quad (8)$$

* This work was done at RCA Laboratories, Princeton, New Jersey, in 1947 while the writer was a member of its research staff.

[1] A. Hondros, Ann. d. Physik **30**, 905 (1909); A. Hondros and P. Debye, Ann. d. Physik **32**, 465 (1910).

[2] Carson, Mead, and Schelkunoff, Bell Sys. Tech. J. **15**, 310 (1936).

[3] S. A. Schelkunoff, *Electromagnetic Waves* (D. Van Nostrand Company, Inc., New York, 1943), pp. 425–428.

[4] C. H. Chandler, J. A. Phys. **20**, 1188 (1949).

TABLE I.

		Transverse magnetic mode				Transverse electric mode			
q	$-x(q)$	p	$2a/\lambda_0$*	U	R	p	$2a/\lambda_0$*	U	R
0.1	40.60	2.431	0.620	1.001	0.089	2.415	0.616	1.001	0.202
0.2	13.625	2.481	0.634	1.005	0.125	2.435	0.623	1.005	0.266
0.3	7.422	2.536	0.651	1.011	0.156	2.459	0.631	1.011	0.319
0.4	4.900	2.576	0.669	1.018	0.186	2.488	0.642	1.019	0.364
0.6	2.793	2.713	0.708	1.036	0.245	2.541	0.665	1.040	0.439
0.8	1.9054	2.818	0.746	1.057	0.302	2.577	0.688	1.066	0.496
1.0	1.4296	2.911	0.784	1.079	0.357	2.651	0.722	1.093	0.538
1.2	1.1371	2.992	0.822	1.103	0.408	2.702	0.754	1.121	0.571
1.5	0.8649	3.094	0.876	1.139	0.474	2.774	0.804	1.163	0.605
2.0	0.6140	3.223	0.967	1.197	0.555	2.879	0.894	1.228	0.637
3.0	0.3853	3.387	1.153	1.298	0.632	3.045	1.089	1.330	0.658
4.0	0.2797	3.484	1.352	1.374	0.654	3.165	1.300	1.400	0.660

* At cut-off $2a/\lambda_0=0.613$.

By means of (6)–(8) it is possible to express the entire solution in terms of p and q. First, we have from the continuity of the tangential components (1) and (2) at the boundary

$$C/A=D/B=[J_n(p)]/[K_n(q)],$$

and furthermore we find

$$B/A=D/C=(\epsilon_2/\mu)^{\frac{1}{2}}V\equiv V/\eta$$

where η is the intrinsic impedance of the outer space. The phase constant in the rod is given by

$$\delta/\omega=U/c, \tag{9}$$

whence $U=\lambda_0/\lambda$, the ratio of free-space wave-length to actual wave-length. The calculations that lead to these results are straightforward. The solution of Eq. (5) with the subsidiary Eq. (4) must be carried out by numerical methods. For $n=0$ and $n=1$ the functions J_n and K_n are tabulated in Watson's treatise on Bessel functions, so that the computations offer no particular difficulties. For each fixed value of n the secular equation has an infinite number of solutions, one in each interval between successive zeros of $J_n(p)$. We shall confine ourselves to the lowest of these possible modes, the one that has no radial node inside the rod.

DIELECTRIC LOSS

The loss can be calculated by a perturbation method, assuming that the power lost per wave-length along the rod is small compared to the power flowing along the rod. The mean Poynting vector, S, is clearly parallel to the rod axis, since there is no radiation perpendicular to the rod at large distances. Then from Poynting's theorem,

$$\int S_z d\tau_2-\int S_z d\tau_1=-\sigma\int E^2 dv,$$

where the surfaces of integration at the left-hand side are two planes perpendicular to the rod axis, and the volume at the right-hand side is the section of the rod between these planes, it being assumed that $\sigma=0$ outside the rod. Then in the limit

$$\frac{d\Phi}{dz}\equiv\frac{d}{dz}\int S_z d\tau=-\sigma\int E^2 d\tau.$$

Disregarding signs, we find the attenuation given by

$$\left|\frac{1}{\Phi}\frac{d\Phi}{dz}\right|=\frac{\sigma\int_0^a |E|^2\rho d\rho}{\left|\int_0^a S_z\rho d\rho+\int_a^\infty S_z\rho d\rho\right|}, \tag{10}$$

where

$$S_z=E_\rho H_\phi^*-E_\phi H_\rho^*.$$

We introduce the dimensionless quantity R by

$$|(1/\Phi)(d\Phi/dz)|\equiv\sigma\eta R. \tag{11}$$

We find then in technical units:

$$\text{attenuation}=2729(\epsilon\phi/\lambda_0)R(\text{decibels/meter}),$$

where λ_0 is in cm. Here we have introduced the power factor of the material

$$\phi\equiv\sigma/\epsilon_1\omega.$$

It may be noted that for a plane wave in an infinite homogeneous medium of conductivity σ one has $R=1/(\epsilon)^{\frac{1}{2}}$. For the lowest three modes, which are discussed below, the expressions for R are as follows:

For $n=0$, transverse magnetic wave

$$R=\left|\frac{\dfrac{\epsilon-1}{q^2}\dfrac{f^2+(1/p^2)}{1/p^2+(1/q^2)}+U^2\left(f^2+\dfrac{2f+1}{p^2}\right)}{\epsilon U\left(f^2+\dfrac{2f+1}{p^2}\right)-U\left(g^2+\dfrac{2g-1}{q^2}\right)}\right|.$$

For $n=0$, transverse electric wave

$$R=\left|\frac{f^2+\dfrac{2f+1}{p^2}}{U\left(f^2+\dfrac{2f+1}{p^2}-g^2-\dfrac{2g-1}{q^2}\right)}\right|.$$

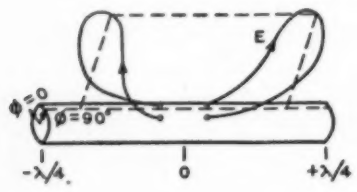

FIG. 1. Typical field line, "dipole" mode.

For $n=1$, the "dipole" mode

$$R=\left|\frac{\frac{\epsilon-1}{q^2}\frac{f^2+(1/p^2)-(1/p^4)}{(1/p^2+1/q^2)}+(U^2+V^2)X+\frac{4UV}{p^4}}{UX(\epsilon+V^2)+UY(1+V^2)+\frac{2V}{p^4}(\epsilon+U^2)-\frac{2V}{q^4}(1+U^2)}\right|,$$

where

$$X=f^2+(2f+1)/p^2-1/p^4,$$
$$Y=-g^2-(2g-1)/q^2+1/q^4.$$

In the limiting case of very small q and not too large p, the last formula goes over into

$$R=q^2[4/p^4+(\epsilon-1)/4p^2-(\epsilon+1)/32].$$

It should be noted that the quantities p, q, f, g, etc., are, of course, different for each of these waves and must in each case be found by numerical solution of the secular equation.

DISCUSSION

As formulas (1) and (2) show, the field of the nth order mode depends on the azimuth as $\cos n\phi$ or $\sin n\phi$. For $n=0$ we have rotationally symmetrical modes, and there are two of them since the secular Eq. (5) separates into two,

$$\epsilon f+g=0, \tag{12}$$

$$f+g=0. \tag{13}$$

The solutions of (12) give the transverse magnetic modes, the magnetic lines of force being circles centered on the rod axis. The electric lines of force lie in the meridional planes through the rod axis; they go to infinity and approach asymptotically planes perpendicular to the rod that are spaced $\lambda/2$ apart where $\lambda=2\pi/\delta$. The solutions of (13) give the circularly polarized transverse electric mode, which is closely analogous to the transverse magnetic mode with the roles of the magnetic and electric field vectors interchanged.

All numerical values depend essentially on the relative dielectric constant ϵ, and computations were carried out for polystyrene, $\epsilon=2.56$. The cut-off for both of these modes occurs at $2a/\lambda_0=0.613$. Table I gives a few values of the attenuation factor R for these modes.

As $2a/\lambda_0$ increases beyond the cut-off value, R goes through a very shallow maximum and asymptotically converges toward the value $1/(\epsilon)^{\frac{1}{2}}=0.625$ which is the attenuation factor for a plane wave in an infinite medium.

TABLE II.

Dipole mode, $n=1$							
q	p	$2a/\lambda_0$	f	$-g$	U	V	R
$2\cdot10^{-5}$	0.559	0.1425	2.947	$2.5\cdot10^{9}$	1	1	$1.7\cdot10^{-8}$
$2\cdot10^{-4}$	0.626	0.1595	2.298	$2.5\cdot10^{7}$	1	1	$1.1\cdot10^{-6}$
$2\cdot10^{-3}$	0.724	0.1845	1.6524	$2.5\cdot10^{5}$	1	1	$6.1\cdot10^{-5}$
0.02	0.880	0.224	1.0328	2504	1	1	0.0028
0.04	0.966	0.246	0.8115	628.3	1.001	0.999	0.0078
0.06	1.028	0.262	0.6846	280.7	1.005	0.998	0.0140
0.10	1.101	0.282	0.5598	102.46	1.007	0.996	0.0313
0.20	1.246	0.322	0.3761	26.83	1.020	0.989	0.0812
0.30	1.342	0.350	0.2841	12.608	1.036	0.982	0.1363
0.40	1.417	0.375	0.2241	7.526	1.056	0.976	0.1963
0.50	1.483	0.399	0.1781	5.116	1.077	0.971	0.248
0.60	1.538	0.421	0.1438	3.772	1.098	0.969	0.301
0.80	1.627	0.462	0.0937	2.383	1.142	0.968	0.394
1.0	1.698	0.502	0.0601	1.6995	1.184	0.971	0.438
1.2	1.755	0.542	0.0305	1.3052	1.223	0.981	0.512
1.5	1.824	0.602	+0.0067	0.9583	1.276	0.995	0.567
2.0	1.909	0.705	−0.0250	0.6572	1.348	1.028	0.610
2.5	1.971	0.811	−0.0463	0.4975	1.400	1.064	0.630
3.0	2.018	0.922	−0.0617	0.3995	1.440	1.099	0.638
3.5	2.058	1.035	−0.0743	0.3334	1.469	1.133	0.641
4.0	2.089	1.150	−0.0838	0.2860	1.492	1.163	0.641
4.8	2.129	1.338	−0.0958	0.2329	1.518	1.206	0.640

The "dipole" wave, $n=1$, may be roughly described as a sinusoidal dielectric polarization perpendicular to the rod and traveling along it. The structure of the field is fairly complicated, and Fig. 1 shows a typical electric line of force, or rather its part outside of the rod. The magnetic field is similar, but rotated 90° about the rod axis. There is no finite cut-off so that the rod can carry waves of arbitrary length in this mode. Table II gives some selected values of the quantities entering into the solution that have been defined previously.

Again for sufficiently large values of $2a/\lambda_0$, the attenuation factor R tends toward the plane-wave value 0.625. For small values of $2a/\lambda_0$ the attenuation becomes small. This is attributable to the fact that the energy of the wave field is practically all outside the rod, and there is no dielectric loss in the outer space. In Fig. 2, R is plotted as a function of $2a/\lambda_0$, summarizing the attenuation data for all three modes.

The radial dependence in outer space is given by $K_1(q\rho/a)$ where K_1 is a solution of the second kind of

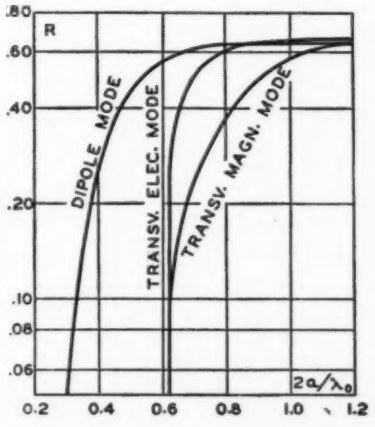

FIG. 2. Attenuation factor *versus* diameter in free-space wave-lengths.

Bessel's differential equation. The dominant factor in the asymptotic development of K_1 is $e^{-qp/a}$. As Table II shows, q becomes small with extreme rapidity as λ_0 increases. This means that the electromagnetic field energy is no longer concentrated in the immediate neighborhood of the rod, but is spread out over the interior of a cylinder whose radius is of the order a/q. One might at once expect that this results in a low stability of such a rod with respect to radiation: a small curvature of the rod will result in appreciable radiative losses; the field no longer follows the rod in its entirety. This presumption is borne out by observations.[4] The phenomenon occurs equally for the circular modes, $n=0$, but then it takes place in the immediate vicinity of the cut-off, $q\to 0$. The difficult task of calculating the radiative losses for a slightly curved rod has not been undertaken, as this would require a much more elaborate analysis.

The Traveling-Wave Tube (Discussion of Waves for Large Amplitudes)*

L. BRILLOUIN†
Cruft Laboratory, Harvard University, Cambridge, Massachusetts
(Received May 25, 1949)

The traveling-wave amplifier is a typical structure where E-M waves and electrons, traveling with approximately the same velocity, exhibit a strong interaction. The problem has usually been discussed for the case of weak waves with approximations corresponding to a small signal theory. It is interesting to state the limitations of this theory and to discuss the behavior of such tubes for strong signals. It seems that the amplified wave obtained in the case of small signals is progressively distorted until a final stage is reached where no further amplification is possible. The type of final distorted wave depends essentially upon all the details of the structure. In many cases where a complete investigation was possible, some strange types of shock waves were obtained, with a complete bunching of the space charge. A similar solution also applies to the linear accelerators or to the synchrotrons.

I. INTRODUCTION

THE problem of traveling-wave tubes will be discussed for a typical structure, where it is possible to write all equations rigorously. Approximations will be omitted in the first sections in order to obtain a set of equations that can be applied to a discussion of waves of large amplitude.

We first use this rigorous theory for a discussion of the properties of waves of small amplitude (Sections I, V, VI) and we obtain the usual theory of traveling-wave amplifiers, together with a statement about the precise limits of validity of this small signal theory. This discussion corresponds to the problem of "class-A" amplification. We will investigate later on the case of large amplitudes, and "class-B" or "-C" problems for traveling-wave tubes.

The point of departure is represented by Eqs. (5), (6), and (13) that are obtained under the following assumptions:

A. Beam with transverse stability, all electronic motions being in the x direction only.

B. Single-stream motion, all electrons at x and t having the same velocity v. This assumption is comparatively trivial in fluid mechanics, but it is not necessarily so in electronics. A number of cases have been discovered where double or multiple streams of electrons may cross at the same point. Assumption B must therefore be considered as a definite limitation to the theory.

II. STATEMENT OF THE PROBLEM. A SIMPLIFIED MODEL

The interaction between a beam of particles and a wave, both traveling with almost the same velocity, can be discussed on a simplified model, like the one represented in Fig. 1. Let us call

$L_0=Ld_0$ the self-induction, per section $\Delta x=d_0$,
$C_0=Cd_0$ the capacity, per section,
I_n the current in L_0, section n,
$q_n'=\rho_n d_0$ the electric charge in the beam, in section n,
v the velocity of the particles in the beam,
Q_n, V_n charge and potential on the capacity n.

We obtain the following equations along the line, where dissipation is supposed to be negligible:

$$\begin{gathered} I_n-I_{n+1}=\partial q_n/\partial t, \\ L_0(\partial I_n/\partial t)=V_{n-1}-V_n \qquad V_n=Q_n/C_0, \\ Q_n=q_n+q_n'=q_n+\rho_n d_0, \end{gathered} \tag{1}$$

where q_n is the charge brought upon the capacity n by the currents along the line. The beam has a charge q_n' in the guiding section G_n, and induces a charge $-q_n'$ on the wall of that section which calls for an additional q_n' on the capacity n. We now take the time derivative of

* The research reported in this document was made possible through support extended Cruft Laboratory, Harvard University, jointly by the Navy Department (ONR), the Signal Corps of the U. S. Army, and the U. S. Air Force, under ONR contract N5ori-76, T. O. 1.

† Now with the International Business Machines Corporation, New York.

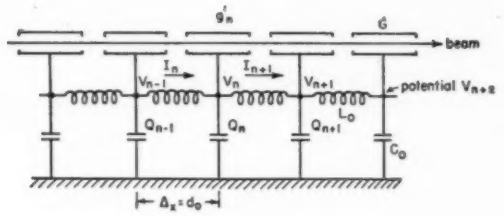

FIG. 1.

Eqs. (1) and combine them:

$$\partial/\partial t(I_n - I_{n+1}) = (1/L_0)(V_{n-1} + V_{n+1} - 2V_n) = \partial^2 q_n/\partial t^2 = \partial^2/\partial t^2(C_0 V_n - \rho_n d_0); \quad (2)$$

hence

$$\frac{V_{n-1} + V_{n+1} - 2V_n}{d_0^2} - LC\frac{\partial^2 V_n}{\partial t^2} = -L\frac{\partial^2 \rho_n}{\partial t^2}. \quad (3)$$

If the sections are very short compared with the wavelength, we may go to the limit $d_0 \to 0$ and replace the first term by $\partial^2 V_n/\partial x^2$.

For the beam itself, we must write the equation of conservation of electricity

$$\partial/\partial x(\rho v) = -\partial\rho/\partial t, \quad (4)$$

which can also be expressed as

$$(d/dt)\rho = -\rho(\partial v/\partial x) \quad d/dt = \partial/\partial t + v(\partial/\partial x); \quad (5)$$

and the equation of motion

$$(d/dt)v = -e/m(\partial V/\partial x) \quad (6)$$

where d/dt is a derivative taken along the trajectory, following the motion of a charged particle of the beam.

III. ENERGY DENSITY, ENERGY FLUX, AND GENERAL EQUATION FOR WAVE PROPAGATION

The total energy of the system, per unit length of the structure, is

$$\mathcal{E} = \tfrac{1}{2}LI^2 + 1/2C(q/d_0 + \rho)^2 + (m/2e)\rho v^2, \quad (7)$$

where the last term represents the kinetic energy density $\mathcal{E}_{kin}$ of the beam, m/e being the ratio of mass to electric charge for the particles. We now want to define the flux Φ corresponding to a flow of energy along the structure by the relation

$$\partial\Phi/\partial x = -\partial\mathcal{E}/\partial t, \quad (8)$$

which expresses the principle of energy conservation. Differentiating Eq. (7) we obtain

$$\frac{\partial\mathcal{E}}{\partial t} = LI\frac{\partial I}{\partial t} + \frac{1}{C}\left(\frac{q}{d_0} + \rho\right)\left(\frac{1}{d_0}\frac{\partial q}{\partial t} + \frac{\partial\rho}{\partial t}\right) + \frac{m}{e}\rho v\frac{\partial v}{\partial t} + \frac{m}{2e}v^2\frac{\partial\rho}{\partial t}. \quad (9)$$

Using Eqs. (2), (3), (4), (5), we write

$$\frac{\partial\mathcal{E}}{\partial t} = -I\frac{\partial V}{\partial x} + V\left(-\frac{\partial I}{\partial x} - \frac{\partial(\rho v)}{\partial x}\right) + \frac{m}{e}\rho v\frac{\partial v}{\partial t} + \frac{m}{e}v^2\left(\frac{1}{2}\frac{\partial\rho}{\partial t} - \rho\frac{\partial v}{\partial x}\right). \quad (10)$$

We may now use Eq. (6) to transform the third term, and group the terms together

$$\frac{\partial\mathcal{E}}{\partial t} = -\frac{\partial}{\partial x}[V(I + \rho v)] - \frac{m}{e}v^2\left[\frac{1}{2}\frac{\partial}{\partial x}(\rho v) + \rho\frac{\partial v}{\partial x}\right]. \quad (11)$$

Comparing Eqs. (8) and (11), we obtain the energy flux

$$\Phi = V(I + \rho v) + (m/2e)\rho v^3. \quad (12)$$

The meaning of this expression is obvious; the flow of energy contains as a first contribution the increase in potential energy, when a total current $I + \rho v$ (I along the line and ρv in the beam) enters a cell at potential V. The last term represents the flow of kinetic energy in the beam: the kinetic energy density is $\mathcal{E}_{kin} = (m/2e)\rho v^2$, and the rate of flow is $\mathcal{E}_{kin} v$, since v is the velocity of the flow.

The fundamental equations for wave propagation along the system are Eqs. (2) to (7). From Eq. (3) we

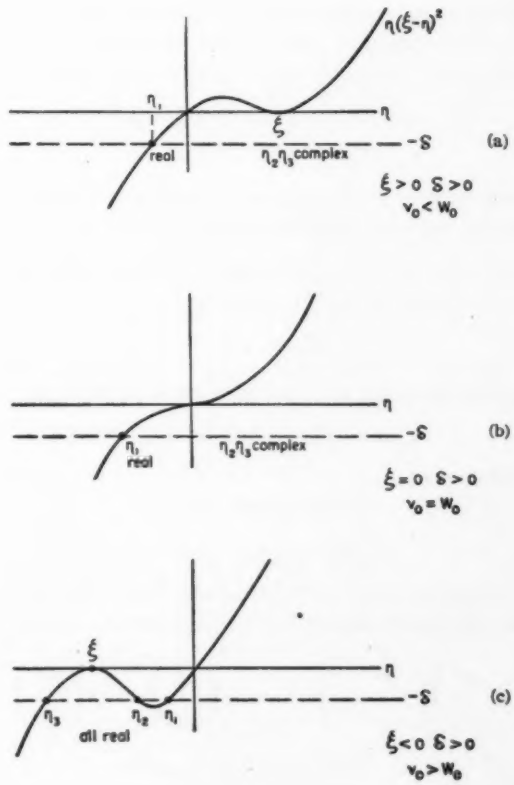

FIG. 2.

obtain

$$\frac{\partial^2 V}{\partial x^2} - LC\frac{\partial^2 V}{\partial t^2} = -L\frac{\partial^2 \rho}{\partial t^2}. \tag{13}$$

This is an equation for propagation along the *LC* line, with a right-hand term in $-\partial^2\rho/\partial t^2$ that represents the reaction of the beam on the line. The reverse action, of the line on the beam, is represented by the equation of motion (6). Up to now, no approximations have been introduced, and our set of equations should represent rigorously the behavior of the simplified linear model represented in Fig. 1, with infinitely short sections.

Many authors dealing with problems of this type have failed to write the complete set of fundamental equations. They have obtained an expression somewhat similar to Eq. (13) but with a different right-hand term, proportional to (ρv) or to ρ, with an arbitrary "coefficient of coupling." This means that energy conservation could not be satisfied with such a system of equations, since the test of this section would fail. We may now keep V, ρ, and v as variables and use Eqs. (5), (6), (13) as our basis for future discussion.

The *characteristic* feature of this system is the combination of *two equations*, (5) and (6), containing d/dt with a *wave equation* (13). The system is *non-linear* because of the terms in $v(\partial v/\partial x)$ occurring in dv/dt, and also because of $\rho(\partial v/\partial x)$ in Eq. (5).

IV. SMALL-SIGNAL THEORY (CLASS A)

The small signal theory rests upon the assumption of a strong beam coupled with a weak wave, so that the perturbation of the beam should remain small:

$$\left.\begin{aligned} \rho &= \rho_0 + \rho_1 e^{j\omega t-\gamma x} \quad \rho_1 \ll \rho_0 \\ v &= v_0 + v_1 e^{j\omega t-\gamma x} \quad v_1 \ll v_0 \end{aligned}\right\}, \tag{14}$$

where γ is the complex propagation constant for the periodic motions. Equation (13) reduces to

$$\left.\begin{aligned} \partial^2 V_1/\partial x^2 - LC(\partial^2 V_1/\partial t^2) &= L\omega^2\rho_1 \quad V = V_1 e^{j\omega t-\gamma x} \\ [\gamma^2 + \omega^2/W_0^2]V_1 &= L\omega^2\rho_1 \end{aligned}\right\} \tag{15}$$

$$1/W_0^2 = LC. \tag{16}$$

Furthermore, we may write in Eqs. (5) and (6)

$$d/dt \approx \partial/\partial t + v_0(\partial/\partial x) = j\omega - v_0\gamma; \tag{17}$$

hence

$$(j\omega - v_0\gamma)\rho_1 = \rho_0\gamma v_1 \tag{18}$$

$$(j\omega - v_0\gamma)v_1 = (e/m)\gamma V_1. \tag{19}$$

Eliminating ρ_1, v_1 and V_1 from the three Eqs. (15), (18), (19), we finally obtain the fundamental condition

$$\left[\gamma^2 + \frac{\omega^2}{W_0^2}\right]\left(j\frac{\omega}{v_0} - \gamma\right)^2 = \frac{e}{m}L\rho_0\left(\frac{\omega\gamma}{v_0}\right)^2 = 2\delta\left(\frac{\omega\gamma}{v_0}\right)^2 \tag{20}$$

$$\text{with } \delta = (e/2m)L\rho_0 \ll 1.$$

The first bracket represents the role played by the line, while the $[j(\omega/v_0)-\gamma]^2$ corresponds to the two d/dt Eqs. (5) and (6) and the right-hand term indicates the coupling between beam and line.

We are interested in the case when v_0 and W_0 are almost equal, beam and line having nearly the same velocity. Let us take

$$1/v_0 = (1/W_0)(1+\xi) \quad \gamma = j(\omega/W_0)(1+\eta). \tag{21}$$

Equation (20) now takes the following shape

$$\eta(2+\eta)(\xi-\eta)^2 = -(e/m)L\rho_0(1+\xi)^2(1+\eta)^2. \tag{22}$$

Assuming v_0 and W_0 to be nearly equal, ξ is small and we have the solutions:

$$\text{either} \quad \eta \text{ small} \qquad \eta(\xi-\eta)^2 \approx -\delta \tag{23}$$

$$\text{or} \quad \eta_4 = -2+\zeta \quad \zeta \approx \delta/4 \text{ small}. \tag{24}$$

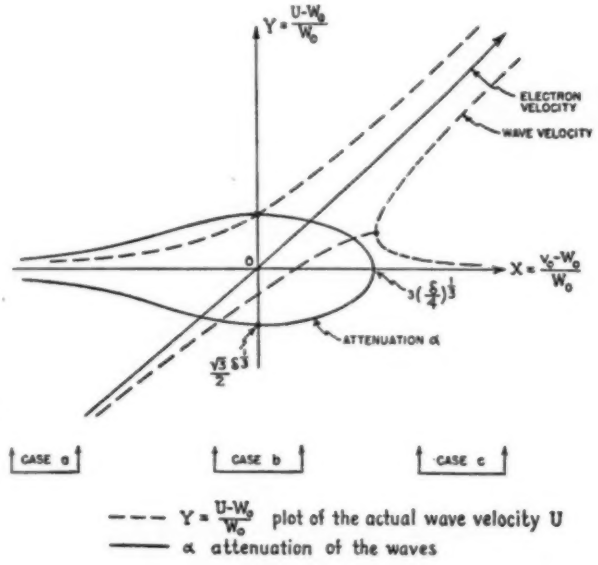

FIG. 3.

The quantity δ is a pure number that usually remains very small. Condition (23) gives three solutions η_1, η_2 and η_3, all of which correspond to waves propagating forward, with or without attenuation. The solution η_4 corresponds to a wave propagating backward, since it yields

$$\gamma_4 = -j(\omega/W_0)[1-(\delta/4)]. \tag{25}$$

In our present problem, the quantity δ is positive since e and ρ_0 both have the same sign, but there are other problems where δ can obtain plus or minus signs, or even be a complex quantity.

The discussion for $\delta > 0$ and η small can be made graphically as shown on Fig. 2. We can also proceed with an analytical discussion:

Assuming $|\xi| \gg |\delta|^{\frac{1}{3}}$ we have

$$\left.\begin{matrix} \eta_1 \\ \eta_2 \\ \eta_3 \end{matrix}\right\} \approx -\frac{\delta}{\xi^2} = \xi \pm \left(-\frac{\delta}{\xi}\right)^{\frac{1}{2}}. \tag{26a, c}$$

This covers cases (a) and (c) of Fig. 2 according to the sign of $-\delta/\xi$ that may give a real or imaginary square root.

Assuming $|\xi| \ll |\delta|^{\frac{1}{3}}$ we obtain

$$\eta_1, \eta_2, \eta_3 = \delta^{\frac{1}{3}}, \delta^{\frac{1}{3}} e^{j(2\pi/3)}, \delta^{\frac{1}{3}} e^{j(4\pi/3)}. \tag{26b}$$

The results are summarized on Fig. 3, where we use as abscissae the relative velocity $v_0 - W_0$ of the electrons with respect to the unperturbed wave, measured in W_0 units

$$X = (v_0 - W_0)/W_0 = -\xi v_0/W_0 \approx -\xi.$$

The ordinates correspond to the actual velocity U of the three progressive waves and their respective attenuation coefficients α:

$$\eta = \eta_r + j\eta_i \quad \gamma = j(\omega/W_0)(1+\eta) = \alpha + j(\omega/U)$$

$$\alpha = -\frac{\omega}{W_0}\eta_i \quad \frac{1}{U} = \frac{1+\eta_r}{W_0} \quad Y = \frac{U - W_0}{W_0} \approx -\eta_r.$$

This section corresponds to the original discussion of J. R. Pierce (see bibliography at end of paper).

V. INITIAL CONDITIONS

At the input we assume the wave intensity V_1 to be given,* and we have an unmodulated beam; hence

$$x = 0 \quad \rho_1 = 0 \quad v_1 = 0 \quad V_1 \text{ given.} \tag{27}$$

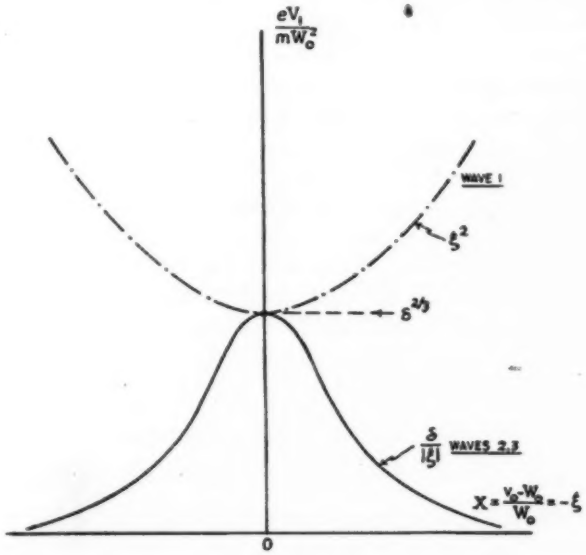

FIG. 4.

We may satisfy these three initial conditions by using a superposition of three forward waves, $\gamma_1\gamma_2\gamma_3$, with amplitudes $A_1A_2A_3$, and we do not need any backward wave A_4. Such a wave would be needed to satisfy boundary conditions at the other end of the tube, but there will be no reflected A_4 wave for a tube of infinite length. Conditions (27) now read, according to (18) and (19):

$$\left.\begin{aligned} A_1 + A_2 + A_3 &= V_1 \\ (m/e)v_1 &= \frac{\gamma_1}{j\omega - v_0\gamma_1}A_1 + \frac{\gamma_2}{j\omega - v_0\gamma_2}A_2 \\ &\quad + \frac{\gamma_3}{j\omega - v_0\gamma_3}A_3 = 0 \\ \frac{m}{e\rho_0}\rho_1 &= \left(\frac{\gamma_1}{j\omega - v_0\gamma_1}\right)^2 A_1 + \left(\frac{\gamma_2}{j\omega - v_0\gamma_2}\right)^2 A_2 \\ &\quad + \left(\frac{\gamma_3}{j\omega - v_0\gamma_3}\right)^2 A_3 = 0 \end{aligned}\right\}, \tag{28}$$

where, assuming ξ and η to remain small,

$$\frac{\gamma_k}{j\omega - v_0\gamma_k} \approx \frac{1}{W_0(\xi - \eta_k)} \quad k = 1, 2, 3, \tag{29}$$

according to (21) and (23). Our conditions (28) now read

$$\sum_k A_k = V_1 \qquad \sum_k \frac{A_k}{\xi - \eta_k} = 0 \qquad \sum_k \frac{A_k}{(\xi - \eta_k)^2} = 0. \tag{30}$$

We may now consider the two alternatives discussed under (26a, c) and (26b). In the first case (26a, c) we have

$$\xi - \eta_1 = \xi + \delta/\xi^2 \approx \xi \quad \xi - \eta_2 = -R \quad \xi - \eta_3 = +R$$
$$R = (-\delta/\xi)^{\frac{1}{2}} \quad |R| \ll |\xi|$$

and the solution of Eqs. (30) reads

$$A_1 \approx V_1 \quad A_2 \approx A_3 \approx -(R^2/2\xi^2)V_1 = (\delta/2\xi^3)V_1. \tag{31}$$

The first unattenuated wave A_1 is predominant and the additional A_2A_3 waves remain small. In the second case (26b) the situation is different.

$$\xi - \eta_1 \approx \delta^{\frac{1}{3}} \quad \xi - \eta_2 \approx \delta^{\frac{1}{3}} e^{i(2\pi/3)} \quad \xi - \eta_3 \approx \delta^{\frac{1}{3}} e^{-i(2\pi/3)}$$
$$A_1 \approx A_2 \approx A_3 = \tfrac{1}{3}V_1; \tag{32}$$

and the three waves play similar roles.

It is interesting to note that each type of wave corresponds to a different bunching of the electronic space charge. From (26) (29) we obtain ($k = 1, 2, 3$)

$$(m/e\rho_0)\rho_{1k} = \frac{A_k}{W_0^2(\xi - \eta_k)^2}, \tag{33}$$

which shows the different behavior of the three progressive waves $k = 1, 2, 3$.

* We assume the characteristic impedances of the feeding line and of our structure to be properly matched, in order to prevent reflections at the input junction. If this were not the case, reflection would occur at this junction and could be computed in the usual way, V_1 still representing the input voltage at the entrance of our structure.

VI. LIMITS OF VALIDITY OF THE SMALL SIGNAL THEORY

The small signal theory developed in the preceding sections is based on the assumptions (14)

$$|\rho_1| \ll |\rho_0| \quad |v_1| \ll v_0, \tag{34}$$

corresponding to a small perturbation of the beam. These conditions must be discussed in order to figure out the actual limitations involved. Equations (18), (19) provide the answer. For each of the three waves we must have

$$\left|\frac{v_1}{v_0}\right| = \frac{e}{mv_0}\frac{V_1}{|(j\omega/\gamma)-v_0|} \ll 1. \tag{35}$$

$$\left|\frac{\rho_1}{\rho_0}\right| = \left|\frac{v_1}{[(j\omega/\gamma)-v_0]}\right| = (e/m)V_1\left|\frac{1}{[(j\omega/\gamma)-v_0]^2}\right| \ll 1. \tag{36}$$

Our propagation constant γ for each wave is

$$\gamma = \alpha + j\beta = \alpha + j(\omega/U), \tag{37}$$

where U is the velocity of the resulting wave and α the (positive or negative) attenuation coefficient. In all practical cases, $|\alpha|$ is small compared to ω/U.

$$(j\omega/\gamma - v_0) \approx U - v_0 + j\alpha(U^2/\omega)\cdots \approx \Delta U \tag{38}$$

with

$$\Delta U = U - v_0,$$

and condition (36) results in

$$(e/m)[V_1/(\Delta U)^2] \ll 1 \qquad eV_1 \ll m(\Delta U)^2. \tag{39}$$

This condition has a simple physical meaning, since $-\Delta U$ is the velocity of the electrons with respect to the actual *resulting* wave, and $\frac{1}{2}m(\Delta U)^2$ represents the kinetic energy of the electrons in a frame of reference moving with the velocity U of the wave under consideration. The potential energy eV_1 of the electrons in the wave must remain very small compared with their kinetic energy $\frac{1}{2}m(\Delta U)^2$ in the moving frame of reference.

When this condition (39) is satisfied, the other condition (35) reads

$$\left|\frac{v_1}{v_0}\right| = \frac{eV_1}{mv_0|\Delta U|} \ll 1 \tag{40}$$

and is automatically fulfilled in all practical cases since v_0 is always much larger than $|\Delta U|$. This discussion proves that the only real limitation to the small signal theory is represented by condition (36).

Let us examine this condition more carefully in connection with the discussion given in Section IV. Assumptions (21) yield

$$\left|\frac{\rho_1}{\rho_0}\right| = \frac{eV_1}{mW_0^2}\frac{(1+\xi)^2(1+\eta)^2}{|\xi-\eta|^2} \approx \frac{eV_1}{mW_0^2}\frac{1}{|\xi-\eta|^2} \ll 1. \tag{41}$$

We computed the η-values for some typical cases. First, we assumed in Eq. (26a, c) a large drift of the electrons through the wave and obtained three waves $\eta_1\eta_2\eta_3$ propagating forward

$$|\xi| = \left|\frac{W_0}{v_0} - 1\right| \gg |\delta|^{\frac{1}{3}}, \tag{42}$$

where $\delta = (e/2m)L\rho_0$.

$$\eta_1 = -\frac{\delta}{\xi^2} \quad \text{very small} \quad |\xi-\eta|^2 \approx \xi^2$$
$$\left.\begin{matrix}\eta_2\\ \eta_3\end{matrix}\right\} = \xi \pm \left(-\frac{\delta}{\xi}\right)^{\frac{1}{2}} \quad |\xi-\eta|^2 = \left|\frac{\delta}{\xi}\right|. \tag{43}$$

In this case the η_2, η_3 waves propagate very nearly with the same velocity v_0 as the particles, and condition (41) is a very stringent limitation to the small signal theory

$$(eV_1/mW_0^2) \ll |\delta/\xi|. \tag{44}$$

Another example was discussed in Section IV, Eq. (26b), and corresponded to

$$|\xi| \ll |\delta|^{\frac{1}{3}}, \tag{45}$$

when all three waves have η-values of the same order of magnitude $\delta^{\frac{1}{3}}$

$$|\xi-\eta|^2 = \delta^{\frac{1}{3}}; \tag{46}$$

hence a limitation to the theory represented by

$$(eV_1/mW_0^2) \ll \delta^{\frac{1}{3}}. \tag{47}$$

These results are summarized in Fig. 4.

The lower curve corresponds to the stringent limitation (41) which occurs when wave number 2 or 3 is excited, because these waves propagate with a velocity very nearly equal to the electron velocity. When only the first wave is excited, the first equation of (43) is applied and the upper curve of Fig. 4 is obtained. This corresponds to a wave interacting very weakly with the electron beam, because its velocity is nearly the unperturbed wave velocity W_0 and differs more and more from the beam velocity when X is increased.

VII. LARGE SIGNAL THEORY

(DISCUSSION OF SOME INVARIANT EXPRESSIONS)

The discussion of the preceding sections shows the exact limitations of the small signal theory. We have obtained, under certain conditions, an amplified wave, whose amplitude increases exponentially. Sooner or later this wave will reach such an amplitude that the preceding theory can no more be used. Non-linear terms in the general equations will begin playing an important role, and we must expect a strong distortion of the wave, together with a limit to its possible increase in amplitude. The discussion of this intermediate stage seems difficult, but we may look for a final stage in which a stable wave is obtained, exhibiting a definite

shape and unable to increase any more. This situation could, to some extent, be compared to that obtained in a Van der Pol oscillator. Such an oscillator starts with almost sinusoidal oscillations of increasing amplitude, and eventually settles upon a large stable oscillation that is no more sinusoida[1], but exhibits a well-defined and stable shape. This is, however, not the only possibility, and it has been pointed out by A. Nordsieck (unpublished report of the Bell Telephone Laboratories) that the oscillations may not reach a stable shape. It can exhibit amplitude oscillations about a certain average value, and the final stage may be a system of beats, the final wave having distorted oscillations with periodic variations of the amplitude. The introduction of some damping terms in the equation would modify the general picture, and might lead to a final stable wave.

It is interesting to note that some expressions remain invariant during the progressive transformation of the amplified wave. We assume a steady operation, during which we maintain a constant excitation on the tube. This may be the case, for instance, if the initial conditions stated in Section V are maintained for a long time, and if we observe the behavior of the system after all transients have died out.

We shall be able to write some relations of the general type

$$\partial\psi/\partial t=\partial\Phi/\partial x, \tag{48a}$$

which indicate conservation of certain properties throughout the structure. Under steady operation the time average of $\partial\psi/\partial t$, at any given point x, is obviously zero, since the process repeats itself and is continuously sustained. Hence the conclusion

$$\langle\partial\Phi\rangle_{Av}/\partial x=0 \qquad \bar{\Phi}=\text{constant}, \tag{48b}$$

where the angular brackets or the upper bar indicate a *time average.*

A first example of an equation of type (48a) is found in Eq. (4) that represents conservation of electricity. The corresponding invariant (48b) is

$$\langle\rho v\rangle_{Av}=J \text{ constant} \tag{49}$$

and corresponds to the invariance of the average electronic current J along the beam.

Next we turn to Eq. (6) and rewrite it as

$$\partial v/\partial t=-\partial/\partial x(\tfrac{1}{2}v^2+(e/m)V), \tag{50}$$

which leads to the conclusion that

$$\tfrac{1}{2}m\langle v^2\rangle+e\bar{V}=\tfrac{1}{2}mv_0^2 = \text{initial kinetic energy per electron} \tag{51}$$

is another invariant along the beam.

Finally we have Eqs. (8) and (12) expressing energy conservation

$$\bar{\Phi}=\langle V(I+\rho v)\rangle_{Av}+(m/2e)\langle\rho v^3\rangle_{Av}=\Phi_0 \text{ constant}. \tag{52}$$

The average energy flux remains constant all along the tube. These three invariants (49), (51) and (52) will be very helpful in the discussion of the progressive change of the wave traveling through the tube. The invariant (51) shows immediately that the wave energy is obtained at the expense of the average kinetic energy of the beam. Let

$$v=u_0(x)+u_1(x,t)$$

be the velocity of electrons at point x and at time t: $u_0(x)$ is the average velocity and u_1 the oscillating part

$$\bar{v}=u_0 \quad \langle u_1\rangle_{Av}=0$$
$$\langle v^2\rangle_{Av}=u_0^2+\langle u_1^2\rangle_{Av}$$
$$\bar{V}=0$$

since the average voltage in the wave remains zero. We thus obtain

$$u_0^2=v_0^2-\langle u_1^2\rangle_{Av}. \tag{51a}$$

This shows that the average velocity u_0 of the beam is always decreased when the oscillations u_1 increase in amplitude.

VIII. STABLE WAVE SYSTEMS OF LARGE AMPLITUDE (CLASS C)

We may now try to discuss the possibility of obtaining stable waves in a traveling-wave tube, with the hope that some of these waves might represent the final stage of the amplified waves of small amplitude.

Our fundamental equations have been written in (5), (6) and (13). Without attempting to make a general discussion of these equations, we are going to investigate the possibility for stable motions, when ρ, v, V depend upon x and t only through the combination

$$\theta=x-u_0t \quad u_0 \text{ constant}. \tag{53}$$

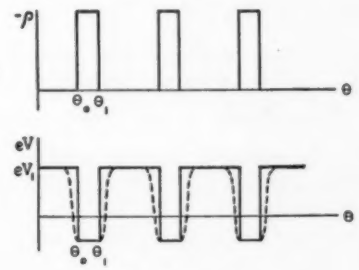

FIG. 5(a).

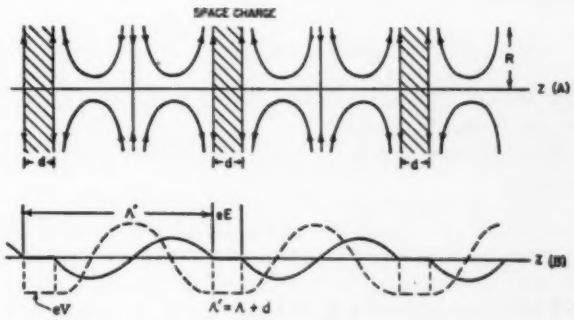

FIG. 5(b).

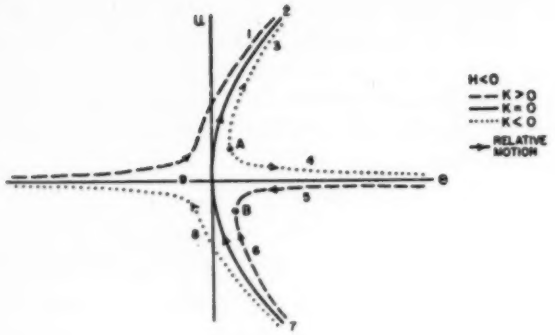

FIG. 6.

This means a stable wave propagating with a velocity u_0 but having an arbitrary shape.

$$\partial/\partial t = -u_0(\partial/\partial\theta) \quad \partial/\partial x = \partial/\partial\theta \tag{54}$$

$$d/dt = (v-u_0)\partial/\partial\theta. \tag{55}$$

Under such an assumption Eqs. (5), (6), (13) now read

$$(v-u_0)(\partial\rho/\partial\theta) = -\rho(\partial v/\partial\theta) \tag{56}$$

$$(v-u_0)(\partial v/\partial\theta) = -e/m(\partial V/\partial\theta) \tag{57}$$

$$\left(1-\frac{u_0^2}{W_0^2}\right)\frac{\partial^2 V}{\partial\theta^2} = -u_0^2 L\frac{\partial^2\rho}{\partial\theta^2} \text{ with } \frac{1}{W_0^2} = LC. \tag{58}$$

The integration is straightforward and introduces four constants, k, h_0, h_1, g.

$$\rho(v-u_0) = k \tag{59}$$

$$\tfrac{1}{2}(v-u_0)^2 + (e/m)V = g \tag{60}$$

since

$$\partial/\partial\theta(v-u_0) = \partial v/\partial\theta$$

and

$$\left(\frac{1}{u_0^2}-\frac{1}{W_0^2}\right)V = -L\rho + h_0 + h_1\theta. \tag{61}$$

Let us define the relative velocity u of electrons with respect to a frame of reference moving with the constant velocity u_0:

$$v-u_0 = u. \tag{62}$$

We obtain from Eqs. (59) (60)

$$\rho u = k \tag{63}$$

$$\tfrac{1}{2}u^2 + (e/m)V = g. \tag{64}$$

The second equation means *energy conservation in the moving frame of reference.*

Turning now to Eq. (61) and making use of Eq. (63), we have

$$\frac{W_0^2-u_0^2}{u_0^2W_0^2}V - h_0 - h_1\theta + L\frac{k}{u} = 0 \tag{65}$$

and with the help of Eq. (64)

$$u^3 + 2u(G+H\theta) - 2K = 0 \tag{66}$$

with

$$K = (e/m)Lk\frac{u_0^2W_0^2}{W_0^2-u_0^2}$$

$$G = -g + (e/m)h_0\frac{u_0^2W_0^2}{W_0^2-u_0^2} \tag{67}$$

$$H = (e/m)h_1\frac{u_0^2W_0^2}{W_0^2-u_0^2}.$$

We have obtained in (66) an equation for u, containing three arbitrary constants G, H and K. We shall consider later the case $H\neq 0$ and we begin with the condition $H=0$, that gives us three constant values u for each G and K value. This, however, means a constant velocity $v=u_0+u$ for the electrons and a constant potential V (Eq. (64)). The result is trivial and of no interest.

Looking again at this problem, we realize that we have introduced an implicit assumption in treating all quantities as continuous with continuous derivatives.

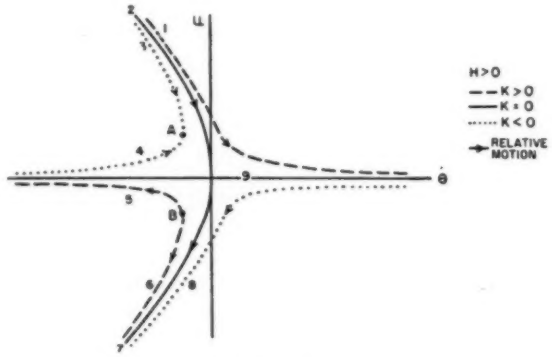

FIG. 7.

Let us show by one example the possibility of obtaining other solutions. The space-charge density need not be continuous. The bunching may become strong enough to leave empty holes between bunches. When $\rho=0$, in such a hole, v can no more be defined, and Eqs. (56) (57) must be revised.

Let us assume the space-charge bunches to move as solid blocks with the velocity

$$v = u_0 \quad u = 0. \tag{68}$$

According to (56) this seems to leave $\rho(\theta)$ arbitrary, provided there is no force acting on the electrons; hence

$$eV = \text{constant} \quad \text{wherever } \rho\neq 0$$

eV must be a minimum for the wave to be stable; hence

$$V = \text{constant, maximum} \quad \text{wherever } \rho\neq 0 \tag{69}$$

since $e<0$. We are now left with the wave equation (58) or its integral form (61) that we write

$$V = V_1 + \frac{u_0^2W_0^2}{u_0^2-W_0^2}L\rho, \tag{70}$$

dropping any $h_1\theta$ term. This makes it possible to have short pulses extending from θ_0 to θ_1, provided they correspond to positive pulses in the voltage. Figure 5 represents such a solution, which might be periodic or aperiodic. The constant term V_1 must be negative in order for the average voltage to be zero and the pulse voltage is positive when

$$u_0 < W_0 \tag{71}$$

since ρ is negative.

This seems to represent a perfectly good solution of our problem. The only correction would arise from the fact that the structure of our Fig. 1 is a low pass filter with a cut-off. This would mean using the rigorous wave equation (3) instead of the simplified Eq. (13). Our Eq. (58) would accordingly be modified and the relation (61) between V and ρ should be revised. A discussion of this problem shows that these corrections would not change the V values in the regions like $\theta_0 < \theta < \theta_1$, where ρ is different from zero. But the V distribution *between* space-charge bunches would be modified and rounded off, as shown by the dotted curve on Fig. 5(a).

It is interesting to note the similarity of these results to those obtained through a different method.[15] The discussion of this other problem leads to the curves plotted on Fig. 5(b), which correspond to a complete rounding off of the eV curve between bunches. It is possible to generalize this result by using a double-stream motion within the space-charge bunches (see Section I, B). One-half of ρ may have a given positive u velocity and the other half a negative $-u$ value, electrons reversing their motions when they reach the limits $\theta_0\theta_1$ of the bunch. This calls again for a constant V_{max} value of the voltage in the region of the bunched charge, and is consistent with Eq. (70). The only change is an increase in the average energy of the wave. Such a generalization may be needed in order to satisfy the invariant condition (51) of Section VII. Of course, this internal vibrational energy would soon be dissipated in practice and the wave would settle down on the previous solution.

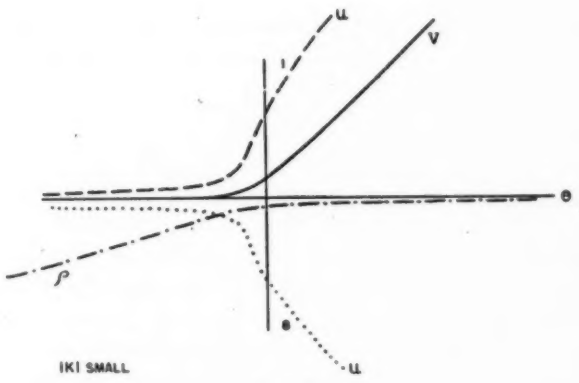

FIG. 8.

IX. DISCUSSION OF THE RESULTS—SHOCK WAVES

Let us now come back to our previous Eq. (66). When H is not zero, we can choose the origin of the θ-coordinates so as to make $G=0$ and write

$$u^3+2H\theta u-2K=0 \quad H\neq 0. \tag{72}$$

This equation is best discussed graphically, as shown on Figs. 6 and 7, that show the type of curves obtained for different signs of H and K. The arrows indicate the direction of *relative* motion: to the right when $u>0$, to the left when $u<0$. When $K=0$ the solution contains always the horizontal axis (9) and the parabolic branch (2), (7).

$$u^2=-2H\theta. \tag{73}$$

Once $u(\theta)$ has been obtained, ρ results from Eq. (63) and V from Eq. (64). Positive or negative u values yield the same potential V, since only the square u^2 of the relative velocity appears in Eq. (64), surprising as it may seem.

We must, however, pay attention to the restrictive condition that ρ must be negative (electronic space-charge); hence u and k must have opposite signs. But k comes in the K-formula (72); hence the following conditions (remembering $e<0$):

				curves	
$u>0$	$k<0$	$K>0$	when $u_0<W_0$	6.1	7.1
		$K<0$	when $u_0>W_0$	6.3	6.4
				7.3	7.4

(74)

$u<0$	$k>0$	$K<0$	when $u_0<W_0$	6.8	7.8
		$K>0$	when $u_0>W_0$	6.5	6.6
				7.5	7.6.

(75)

Curve 1 or 8 extending over the whole range for θ from $-\infty$ to $+\infty$ may correspond to the behavior of an electron beam emitted on the left from an electron gun with velocity u_0.

Curves 3–6 can be used only between $\pm\infty$ and points A or B. The electron gun *and* an electron collector should be used; otherwise the beam becomes completely unstable at either A or B. Curves 2 and 7 ($K=0$) on both figures could be used jointly and yield a double-stream solution with a reversal of the relative velocity at the point $\theta=0$.

Let us consider more carefully the case of curve 1 or curve 8 on Fig. 6. These curves correspond to beams emitted from an electron gun to the left, with an initial absolute velocity u_0; ($u=0$). The beam maintains a velocity nearly equal to u_0 (small relative velocity u) up to the wave-front $\theta=0$, ($x=u_0t$) where the beam is suddenly accelerated ($u>0$, curve 1) or decelerated ($u<0$, curve 8). This means a sort of *shock wave* for the space charge. The space-charge density is large for $\theta<0$, decreases near $\theta=0$, and becomes very small for $\theta>0-$. The potential V is practically constant for

$\theta \ll 0$ and increases linearly for $\theta > 0$ as shown on Fig. 8. On the limit $K=0$ a real shock wave is obtained.

It does not matter whether electrons are accelerated or decelerated on the wave front. Both ρ and V are the same for both cases that differ only in the way according to which the electronic current is emitted from the electron gun. The case of a small K-value results in the following approximations:

$$\theta<0 \qquad u \approx K/H\theta = Lk/h_1\theta \quad h_1>0 \tag{76}$$

$$\rho = k/u \approx (h_1/L)\theta \quad \begin{matrix} k<0 \text{ branch 1} \\ k>0 \text{ branch 8} \end{matrix} \tag{77}$$

$(e/m)V = g_1 - \frac{1}{2}u^2 \approx g_1 - \frac{1}{2}(Lk/h_1\theta)^2$ almost constant by a suitable choice of the zero voltage, $g_1=0$.

$$\theta>0 \quad u^2 \approx -2H\theta \qquad H<0 \tag{78}$$

$$\rho \approx k/(-2H\theta)^{\frac{1}{2}} \quad u_0 < W_0$$

$$(e/m)V \approx g_1 + H\theta. \tag{79}$$

The second formula (76) proves that we must take $h_1>0$ in order to obtain $\rho<0$ for $\theta<0$. Since Fig. 6 corresponds to $H<0$, it means $u_0<W_0$ according to Eq. (72). This checks with conditions (74, 75). The results are plotted on Fig. 8, assuming $g_1=0$.

X. OSCILLATING WAVE OF MODERATELY LARGE AMPLITUDE (CLASS B)

We may now try to investigate what happens to an amplified wave, such as the amplified wave of Section IV, when it reaches such an amplitude that it exceeds the limits discussed in Section VI and reaches class B conditions.

According to the discussion of Section VI we shall define *class* B by the following conditions:

$$\begin{cases} \rho = \rho_0 + \rho_1 \\ \quad \rho_1 \text{ of the same order as } \rho_0 \text{ hence Eq. (36) not valid} \\ v = v_0 + v_1 \quad |v_1| \ll v_0 \quad \text{Eq. (35) still valid.} \end{cases} \tag{80}$$

We must, however, be aware of the fact that the space-charge may become zero, but must not be allowed to change sign since this would have no physical meaning.

$$\rho_0 + \rho_1 \leq 0 \quad \rho_1 \leq -\rho_0. \tag{81}$$

Our basic equations are Eqs. (4), (6) and (13) as usual. We may rewrite (4) in the following way

$$\frac{1}{\rho}\frac{\partial \rho}{\partial t} + \frac{v}{\rho}\frac{\partial \rho}{\partial x} = -\frac{\partial v}{\partial x},$$

which suggests the use of a logarithmic function

$$l = \log|\rho| = \log(-\rho) \quad \rho = -e^l \tag{82}$$

and yields

$$\frac{\partial l}{\partial t} + v_0\frac{\partial l}{\partial x} = -\frac{\partial v_1}{\partial x}, \tag{83}$$

where v has been replaced by the constant v_0 (according to (80)) in the second term. Thus we have succeeded in linearizing the most dangerous of our equations, and at the same time we satisfy condition (81) since the ρ-value of (82) will never change sign, even when l oscillates from $-\infty$ to $+\infty$. Equation (6) reads

$$\frac{\partial v_1}{\partial t} + v_0\frac{\partial v_1}{\partial x} = -\frac{e}{m}\frac{\partial V}{\partial x}, \tag{84}$$

when v is replaced by v_0 according to our assumption (80), and Eq. (13) yields

$$\left(\frac{\partial^2}{\partial x^2} - \frac{1}{W_0^2}\frac{\partial^2}{\partial t^2}\right)\left(\frac{e}{m}V\right) = 2\frac{\delta}{\rho_0}\frac{\partial^2}{\partial t^2}(-\rho)$$

$$= 2\frac{\delta}{\rho_0}\frac{\partial^2}{\partial t^2}(e^l), \tag{85}$$

where δ is the same small parameter defined in Eq. (20). Eliminating v_1 and V from (83), (84) and (85) we obtain the *equation for class* B *approximation.*

$$\left(\frac{\partial^2}{\partial x^2} - \frac{1}{W_0^2}\frac{\partial^2}{\partial t^2}\right)\left(\frac{\partial}{\partial t} + v_0\frac{\partial}{\partial x}\right)^2 l = 2\frac{\delta}{\rho_0}\frac{\partial^4}{\partial x^2 \partial t^2}(e^l). \tag{86}$$

All the non-linear terms have been pushed back into the small right-hand term that represents the small coupling between beam and wave. Let us check how this equation contains the more special case of class A (Section IV) where

$$|\rho_1| \ll |\rho_0| \quad l = \log(-\rho) = \log(-\rho_0) + \log(1+\rho_1/\rho_0) \approx \log(-\rho_0) + \rho_1/\rho_0 \tag{87}$$

$$-e^l = \rho = \rho_0 + \rho_1.$$

Taking for ρ_1 an expression in $e^{j\omega t - \gamma x}$ as in Eq. (14), we see that Eq. (86) reduces to the type (20) previously obtained.

For class B oscillations we have to discuss the role of non-linear terms in the right-hand expression of (86). We are interested in the waves propagating to the right and we want to discuss more especially the case

$$v_0 = W_0, \tag{88}$$

where the velocity of the electrons is equal to that of the free wave. Instead of x and t we take the variables

$$\theta = x - W_0 t \qquad \xi = x$$

$$\frac{\partial}{\partial x} = \frac{\partial}{\partial \theta} + \frac{\partial}{\partial \xi} \qquad \frac{\partial}{\partial t} = -W_0\frac{\partial}{\partial \theta} \tag{89}$$

and Eq. (86) reads

$$\left(2\frac{\partial}{\partial \theta} + \frac{\partial}{\partial \xi}\right)\frac{\partial^2}{\partial \xi^2} l = 2\frac{\delta}{\rho_0}\left(\frac{\partial}{\partial \theta} + \frac{\partial}{\partial \xi}\right)^2 \frac{\partial^2}{\partial \theta^2}(e^l). \tag{90}$$

Furthermore, we assume that for a wave propagating

to the right we shall have

$$\partial/\partial \gg \partial/\partial\xi, \tag{90a}$$

since the ξ-dependence will contain only the slow changes in the shape and amplitude of the waves. Equation (90) then reduces to

$$\frac{\partial^3 l_1}{\partial \xi^3} = -\delta \frac{\rho_{00}}{\rho_0} \frac{\partial^3}{\partial \theta^3}(e^{l_1}), \tag{91}$$

where we have assumed

$$l = l_0 + l_1 \quad l_1 = 0 \quad -\rho_{00} = e^{l_0}. \tag{92}$$

The assumption is that l contains a constant term l_0 plus an oscillating term l_1 whose θ-average is zero. For large oscillations we have

$$\rho = \rho_{00} e^{l_1} = \rho_{00}[1 + l_1 + (1/2)l_1^2 + (1/6)l_1^3 + (1/24)l_1^4 \cdots];$$

hence

$$\rho_0 = \bar{\rho} = \rho_{00}[1 + (1/2)\bar{l_1}^2 + (1/24)\bar{l_1}^4 \cdots] \tag{93}$$

and it becomes obvious that large oscillations have a coupling coefficient $\delta(\rho_{00}/\rho_0) < \delta$ and will probably be less amplified than small oscillations. We have to be careful not to use the complex exponential notations any more, since this method cannot be applied to non-linear problems. Another important point to keep in mind is the complexity of a problem involving a fourth-order partial differential equation, such as (86) or (90). In using the approximation (90a) we have eliminated the reflected wave, but we still have to deal with a third-order partial differential equation. This means that we have to give *three* initial conditions at the input. This situation was discussed in Section V for the case of small signals. In that case, we could solve the problem by using a superposition of three waves, since we were dealing with a linear problem.

For large oscillations and a non-linear equation of type (91) we must give, at the origin $x = 0$, the following input data:

$$l_1 = f(t) \quad \frac{\partial l_1}{\partial x} = g(t) \quad \frac{\partial^2 l_1}{\partial x^2} = h(t), \tag{94}$$

and the partial differential equation yields $\partial^3 l_1/\partial x^3$ and the higher derivatives.

One might be tempted to ask the following question: What is the amplification coefficient for large amplitudes? The answer is that such a question is entirely meaningless. First, while propagating along the line, the wave is amplified (or attenuated) and *distorted;* hence the comparison of the amplitude of the wave at points x and $x+dx$ becomes very difficult. Second, the change in the wave is defined only when all *three* functions f, g and h of Eqs. (94) are given; hence the amplification coefficient (even if conveniently defined) depends upon these three functions in a very complicated fashion. It is therefore impossible to plot a curve representing the amplification coefficient as a function of one parameter (say, the amplitude of the wave).

A similar situation has been recognized long ago in the problem of the Van der Pol oscillator, where non-linearity forbids any simple definition of an amplification coefficient.

This will be understood more clearly if we consider a specific example. Let us assume that we have, at a certain stage, obtained a wave

$$l_1 = A e^{a\xi} \cos(b\theta + g\xi) \quad \phi = b\theta + g\xi. \tag{95}$$

We take a real function, since imaginary exponentials cannot be used in non-linear problems. This is the type of amplified wave that comes from the amplified wave of class A type, where

$$l_1 \approx (\rho_1/\rho_0) \ll 1$$

It is a simple matter to compute the derivatives appearing in Eq. (91) and to obtain

$$\begin{aligned}(\partial^3/\partial\theta^3)(e^{l_1}) &= (l_1\cdots + 3l_1 \cdot l_1 \cdot\cdot + l_1 \cdot^3)e^{l_1} \\ &\approx l_1\cdots + (l_1 l_1\cdots + 3l_1 \cdot l_1 \cdot\cdot) \\ &\quad + (\tfrac{1}{2}l_1^2 l_1\cdots + 3l_1 l_1 \cdot l_1 \cdot\cdot + l_1 \cdot^3) + \cdots,\end{aligned}$$

where the dots mean $\partial/\partial\theta$ and the exponential has been expanded so as to regroup terms of similar degrees. Equation (91) now reads

$$\begin{aligned}&A e^{a\xi}[a(a^2 - 3g^2)\cos\phi + g(g^2 - 3a^2)\sin\phi] \\ &= -\delta \frac{\rho_{00}}{\rho_0} b^3 A e^{a\xi}\Big[\sin\phi + 4A e^{a\xi}\sin\phi\cos\phi \\ &\qquad + A^2 e^{2a\xi}\left(\frac{7}{2}\sin\phi - \frac{9}{2}\sin^3\phi\right) + \cdots\Big] \\ &= -\delta \frac{\rho_{00}}{\rho_0} b^3 A e^{a\xi}\Big[\sin\phi + 2A e^{a\xi}\sin 2\phi \\ &\qquad + A^2 e^{2a\xi}\left(\frac{1}{8}\sin\phi + \frac{9}{8}\sin 3\phi\right)\cdots\Big].\end{aligned}$$

Terms in $\sin 2\phi$, $\sin 3\phi \cdots$ indicate a further distortion of the wave that will destroy progressively the simple type (95) assumed at the input. As far as amplification is concerned, it results from the $\sin\phi$ and $\cos\phi$ terms only:

$$\cos\phi \text{ terms} \quad a(a^2 - 3g^2) = 0 \tag{96}$$

$\sin\phi$ terms

$$g(g^2 - 3a^2) = \delta \frac{\rho_{00}}{\rho_0} b^3 \left[1 + \frac{1}{8} A^2 e^{2a\xi}\cdots\right]. \tag{97}$$

Condition (96) yields the three progressive waves

$$\begin{array}{ll} a = 0 & \text{not amplified} \\ a = -\sqrt{3}\,|g| & \text{attenuated} \\ a = +\sqrt{3}\,|g| & \text{amplified.} \end{array} \tag{98}$$

Let us consider the last wave. Equation (97) gives

$$a^3\frac{8}{3\sqrt{3}}=\delta\frac{\rho_{00}}{\rho_0}b^3\left[1+\frac{1}{8}A^2e^{2\alpha\xi}\right]. \tag{99}$$

The amplification coefficient is proportional to the $\frac{1}{3}$ power of

$$\delta_1=\delta\frac{\rho_{00}}{\rho_0}\left[1+\frac{1}{8}A^2e^{2\alpha\xi}\right]<\delta. \tag{100}$$

Since Eq. (93) gave

$$\frac{\rho_{00}}{\rho_0}\approx 1-\frac{1}{2}l_1^2=1-\frac{1}{4}A^2e^{2\alpha\xi};$$

hence

$$\delta_1=\delta(1-\tfrac{1}{8}A^2e^{2\alpha\xi})<\delta. \tag{101}$$

We may thus conclude that in class B the wave remains approximately sinusoidal in a logarithmic scale and is less and less amplified when it grows up larger. The final stage may be represented by the very large, rectangular, non-amplified oscillations of Section VIII (class C), but this is not certain by any means, and the question of the final shape of the amplified wave remains open.

BIBLIOGRAPHY

R. Kompfner, Wireless World **52**, 369 (1946); Proc. I.R.E. **35**, 124 (1947); Wireless Eng. **24**, 255 (1947).
J. R. Pierce and L. M. Field, Proc. I.R.E. **35**, 108 (1947).
J. R. Pierce, Proc. I.R.E. **35**, 111 (1947).
J. R. Pierce, Bell Lab. Records **24**, 439 (1946).
Blanc-Lapierre, Lapostolle, Voge, and Wallauschek, L'onde Elec. **27**, 1947 (1947).
E. Roubine, L'onde Elec. **27**, 203 (1947).
J. Bernier, L'onde Elec. **27**, 231 (1947).
P. Lapostolle, Comptes Rendus **224** and **268**, 558, 814 (1947). Thèse de Doctorat, Paris, 1947.
A. Blanc-Lapierre, Ann. Telecomm. **1**, 283 (1946).
J. Bernier, Ann. Rad. Elec. **2**, 87, 195 (1947).
O. Doehler and W. Kleen, Ann. Rad. Elec. **2**, 232 (1947).
O. Doehler and W. Kleen, Ann. Rad. Elec. **3**, 124, 184 (1948).
D. L. Benedict, Cruft Laboratory Technical Report No. 30, Harvard University ONR Contract N5ori-76 (February 20 1948).
L. J. Chu and D. Jackson, Research Laboratory of Electronics, M.I.T. Report No. 38, 1947.
L. Brillouin, "Waves and electrons traveling together," Phys. Rev. **74**, 90 (1948).

Distribution of Phases in Two-Phase Solids

LEONARD D. JAFFE
Watertown Arsenal Laboratory, Watertown, Massachusetts

(Received June 8, 1949)

The quasi-equilibrium distribution of a disperse phase, B, within a polycrystalline second phase, A, is investigated by methods of statistical thermodynamics. Phase B is assumed to consist of spherical particles of uniform size within the A crystals, and of lenticular particles of uniform size at the boundaries between two A crystals. The concentration (Mf) of B at the grain boundaries of A is found to be related to the sizes (r_1 and r_2) of the B particles at and away from grain boundaries, in terms of the interfacial energies (γ_{aa} and γ_{ba}), the temperature (T), the over-all concentration (M), and the size of the A crystals (R), by

$$\left(\frac{Mf}{1-Mf}\right)\left(\frac{Mw}{1-Mw}\right)^{-r_1^3/r_2^3}=\exp\left\{-\frac{\gamma_{aa}r_1^2}{kT}\left[\frac{9\pi Z-(9\pi/2)^{\frac{1}{3}}(3Z^3+2\pi)(r_1/r_2)}{3Z^3-4\pi}\right]\right\},$$

where

$$w=1-\frac{2.66fr_1}{R(Z-(\pi/3)Z^{-2})}$$

and

$$Z=\left[\frac{2\pi(4(\gamma_{ba}/\gamma_{aa})+1)}{3(2(\gamma_{ba}/\gamma_{aa})-1)}\right]^{\frac{1}{3}}.$$

Temperature will significantly affect the distribution only if $\gamma_{aa}r_1^2$ is of the order of kT, or if $\gamma_{ba}/\gamma_{aa}\sim\frac{1}{2}$.

INTRODUCTION

TWO-PHASE solids often occur in the form of a distribution of spheroidal particles of a disperse phase, B, in a polycrystalline matrix of a continuous solid phase, A, the particles of B being small compared to the crystals of A. Such a distribution may arise, for example, when phase B has formed by precipitation from phase A. Freshly precipitated particles of B will not in general be spheroidal, but when the precipitation has proceeded so far that phase A is depleted in the precipitating component, the particles will generally approach a spheroidal form under the influence of interfacial tension.

The average concentration, shape, and size of B particles in contact with two or more A crystals may be expected to differ from those for particles located entirely within a crystal ("grain") of A. It appears that the mechanical behavior, in particular, of two-phase solids may be greatly influenced by such differences.

The size of the particles will gradually increase with time and their number will decrease correspondingly. It may prove profitable, nevertheless, to consider that at each instant the particles within the crystals are in thermodynamic equilibrium with those at the grain boundaries, and to examine the concentrations and sizes of particles that will then be found at both sites. If the distribution has in fact arisen by precipitation of B from A, the system may approach this form of quasi-equilibrium at times sufficiently long so that: (a) the precipitation reaction is essentially complete—the

phases approaching equilibrium composition (b) subsequent transient diffusion between grain boundaries and grain interiors, resulting from differences in precipitation rates at the two sites, has become negligible.

EQUILIBRIUM DISTRIBUTION

For simplicity, the particles within the grains will be considered as spheres of a single volume r_2^3. (The subscripts 1 and 2 are used to refer respectively to particles at the grain boundaries and to particles away from the boundaries.) The particles at the boundary between two grains will be assumed to be of a single volume r_1^3 and to have the form giving the lowest interfacial energy per particle: that is, a double convex lens having equal radii of curvature for each surface. The area of the central plane of the lens will be taken as ρ^2. Particles of B located in contact with three or more grains of A will be neglected. It will be considered that the grains may be approximated by 14-sided Kelvin polyhedrons[1] of volume R^3. R is here large compared to r_1 and r_2. Further, the interfacial energies will be taken as independent of crystal orientation.

By setting up the equations for the interfacial energy of a lenticular particle of B, with unknown ratio of thickness to radius, at the interface of two grains of A, and solving under the condition of minimum energy for a particle of fixed volume, it is found that

$$\rho = r_1(Z-(\pi/3)Z^{-2})^{\frac{1}{2}}$$

where

$$Z=\left\{\frac{2\pi[4(\gamma_{ba}/\gamma_{aa})+1]}{3[2(\gamma_{ba}/\gamma_{aa})-1]}\right\}^{\frac{1}{3}}$$

and

γ_{aa} = interfacial energy per unit area of interface between two A grains

γ_{ba} = interfacial energy per unit area of interface between B and A.

Further, the interfacial energy associated with this particle is then

$$\frac{3\rho^2\gamma_{aa}}{(Z^3/\pi)-(5/3)+(4\pi/9)Z^{-3}}. \qquad (1)$$

All energies are here measured from that of the polycrystalline A phase in the absence of B.

For close-packed Kelvin polyhedrons of 14 sides, the interfacial ("grain boundary") area per unit volume is* $2.66/R$.

Let the over-all concentration (volume fraction) of B be M, and the concentration (area fraction) of B at the A grain boundaries be Mf. The number of B particles per unit area of A grain boundary is then Mf/ρ^2, and the number of such particles per unit volume is

$$2.66Mf/R\rho^2.$$

From expression (1), the interfacial energy per unit volume, E_1, associated with B particles at A grain boundaries is then

$$E_1=\frac{2.66Mf\gamma_{aa}}{R}\,\frac{3}{(Z^3/\pi)-(5/3)+(4\pi/9)Z^{-3}}. \qquad (2)$$

The grain boundary area may be considered as divided into cells of area ρ^2. Within each cell may be located the center of one or zero grain boundary particle of B. The Fermi-Dirac statistics are accordingly applicable, so that the entropy S per unit volume is given by

$$S=-kg[N\ln N+(1-N)\ln(1-N)] \qquad (3)$$

where k = Boltzmann's constant, g = number of cells per unit volume, and N = number of particles/number of cells. Here $N_1=Mf$, and g_1 is the grain boundary area per unit volume divided by the area per cell, or $g_1=2.66/R\rho^2$. The entropy per unit volume associated with particles at grain boundaries is therefore

$$S_1=-(2.66k/R\rho^2)[Mf\ln Mf+(1-Mf)\ln(1-Mf)]. \qquad (4)$$

The volume of B at grain boundaries, per unit volume, is

$$(2.66Mfr_1^3)/(R\rho^2).$$

The volume concentration of B not at grain boundaries is consequently Mw, where

$$w=1-(2.66fr_1^3)/(R\rho^2).$$

Since the volume of each B particle not at an A grain boundary is r_2^3, the number of such particles per unit volume is Mw/r_2^3. The interfacial area per particle is $r_2^2(36\pi)^{\frac{1}{3}}$, the interfacial energy per particle is $r_2^2\gamma_{ba}(36\pi)^{\frac{1}{3}}$, and the interfacial energy per unit volume

$$E_2=(Mw\gamma_{ba}/r_2)(36\pi)^{\frac{1}{3}}. \qquad (5)$$

The volume not within r_2 of a grain boundary is practically equal to the total volume, since $r_2 \ll R$. This volume may be divided into cells of volume r_2^3, each of which may contain the center of one or zero particle of B. Applying Eq. (3), with $N_2=Mw$ and $g_2=1/r_2^3$,

$$S_2=-(k/r_2^3)[Mw\ln Mw+(1-Mw)\ln(1-Ww)]. \qquad (6)$$

For equilibrium

$$\partial G/\partial f=0 \qquad (7)$$

where the free energy per unit volume

$$G=(E_1+E_2)-T(S_1+S_2).$$

[1] W. Thomson (Lord Kelvin), "Division of space with minimum partitional area," Phil. Mag. 24, 503–514 (1887).

* Utilizing computations of Kaiser (see reference 2) for plane-sided polyhedrons. Unpublished work by O. Bowie and L. Malvern shows that the curvature of the faces of the Kelvin polyhedrons reduces their area/volume ratio by less than 0.2 percent, which is within the precision of the value 2.66.

[2] H. F. Kaiser, "Estimation of inter-granular surfaces and volumes in metals," Metals and Alloys 9, 23–26 (1938).

Substituting Eqs. (2), (4)–(6) in Eq. (7) and simplifying, there is obtained

$$\left(\frac{Mf}{1-Mf}\right)\left(\frac{Mw}{1-Mw}\right)^{-r_1^3/r_2^3}$$

$$=\exp\left\{-\frac{\gamma_{aa}r_1^2}{kT}\left[\frac{9\pi Z-(9\pi/2)^{\frac{1}{3}}(3Z^3+2\pi)(r_1/r_2)}{3Z^3-4\pi}\right]\right\}. \quad (8)$$

DISCUSSION

There is only a single reliable datum on the surface or interfacial energies of solids: 1370 ergs/cm² for the surface energy of copper (at its melting point).[3] The surface energy of liquids is[4] of the order 30 to 3000 ergs/cm². The surface energies of solids may be assumed to be of the same magnitude. The interfacial energy between grains of the same solid phase appears to be[5] "a small fraction" of their surface energy. Hence γ_{aa} may be taken to be of the order of 10^{-2} to 10^{2} ergs/cm². For solids under atmospheric pressure, $T<4000°$K. Then for $(\gamma_{aa}r_1^2/kT)\sim 1$, $r_1<7\times10^{-8}$ cm. If r_1 is much larger than this, $(\gamma_{aa}r_1^2/kT)\gg 1$ (meaning that the entropy terms in Eq. (7) are negligible compared to the energy terms). Under this condition, if the exponent in Eq. (8) is positive, the concentration of phase B at grain boundaries (Mf) will be close to unity or the concentration within the grains (Mw) will be close to zero. If the exponent is negative, the concentration at grain boundaries will be close to zero. This concentration will change from near 0 to near 1 as the ratio r_1/r_2 increases, the change taking place very sharply as r_1/r_2 passes through a constant of the order of unity.

Since the size of the grain boundary particles must be real, the solution of Eq. (8) is of physical significance only when $\gamma_{ba}/\gamma_{aa}\geq\frac{1}{2}$. A limiting case of interest develops when $\gamma_{ba}/\gamma_{aa}\rightarrow\frac{1}{2}$. The radius of the grain boundary particles $\rho\rightarrow\infty$ and their thickness approaches zero ("monomolecular film"). Moreover, for grain boundary particles within the size range $r_2^2\gg r_1^2\gg kT/\gamma_{aa}$, the grain boundary concentration Mf approaches a limit greater than $\frac{1}{2}$ (unless $Mw\rightarrow 0$). On the other hand, away from the limit, $Mf\sim 0$ for this size range. If, for example, $r_1/r_2=0.1$, $Mf\rightarrow 0$ as $\gamma_{ba}/\gamma_{aa}\rightarrow 0.500$ but $Mf>\frac{1}{2}$ at $\gamma_{ba}/\gamma_{aa}=0.515$. If $r_1/r_2=0.01$, $Mf>\frac{1}{2}$ at $\gamma_{ba}/\gamma_{aa}=0.5005$. If $r_1/r_2=0.001$, $Mf>\frac{1}{2}$ at $\gamma_{ba}/\gamma_{aa}\doteq 0.500015$, and at $r_1/r_2=0.0001$, the transition is between 0.5 and 0.5000005. A very small difference in γ_{ba}/γ_{aa}, when the quantity itself is near $\frac{1}{2}$, may thus produce a large difference in the distribution of phases. Examples have been given by Smith.[6]

EFFECT OF TEMPERATURE

Temperature will have a significant effect upon the distribution only if $\gamma_{aa}r_1^2$ is of the order of kT, or if $\gamma_{ba}/\gamma_{aa}\sim\frac{1}{2}$. If $\gamma_{aa}r_1^2$ is of the order of kT, r_1/r_2 will ordinarily be small compared to unity; at low temperatures the concentration of B at grain boundaries (Mf) will then approximate 0 and at high temperatures $\frac{1}{2}$ (unless the concentration within the grains (Mw) first approaches 0).

When $\gamma_{ba}/\gamma_{aa}\sim\frac{1}{2}$, a change in temperature, which is likely to effect a small change in this ratio, may completely change the concentration at grain boundaries.

CONSEQUENCES

When particles of one phase are dispersed in another, polycrystalline, phase, particles larger than 700A eventually concentrate at grain boundaries or interiors as governed by interfacial energy considerations. For smaller grain boundary particles entropy may also have to be considered. When these grain boundary particles are sufficiently small—in particular, small compared to the particles within the grains—their concentration will approach zero at low temperatures, but at high temperatures they will cover almost one-half the grain boundary area.

If the interfacial energy between the particles and the matrix approximates half the interfacial energy between crystals of the matrix, behavior will be different from that just described. Under this condition, a change of a fraction of a percent in either interfacial energy, as might readily be caused by a small temperature difference or by a very small percentage of dissolved impurity, may radically affect the phase distribution: grain boundaries practically free from particles may become almost completely covered by particles, in the form of very thin films.

An application of the theory is described in a separate publication.[7]

ACKNOWLEDGMENT

The author would like to thank Mr. O. Bowie of Watertown Arsenal and Dr. A. J. Shaler of Massachusetts Institute of Technology for their valuable criticisms of the manuscript.

[3] Udin, Shaler, and Wulff, "Surface tension of solid copper," Trans. A.I.M.E. 185, 186–190 (1949).

[4] N. K. Adam, *Physics and Chemistry of Surfaces* (Oxford University Press, London, 1941).

[5] C. S. Smith, "Eighth quarterly report to ONR on deformation of metals," Institute of Metals, University of Chicago, 1948.

[6] C. S. Smith, "Grains, phases, and interfaces: an interpretation of microstructure," Trans. A.I.M.E. 175, 15–51 (1948).

[7] L. D. Jaffe, "Carbide distribution as a possible cause of temper brittleness," Journal of the Iron and Steel Institute (to be published).

An Aluminum-Beryllium Alloy for Substrate and Replica Preparations in Electron Microscopy[1]

WILBUR KAYE
Research Laboratories, Tennessee Eastman Corporation, Kingsport, Tennessee
(Received June 8, 1949)

A technique of specimen preparation especially suited to the study of polymeric molecules and aggregates is presented. With slight modifications it is applicable to the preparation of replicas of a wide variety of surfaces where the action of heat, pressure, and solvents must be minimized. The method owes its superiority to the use of an aluminum-beryllium alloy of high strength, low scattering power and nearly amorphous structure. A layer of evaporated hydrophilic material facilitates the separation of the metal film from the mounting surface. Micrographs are presented showing certain applications of the method.

A MAJOR problem in the use of the electron microscope near its ultimate resolution concerns the film upon which the objects under study are mounted or supported. The perfectly smooth mounting surface, of course, is an ideal only, due to the close proximity of the ultimate microscope resolving power with atomic dimensions. Actually, to the author's knowledge, there has never been observed a surface which was smooth over any appreciable area ($>10^{-8}$ cm^2) to the extent of possessing no elevations above a mean surface level greater than 10 angstroms. However, for certain applications where solvent, temperature, and pressure effects must be minimized an alloy of aluminum and beryllium has been found to possess properties superior to any of the conventional mounting films.

For purposes of nomenclature and introduction Fig. 1 has been drawn showing a composite film of the type discussed in this paper. For certain applications one or more of the layers illustrated may be omitted.

The layer possessing the strength to support the composite film across the openings in a 200-mesh screen must be relatively thick and therefore must be composed of a material exhibiting low scattering power to the electron beam. This film may be either above or below the sample and shadow layer or, as in Fig. 1, on both sides. If it is situated underneath the specimen this substrate film must deposit uniformly or at least introduce a minimum of surface detail in addition to that present in the mounting surface and stripping layer. Such surface detail as persists on this surface will later mask the appearance of objects of like size under study. Factors concerning the solubility, ease of preparation, electrical conductivity, thermal expansion, and decomposition of the substrate also enter into consideration.

Substrate and support films are conventionally composed of silica or polymeric materials (Formvar, collodion),[2] although metallic films (aluminum and beryllium) have been used.[3,4] In general, a substrate is selected when the specimen is to be studied without shadowing while a support is chosen for preshadowing techniques. The reason for the selection of the position of the supporting film is largely dictated by the fine detail which is always introduced when a thick film deposited by evaporation is shadowed.[2]

The techniques reported in this paper have been developed for the study of organic polymer molecules and surfaces. Preshadowing techniques in which the supporting layer is deposited after shadowing frequently cannot be used when it is desired to study the molecular aggregates because of the large variations in surface elevation. The elimination of solvent and swelling effects necessitated the use of inorganic substrates.

While films of silica fulfill the basic requirements for such a substrate we have found an alloy of aluminum and beryllium to possess superior features with respect to strength per unit of scattering power, adhesion of shadow layer, electrical conductivity, and ease of preparation. By alloying these two light metals it is possible to reduce greatly the granularity of structure, thus partially overcoming their greatest handicap. The difficulty of stripping these metals has been overcome by the use of an evaporated hydrophilic layer deposited prior to the substrate.

SYNOPSIS OF THE METHOD

In order that the reader may understand the over-all procedure before discussing the details, the following is

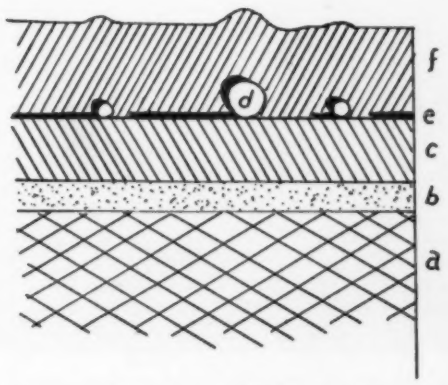

FIG. 1. Cross section of composite film: a. Mounting surface. b. Stripping layer. c. Substrate layer. d. Sample layer. e. Shadow layer. f. Support layer.

[1] Presented in part before the E. F. Burton Memorial Meeting of the Electron Microscope Society of America, Toronto, September, 1948.
[2] R. C. Williams and R. C. Backus, J. App. Phys. **20**, 98 (1949).
[3] N. Hast, Nature **159**, 354, 370 (1947); **162**, 892 (1948).
[4] Rudiger, Naturwiss. **30**, 279 (1942).

a brief description of the preparation for isolated objects (molecules and aggregates). Later the modifications for the preparation of surface replicas will be discussed.

First, the surface (e.g., glass slide) upon which the substrate is to be deposited is carefully cleaned, placed in the vacuum and coated with a thin hydrophilic film (stripping layer). Without breaking the vacuum a layer of aluminum-beryllium alloy (substrate) is deposited. This prepared surface is then removed from the vacuum, the sample is deposited on this substrate surface, returned to the vacuum and shadowed obliquely with a layer of platinum-palladium alloy. After removal from the vacuum the composite "sandwich" of metal and sample layers is stripped with water from the glass slide, etc., and mounted on a 200-mesh screen for insertion in the microscope.

THE MOUNTING SURFACE

Considerable effort was expended in attempting to obtain sample preparations free of irregular elevations as evidenced in the final composite of metal layers. The source of this surface detail has been found in both the mounting surface and the substrate. Surfaces of glass, mica, rock salt, and organic glasses (sugars) have been used. Of these glass and mica proved best. Freshly cleaved mica surfaces have been used with success by others.[6] They do not require a cleaning treatment but are unsuited to preshadowing since chromium and the noble metals have been observed to aggregate when deposited directly on mica.

In general, glass slides have been used as mounting surfaces because of their availability, convenient size, and surface flatness. Only a mild cleaning treatment with soap and water is necessary. Prolonged cleaning or the use of corrosive cleaners appears to etch the surface.

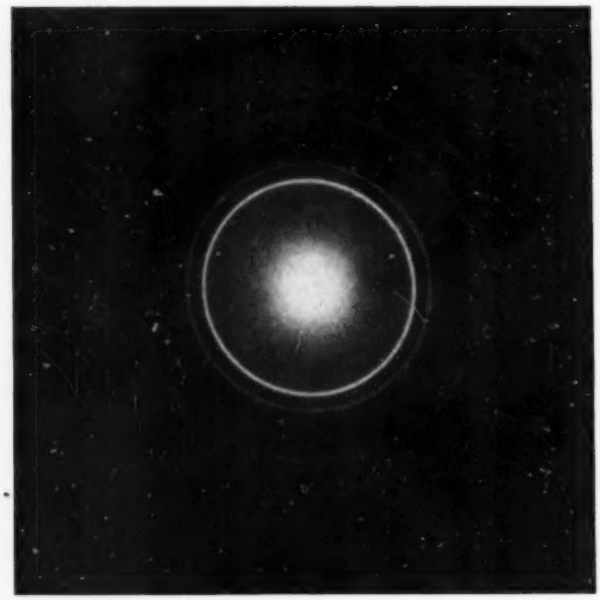

FIG. 2. Electron diffraction pattern of pure aluminum film.

[6] V. J. Schaefer and D. Harker, J. App. Phys. 13, 427 (1942).

THE STRIPPING LAYER

Readily oxidizable metals such as aluminum and beryllium do not strip from clean glass or mica surfaces; hence, it is necessary when using these metals to deposit a layer of hydrophilic material on the mounting surface.[2] The most successful solid materials used for this purpose may be classed in three groups—sugars, wetting agents, and oxide glasses. All are deposited onto the mounting surface by evaporation in the vacuum.

Of the sugars tried, galactose and sucrose have been quite satisfactory when the relative humidity of the laboratory did not exceed 50 percent. At humidities higher than this the films cracked excessively owing to the large attraction of the sugar for atmospheric water vapor.

Only two wetting agents have been used, sodium octyl and capryl phosphates manufactured by Victor Chemical Company as "Victawet" wetting agents. They are satisfactory at relative humidities below 75 percent. These wetting agents require a heat treatment (by irradiation from a hot filament) after deposition apparently to orient the molecules on the mounting surface.

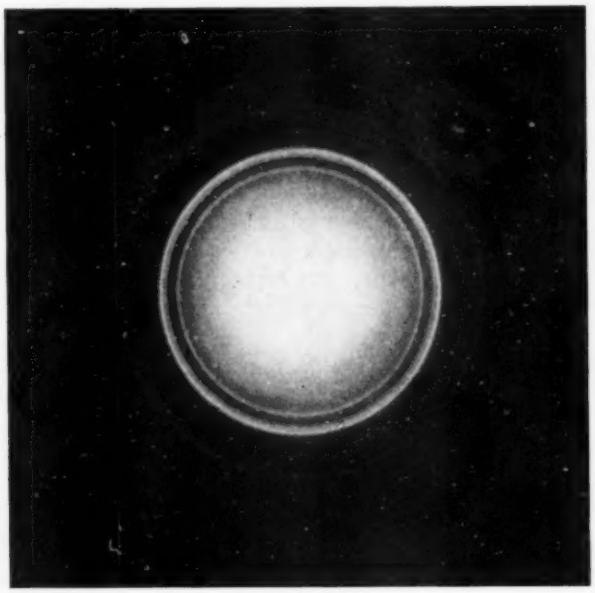

FIG. 3. Electron diffraction pattern of pure beryllium film.

Lithium and boron oxides have been used successfully. The boron oxide is particularly good for four reasons: (1) ready availability from thermal decomposition of boric acid, (2) negligible crystalline structure, (3) easy evaporation, and (4) solubility in water.

This stripping layer is deposited by evaporation in the vacuum immediately prior to deposition of the

substrate. It is essential that the vacuum not be broken between the deposition of stripping and substrate layers. If air is admitted between these two operations the latter film will be weak, giving the appearance of having been converted to the oxide. This may explain the oxide diffraction patterns reported for these films.

The final metal film is stripped most conveniently from glass slides by placing a single drop of water in one corner of the slide whereupon the water will creep under the film. After loosening the film a few drops of water suffice to raise the metal film high enough to place a circular 200-mesh screen, held by a pair of forceps, under the film. The screen and metal film are removed from the slide and dried on a filter paper.

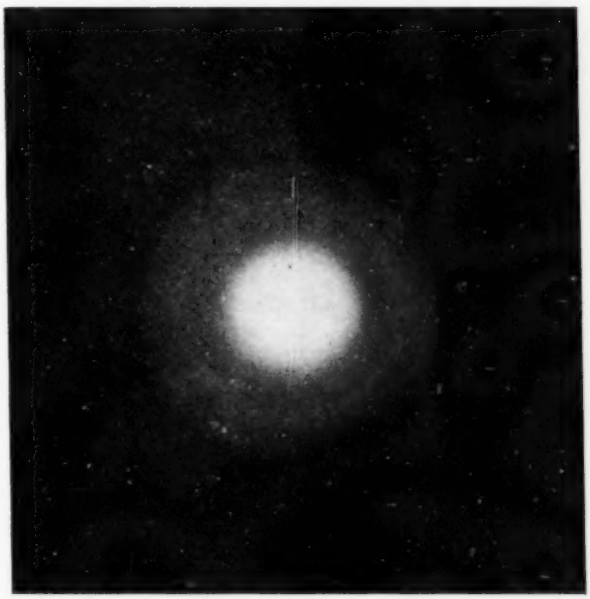

FIG. 4. Electron diffraction pattern of Al-Be alloy film.

THE SUBSTRATE

The ideal substrate is one having negligible scattering power toward electrons and no perceptible irregularities in surface elevation when its thickness is sufficient to remain intact across the openings in a 200-mesh screen.

Films of the pure metals, aluminum and beryllium, proved to have far too much crystalline detail to be of value when shadowed. However, an alloy containing approximately 40 percent aluminum and 60 percent beryllium was found to possess very little crystalline structure. Electron diffraction patterns of these pure metals and the alloy were taken to verify the crystalline nature of the films. Figures 2 and 3 show the patterns from aluminum and beryllium respectively. These patterns were obtained with no difficulty and indicate the expected crystalline nature of the films. Figure 4 shows the essentially amorphous nature of the alloy. This alloy diffraction pattern required about four times longer exposure time to obtain the negative and has been printed on paper of higher contrast than Figs. 2 and 3.

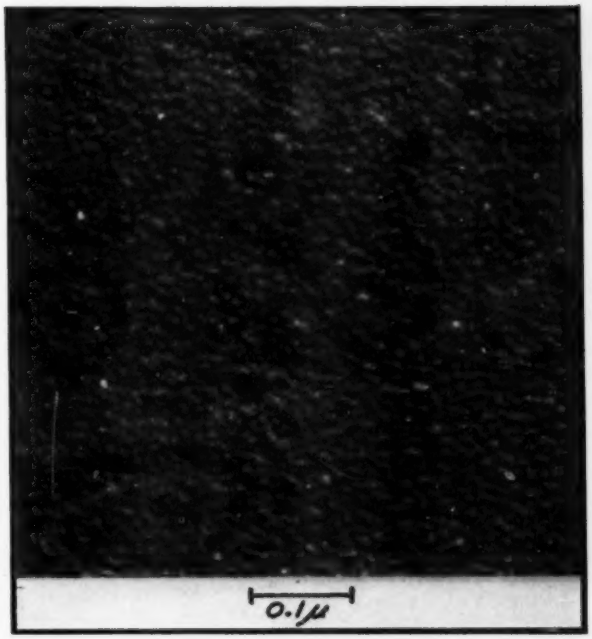

FIG. 5. Shadowed substrate. Fused glass mounting surface. Boron oxide stripping layer. Al-Be substrate. Pt-Pd shadow (4:1).

For most of the micrographs illustrated in this paper the alloy was deposited from a tungsten helix loaded with appropriate amounts of the two elements. Since the aluminum evaporates at considerably lower temperatures than the beryllium, it was necessary when first charging a helix to fuse the elements together before placing the sample in the vacuum. More recently an alloy of 54.94 percent beryllium in aluminum has been obtained from The Brush Beryllium Company of Cleveland, Ohio. The alloy is deposited on the stripping layer to a thickness which will just cause the image of a white piece of paper underneath the glass mounting surface to disappear when illuminated from above the surface: this thickness corresponds to approximately 100A.

The inclusion of another element with aluminum and beryllium (silicon, boron, magnesium, or titanium) did not prove beneficial and did increase the rate of chemical attack by water in the stripping operation.

It has been noticed repeatedly that metallic films of aluminum-beryllium alloy do not darken as rapidly when placed in the electron beam as do the polymer films.

THE SHADOW LAYER

Omitting the specimen layer for the moment, the shadow layer techniques used here do not differ from conventional methods. Uranium, uranium sulfide, gold, platinum, palladium, and chromium have been used as shadow layers with almost equal success. We have generally favored an alloy of platinum and palladium.[2] When deposited directly on the aluminum-beryllium substrate the shadow layer will not aggregate even with

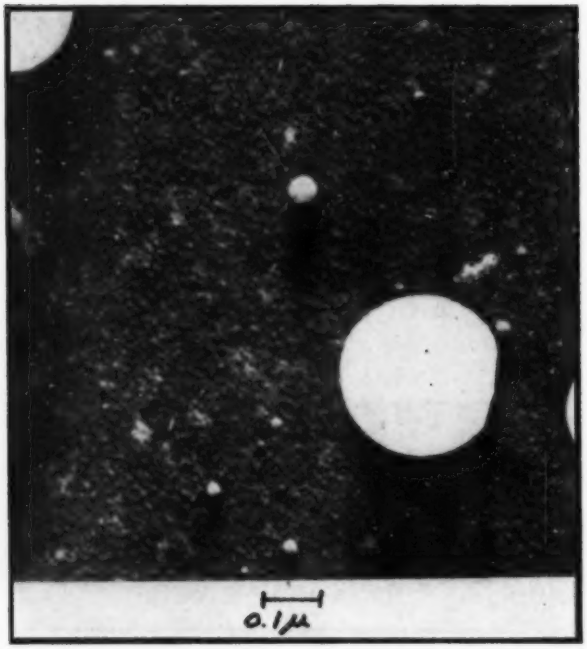

FIG. 6. Polystyrene dispersed with 2-methyl-1,3-pentanediol. Glass mounting surface. Galactose stripping layer. Al-Be substrate. Pt-Pd shadow.

the use of pure gold for the shadow layer. According to the explanation of Picard and Duffendock[6] this lack of aggregation would seem to be due to the force fields set up between the atomic lattices of the substrate and shadow layers.

When the noble metals are used for shadowing there is obviously an electrolytic couple present which can lead to dissolution of the aluminum-beryllium substrate during the stripping operation. This effect may be observed optically where it is accompanied by the evolution of a gas. The resulting films are nearly transparent and weak, although when the transparent regions exist only in microscopic areas the micrographs show considerable enhancement of contrast. Presumably in these regions the shadow layer is supporting itself. However, if distilled water reasonably free of salts or acids is used and the films are mounted and dried rapidly the composite film will not suffer perceptible dissolution.

Figure 5 shows a micrograph of an aluminum-beryllium substrate shadowed with platinum-palladium and stripped by means of a boron oxide film on a fused glass surface. At this high magnification the pebble-like appearance of the surface is quite evident; however, the contrast has been enhanced photographically. Had some larger object appeared in the field, a greater latitude of contrast would have been desired with a consequent reduction in the contrast of the slight structure of the substrate. Unfortunately, this surface detail does limit the observation of such small objects as polymer molecules.

[6] R. J. Picard and O. S. Duffendock, J. App. Phys. 14, 291 (1943).

THE SPECIMEN

The technique thus far described is best adapted to the study of polymer molecules and aggregates deposited from non-aqueous solutions. It is usually possible to isolate the individual molecules by using polymer concentrations below 0.01 percent. Two factors must be accurately controlled if these micrographs are to be reproducible: the thickness of solution deposited on the substrate before evaporation, and the concentration of precipitant.

The solution is prepared by dissolving the polymer in a good low boiling solvent, then adding approximately 0.5 percent of a higher boiling liquid which behaves as a non-solvent toward the polymer. In the course of the evaporation the solution becomes more concentrated in non-solvent until a point is reached where the polymer precipitates. If the polymer concentration were originally sufficiently low, the molecules will be isolated; otherwise aggregates will be deposited. If purified, freshly distilled solvents and precipitants (non-solvents) are used, the concentration of precipitant may be controlled satisfactorily. However, water in the form of an impurity or produced by condensation may be present and usually acts as a powerful precipitant.

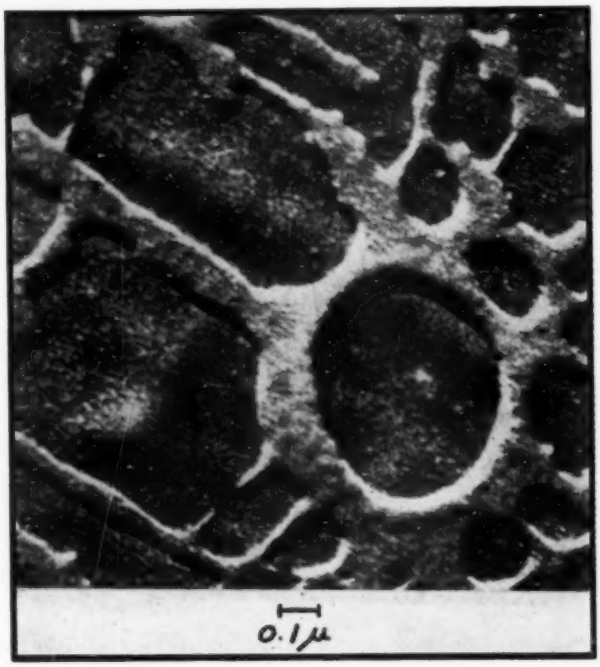

FIG. 7. Polystyrene dispersed with ethylene glycol. Glass mounting surface. Galactose stripping layer. Al-Be substrate. Pt-Pd shadow.

Provided the solution wets the substrate, a film applicator[7] may be used to control the thickness of the deposited solution. Precipitants containing two or more polar groups per molecule will usually wet the surface. Unfortunately, most solutions will not wet the surface

[7] Bird and Son, Inc., East Walpole, Massachusetts.

and must be spread continuously over a definite area until evaporation is complete.

The influence of the nature of the precipitant on a solution is illustrated in Figs. 6 and 7 showing a commercial injection grade polystyrene 0.1 percent in tetrahydrofuran solvent. In Fig. 6 the polymer was precipitated with 2-methyl-1,3-pentanediol. The molecules aggregate in very smooth-surfaced spheres. Figure 7 illustrates the behavior of the same polystyrene precipitated with ethylene glycol. The general appearance of the aggregates is entirely different and the surface structure suggests the possibility of partial isolation of molecular fragments.

Figure 8 illustrates the possibility of isolating and observing individual molecules. This micrograph was taken of polymethyl methacrylate (cast) precipitated from solution at a concentration of two parts per million

FIG. 8. Polymethyl methacrylate. Glass mounting surface. Sodium octyl phosphate stripping layer. Al-Be substrate. Pt-Pd shadow. 0.0002 percent polymethyl methacrylate in tetrahydrofuran solvent containing 0.5 percent 2-methyl-1,3-pentanediol.

in tetrahydrofuran solvent with 0.5 percent of 2-methyl-1,3-pentanediol as precipitant. Calculations based on the viscosity of a solution of this polymer indicate a molecular weight in the neighborhood of three million. If the equivalent density of these precipitated molecules were determined, the molecular weight could be calculated from the electron micrographs. Some studies of this approach to molecular weight determinations have already been made.[8,9]

[8] B. M. Siegel, D. H. Johnson, and H. F. Mark, paper presented to the Electron Microscope Society of America, Toronto, September, 1948.

[9] R. F. Boyer and R. D. Heidenrech, J. App. Phys. **16**, 621 (1945).

With the proper adjustment of concentration it is possible to deposit a continuous polymer film one molecule thick. Figure 9 was taken of such a preparation of cellulose acetate (0.1 percent) in acetone containing 2.5 percent water. With this concentration of water the attractions between molecules are weak resulting in a more or less continuous film in which it is believed the individual molecules can be discerned. Similar preparations of cellulose acetate films from solutions containing considerably less water do not show appreciable detail which could be attributable to individual molecules and the molecules appear tightly interlaced. The preparation illustrated in Fig. 9 was made using a silica substrate and illustrates an effect frequently observed with silica and less often with metallic substrates, namely, the poor adhesion between sample and substrate. In this figure a break in the substrate has pulled the sample loose from the substrate and along with it all of the shadow layer. This places the shadowed sample in the optimum position for studying the molecular outlines.

REPLICA PREPARATION

If the technique described above is altered slightly, it is possible to prepare surface replicas with considerable ease. If the surface is relatively smooth, the replicas may be prepared in exactly the same manner as described above with the exception that the vacuum need not be broken between the deposition of substrate and shadow layer. Somewhat improved results will be obtained, however, if both a substrate and support layer are used. In this case the substrate layer should be only

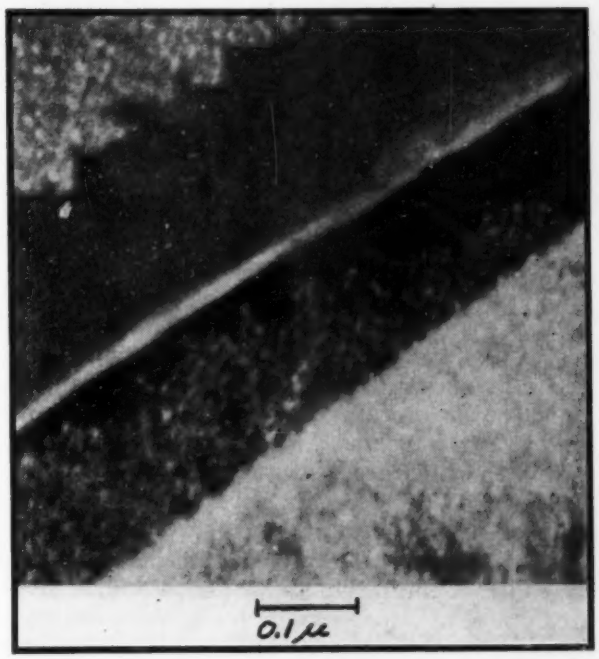

FIG. 9. Cellulose acetate from acetone containing 2.5 percent water. Silica substrate. Galactose stripping layer. Platinum-palladium shadow.

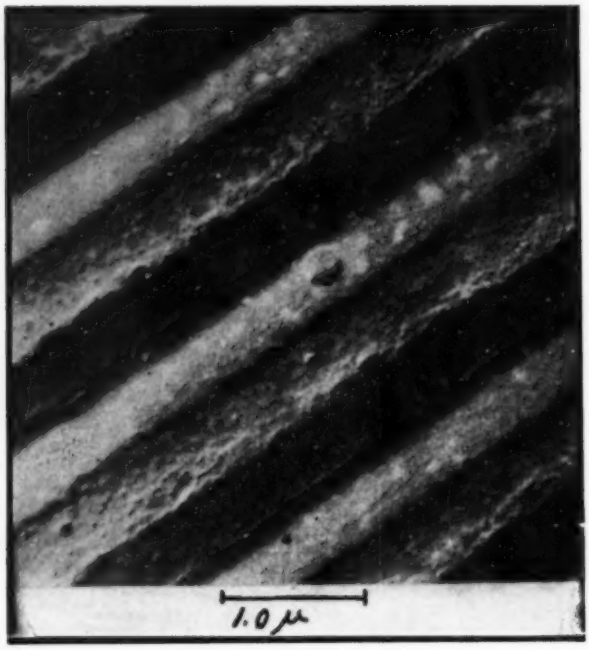

FIG. 10. Replica of 15,000 line per inch metal grating. Sodium capryl phosphate stripping layer. Al-Be substrate. Pt-Pd shadow.

10–20A thick, the main strength of the film residing in the support or backing layer. By proceeding in this manner the shadow layer is deposited on a metal substrate, but the substrate is so thin as not to mask appreciably the fine detail of the surface. Frequently when the shadow layer is deposited directly on the stripping layer and sometimes on the sample surface, it will show signs of aggregating.

Figure 10 illustrates such a replica of a 15,000 line per inch metal grating.[10] There is good reason to believe that replicas of this type are superior to polymer replicas in respect to dimensional distortions produced in the stripping operation and the heat of the electron beam.

If the surface under investigation is very rough, it may be impossible to strip the replica from the surface irrespective of the nature of the stripping layer. Such replicas can be mounted if the underlying surface can be dissolved in a solvent which does not attack the replica. Under such conditions it is usually necessary to deposit a thicker than normal support layer to withstand the abuse of dissolving the underlying material. In this manner replicas of the broken surface of plastics have been obtained showing severe roughness.

Perhaps one of the most novel uses of the replica technique is associated with the study of polymer fibers. It is possible to prepare good replicas of individual fibers by either of the replica techniques described above, although some superiority of resolution seems to be obtained by eliminating the stripping layer. Figure 11 shows a replica of a 4-denier cellulose acetate fiber. Only a portion of the fiber is visible. No stripping layer was used, the replica being separated from the fiber by placing the coated fiber directly on the 200-mesh screen which is mounted on a piece of filter paper. Observing the operations under a binocular microscope approximately one milliliter of acetone is allowed to flow slowly onto the screen and fiber from an eyedropper. The acetone containing dissolved cellulose acetate flows rapidly away into the filter paper thus effecting a rapid and convenient separation of replica from fiber. The replica is left in immediate position for mounting in the microscope.

[10] Baird Associates, Cambridge, Massachusetts.

SUMMARY

A method of specimen preparation especially suited to studying polymeric molecules and aggregates has been presented. With slight modification the method is applicable to the preparation of surface replicas where heat, pressure or solvent action must be minimized.

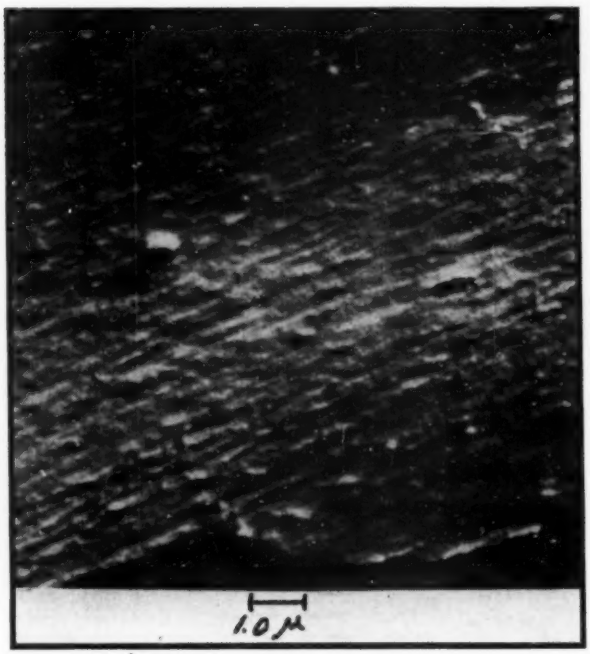

FIG. 11. Replica of 4-denier cellulose acetate fiber. Al-Be substrate. Pt-Pd shadow. Al-Be support layer.

The method owes its merits largely to the aluminum-beryllium substrate which has certain advantages over other substrates because of the following properties:

(a) Low density.
(b) High strength.
(c) Good electrical conductivity.
(d) Insolubility in nearly all solvents.
(e) Little fine structure attributable to substrate.
(f) Very little motion in the electron beam.
(g) Good adhesion of shadow layer to substrate.
(h) Quick replica preparation.

Method for the Quantitative Evaluation of X-Ray Patterns from Mixed Powders

J. C. M. Brentano
Northwestern University, Evanston, Illinois
(Received June 29, 1948; revised June 21, 1949)

The quantitative evaluation of the constituents of mixtures from x-ray powder diffraction patterns has been highly successful in certain cases, but has been found subjected to limitations as an analytical tool of more general use. These arise from a number of effects which interfere with a simple interpretation of the patterns. The paper discusses the basic aspects of these interferences, in particular of those which result from superpositions of lines, and develops a method which takes account of them. The method is adapted to meet such cases where the constituents or impurities which interfere with the regular patterns are unknown.

I. INTRODUCTION

THE qualitative determination of chemical constituents and morphological phases of a mixture from their characteristic x-ray powder diffraction patterns has acquired a definite place among analytical methods. While often inferior in speed and in sensitivity to chemical analysis, the x-ray method indicates directly the constituents present in their particular morphological and crystallographic state; it can be used to distinguish between constituents which are difficult to separate and identify when simultaneously present in a mixture. Through the work of Hanawalt, Frevel, Davey, and others,[1] the qualitative side of this procedure has been developed into the identification method supported by a card index and a reference system for identifying characteristic line patterns of a powder mix. The quantitative determination of the relative amounts of the constituents of a mixed sample from the intensities of the x-ray diffraction patterns is less well established and various workers who made such evaluations report accuracies which are greatly at variance.[2] In the present paper it is proposed to discuss some general aspects which apply to such quantitative measurements and to outline a method which takes account of them.

A distinction should be drawn in the first place between repeated measurements of the same mixes or evaluations of mixes containing different amounts of the same constituents, when particle sizes and microcrystalline subdivision of the powder are the same and line contour, extinction, differential absorption and interferences by superpositions are either the same or vary in a simple way, on the one hand, and, on the other hand, determinations of the relative amounts of constituents in samples from different sources for which particle sizes and microcrystalline constitution differ. While it is comparatively easy to obtain a high degree of accuracy in the first case, which is essentially a test for the measuring device as such, this accuracy is of little significance with regard to the case of more general interest of evaluating mixtures of different origin or which have undergone different ways of processing, when the particle sizes and microcrystalline subdivision vary and added constituents may be present in one sample which are absent in another. The requirements of the more general case are to be considered here.

II. EXPERIMENTAL CONDITIONS

The arrangements for the measurements to which our discussion refers are indicated in Fig. 1. A monochromatic x-ray beam collimated by a slit system A is incident on the microcrystalline material in C in the shape of a rod (a) or of a flat or concave layer (b) and (c). The rod or layer is, in general, rotated and the geometry of the instrument for the rod is such that it is "bathed" at all times in an x-ray beam of uniform specific intensity; for the layer, the geometry is such that it is sufficiently extended to receive the full width of the incident x-ray beam for all angular positions taken in the course of its oscillation. There is no preferential orientation of the crystallites; this can be secured by rotating the specimen or by a suitable way of packing it.

With a counter or ionization chamber (Fig. 1(c)) the diffraction pattern is observed by scanning, when the entrance slit of the counter or ionization chamber is moved with uniform angular velocity along circle B of radius b, while the powder is steadily rotated so as to satisfy a parafocusing condition for each angular setting of the slit. For photographic recording the film is placed in B and for the flat or concave layer (Fig. 1(b)), this is rotated about a vertical axis. Conjointly with the oscillation of the layer, a screen D with a finite opening δ is rotated at uniform velocity in front of B. The parafocusing condition[3] is then satisfied for the center of the

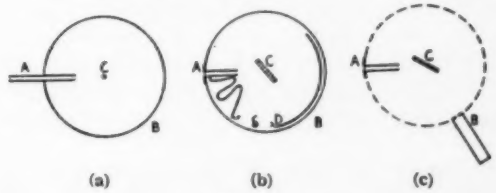

FIG. 1.

[1] An informative account of this method has been given by L. K. Frevel, Ind. Eng. Chem. Anal. Ed. **16**, 209 (1944), where earlier references can be found.

[2] G. L. Clark and D. H. Reynolds, Ind. Eng. Chem. Anal. Ed. **8**, 36 (1936). Grass and Martin, Ind. Eng. Chem. Anal. Ed. **16**, 95 (1944). S. Brosky, P.T.L. News 12 (1945). J. W. Ballard and H. H. Schrenk, U. S. Bureau of Mines Research J. 3888 (1946). Klug, Alexander, and Kummer, Anal. Chem. **20**, 607 (1948), J. Ind. Hygiene and Toxicology **30**, 166 (1948). G. S. Smith and R. L. Barrett, J. App. Phys. **18**, 177 (1947).

[3] J. C. M. Brentano, J. App. Phys. **17**, 420 (1946).

opening. In this case each point of the film receives the diffracted radiation while the powder layer is rotated through an angular range.

III. THE SCATTERED INTENSITY FROM A SMALL VOLUME ELEMENT OF AN "IDEALLY IMPERFECT" MICROCRYSTALLINE POWDER

The scattered intensity for the phase-related diffraction of monochromatic radiation of wave-length λ for a specific "reflection" i from a volume element dV so small as to produce no appreciable absorption is given by an expression of the type[4]

$$dP_{bi}=IQ_iG_i dV, \tag{1}$$

in which dP_{bi} is the diffracted intensity for the reflection i measured at the distance b from the powder, I is the specific intensity of the incident beam, Q_i expresses the scattering power of the particular set of lattice planes i. The classical value of Q_i is

$$Q_i=\frac{\epsilon^4}{m^2c^4}F_i^2N^2\frac{\lambda^3}{\sin 2\theta}\frac{1+\cos^2 2\theta}{2},$$

in which F_i and N are the scattering factor per unit cell for the particular reflection and the number of unit cells per unit volume. This expression and also expression (1) assume that the microcrystalline domains are so small that no appreciable extinction arises.

G_i takes account of the multiplicity factor p_i, i.e., the probability for the particular reflection i to take place as given by the number of times the set of lattice planes i occurs on the crystal form. It further takes account of the instrumental conditions. When measuring the integrated intensity P_b of a reflection for which the diffraction angle is 2θ by scanning across the full width of the line, as recorded on a photographic film placed at a distance b, G_i comprises a term $1/8\pi b\sin\theta$; when using an ionization chamber or counter, it comprises a further term which takes account of the height of the entrance slit.

Substituting $dm=\rho dV$, where ρ is the density,

$$dP_{bi}=IQ_iG_i dm/\rho.$$

For the ratio of two reflections i and j from two constituents A and B forming a powder mix,[5]

$$dP_{Ai}/dP_{Bj}=\frac{Q_{Ai}G_{Ai}\rho_B dm_A}{Q_{Bj}G_{Bj}\rho_A dm_B}. \tag{2}$$

It will be noted that the densities ρ_A and ρ_B are not the densities of the constituents A and B in the powder mix, but the densities for volumes fully occupied by A or B; they can thus be considered as constants characteristic of the particular constituents.

Expression

$$(P_{Ai}/P_{Bj})_1=\frac{Q_{Ai}G_{Ai}\rho_B}{Q_{Bj}G_{Aj}\rho_A} \tag{3}$$

is the *unit mass-ratio* term, which establishes the relative intensities of the reflections i and j for the constituents A and B, respectively, diffracted at the glancing angles θ_{Ai} and θ_{Bj} for the particular wave-length, when the mass ratio is unity.

If the experimental conditions are such that expression (2) can be applied to measurements with finite quantities of powder, the unit mass-ratio term $(P_{Ai}/P_{Bj})_1$ can be determined experimentally. Any unknown mass ratio m_A/m_B is then determined from

$$m_A/m_B=(P_{Ai}/P_{Bj})_{m_A/m_B}/(P_{Ai}/P_{Bj})_1. \tag{4}$$

Expression (4) also establishes the way for determining the unit mass-ratio term from measurements made with a mixture of the constituents in any known mass ratio. The unit mass-ratio term is characteristic for the particular reflections i and j of the constituents A and B. It is independent of the particular physical conditions of the material so long as the conditions set out at the beginning of this section are satisfied and so long as no preferential orientation occurs.

The expressions (1) and (2) are functions of the wave-length. Insofar as the Q terms depend on the wave-length explicitly, this dependency cancels out in arriving at P_A/P_B. These expressions contain, however, also trigonometric terms of θ, which on the ground of the Bragg relation $\sin\theta=n\lambda/2d$, change with wave-length. Q is further a function of the atomic structure factors of the chemical elements entering in each constituent and while these are in a general way a function of $\sin\theta/\lambda$, and thus for a given reflection independent of the wave-length, sudden changes of the atomic structure factor by 1.3 for the K edge and by approximately 5.6 for the L edges occur when the wave-length changes from values greater than the K or L absorption edges to values which are smaller. These changes can in some instances produce quite considerable variations of the P_A/P_B values. Unit mass-ratio terms, determined for one wave-length, can thus not readily be applied to measurements done with a different wave-length.

IV. ABSORPTION

The actual powder specimens do, in general, not conform with the condition of negligible absorption; larger specimens are used not only for intensity reasons, but also because the angle of response of the individual set of lattice planes within which it contributes to the diffracted intensity is very small. Assuming an angle of response of 10″ of arc, which in order of magnitude applies to well-developed crystallites and medium atomic numbers, the chance probability for a set of lattice planes to

[4] C. G. Darwin, Phil. Mag. **27**, 325, 675 (1914) and **44**, 443 (1926). Bragg, Darwin, and James, Phil Mag. **1**, 897 (1926). P. Ewald, Ann. d. Physik **54**, 519, 577 (1917); *Handbuch der Physik* (1933), Vol. 23 (2). J. A. Prins, Zeits. f. Physik **63**. 477 (1930).

[5] J. C. M. Brentano, Phil. Mag. **6**, 178 (1928).

be in a reflecting position with respect to a parallel incident beam and a beam diffracted in a definite direction or to a definite point, is 6.6×10^{-6}. Even when the multiplicity factor p is high, the powder must be very finely subdivided and comprise a very large number of crystalline domains in order to avoid that the contributions from the individual crystallites produce spottiness.

The number of crystallites contributing to each reflection can be somewhat increased by suitable geometrical conditions, in particular by using slits and wide beams instead of pinholes, but more effectively by rotating the powder and by increasing its volume. Rotation of the powder rod is used in the Debye camera. With the flat powder disk in the arrangement proposed by the writer,[6] each point on B (Fig. 1 (b)) receives the diffracted radiation for a range of angular settings of the powder determined by the aperture δ of the rotating diaphragm and the ratio of angular velocities of diaphragm and powder. The usual apertures are 40° to 60°. The powder volume is increased by displacing the Debye powder rod axially (Barrett) and for the flat layer by utilizing an off-center area of an extending rotating disk, so that a large area of the powder surface contributes to the reflection.[3]

With the counter used in the so-called spectrometer arrangement (Fig. 1 (c)), one definite orientation of the powder layer is associated with each setting of the powder so that the number of domains participating in each reflection is small. Alexander, Klug, and Kummer[7] have discussed the statistical intensity fluctuations resulting from the limited number of domains for this instrument; it is particularly suited for such a study in view of the large fluctuation associated with the small number of domains participating in each reflection.

With a powder rod absorption modifies the relative intensities of reflections occurring at different angles in a way which is a function of the angle which varies with shape and absorption coefficient of the rod. When these data are known, allowance can be made for absorption, and methods for doing this have been proposed by Claassen, Rusterholz, Warren, Wilchinsky, and others.[8] The effect of absorption can be reduced by using more penetrating radiation. Molybdenum $K\alpha$-radiation has been recommended in conjunction with the identification card index.

The writer has discussed the geometry of the flat and curved powder layer in relation to the design of a goniometer[3, 5, 6] and has shown that for a layer, which is sufficiently thick to fully absorb the incident beam, the absorption term for the diffracted intensities is the same for all angles so long as a parafocusing condition is satisfied, which is the condition for obtaining sharp lines for an incident beam of finite angular aperture. Relative intensities are then independent of the absorption coefficient and the same as those for a small powder volume of negligible absorption. The actual powder volumes used can be very large, larger than with the Debye rod. With this method the absorption coefficient of the powder does therefore not need to be known and experimental unit mass-ratio terms can be established which are applicable to powder mixes of varied absorption characteristics. For angular settings which deviate from the parafocusing condition the absorption term varies with the setting, but in such a way that relative intensities are a function of the setting only.[9] Conditions can thus be established for which the results obtained with different materials are readily comparable.

V. PRIMARY EXTINCTION

Relation (1) applies to an aggregate of "ideally imperfect" crystals, an established expression for indicating that the microcrystalline domains comprise a sufficient number of regularly spaced lattice planes to give well-defined reflections, while they are, on the other hand, sufficiently small not to give rise to appreciable extinction. The diffracted intensities are then proportionate to the volumes occupied.

For large domains primary extinction, i.e., the weakening of the reflected intensity due to the interference between the incident and diffracted wave systems for a crystallite set in a diffracting position, reduces the diffracted intensities. This effect increases with the size of the domains.[10]

An approximative expression for estimating the relative intensity reduction due to primary extinction given by Darwin is $(\tanh qn/qn)^2$, where q is the scattering power per lattice plane and n is the number of regularly spaced planes of a domain giving phase-related coherent scattering. Introducing numerical values it is seen that for lattices composed of heavy atoms extinction becomes noticeable when n exceeds 100, for light atoms or atoms of medium atomic weight, when it exceeds 1000.

Account must be taken of primary extinction whenever comparing samples comprising crystallites with large well-developed crystalline domains, when the unit ratio term established for one sample may not apply to a sample with constituents having a different degree of extinction. It should be noted that extinction is much more pronounced for the strong reflections at small angles for which Q is large, than for weak reflections, occurring in general at large angles, for which it is small, so that by comparing the relative intensities of lines at small and large angles an indication can be obtained whether extinction differs in the two samples.

Indication for the absence of extinction can also be

[6] J. C. M. Brentano, Proc. Phys. Soc. **37**, 184 (1925) and **49**, 61 (1937).

[7] Alexander, Klug, and Kummer, ASXRED Summer Meeting (1947), J. App. Phys. **19**, 742 (1948).

[8] A. Claassen, Phil. Mag. (7) **9**, 57 (1930). A. Rusterholz, Helv. Phys. Acta. **4**, 68 (1931). B. E. Warren, J. App. Phys. **16**, 614 (1945). Z. W. Wilchinsky, J. App. Phys. **28**, 260 (1947).

[9] J. C. M. Brentano, Proc. Phys. Soc. **47**, 932 (1935).

[10] C. G. Darwin, Phil. Mag. **43**, 800 (1922). Bragg, Darwin, and James, Phil. Mag. **1**, 897 (1926). For more references see A. H. Compton and S. K. Allison, *X-Rays in Theory and Experiment* (D. Van Nostrand Company, Inc., New York, 1935).

TABLE I.

$\mu B/\mu A$ \ $1-e^{-\mu Bz}$	0.005	0.1	0.2	0.3	0.4	0.5	0.7	0.9
1.5	1.019	1.034	1.072	1.113	1.158	1.208	1.318	1.442
2	1.022	1.052	1.111	1.178	1.249	1.334	1.540	1.818
4	1.047	1.078	1.170	1.281	1.410	1.560	2.405	2.760
10	1.058	1.103	1.223	1.350	1.520	1.727	2.850	3.725

obtained from the broadening of the lines. When the lines are distinctly broadened, without showing a narrow central peak, indicating that the crystalline domains are generally small and not of the type referred to further on as "vanishing size distribution," it can be expected that extinction will be small.

In a general way large extinction is encountered with particles obtained by distillation or precipitation while it is small for particles obtained by reduction or oxidation, or, in general, by such processes which lead to the breaking up of a lattice and its replacement by another lattice, when no opportunity is given for the crystallites to grow. Little can be done to eliminate extinction by mechanical grinding. Intensity measurements for the quantitative evaluation of the constituents are then best done in a range of large angles.

VI. DIFFERENTIAL ABSORPTION

Apart from the effect of absorption in the powder layer as a whole, there is an absorption effect peculiar to a mixed powder, which arises when the powder particles are so large that the absorption in the individual particle becomes appreciable. We called this effect differential absorption because it affects the relative line intensities only then when the particle absorptions for the constituents differ. Glocker and Schaefer[11] have described and fully discussed this effect in relation to the Debye-Scherrer rod. The writer has discussed it in connection with the use of the flat powder layer.[9] More recently it has been discussed again by Taylor, Brindley, de Wolff, and Fitzwilliams.[12]

We see the origin of this effect if we consider that whenever there is appreciable absorption, the contribution from those parts of the powder volume which are so placed that the incident and the diffracted x-ray beams suffer appreciable absorption, is reduced in comparison with the contribution from those parts for which the absorption is small. As long as this reduction affects equally the reflections from each constituent, i.e., as long as the probability of a certain absorption loss is the same for, say, two constituents A and B, the relative intensities of the A and B reflections will not be affected and the effective ratio of the volumes which contribute to the diffracted intensities will be the same as the ratio of the volumes occupied in the powder mix. When, however, the absorption in the individual particle is appreciable, then the very fact that the diffraction takes place from a particle with greater absorption affects its intensity so that on the average the absorption reduces more the intensities of reflections from that constituent for which particle absorption is greater.

It is futile to establish quantitative expressions for this effect in a form in which they can be compared with experimental results since the magnitude of differential absorption depends not only on the absorption coefficients, but also on the distribution of particle sizes and shapes.

Table I from the earlier paper by the writer gives data for estimating the magnitude of differential absorption for a flat layer on the assumption that the layer is composed of blocks of two constituents A and B and that z is the length of the path of the x-ray beam in each block. The intensity of the beam after passing through one particle is then reduced to $Ie^{-\mu z}$, where I is the intensity and μ is the absorption coefficient. Assuming that particle absorption is significant for the constituent B, then the values in the table give the correction factor R in terms of the ratio of the absorption coefficients $\mu B/\mu A$ and of the particle absorption $1-e^{-\mu Bz}$ for the constituent for which this is large. R is the relative error introduced by differential absorption or the correction factor with which the measured B reflections should be multiplied.

As indicated, Table I cannot be used for correcting

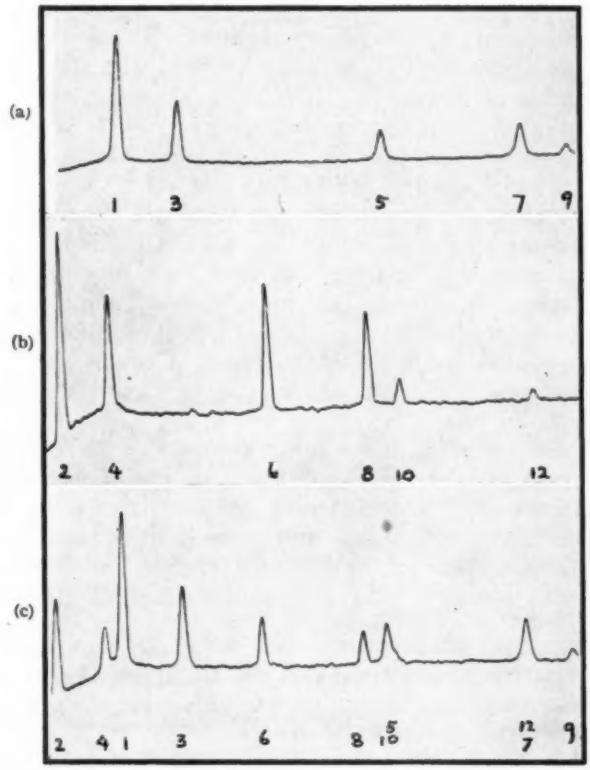

FIG. 2.

[11] K. Schaefer, Zeits. f. Physik 86, 738 (1933). R. Glocker and K. Schaefer, Zeits. f. Physik 73, 289 (1933).

[12] A. Taylor, Phil. Mag. 35, 632 (1944). J. W. Brindley, Phil. Mag. 36, 347 (1945). P. M. de Wolff, Physica 13, 62 (1947). J. W. Fitzwilliams, ASXRED Summer Meeting (1947).

TABLE II.

	Ni P_{bi}	Ni S_i	7E P_{bi}	7E T_i
1	2.04	48.8	3.20	1.56
3	1.00	100	1.57	1.57
5	0.48	208	0.78	1.62
7	0.52	192	0.85	1.63
9	0.18	555	0.25	1.49
	Cu_2O			
2	1.69	59.2	1.75	1.03
4	0.87	115	0.82	0.96
6	1.00	100	1.00	1.00
8	0.70	143	0.68	0.97
10	0.195	513	0.78	4.0
12	0.085	1180	0.85	10.0

TABLE III.

	6D P_{bi}	6D T_i
1	1.14	0.56
3	0.575	0.575
5	0.54	1.12
7	0.35	0.67
9	0.10	0.56
2	1.75	1.04
4	0.87	0.99
6	1.00	1.00
8	0.73	1.04
10	0.54	2.76
12	0.35	4.13

actually observed values; it has the significance of giving an outside estimation of the possible errors which arise when adequate subdivision is not fulfilled.

It will be seen from Table I that so long as the absorption in the individual particle is small or the absorption coefficient nearly the same for the particles of each constituent, the effect of differential absorption can be neglected. It becomes significant when the absorption coefficients for the particles of the two constituents are widely different and absorption in the individual particle is appreciable. Particles which are so large that they give rise to marked differential absorption will, if constituted of single microcrystals, in general show large extinction and be unsuitable for quantitative measurements. The limiting factor is then extinction. For aggregates of small domains it is differential absorption. One occasion for large differential absorption arises when a standardizing substance is introduced to a powder mix without proper dispersion; the presence of large agglomerates may then give rise to serious errors. This can be avoided by adequate mixing. It is also advisable to use standardizing substances with absorption coefficients which do not differ too much from the absorption coefficients of the constituents with which they are mixed. We found it useful to use admixtures of brittle substances like fine silica powder, which have the effect of breaking down such agglomerates. Differential absorption is small for such specimens which by the process of their formation constitute an intimate mixture.

A ready check on the presence of differential absorption is obtained by comparing the relative intensities of the reflections for the various constituents for different wave-lengths since it decreases rapidly for shorter wave-lengths when particle absorption falls off.

VII. THE METHOD OF LINE SELECTION

The evaluation of the mass ratio of two constituents outlined in Section III, expression (4), can in principle be based on the comparison of any two strong lines chosen from the patterns of two substances A and B. This fails, however, to take advantage of the full number of data supplied by the line patterns and is further exposed to the danger that the lines chosen may be affected by superpositions. Such superpositions arise when lines of one constituent are placed at nearly the same angles as lines or background discontinuities of another. Background discontinuities result from heat motion as shown by the theory of Waller and Zachariasen. Baxter and the writer[13] have discussed further background steps which arise when the radiation used is not strictly monochromatic. These are due to the fact that each lattice spacing of the crystal powder acts like the diffracting spacing in a single crystal spectrometer and throws out a spectrum in which absorption steps and eventual characteristic radiations, which are not fully filtered out, occur at various angles. The background is in this way riddled with discontinuities which may alter the measured line intensities by two percent or more. Much larger intensity changes are produced when diffraction lines from one line pattern superpose with lines of the other.

In earlier work, in which we were interested in developing the mixed powder method for obtaining relative F values, we proposed to make use of selected lines only. The method of selection then proposed was based on a detailed survey of calculated line patterns and background steps. This procedure is not practicable in the case of mixtures of varying constituents, which sometimes are unknown or which are present in the form of accidental impurities.

A criterion for line selection which utilizes all lines which are free of superpositions can be obtained by considering that whenever a group of lines characteristic of a certain constituent appears in a mixed pattern, the relative line intensities of the group, so far as they are not affected by background irregularities or by other superpositions, should always be the same and should be the same as the relative intensities of the lines recorded from a specimen containing that particular constituent only. This should hold good so long as the line patterns are obtained for the same wave-length and under conditions in which the relative intensities are not affected by absorption or by extinction. Whenever the intensity

[13] A. Baxter and J. C. M. Brentano, Phil. Mag. (7) 24, 473 (1937).

of a line is affected by superpositions or by a background discontinuity, the relative intensity of the particular line will be altered.

To carry out this selection method a pattern is obtained for each separate constituent using a flat or curved powder layer conforming with the conditions discussed in Sections II and IV, when the relative line intensities are the same as are obtained for a powder specimen with negligible absorption. Such a pattern could also be obtained with a Debye camera when absorption is made negligible by using short wave radiation or by applying appropriate corrections. The relative integrated intensities are evaluated and the reciprocals of these intensities in terms of an arbitrary scale are noted for each line. We call these numbers *reciprocal intensity factors*; they are established for samples containing one constituent only. It will then be seen that whenever the group of lines of that constituent appears in a mixed pattern the products of the integrated line intensities and the corresponding reciprocal intensity factors will have the same value for all lines so far as they are free from interferences. These products plotted against deflection angles should be at constant height while for the reflections which have been affected by superpositions they will be at different heights. The common height for the lines which are free from superpositions when some normalizing procedure has been applied, i.e., when the lines are expressed in terms of a common reference standard, sets then a measure for the intensity of reflection for the particular constituent in the mixture and establishes what we may designate as a P^* value, which now is not associated with one particular reflection but becomes a measure for the intensity of reflection of the constituent in the specific mixture. $(P_A^*/P_B^*)_{m_A/m_B}$ values can thus be established and can be interpreted in terms of a $(P_A^*/P_B^*)_1$ unit mass-ratio term provided they are expressed in terms of the same common reference standard. These can be used to evaluate the relative amounts of two constituents A and B in the same way as the P_{Ai}/P_{Bj} values established for particular reflections.

To illustrate the method by an example, Fig. 2(a) and (b) show the microdensitometer tracings of part of the line patterns of powders of nickel and cuprous oxide, both taken with Cu$K\alpha$-radiation and recorded with a microdensitometer using a converter,[14] so that the tracing heights are directly proportionate to x-ray intensities. Figure 2(c) gives the tracing for a mixed sample (Mix 7E).

Table II shows the way the selection method is applied to the lines of a mixture. The first column identifies the various reflections by reference numbers. The second column gives the integrated line intensities P_b for the patterns taken with the samples of Ni and Cu_2O only, plotted in arbitrary units. The third column gives the reciprocal intensity factors S_i from the preceding column. Such data are prepared in a general way for each constituent which is to be evaluated.

The next two columns refer to a particular mixture (7E). Column four gives the measured P_{bi} values for the lines of the mixture and column five under T_i the products of these P_{bi} values and the corresponding S_i values of column three. The intensities are expressed in terms of line 6 of cuprous oxide. Any other line could act as reference standard provided both the nickel and cuprous oxide lines are expressed in terms of the same standard. Considering the nickel reflections it will be seen that the T_i values are nearly equal except for the reflections 5 and 7. These two reflections will thus be eliminated in the quantitative evaluation of mass ratios. A glance at the tracing for pure cuprous oxide, Fig. 2(b), will show that the lines 5 and 7 of nickel superpose with the lines 10 and 12 of cuprous oxide; for the lines 5 and 10 the interference can be noticed from the contour of the lines; for the lines 7 and 12 the superposition is so close that the line contour would not have revealed it.

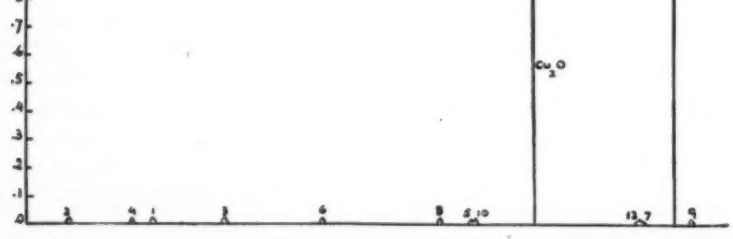

FIG. 3.

[14] J. C. M. Brentano, Phys. Rev. **72**, 166 (1947).

The same criterion applied to the cuprous oxide reflections (lower part of Table II) indicates that the T_i values for the reflections 10 and 12 are at variance with respect to the other lines of the group and that these should be rejected. This was to be expected from the findings for nickel. The table also shows that no other lines are affected.

Figure 3 illustrates the way these data are utilized for carrying out the line selection and establishing a $P_{Ni}^*/P_{Cu_2O}^*$ value by a graphical procedure. In Fig. 3 the T_i values, i.e., the products of the integrated intensities for the lines of the mixed sample multiplied with the reciprocal intensity factors, are plotted against deflection angles. The heights of the horizontal lines P_{Ni}^* and $P_{Cu_2O}^*$ represent the average values of T_i for nickel and cuprous oxide for the mixed powder. They have been drawn disregarding those T_i values which are rejected. The ratio of the P^* values so established is $P_{Ni}^*/P_{Cu_2O}^*=1.563$.

The evaluation of the mass ratio is illustrated by Table III and Fig. 4, which refers to a sample 6D of nickel and cuprous oxide mixed in the proportion of equal masses. The T_i values plotted in Fig. 4 lead to a value $P_{Ni}^*/P_{Cu_2O}^*=0.565$. This is the unit mass-ratio term; applied to the previous sample it gives the mass ratio of nickel and cuprous oxide in sample 7E as 2.77. The actual mass-ratio determined by weighing was 2.82 so that the discrepancy is 1.8 percent. The error of photographic intensity measurements based on the integration over the line width is about 1.5 percent; the accuracy corresponds thus well to the accuracy expected.

The Ni and Cu_2O mixture was chosen as representing a somewhat typical case insofar as the Ni powder was rather coarse, containing large crystallites, while the Cu_2O powder was finely subdivided; recorded on a stationary film it gave distinctly broadened lines. The line patterns are on the other hand rather simple with few superpositions and with only two constituents and it was clear which lines are to be rejected. In the case of very weak lines, for instance due to impurities, it must be decided where the limit of the accidental error should be set in order to determine which lines are to be rejected. This will largely influence the accuracy of the results.

Three kinds of deviations of the individual T_i values as plotted in Figs. 3 and 4 should be considered:

(1) Some deviations are introduced by accidental errors due to the limited accuracy of each integrated intensity measurement. In determining the P^* value an appropriate weight will be given to each point. Weak lines with large reciprocal intensity factors will, in general, be less accurate.

(2) Systematic errors introduced by superpositions are a second cause for deviations. These have already been discussed. Such lines are disregarded in the determination of the P^* value. A survey of the method will indicate the limit of deviation which may be regarded as a systematic deviation of this kind.

(3) A third systematic deviation is shown by a slope of the T_i values for one or for both substances, which, in general, is accentuated or appears only for the first few lines at small angles. This indicates that primary extinction differs for the sample used in preparing the single-constituent pattern and the same constituent in the mixed powder. If, for instance, the T_i values for strong reflections at small angles of constituent A in the mixed sample show a systematic deficiency in height, compared with the values for larger angles, this would indicate that primary extinction for this constituent in the composite sample was greater than for the same constituent in the sample used for preparing the single-constituent pattern from which the reciprocal intensity factors S_i were derived.

Applied to the evaluation of two constituents the method requires the taking of three preliminary patterns: one for each single constituent and one composite

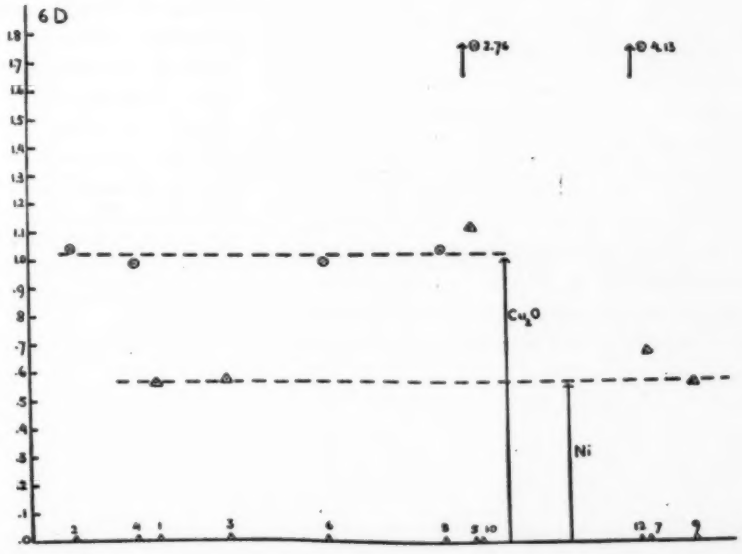

FIG. 4.

pattern for the two constituents mixed in the ratio 1:1 or other known ratio. These reference patterns, once established, will be used for any mixed sample of the two constituents and will, in general, have been made with samples of different origin than those for which the mass ratio is to be determined.

When several constituents are to be evaluated one pattern for each constituent is necessary and one containing the mixture of the constituents in a known ratio. If one common constituent is present in all mixed samples of a group, this can be used as a common reference substance in terms of which the masses of the other constituents are determined on the ground of a composite pattern from a mixed sample which contains all the constituents in known proportions. It is in general, however, more convenient to establish a series of binary mixed powder patterns containing this constituent and one of the others. This avoids overcrowded patterns in which superpositions eliminate a great number of lines which could be used in such cases where some of the constituents are absent.

Alternately a separate reference substance can be added to the mixture; it will then be advantageous to choose a substance which gives good line contours and has an absorption coefficient which does not differ too much from the absorption coefficients of the other constituents so as to eliminate the danger of differential absorption for a powder which is not intimately dispersed. This admixture can then be added in such an amount that its line intensities fall between the extreme intensities of the lines which are to be compared.

VIII. ACCURACY

The accuracy of the method is essentially determined by the accuracy to which integrated intensities of reflections can be evaluated.

This is not expressed by the accuracy to which repeated measurements of the same lines can be reproduced, but by that to which correct integrated intensities of reflections can be obtained for lines with varied intensity distribution or line contour.

This contour is determined by the distribution of the crystalline domains as to size and regularity; the larger and more regular domains giving rise to the narrow peak and the less regular developed crystallites giving rise to the broadened foot. It is because of this varying line contour that integrated intensities cannot be expressed by the product of peak intensity by half-height width or by some other estimation based on the assumption of a definite line shape. A high narrow peak accompanied by an extended low intensity foot is unfavorable since both, counter and photographic methods, lose in accuracy when applied to an extended intensity range. For low intensities the accuracy is affected by statistical fluctuations, while, when recording at a high intensity rate so as to reduce such fluctuations, the high intensity peak falls outside the proportionate response of the counter or photographically leads to such high film densities that photographic materials give an inadequate response. In the example of Section VII this was avoided by projecting the line pattern on a photographic film which was rocked throughout the exposure at a uniform angular velocity.[15] The range of rocking was 30″ of arc, which is less than the total width of the broader lines. The high intensity peak is thus spread out with a corresponding reduction in intensity, while the more extended foot is little affected. This technique broadens the lines and eventually produces superpositions of lines placed in close proximity which otherwise would not arise; it improves, however, the accuracy to which the lines can be measured to a considerable extent. It also reduces the spottiness discussed in Section IV which arises with particles comprising large domains.

By using such techniques it is, in general, possible to obtain good intensity data except for the case which we called "vanishing size distribution," when a substantial part of the crystalline domains is so small or so deformed that the reflections present an extended low density tail or foot. Not only is such a tailing-off foot difficult to evaluate against the background, but also do these broad lines give rise to so many superpositions that it is difficult to obtain any lines free of interferences. Substances of this type are unsuited for quantitative evaluations.

On the other hand, evaluations are greatly simplified when the constituents in all samples and also in the samples used for establishing the unit mass-ratio terms are of the same origin, i.e., all possess the same microcrystalline habitus as to distribution of domain sizes and microcrystalline regularity. In such cases, where the intensity distribution for a line is the same in all samples, the areas subtended by the line contours of corresponding lines are proportionate to the line heights. This dispenses with the necessity of measuring integrated intensities correctly. The counter or the photographic method used in conjunction with a converter which traces heights proportionate to x-ray intensities will then give tracings in which the heights can be interpreted as integrated line intensity values. Attention must then only be given to superpositions by applying the selection method to the peak intensities.

[15] J. C. M. Brentano, J. Opt. Soc. Am. 35, 382 (1945).

The Physical Properties of Titanium. I. Emissivity and Resistivity of the Commercial Metal

WALTER C. MICHELS AND SALLY WILFORD
Bryn Mawr College, Bryn Mawr, Pennsylvania
(Received June 28, 1949)

The resistivity and the total emissivity of commercial titanium have been measured over the temperature range from room temperature to 1400°K. The resistivity at 20°C is 78.6 microhm cm. Above this temperature it increases to a flat maximum of 182 microhm cm at the temperature of the hexagonal-body-centered cubic transformation. The total emissivity is about 0.31 at low temperatures and there is some indication that it shows a maximum near the transition temperature. The spectral emissivity and the brightness temperature scale are also determined over the range of 1000°K–1400°K.

THE recent availability of relatively pure titanium has made possible detailed studies of the properties of this element. The present paper reports measurements of the resistivity and the emissivities of samples supplied by the Remington Arms Company and supposedly typical of their present production. It will be shown later that there is reason to doubt whether the purity of some of these samples is as high as might be desired. Some of the results obtained must therefore be taken as preliminary, but the current interest in the properties of titanium, the fact that they are applicable to commercially available titanium, and the further fact that one of us (S.W.) is leaving this laboratory are reasons for immediate publication.

Measurements of the resistivity of titanium have been reported by several authors.[1–5] There are considerable disagreements among the various data reported and it has been apparent in each study of the material that small amounts of impurities, probably in the form of oxides or nitrides, produce relatively great effects. It is therefore clear that the only meaningful measurements at high temperatures are those taken on material of initially high purity, under good vacuum conditions. Probably the only reported measurements which satisfy these conditions are those of Burgers and his coworkers.[6–7] These authors have demonstrated that pure titanium undergoes a transition from hexagonal to body-centered cubic form at 882±20°C and that its resistivity shows a sharp decrease of about 6 percent as the material passes from the low temperature α- to the high temperature β-modification.

In the present work, the brightness temperature scale was first determined. Since the rolling of thin sheets of titanium offers great difficulties, conduction heating of a conventional wedge or cylinder was impractical. Measurements were therefore made on an induction heated sample of quarter-inch rolled rod, drilled to the cross section shown in Fig. 1. This sample was mounted with its axis vertical in a Pyrex tube connected to an all glass vacuum system. It was inductively coupled to an Ajax 3KW heater which could be adjusted and controlled well enough so that the temperature of the sample as observed with a Leeds and Northrup optical pyrometer remained constant to within ±4°C at a given setting of the furnace. It was possible to maintain a vacuum of 10^{-6} mm or better during most of the runs, and the pressure never exceeded 10^{-5} mm. At least four pairs of pyrometer readings were taken on the "blackbody" hole in the side of the rod and on the titanium surface adjoining this hole at each temperature at which steady conditions were obtained. Individual sets of readings generally showed mean deviations of about ±2° during such a run.

The lower curve of Fig. 1 shows a plot of the difference $(T-S)$ between the blackbody and the titanium brightness temperature at 0.665μ as a function of the Kelvin temperature of the body. The latter is the temperature found for the blackbody hole, after correction for light absorption in the window of the Pyrex tube. The pyrometer was calibrated against a blackbody furnace at the gold point and it is believed that the absolute temperature measurements are good to ±5°. The points shown on this curve represent average values of $T-S$ for four pairs of readings. The upper

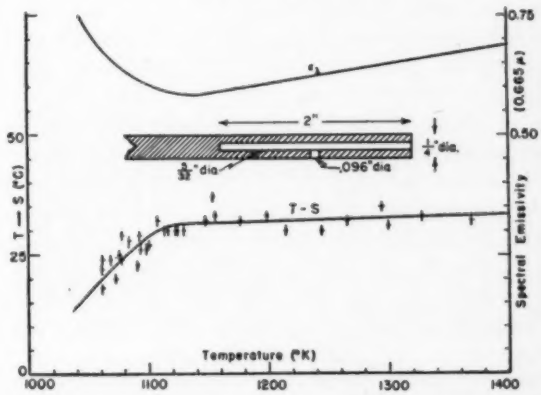

FIG. 1. The brightness temperature scale.

[1] J. Koenigsberger and K. Schilling, Ann. d. Physik **32**, 179 (1910).
[2] P. Clausing and J. Moubis, Physica **7**, 245 (1927).
[3] J. H. de Boer and P. Clausing, Physica **10**, 267 (1930).
[4] Jager, Rosenbohm, and Fonteyne, Rec. Trav. Chim. **55**, 615 (1936).
[5] H. H. Potter, Proc. Phys. Soc. London **53**, 695 (1941).
[6] W. G. Burgers and F. M. Jacobs, Zeits. f. Kristall. (A)**94**, 299 (1936).
[7] de Boer, Burgers, and Fast, Proc. Acad. Amst. **39**, 515 (1936).

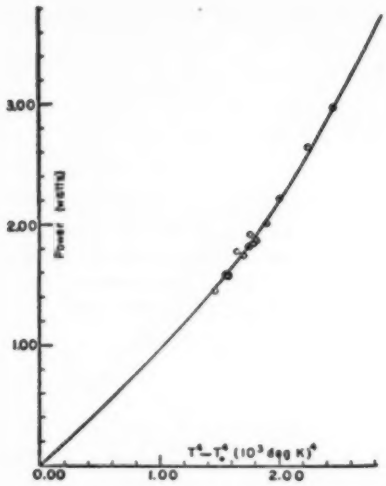

FIG. 2. Determination of the power *vs.* temperature relation.

curve of Fig. 1 shows the spectral emissivity (ϵ_λ) as calculated from the smooth curve of $T-S$. The lower temperature limit of the measurements was determined by the lowest brightness at which adequate pyrometer matches could be made, the upper temperature limit of about 1400°K was set by the increasing vapor pressure of the titanium, which led to appreciable sublimation onto the window of the tube.

The very high value of the spectral emissivity is noteworthy. Such a value might be expected to result from the relatively high resistivity of titanium, but we shall see later that the minimum of the emissivity curve occurs at a temperature at which the observed resistivity of the material is a maximum. The emissivity obtained here is slightly higher than the single value measured by Voogd,[7] who found a value of 40° for $T-S$ at 1155°K. It is also somewhat above the values reported as a result of the measurements of J. Went.[8]

During the course of these measurements, an attempt was made to find whether the spectral emissivity showed a sharp discontinuity at the transition temperature, similar to the discontinuities found by Wahlin and Knop[9] in ferromagnetic materials. Repeated runs in the neighborhood of the transition temperature indicated that such a discontinuity, if it occurs, is smaller than the uncertainties in the present measurement.

Resistivity measurements were made on several samples of 0.0424-cm diameter wire. The wires used were of about 12 cm length and were held taut by a tungsten spiral at one end. Fine platinum or nickel probes were attached so that the potential across a central section of the wire (3–6 cm long) could be measured. The observed brightness of this central section indicated that the temperature over it was constant within ±4°C. The current through the wire was measured by potentiometric determination of the drop across a standard series resistor and the potential drop across the central section was determined with the same potentiometer, a Rubicon Model *B*. Double pairs of readings, with a current reversed between them, were always used to eliminate thermal e.m.f.'s.

During the preliminary outgassing of the apparatus, resistance measurements were made at temperatures between 20°C and 440°C, with the current in the wire so low that it produced negligible heating effects. The furnace temperature was measured by two chromel-alumel thermocouples mounted near the top and bottom of the Pyrex tube containing the wire. These couples indicated temperatures which were constant to ±2°C during the measurements. Measurements were next made with conduction heating of the wires in the temperature range for which the brightness temperature scale had previously been determined. During these measurements, the temperatures were determined by optical pyrometry. Since the wire was initially very dark in color, probably due to oxide layers formed during drawing and annealing, it was necessary that it be heated at temperatures above 1000°C for some time before exact temperature measurements could be taken. Subsequent to this heating the wire showed an appearance quite similar to that of the rod used for the spectral emissivity measurements. Since the first low temperature measurements were made before the heating of the wire to above its transition point while the later high temperature measurements were made after such heating, it was necessary to check for hysteresis effects. In order to do this a temperature-power scale was determined from the high temperature measurements. Figure 2 indicates the way in which this was done. On this figure the power dissipated in the center, constant temperature section of the wire is plotted against the difference of the fourth powers of the wire temperature T and the ambient temperature T_0. Since this plot would yield a straight line were the total emissivity constant and since it is known to pass through the origin, interpolation over the temperature range from room temperature to 1050°K

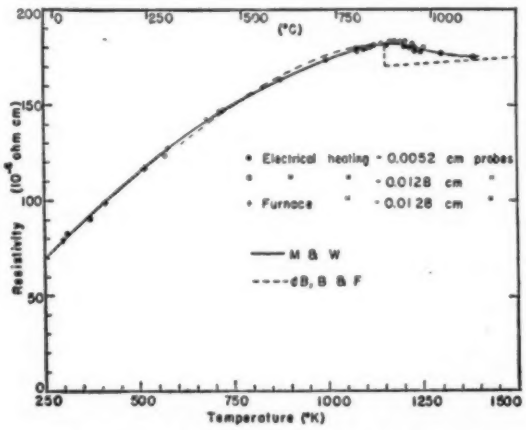

FIG. 3. Resistivity *vs.* temperature for titanium wire.

[8] Campbell, Jaffee, Blocher, Gurland, and Gonser, J. Electrochem. Soc. 93, 271 (1948).

[9] H. B. Wahlin and H. W. Knop, Phys. Rev. 74, 687 (1948).

could be done with considerable accuracy. Measurements made over this range with conduction heating of the wire checked satisfactorily with those made with furnace heating.

Figure 3 shows the resistivities obtained over the series of measurements. The most pronounced feature of this curve is the decrease in resistivity in the temperature range above 1150°K. When this result was first obtained, it was suspected that a true resistance-temperature curve might show a sharp break at the transition point as reported by de Bohr, Burgers, and Fast[7] and that the apparent gradual change might be due to local cooling by the potential probes. To check this, subsequent measurements were made with the distance between probes being changed by a factor of 2 and the diameters of the probe wires being changed by a slightly greater factor. As is shown in the figure, results obtained under these conditions were not significantly different from the initial results. It therefore appears that the gradual change in the resistivity is typical of commercial titanium.

We have been informed by E. L. Wemple of the Remington Arms Company that during the drawing process the wires which we used were annealed several times in air at a temperature of 1200°C and once in a vacuum of about 10^{-3} mm at 1400°C. In view of the high affinity of titanium for oxygen and nitrogen and of the irreversibility of the reaction with nitrogen, it appears probable that appreciable contamination may be present and that the sharp break in resistance at the transition point may be typical of the pure material while the behavior shown here is typical of commercial wire. The paper of de Boer, Burgers, and Fast does not give absolute resistivities, nor does it show absolute temperatures except at the transition point. In order to compare their results with ours, we have assumed their resistivity just below the transition to be equal to the maximum resistivity which we observed. We have also assumed the absolute temperature of their sample over a limited range to be proportional to the fourth root of the power input. The dashed curve in Fig. 3 results from these assumptions. Since it agrees quite well with our measurements below the transition point and since the two sets of measurements are asymptotic at high temperatures, it is evident that the small impurities present in the wire have little effect outside the temperature range 1150°K–1350°K.

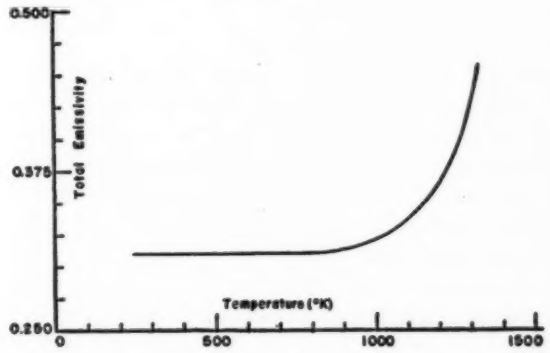

FIG. 4. The total emissivity vs. temperature.

TABLE I. Properties of commercial titanium wire.

Temperature (°K)	Resistivity (microhm cm)	Temperature coefficient of resistivity (10^{-3}/°C)	Brightness temperature.	Spectral emissivity (0.665μ)	Total emissivity	Temperature (°C)
300	79.8	2.18	—	—	0.31	27
400	97.2	1.78	—	—	0.31	127
500	114.5	1.51	—	—	0.31	227
600	130.8	1.13	—	—	0.31	327
700	144.5	0.85	—	—	0.31	427
800	155.7	0.64	—	—	0.31	527
900	165.1	0.52	—	—	0.32	627
1000	173.4	0.44	—	—	0.32	727
1050	177.2	0.41	1033	0.72	0.33	777
1100	180.6	0.34	1072	0.60	0.34	827
1150	182.3	0.03	1118	0.59	0.35	877
1200	181.5	−0.20	1168	0.60	0.37	927
1250	178.8	−0.29	1218	0.63	0.40	977
1300	176.6	−0.20	1268	0.65	0.44	1027
1350	175.3	−0.08	1317	0.67	—	1077
1400	175.0	0.00	1366	0.69	—	1127

The room temperature resistivity agrees quite closely with the earlier determinations of Clausing and his coworkers,[2-3] but is considerably higher than the latest value reported by de Boer and Clausing[3] and that given by Fast.[10] Since the temperature coefficient of resistivity found here is lower than that found for the low resistivity samples by a factor almost equal to the inverse ratio of the resistivities, it seems probable that the difference in our results is due to impurities, and that the results reported here are typical only of the commercial material.

During the course of these measurements the samples were repeatedly heated and cooled, with observations being taken in almost random order. Within the accuracy of the measurements, no hysteresis effects similar to those reported in the literature[1,4] were found. A clue to the reason for the occurrence for such effects is furnished by one accidental observation. During the final readings on one sample a power interruption stopped the action of the mercury diffusion pump and the pressure rose to about 10^{-3} mm with the wire at high temperature. The resistivity at this temperature was not changed but measurements made after cooling yielded resistivities distinctly higher than those found in other samples. The resistivity at room temperature had increased by about 25 percent. Subsequent heating of this sample above the transition point at high vacuum did not restore the original condition.

The same data that were used to determine the temperature scale as a function of power allowed the calculation of the total emissivity ϵ_T of titanium. Since the power dissipated in the central section of the wire is

$$P = 2\pi a L \epsilon_T \sigma (T^4 - T_0^4),$$

[10] J. D. Fast, Zeits. f. Anorg. Allgen. Chemie **241**, 42 (1939).

where a is the radius of the wire, L is the distance between potential probes, and σ is the Stefan-Boltzmann constant, curves similar to that shown in Fig. 2 yield the total emissivity. Figure 4 shows a plot of the observed total emissivity against temperature. The only result in the literature with which our measurement may be compared is that of Carpenter and Reavel[11] who state that the total power dissipated varies as the 4.4 power of the temperature and that the total emissivity is 0.30 at 1700°K. Comparison of the two results indicates a probable maximum in the total emissivity at or near the transition point. It is of some interest to note that the total emissivity is not as high, relative to other metals, as is the spectral emissivity in the red.

A summary of the results obtained in this study is shown in Table I. The resistivities and the total emissivities given are based on the radius and length as measured at room temperature, i.e. they have not been corrected for thermal expansion. Because of the suspected impurities in the wire samples, it is probable that the values of resistivity and total emissivity in the temperature range above 1150°K are not typical of pure titanium. Subject to this qualification, it is estimated that the uncertainty in spectral emissivity measurements is ± 0.02, in the resistivity ± 1 percent, and in the total emissivity is ± 10 percent.

This work has been done as part of a program of solid state studies which is supported in part by a Frederick Gardner Cottrell Grant of the Research Corporation. The authors wish to express their gratitude for this help. Thanks are also due to Mr. C. I. Bradford and Mr. E. L. Wemple of the Remington Arms Company, who supplied the titanium samples and who have been very helpful in making available the experience which their organization has had with titanium.

[11] L. G. Carpenter and F. R. Reavel, Nature **163**, 527 (1949).

Grain Boundary Relaxation and the Mechanism of Embrittlement of Copper by Bismuth*

T'ING-SUI KÊ
Institute for the Study of Metals, The University of Chicago, Chicago, Illinois
(Received July 1, 1949)

The embrittlement of copper by small amounts of bismuth has been known for many years. Voce and Hallowes proposed recently that the agent responsible for embrittlement is bismuth present in the form of thin films at copper grain boundaries. In order to examine this picture from a different angle, internal friction and elastic modulus measurements were made on copper specimens free from and containing bismuth up to 0.01 percent with a frequency of transverse vibration of about 1000 cycles per second from −50°C to 550°C. It has been found that: (1) In the bismuth-bearing copper heat-treated to be brittle, there is no abrupt change in elastic modulus in passing through the melting point of bismuth (271°C). (2) The internal friction peak (around 500°C) associated with the stress relaxation across copper grain boundaries was reduced by the presence of bismuth, indicating that some bismuth did go to the grain boundaries. (3) Each bismuth-bearing specimen gives an internal friction peak around 290°C and the height of this peak varies approximately linearly with the bismuth content. This "bismuth peak" is correlated to the embrittlement of copper. It was subsequently utilized in studying the effect of cold-work, heat treatment and the rate of cooling upon the embrittlement of copper by bismuth. The effect of previous cold-work was found only to speed up the precipitation of bismuth to the grain boundaries the rate of which is very slow at low temperatures.

The data presented above corroborate the proposition that embrittlement of copper is caused by bismuth present at copper grain boundaries. However, it appears that the bismuth is distributed in a highly heterogeneous manner. Across most of the boundaries no appreciable amount of bismuth is precipitated, at least not enough to influence the grain boundary viscosity. It is these grain boundaries which give rise to that internal friction peak characteristic of pure copper. Across a few of the grain boundaries enough bismuth is precipitated to markedly decrease the grain boundary viscosity. Since no discontinuous behavior is observed as the temperature passes through the melting point of pure bismuth, it is concluded that the film of bismuth along these boundaries is not of sufficient thickness as to acquire the properties of crystalline bismuth.

INTRODUCTION

THE embrittlement of copper by a small amount of bismuth has been known for many years. As early as 1929, Blazey[1] has shown that embrittlement is due to the presence of bismuth in copper. Later, he has also described the working and annealing conditions under which this embrittlement occurs.[2] In a discussion of Blazey's paper, Smith[3] has pointed out that the dependence of embrittlement on heat treatment may be understood "if we assume the solubility of bismuth in copper increases with temperature. Annealing above a certain critical temperature for each composition will result in complete solution of bismuth, giving a tough alloy. On the other hand, if the metal is reannealed below the critical temperature, the bismuth will be precipitated, and, since it will most probably be

* This research has been supported by ONR (Contract No. N-6ori-20-IV, NR 019 302).
[1] C. Blazey, J. Inst. Metals **41**, 32 (1929).
[2] C. Blazey, J. Inst. Metals **46**, 353 (1931).
[3] Cyril S. Smith, discussion of reference 1.

formed along the grain boundaries and cleavage planes, it will render the metal brittle."

An extensive study has been recently undertaken by Voce and Hallowes[4] on the elucidation of the mechanism of embrittlement. The effect of bismuth on embrittlement was studied by notched-bar tests at temperature and by notched-bar and reverse-bend tests after quenching from the annealing temperature. Figure 1 shows some typical results obtained by them for deoxidized copper containing 0.01 percent of bismuth. It illustrates how embrittlement is influenced by heat treatment. The ordinates give the foot-pound value at which failure occurs in a notched-bar specimen. A higher foot-pound value indicates a higher ductility. Part (a) shows the cases of copper free from bismuth: curve A, when notched-bar test was made at room temperature after the specimen was quenched from the temperature shown; curve B, when the test was made at the annealing temperature. Part (b) shows the corresponding

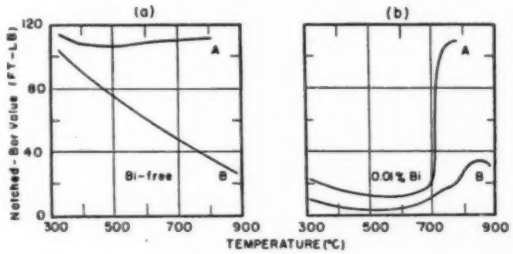

FIG. 1. Effect of heat treatment on the embrittlement of copper by bismuth (after Voce and Hallowes). (a) Copper free from bismuth; (b) copper containing 0.01 percent of bismuth.

A: Test at room temperature on quenched specimens.
B: Test at annealing temperatures.

cases when 0.01 percent of bismuth was added. It is seen that below the temperature 650°C or so the copper containing bismuth is much more brittle than copper free from bismuth for both tests at room and at the annealing temperatures. As a result of their mechanical testings and metallographic examinations Voce and Hallowes suggested that the substance responsible for the embrittlement of copper by bismuth is a thin film of elementary bismuth at the grain boundaries.

It has lately been demonstrated that the internal friction peak (*versus* temperature) associated with the viscous behavior of grain boundaries in metals is very sensitive to mechanical and thermal treatments, and to the presence of impurities at the grain boundaries.[5] Bismuth at the copper grain boundaries, if present, should modify the grain boundary internal friction peak of copper. The purpose of the present research is thus to examine Voce and Hallowes' suggestion concerning the mechanism of embrittlement of copper by bismuth from a different angle by measuring the internal friction of copper specimens containing and free from bismuth.[6]

THE SPECIMENS

The copper specimens free from and containing various amounts of bismuth (0.0026, 0.0050, 0.010 percent) were supplied by British Non-Ferrous Metals Research Association, London, England. They were received in the form of cold-rolled bars with dimensions of 0.4 in.×0.5 in.×8 in. They are identical in mechanical and thermal treatments to those specimens used by Voce and Hallowes in making mechanical tests and metallographical examinations. These specimens were phosphorous-deoxidized under industrial conditions. The residual phosphorus content was approximately 0.04 percent in all cases.

The subsequent annealings on these specimens were also made following the procedures given by Voce and Hallowes. This renders possible the direct comparison of the results of the present measurements with those of Voce and Hallowes.

APPARATUS FOR MEASUREMENT OF INTERNAL FRICTION

The arrangement for making internal friction measurements on these specimens is shown in Fig. 2. A thin iron disk was attached by Insalute cement to each end of the specimen with the plane of the disk facing downward. The specimen was supported horizontally at its nodes of vibration. C_1 and C_2 are two electromagnetic coils made by winding glass-insulated copper wires around Alnico magnets as shown. They were placed immediately beneath the iron disks. Coil C_1 was connected

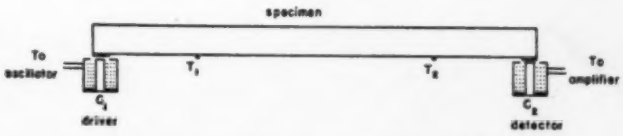

FIG. 2. Arrangement for measuring internal friction of bar specimens in transverse vibration.

to the output of a Hewlett-Packard audio oscillator. The transverse vibration of the specimen was excited by tuning the oscillator to the resonance frequency of the specimen. Fine frequency adjustment was made by means of an auxiliary set of adjustable resistors introduced in the RC circuit of the oscillator. The signal was picked up from the other end of the specimen by coil C_2, and was amplified by a separate audio amplifier. It was then received on the screen of a cathode-ray oscillograph. For measurements of high internal friction, a parallel T network was introduced in the amplifier to reduce noise background.

The frequency of the first mode of transverse vibra-

[4] E. Voce and A. P. C. Hallowes, J. Inst. Metals **73**, 323 (1947).
[5] T. S. Kê, J. App. Phys. **20**, 274 (1949).
[6] A preliminary report of this work has been given before the 291st meeting of the Am. Phys. Soc., March 10, 1949; T. S. Kê, Phys. Rev. **75**, 1626A (1949).

tion of the specimens has been found to be about 1000 cycles per second. The internal friction was measured either by the free decay method by observing the time t required for the amplitude of transverse vibration (which is proportional to the height of signal received on the oscillograph screen) to decay to one nth of its initial value, or by determining the half-width Δf of the amplitude resonance curve. Then the internal friction is given[7] in the former case by

$$Q^{-1}=\ln n/\pi tf,$$

and in the latter by

$$Q^{-1}=\Delta f/3^{\frac{1}{2}}f,$$

where f is the resonance frequency.

In order to measure the temperature of the specimen itself the specimen was supported at T_1 and T_2 with, respectively, very fine alumel and p-chromel wires. The hot junction of this thermocouple is, thus, the specimen itself.

The arrangement shown in Fig. 2 was mounted on a slotted metal plate and the plate was slid into a vacuum furnace with the specimen situated at the constant temperature region of the furnace. The temperature of the furnace was regulated by an electronic temperature controller[8] to within ± 1°C. After the furnace was evacuated by a mechanical pump, 99.8 percent argon was admitted to the furnace after it was purified from oxygen by passing through copper chips heated at 500°C. The flow of purified argon through the furnace was kept at a slightly positive pressure. The arrangement of the whole apparatus is shown in Fig. 3.

For internal friction measurements below room temperature, the arrangement shown in Fig. 2 was mounted in a well-insulated woodbox having a compartment for dry ice. A blower inside the box kept the temperature uniform.

RESULTS AND DISCUSSION

Before measurement, all the specimens were annealed at 550°C in vacuum for ½ hour. After this treatment, the bismuth-bearing copper specimens are brittle according to the criteria given by Voce and Hallowes.

A. Elastic Modulus

In Voce and Hallowes' suggestion that the substance responsible for the embrittlement of copper by bismuth is a film of elementary bismuth at the grain boundaries, they pointed out that this concept is inconsistent with the observation that no change in embrittlement was detected in passing through the melting point of bismuth (271°C). The bismuth film they meant is thus a film so thick that we can speak of the melting point of bismuth. If this is the case, then the stress relaxation across these bismuth films would start at a temperature much lower than the melting point of bismuth, causing a drop of the elastic modulus.

The variation of "elastic modulus" with temperature

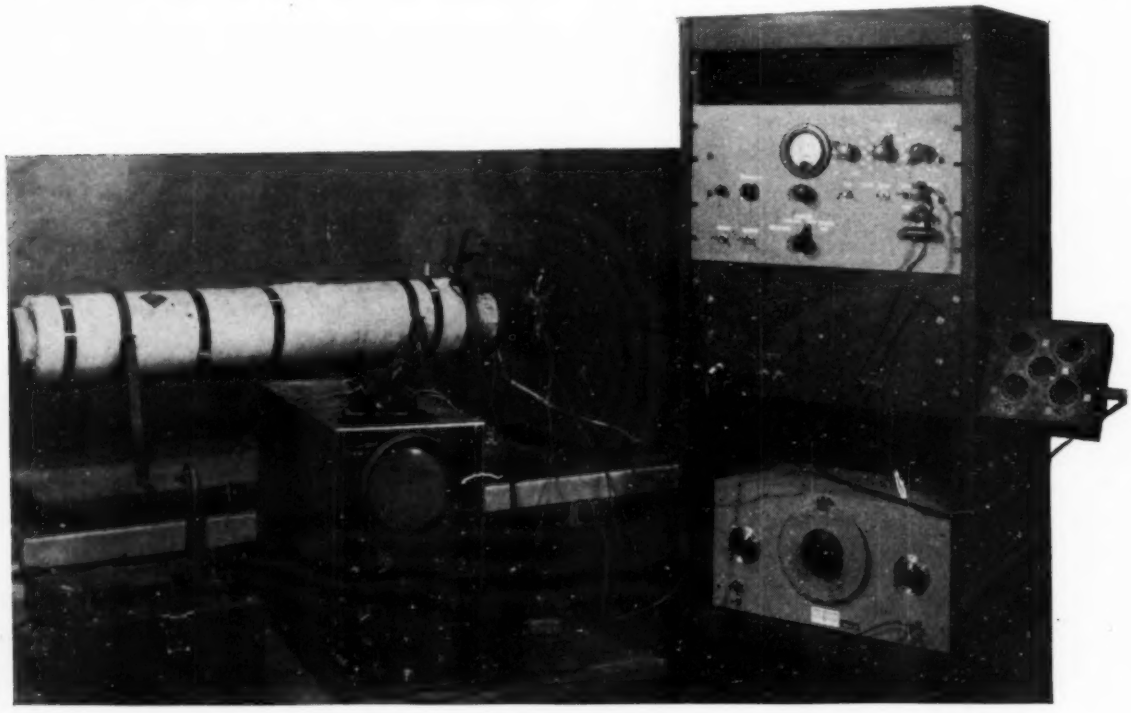

FIG. 3. Complete set-up of the apparatus for measurement of internal friction.

[7] F. C. Rose and C. Zener, Phys. Rev. **56**, 343 (1939).
[8] David Lazarus and A. W. Lawson, Rev. Sci. Inst. **18**, 730 (1947).

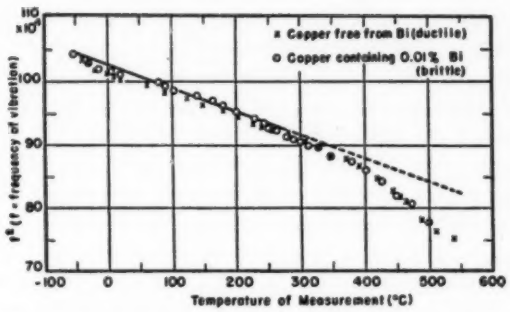

FIG. 4. Variation of elastic modulus with temperature of copper specimens free from and containing 0.01 percent of bismuth.

of copper specimens free from and containing 0.01 percent of bismuth is shown in Fig. 4. The elastic modulus at a given temperature is proportional to the square of the natural frequency of vibration which was taken as the resonant frequency since the damping concerned is small. The curve is essentially a straight line at low temperatures and a rapid change in curvature starts around 300°C. This rapid change occurs in both the bismuth-free specimen and the bismuth-bearing specimen. Previous work shows that this rapid change is associated with the stress relaxation across the grain boundaries in copper.[5] It can also be shown that the maximum curvature change would occur around 500°C in high purity copper.[5]

Figure 4 shows there is no appreciable difference in the elastic modulus curves of the bismuth-free specimen (ductile) and of the bismuth-bearing specimen (brittle). However, the question may arise that the stress relaxation across these "bismuth films" might have started at a very low temperature and have been completed at −50°C, the lowest temperature of measurement shown in Fig. 4. However, the dimensions of the bismuth-free and the bismuth-bearing specimen have been made as identical as possible. If stress relaxation had occurred and been completed in the bismuth-bearing specimen, then the elastic modulus of this specimen should be approximately 30 percent lower than that of the bismuth-free specimen at temperatures where the stress relaxation across the "bismuth films" (assumed to be distributed throughout all the copper grain boundaries) had been completed.[9] Figure 4 shows this is not the case.

The discussion made above indicates that under the conditions which the copper is embrittled by bismuth, the bismuth could not have formed a film so thick at the grain boundaries that we can speak of a melting point of bismuth. This is consistent with the observation that there is no abrupt change in elastic modulus of the bismuth bearing specimen in passing through the melting point of bismuth (Fig. 4).

B. Internal Friction

Figure 5 shows the variation of internal friction with temperature in copper specimens free from and containing various amounts of bismuth, as indicated. From earlier measurements on copper specimens,[5] we know that the portion of internal friction in the right-hand side of the figure is associated with the stress relaxation across copper grain boundaries. The internal friction peak would occur around 500°C for the frequency of vibration used which is about 1000 cycles per second. It is seen that this portion of internal friction was reduced by the presence of bismuth. This shows that under embrittlement conditions, some bismuth did precipitate at the grain boundaries, as we have demonstrated previously that the presence of impurities at grain boundaries reduces grain boundary relaxation.[5]

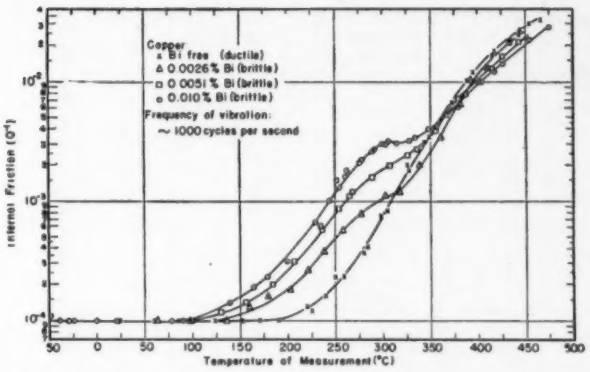

FIG. 5. Variation of internal friction with temperature of copper specimens free from and containing various amounts of bismuth at a frequency of transverse vibration of about 1000 cycles per second.

The internal friction measurements have been taken at temperatures both above and below room temperature down to −50°C. Although the measurement of internal friction is very sensitive using the apparatus described, no appreciable difference in internal friction was detected in the bismuth-free copper and the bis-

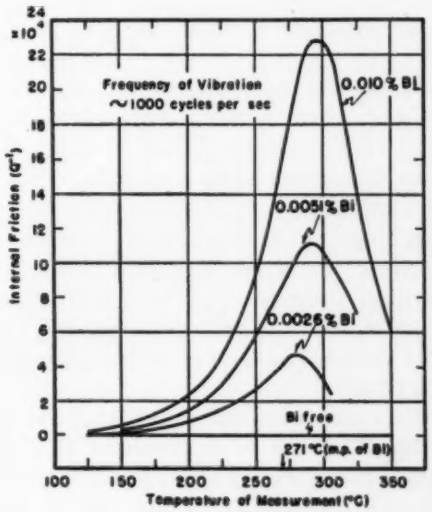

FIG. 6. Internal friction peaks (*versus* temperature) observed in copper specimens containing small amounts of bismuth (the value of internal friction shown is to be multiplied by 10^{-4} instead of 10^{4}).

[9] T. S. Kê, Phys. Rev. **71**, 533 (1947).

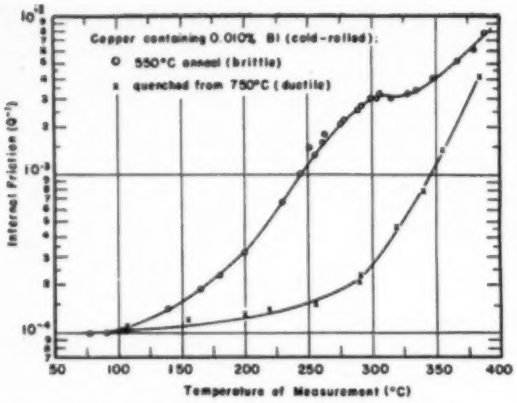
Copper containing 0.010% Bi (cold-rolled):
○ 550°C anneal (brittle)
× quenched from 750°C (ductile)
Internal Friction (Q⁻¹)
Temperature of Measurement (°C)

FIG. 7. Effect of high temperature anneal on the internal friction of bismuth-bearing copper specimen.

muth-bearing copper up to a temperature of 100°C. However, for temperatures above 100°C, the measurements revealed that the internal friction curves of the bismuth-bearing specimens are composed of two portions. One portion is associated with the stress relaxation across the grain boundaries of copper (at the extreme right of Fig. 5), the other portion is the additional contribution because of the presence of bismuth in copper (at the middle portion of Fig. 5). Metallographic examination shows that the grain size of the bismuth-bearing specimens is similar to that of the specimen free from bismuth. Both have an average grain diameter of about 0.05 mm. Since the mechanical and thermal treatments on both specimens are identical, the influence of bismuth can be best shown by subtracting the internal friction curve of the copper specimen from the curves of the bismuth-bearing copper specimens. Then each bismuth-bearing specimen gives an internal friction peak around 290°C as shown in Fig. 6. These internal friction peaks are the additional contribution because of the presence of bismuth in copper. The height of the peak which will be referred to later as the "bismuth peak," varies approximately linearly with the bismuth content. It is to be noticed that the height of the "bismuth peak" is much smaller than that of the peak characteristic of pure copper.

Now, we should emphasize two facts which are revealed in Figs. 5 and 6. (1) This bismuth peak is complementary with the internal friction associated with the original copper grain boundaries. One increases while the other decreases; (2) the occurrence of these bismuth peaks are correlated to the embrittlement of copper by bismuth. The specimen is brittle when there is a bismuth peak.

These observations indicate that the occurrence of the "bismuth peak" is due to the presence of bismuth at copper grain boundaries. Furthermore, they also indicate that the distribution of bismuth at the grain boundaries is highly heterogeneous. Across most of the boundaries no appreciable amount of bismuth is precipitated, at least not enough to influence the grain boundary viscosity. It is these grain boundaries which give rise to that internal friction peak characteristic of pure copper as shown in the extreme right-hand side of Fig. 5. Across a few of the grain boundaries enough bismuth is precipitated to decrease markedly the grain boundary viscosity. This causes a shift of the internal friction peak to 290°C which is much lower than that of copper grain boundary peak around 500°C.

Such a high concentration of bismuth at copper grain boundaries is different from the concept of a bismuth film. This high concentration bismuth may be sufficient to loosen the adhesive force between the copper grains causing embrittlement of copper yet it does not acquire the properties of crystalline bismuth.

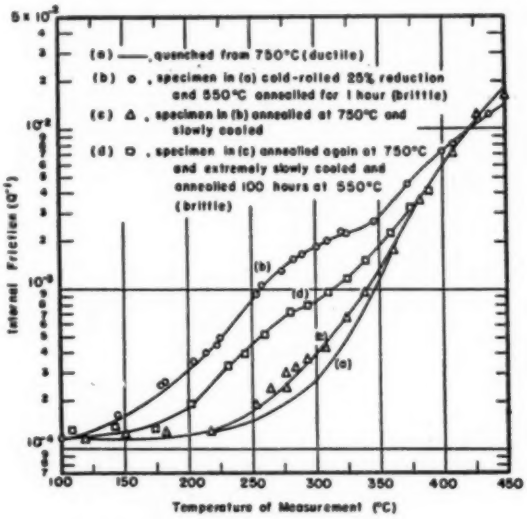
(a) ——, quenched from 750°C (ductile)
(b) ○, specimen in (a) cold-rolled 25% reduction and 550°C annealed for 1 hour (brittle)
(c) △, specimen in (b) annealed at 750°C and slowly cooled
(d) □, specimen in (c) annealed again at 750°C and extremely slowly cooled and annealed 100 hours at 550°C (brittle)
Internal Friction (Q⁻¹)
Temperature of Measurement (°C)

FIG. 8. Effect of cold-work and slow cooling on the internal friction of bismuth-bearing copper specimen.

The experiments to be described below will confirm our concept that the "bismuth peak" observed is due to the presence of bismuth at copper grain boundaries.

C. Effect of Cold-Work and Heat Treatment

When the specimens were annealed again at 750°C in vacuum for one hour and then quenched in water, the internal friction peak attributed to the presence of bismuth completely disappeared. This is shown by the lower curve of Fig. 7 for the specimen containing 0.01 percent of bismuth. According to Voce and Hallowes, the bismuth-bearing specimens are ductile after such a heat treatment. This again demonstrates the correlations of the embrittlement and the "bismuth peak." This observation on the effect of heat treatment is consistent with Smith's remark that the bismuth retains in the solid solution after being quenched from 750°C.[3]

The observations so far seem to indicate that embrittlement of copper and the presence of the "bismuth peak" are caused by the precipitation of bismuth from solid solution to somewhere in the specimen. We have shown above that bismuth did precipitate at the grain

boundaries. Now the question is whether the precipitation of bismuth at the grain boundaries is the only agent responsible for embrittlement.

We have mentioned above that the specimens were originally cold-rolled to 50 percent reduction in thickness and were annealed at 550°C for ½ hour. The bismuth-bearing specimens are brittle under these conditions and bismuth peaks have been observed. When these specimens were annealed again and quenched from 750°C, they became ductile and the bismuth peak also disappeared. Now, if the occurrence of the bismuth peak and the embrittlement resulted from the precipitation of bismuth at the copper grain boundaries, then the bismuth in a specimen quenched from 750°C should re-precipitate at the grain boundaries if we re-anneal the specimen at 550°C or so. To our surprise, the internal friction curve did not change after the specimen was re-annealed at 550°C for one hour and again for twenty-four hours. This is quite puzzling considerin the fact that before the heating at 750°C, one-half hour anneal at 550°C was sufficient to embrittle the specimen and cause the presence of the bismuth peak.

The only difference between the original specimen and the specimen heated at 750°C is that the original specimen was subjected to a cold-work of 50 percent reduction in thickness. Although the specimen has been completely recrystallized after the annealing for ½ hour at 550°C, some effect of the previous cold-work may still persist after the annealing only to be eliminated by the subsequent annealing at 750°C. In order to test the effect of cold-work, the bismuth-bearing specimen quenched from 750°C, which is still ductile after annealing at 550°C for more than twenty-four hours, was cold-rolled about 25 percent reduction in thickness. It was then annealed at 550°C for one hour. Under these conditions the bismuth peak reappeared as shown in Fig. 8 and the specimen became brittle again according to Voce and Hallowes. It thus appears that cold-working on the specimen is also a necessary condition for the embrittlement and the appearance of the bismuth peak.

However, it is conceivable that cold-working the specimen before the 550°C annealing will hasten the precipitation and magnify the effects. The specimen described above was then annealed at 750°C for 1 hour and cooled slowly in furnace so that the temperature dropped from 750°C to 550°C in about half an hour. The internal friction curve after this treatment is shown as (c) in Fig. 8. There appears to be a small peak in comparison with that of the specimen quenched from 750°C. Encouraged by this observation, the specimen was again annealed at 750°C for one-half hour and cooled extremely slowly in the furnace by reducing the furnace temperature by 2°C step for every 5 minutes. The temperature was lowered to 550°C in about three and a half hours and then annealed at 550°C for 100 hours. The internal friction curve after such a treatment is shown by (d) in Fig. 8. Now the bismuth peak is well developed although it is still smaller in comparison with that of the original specimen shown by (b).

All the observations on the effect of cold-work and heat treatment described above are consistent with Voce and Hallowes' results of notched-bar tests. The effect of cold-working is thus only to speed up the precipitation of bismuth to the grain boundaries. The difference between (b) and (d) in Fig. 8 "might have disappeared if the cooling rate had been slower, but there is also the possibility that a certain amount of bismuth might be retained within the stable grains during cooling"—(Voce and Hallowes). The possible role of slip bands and dislocations in connection with the embrittlement and the occurrence of bismuth peak seems to be removed because of the conclusive evidence shown in Fig. 8.

CONCLUDING REMARKS

The data presented above corroborate the proposition that the embrittlement is caused by bismuth present at copper grain boundaries. However, it appears that the bismuth is distributed in a highly heterogeneous manner. Across most of the boundaries no appreciable amount of bismuth is precipitated, at least not enough to influence the grain boundary viscosity. Across a few of the grain boundaries enough bismuth is precipitated to decrease markedly the grain boundary viscosity. Since no discontinuous behavior is observed as the temperature passes through the melting point of pure bismuth, it is concluded that the film of bismuth along these boundaries is not of sufficient thickness as to acquire the properties of crystalline bismuth.

In conclusion, the author is deeply indebted to Dr. G. L. Bailey, Director of British Non-Ferrous Metals Research Association, London, England, for supplying the copper specimens free from and containing various amounts of bismuth. He is also indebted to Professors C. S. Smith and C. Zener of this Institute for their constant interest in this problem and valuable discussions. He wishes to thank Mr. Marc Ross for his help in taking measurements.

Collimation Error in Small Angle X-Ray Scattering*

K. L. YUDOWITCH
Department of Physics, Florida State University
(Received July 5, 1949)

It has been shown that excessive error may be introduced in small angle x-ray scattering by the use of an incident beam of finite cross section. To account for this error the usual procedure has required multiple integrations for rays reaching a single point P on the film from all points within each slit. However, the common effect from both finite slit height and width is a range of scattering angle for rays reaching P. The integrations over each slit dimension are reduced to a single integration over scattering angle, which entails finding the limits of scattering angle.

The assumption of a constant distribution of intensity throughout the range allows the range of scattering angle $\delta\epsilon$ to be taken as a measure of the collimation error. Minimization of $\delta\epsilon$ permits determination of optimum values of slit height-width ratio. For two slit collimation, it further leads to determination of optimum slit spacing and optimum relative slit sizes.

IT has been indicated[1] in geometric arrangements employed in small angle x-ray scattering that excessive error may be introduced by the use of an incident beam of finite cross section. The error arises from the fact that the scattering source is not a point; and, with one arrangement, the incident rays are not parallel.

Using photographic detection and subsequent microphotometering, the error inherent in the use of a finite microphotometer slit can be made negligible.[1] The major collimation error is then to be found in the beam-defining slits.

The common effect from both a finite area of scattering and a nonparallel or skew incident beam is a range of scattering angles $\delta\epsilon$ for rays reaching a point P on the film. In this discussion only points P on a horizontal axis in the film are considered.

When the angular distribution of intensity of radiation scattered at small angles is used to measure the size of the scattering particles, depending somewhat on the shape of the scattering particles,[2] a Bessel function, a complex trigonometric function or an exponential function may describe the intensity distribution. In general, the intensity is a function of $\epsilon R/\lambda$ where ϵ is the scattering angle, R the particle radius, and λ the radiation wave-length.[3]

The experimental collimation error may be measured by the range of variation $\delta(\epsilon R/\lambda)$. Where $\delta\lambda$ and δR can be made negligible (monochromatic radiation and mono-dispersed specimen), the collimation error becomes simply $(R/\lambda)\delta\epsilon$. Whereas R is prescribed by the nature of specimen chosen for study, λ and $\delta\epsilon$ are experimental variables. The collimation error has been reduced by the use of large values of λ.[1] The present investigation is confined to a study of the determination of range in scattering angle $\delta\epsilon$. The correction in the intensity is made by utilizing the integral expression:[1]

$$I_P = \int_{\epsilon_2}^{\epsilon_1} [I_\epsilon/\zeta] n(\epsilon) d\epsilon, \tag{1}$$

where $I_P \equiv$ intensity scattered to point P on film, $\epsilon_2 \equiv$ minimum scattering angle, $\epsilon_1 \equiv$ maximum scattering angle, $N(\epsilon)d\epsilon \equiv$ incident power which scatters to P at angles ϵ to $\epsilon + d\epsilon$, $\zeta \equiv$ total power incient on sample, and $I_\epsilon \equiv$ intensity theoretically scattered at angle ϵ.

It is interesting to note the procedure followed by other workers.[4] By considering separately the effects of the height and width of each slit, they are led to multiple integrations over each height and width. These multiple integrations are here reduced to a single integration over scattering angle by the simple expedient of geometrically determining the limits of integration. Bolduan and Bear[5] consider the optimum two-slit collimation for resolution of consecutive diffraction orders of a single spacing.

CASE I: CURVED CRYSTAL REFLECTED

Three experimental arrangements have been used. The first and least common arrangement[6] utilizes a

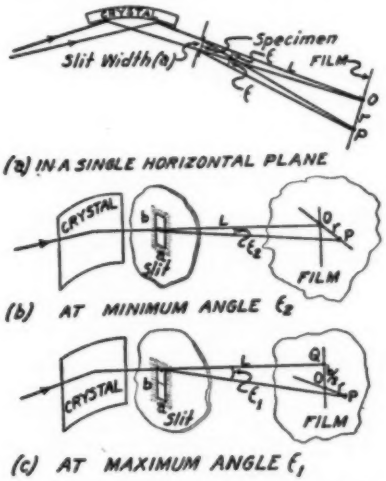

FIG. 1. Scattering of curved crystal reflected radiation to a point (P).

* This study was made in connection with work under Research and Development Contract W-18-064-CM-229 with the U. S. Army Chemical Corps, Camp Detrick, Maryland.

[1] K. L. Yudowitch, J. App. Phys. **20**, 174 (1949).

[2] A. L. Patterson, Phys. Rev. **56**, 972 (1939).

[3] A. Guinier, Ann. de physique **12**, 161 (1939); R. von Nardroff, Phys. Rev. **28**, 240 (1926); J. Slater and N. H. Frank, *Introduction to Theoretical Physics* (McGraw-Hill Book Company, Inc., New York, 1933), p. 324.

[4] C. G. Shull and L. C. Roess, J. App. Phys. **18**, 295 (1947).

[5] O. E. A. Bolduan and R. S. Bear, J. App. Phys. **20**, 983 (1949).

[6] A. Guinier, J. de Chim. Physique **40**, 133 (1943).

curved crystal to produce a beam which converges in a line on the photographic film.

Figure 1(a) shows this arrangement for a slit of negligible height b. All rays shown lie in a horizontal plane; the crystal acts much as a cylindrical mirror and there is no vertical divergence. It is assumed that the crystal is perfect and that the radiation striking the crystal is parallel and originates in a perfect line source.

It is evident from the figure that no error is introduced by the slit width a, as any horizontal spread of the beam is focused at the film. The slit width is dictated only by the extent of the crystal. The minimum scattering angle for a ray reaching P is seen from Fig. 1(b) to be $\epsilon_2=r/L$. The incident ray for this condition is any ray striking the sample on a horizontal line through its center. The maximum scattering angle is achieved by a ray reaching P from any point on either top or bottom edge of the slit. This scattering angle is seen from Fig. 1(c) to be $\epsilon_1=[r^2+(b/2)^2]^{\frac{1}{2}}/L$. Then

$$\delta\epsilon=\epsilon_1-\epsilon_2=\{[r^2+(b/2)^2]^{\frac{1}{2}}-r\}/L,$$

where r, L, b are shown on the figures. Or

$$\delta\epsilon=[\epsilon^2+(\phi_1(k)^{\frac{1}{2}})^2]^{\frac{1}{2}}-\epsilon, \qquad (2)$$

where $\epsilon\equiv$scattering angle (r/L), $a\equiv$slit width, $A\equiv$slit area (ab), $k\equiv$slit eccentricity (b/a), and $\phi_1\equiv(A)^{\frac{1}{2}}/2L$.

The error as measured by $\delta\epsilon$ is seen from Eq. (2) to vanish for vanishing slit height b or infinite slit—film distance L. This error dependence on slit height b and film distance L is just what is physically expected. The error decreases with increasing ϵ from a value $\phi_1(k)^{\frac{1}{2}}$ at $\epsilon=0$. Actually ϵ is limited by initial physical considerations to values greater than zero but much smaller than unity.

As the scattered intensity reaching the film is proportional to the slit area A and inversely proportional to the specimen film distance L, we may write $I\propto A/L^2$ or ϕ_1^2. Thus for constant intensity, ϕ_1, and hence the error $\delta\epsilon$, are not affected by jointly varying the slit area and specimen—film distance so as to keep the intensity constant. These absolute dimensions may thus be selected with considerations for convenience.

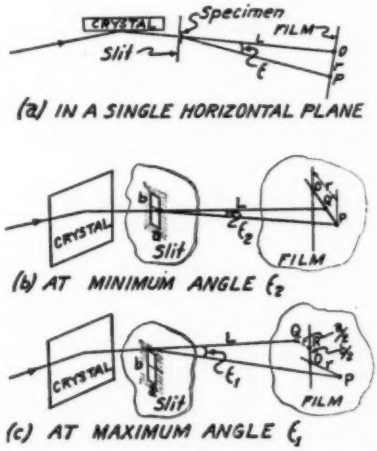

FIG. 2. Scattering of plane crystal reflected radiation to a point (P).

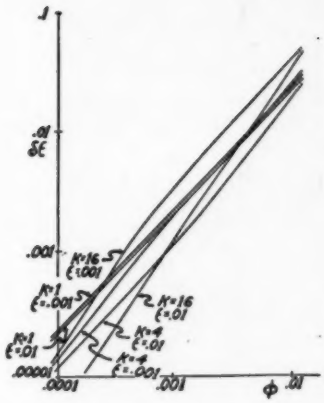

FIG. 3. Collimation error ($\delta\epsilon$) *vs.* geometric factor (ϕ).

CASE II: PLANE CRYSTAL REFLECTED

The second arrangement utilizes a plane crystal to produce a parallel beam.[4,7] The beam is defined by a single slit as shown in Fig. 2(a) for a vanishing small slit. All rays striking the sample are parallel. It is assumed that the radiation incident on the crystal is parallel and the crystal perfect.

The minimum scattering angle is seen at once from Fig. 2(b) to be $\epsilon_2=[r-a/2]/L$. From Fig. 2(c) the maximum scattering angle is $\epsilon_1=[(r+a/2)^2+(b/2)^2]^{\frac{1}{2}}/L$. Then

$$\delta\epsilon=[(\epsilon+\phi_1/(k)^{\frac{1}{2}})^2+(\phi_1(k)^{\frac{1}{2}})^2]^{\frac{1}{2}}-\epsilon+\phi_1/(k)^{\frac{1}{2}}. \qquad (3)$$

Again the error dependence on film distance L and slit area A is as expected, $\delta\epsilon$ vanishing for vanishing A or infinite L. $\delta\epsilon$ decreases with increasing ϵ from a value at $\epsilon=0$: $\delta\epsilon=\phi_1/(k)^{\frac{1}{2}}[1+(k^2+1)^{\frac{1}{2}}]$. This minimum value is seen to be somewhat greater than the value $\phi_1(k)^{\frac{1}{2}}$ for case I.

More interesting here is the effect of slit eccentricity k on the error $\delta\epsilon$. It is seen from Eq. (3) that $\delta\epsilon$ becomes infinite for k either vanishing or infinite. This indicates a finite value of k for which $\delta\epsilon$ is a minimum. To determine the value of k for which $\delta\epsilon$ is a minimum, the derivative of $\delta\epsilon$ with espect to k is set equal to zero, ϵ and ϕ_1 being held constant.

This results in a quartic equation in k:

$$k_{\rm opt}{}^4-6k_{\rm opt}{}^2-4Xk_{\rm opt}+9=0, \qquad (4)$$

where

$$X=\epsilon^2/\phi_1{}^2. \qquad (5)$$

The solution of this equation is:

$$k_{\rm opt}=Y+[3-Y^2+X/Y]^{\frac{1}{2}}, \qquad (6)$$

where

$$Y\equiv\{1+[1+X/8+(16X+X^2)^{\frac{1}{2}}/8]^{\frac{1}{3}}+[1+X/8-(16X+X^2)^{\frac{1}{2}}/8]^{\frac{1}{3}}\}^{\frac{1}{2}}. \qquad (7)$$

[7] B. E. Warren, Phys. Rev. **49**, 885 (1936).

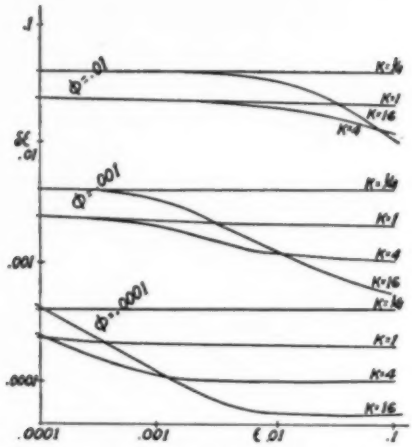

FIG. 4. Collimation error ($\delta\epsilon$) *vs.* scattering angle (ϵ).

The other three roots are negative or imaginary. For $X=0$ ($\epsilon=0$), note that $k_{opt}=\sqrt{3}$.

It is informative to note graphically the dependence of the collimation error $\delta\epsilon$ upon ϕ_1, ϵ, and k. These are shown in Figs. 3–5, respectively, for selected reasonable values of the parameters involved.

Figure 3 shows the dependence of error on ϕ_1 to be nearly linear, even as it might be expected.

The decrease of error with scattering angle is seen from Fig. 4 to depend upon the slit eccentricity, the effect being most pronounced with tall slits.

Figure 5 bears out the prediction of the existence of an optimum slit eccentricity to give a minimum collimation error. The value of the optimum eccentricity is seen to depend sharply on the scattering angle and somewhat less upon ϕ_1.

Further information on the optimum values of eccentricity k may be seen from a plot (Fig. 6) of the optimum k *vs.* X as given by Eqs. (6) and (7). Note all quantities plotted in Figs. 3–6 are dimensionless numerics.

As for the curved crystal case, the error $\delta\epsilon$ is unaffected by jointly varying the slit area and specimen-film distance, keeping the intensity constant.

CASE III: TWO EQUAL SLITS

The third and experimentally simplest arrangement utilizes two identical slits to define the beam,[8] the source being broad enough to "fill" the slits. Figure 7(a) shows this for vanishingly small slits, separated by a distance 1. In this case the rays striking the sample at slit 2 are not all parallel.

The minimum scattering angle occurs for that ray which grazes the middle of the vertical edges as in Fig. 7(b). This ray, proceeding unimpeded, would strike the film at point Q. The ray reaching P is scattered through an angle measured by QP/L. This minimum scattering angle may be expressed as $\epsilon_2=(r-\alpha a)/L$, where $\alpha\equiv(2L+l)/2l$.

[8] Jellinek, Solomon, and Fankuchen, Ind. Eng. Chem. (Anal. Ed.) **18**, 172 (1946). R. S. Bear, J. Am. Chem. Soc. **66**, 1297 (1944).

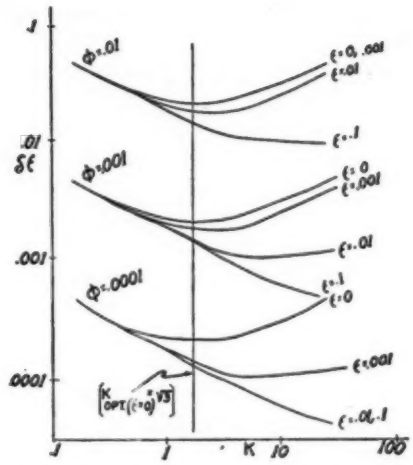

FIG. 5. Collimation error ($\delta\epsilon$) *vs.* slit eccentricity (k).

The maximum scattering angle can be found by examining Fig. 7(c). The distances OR and QR are readily shown to be αa and αb, respectively. Then the maximum angle is given by $\epsilon_1=[(r+\alpha a)^2+(\alpha b)^2]^{\frac{1}{2}}/L$. Then

$$\delta\epsilon=[(\epsilon+\phi_2/(k)^{\frac{1}{2}})^2+(\phi_2(k)^{\frac{1}{2}})^2]^{\frac{1}{2}}-\epsilon+\phi_2/(k)^{\frac{1}{2}}, \quad (3')$$

where

$$\phi_2\equiv\alpha(A^{\frac{1}{2}})/L.$$

The collimation error $\delta\epsilon$ vanishes for vanishing slit area A, infinite slit separation l or infinite slit-film distance L. Again $\delta\epsilon$ decreases with increasing ϵ from a value at $\epsilon=0$: $\delta\epsilon=\phi_2/(k)^{\frac{1}{2}}[1+(k^2+1)^{\frac{1}{2}}]$. This value is seen to be greater than in case II by the factor $2\alpha(>1)$.

Again we see $\delta\epsilon$ becomes infinite for k either vanishing or infinite. In fact, it will be noted that Eq. (3′) is identical with Eq. (3) except that ϕ_1 is everywhere replaced by ϕ_2. Hence Eqs. (4), (6), and (7) follow at once, except that X is now given by Eq. (5′):

$$X=\epsilon^2/\phi_2^2. \quad (5')$$

Due to the similarity, it is quite possible to use the graphs of case II to represent case III, simply replacing values of ϕ_1 with values of ϕ_2.

The intensity of radiation reaching the film is proportional to the product of the slit areas and inversely

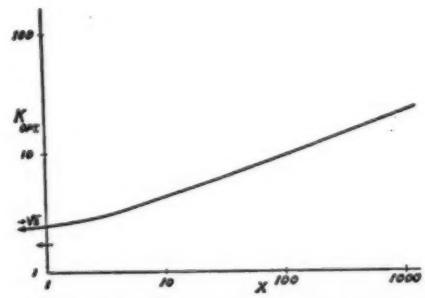

FIG. 6. Optimum slit eccentricity (k_{opt}) *vs.* (X).

proportional to the squares of both the slit separation and the specimen-film distance: $I \propto A^2/L^2l^2$. Thus again the error $\delta\epsilon$ is unaffected by jointly varying the slit areas and slit-film distances, keeping the intensity constant.

However, it is of interest to consider the optimum ratio of slit separation l and slit-film distance L. This is done by minimizing ϕ_2 as it is clear that $\delta\epsilon$ is a minimum for ϕ_2 a minimum. Then for constant intensity and a given slit area A, the product Ll must be constant.

$$(d/dL)(\phi_1)=(A^{\frac{1}{2}})/2(d/dL)(1/L+2/l)=0,$$
$$l=2L,$$

whence $\alpha=1$ and $\phi_2=(A^{\frac{1}{2}})/L$. Thus the optimum ratio of slit separation to slit-film distance is 2:1.

CASE IV: TWO UNEQUAL SLITS

Avoiding the assumption of equal slits leads to somewhat more complicated expressions for the extreme scattering angles. If slit 1 in Fig. 7 has dimensions $a_1 \times b_1$ and slit 2, dimensions $a_2 \times b_2$, the minimum scattering angle becomes: $\epsilon_2=[r-\theta_a]/L$, where

$$\theta_a \equiv a_2/2+(a_1+a_2)L/2l.$$

The maximum scattering angle becomes

$$\epsilon_1=[(r+\theta_a)^2+(\theta_b)^2]^{\frac{1}{2}}/L,$$

where

$$\theta_b \equiv b_2/2+(b_1+b_2)L/2l$$
$$\delta\epsilon=[(r+\theta_a)^2+(\theta_b)^2]^{\frac{1}{2}}/L-[r-\theta_a]/L. \qquad (8)$$

Holding everything constant except a_1 and a_2 and setting $a_2=(a_1a_2)/a_1$, where (a_1a_2) is constant

$$(d/da_1)(\delta\epsilon)=(d/da_1)(\theta_a)=0$$
$$a_2=a_1L/(L+l).$$

Similarly, for varying b_1 and b_2

$$(d/db_1)(\delta\epsilon)=(d/db_1)(\theta_b)=0$$
$$b_2=b_1L/(L+l).$$

Thus

$$b_2/a_2=b_1/a_1$$

or

$$k_2=k_1\equiv k.$$

For minimum error then

$$\theta_a=a_1L/l$$
$$\theta_b=b_1L/l.$$

Then

$$\delta\epsilon=[(\epsilon+\phi_3/(k)^{\frac{1}{2}})^2+(\phi_3(k)^{\frac{1}{2}})^2]^{\frac{1}{2}}-\epsilon+\phi_3/(k)^{\frac{1}{2}} \qquad (9)$$

where

$$\phi_3 \equiv (A_2)^{\frac{1}{2}}(L+l)/Ll.$$

The collimation error $\delta\epsilon$ again vanishes for vanishing slit areas or infinite slit-film distances, $\delta\epsilon$ decreasing with increasing from a value at $\epsilon=0$: $\delta\epsilon=\phi_3/(k)^{\frac{1}{2}}[1+(k^2+1)^{\frac{1}{2}}]$. As for the equal slits, the error $\delta\epsilon$ is unaffected by jointly varying the slit areas and slit-film distances, keeping the intensity constant. The intensity dependence is again as in case III: $I \propto A_1A_2/L^2l^2$. Again the error is minimized for minimum ϕ_3

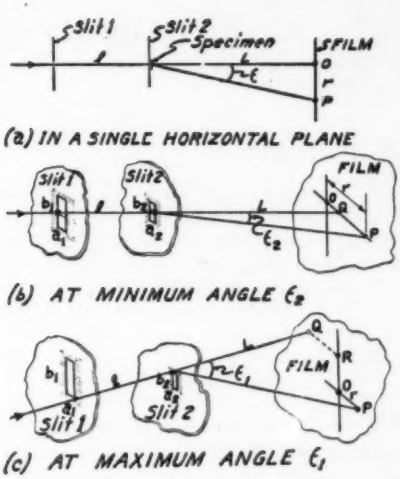

FIG. 7. Scattering of slit collimated radiation to a point (P).

$$(d/dL)(\phi_3)=(A_2)^{\frac{1}{2}}(d/dL)(1/L+1/l)=0$$
$$l=L,$$

whence $a_1=2a_2$, $b_1=2b_2$, $A_1=4A_2$, and $\phi_3=(A_1)^{\frac{1}{2}}/L$.

The unscattered beam occupies a half-width at the film of just θ_a. If L and 1 are fixed and the product (a_1a_2) again held constant for a given intensity, the unscattered beam width may be minimized: $(d/da_1)(\theta_a)=0$.

This yields $a_2=a_1L/(L+l)$ as before, which becomes $a_1=2a_2$ for $l=L$. This means then that the slit-width ratio for minimum error is identical with the slit-width ratio for a minimum width unscattered beam. This last condition is most important in that the width of the unscattered beam contributes to determination of the limitation of the range of applicability of conventional small angle scattering measurements.[1] The largest particle size which may be measured to within five percent inherent error has a radius: $R_{\max}=\lambda L/4\theta_a=\lambda L/4a_1$. In practice it is difficult to make $L>500a_1$. Then $R_{\max}=125\lambda$(200A for Cu$-k\alpha$, 1000A for Al$-k\alpha$).

It is clear that, in general, the optimum conditions for case IV lead to a smaller error than the optimum conditions for the restricted case III.

CONCLUSION

Instead of using arbitrary intuitive guidance in setting up an experiment in small-angle scattering, it is possible to deduce optimum geometric conditions. In the case of radiation reflected from a plane crystal, one may determine from Fig. 6 the slit height-width ratio for minimizing the geometric error for radiation scattered at a given angle. In the case of radiation collimated by two slits, the same graph is used, noting only that the abscissa is slightly different. In the two slit cases it has also been shown that the geometric error is minimized for equal slit separation and specimen-film distance, and for the second slit (at the specimen) having half the linear dimensions of the first slit (at the source).

Magnetite Concrete for Radiation Shielding

E. Creutz and K. Downes
Department of Physics, Carnegie Institute of Technology, Pittsburgh, Pennsylvania
(Received July 11, 1949)

A concrete containing only magnetite ore concentrate, cement, and water is found to have appreciably better shielding properties than ordinary concrete, and to possess good strength and ease of handling. Exceptionally high moisture content, although gradually lost by diffusion, decreases by only about 50 percent in thirty years in an eight-foot thick wall. Its use is desirable under certain conditions because of space economy due to its high density.

INTRODUCTION

SHIELDING material for high energy nuclear particle accelerators should contain elements of rather high atomic weight for inelastic scattering of fast neutrons. It should also contain appreciable hydrogen content to slow down moderate energy neutrons. High density is desirable to conserve floor space, which in large accelerator buildings is unusually expensive because of special facilities such as overhead cranes and other devices necessitating high head room. Concrete containing magnetite as most or all of the aggregate has been used as ballast blocks by the Navy. However, samples of this, examined several years after manufacture, contained only about two percent by weight of moisture. Furthermore, since mechanical, chemical, and handling data were not readily available, the following experiments were carried out to determine an optimum mixture of magnetite, cement, and water, and to estimate the rate of loss of water by diffusion from the shielding planned for the 400-Mev proton synchro-cyclotron at Carnegie Institute of Technology being built in cooperation with the Joint Office of Naval Research and Atomic Energy Commission Program.

MAGNETITE ORE

Magnetite is available in the Pittsburgh area in the form of a black sand, approximately 99 percent of which passes a 16-mesh screen and approximately 45 percent of which passes a 100-mesh screen. As received, it contains several percent of moisture—all weights quoted here are on the basis of dried material. It is used as feed for some of the local blast furnaces. The two sources are the Tahawis Mine of the Titanium Division of the National Lead Company and the Benson Mine of the Jones and Laughlin Steel Corporation, both in the Adirondack Mountains. That from the first source is called MacIntyre concentrate and that from the second Benson ore concentrate. The chief difference between these two ores is the titanium content. Typical chemical analyses are given in Table I. The cost of either ore in large lots is about $5.50 per gross ton, f.o.b. the mine.

Table I. Chemical analysis of magnetite ores.

Chemical	Benson ore	MacIntyre ore
Fe	62.5 percent	56–58 percent
SiO_2	5.5	2–2.5
MnO	0.35	0.3
Al_2O_3	2.0	4–5
CaO		0.8
MgO		1.5
Cr_2O_3		0.29
TiO_2	1.0	10–11

TEST SAMPLES

To determine the optimum mixture of magnetite ore, Portland cement, and water, the following tests were run, with the help of Mr. B. Kambouris of the Civil Engineering Department. Cylinders two inches in diameter and four inches long were made, using magnetite-to-cement ratios of 4:1, 5:1, and 6:1 by weight with various amounts of water in each case. These cylinders were cured for 28 days in 100 percent relative humidity and then tested to destruction in a compression machine. Results of these strength tests are shown in Fig. 1. The same cylinders were used for density measurements. There is fair correlation between strength and density for water contents greater than ten percent by weight. Somewhat higher densities can be obtained with less water than this but at a serious loss of strength. The measured densities are shown in Fig. 2. From these results it was decided to use a mixture of five parts by weight of dry magnetite to one part by weight of cement with a water-cement ratio of $8\frac{1}{2}$ gallons per sack of cement, which corresponds to 11 percent of water in the mix. It was found in the compression tests that instead of the usual cup- and cone-type failure, these cylinders broke with more or less straight radial cracks. This seems to indicate that the failure was in tension across a diameter, indicating that the bond strength between cement and magnetite particles is lower compared to the shear strength than is the case with more conventional concretes.

SHRINKAGE

Due to the small particle size of the magnetite ore, abnormally large shrinkage of the concrete was considered a possibility. The following experiment was done to measure the shrinkage: a three-inch brass tube six feet long was split along its diameter, and No. 60 holes were drilled at two-inch intervals along one element of the cylinder. The distance between these holes

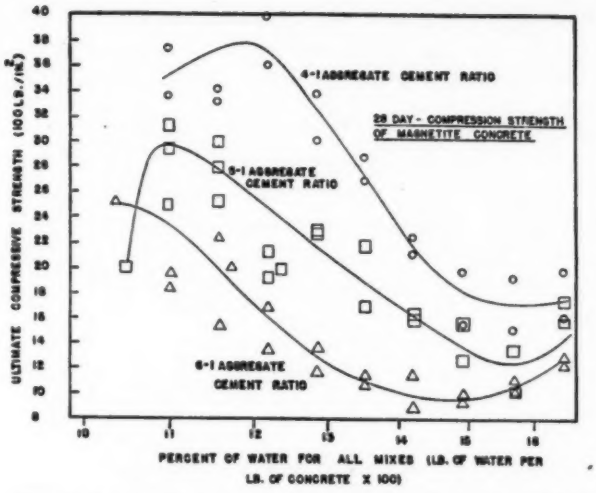
4-1 AGGREGATE CEMENT RATIO
28 DAY - COMPRESSION STRENGTH OF MAGNETITE CONCRETE
5-1 AGGREGATE CEMENT RATIO
6-1 AGGREGATE CEMENT RATIO
ULTIMATE COMPRESSIVE STRENGTH (100 LB./IN.²)
PERCENT OF WATER FOR ALL MIXES (LB. OF WATER PER LB. OF CONCRETE X 100)

FIG. 1. Compressive strength of magnetite concrete samples of various total water contents and three different aggregate to cement ratios.

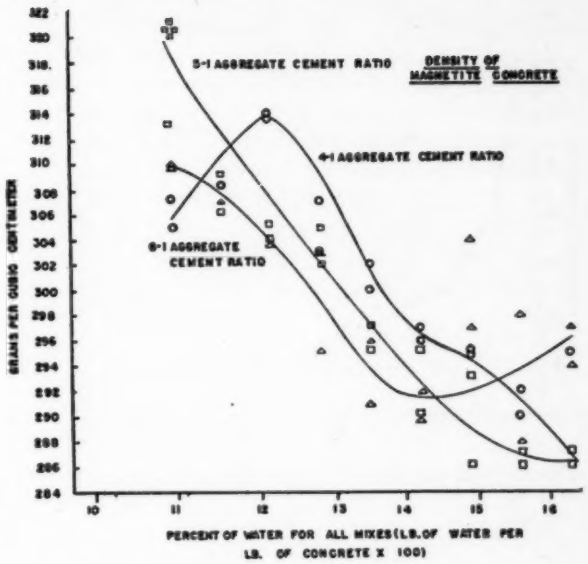
5-1 AGGREGATE CEMENT RATIO
DENSITY OF MAGNETITE CONCRETE
4-1 AGGREGATE CEMENT RATIO
6-1 AGGREGATE CEMENT RATIO
GRAMS PER CUBIC CENTIMETER
PERCENT OF WATER FOR ALL MIXES (LB. OF WATER PER LB. OF CONCRETE X 100)

FIG. 2. Density of magnetite concrete samples of various mixes.

was measured with a cathetometer with an accuracy of 0.05 mm. The tube was then filled with concrete and pins inserted in the holes before it set. After 48 hours the tube was removed and the positions of the pins read with the cathetometer. The results were tabulated to give the position of the pins as distances from the top of the concrete. The differences between these distances before setting and after setting of the concrete were then plotted as a function of their position before setting as shown in Fig. 3. As can be seen from the curve, only the top 20 cm of the column shrinks appreciably, and its shrinkage does not exceed one percent. The top surface of the column formed a fine gray powder which could be brushed off after setting, indicating some segregation of the cement and magnetite particles. The position of the pins was re-measured at 96 hours after setting, and no appreciable change in the shrinkage was found, indicating that it is primarily a phenomenon occurring during setting of the concrete.

MOISTURE CONTENT AND DIFFUSIVITY

An important factor in the low energy neutron attenuation of shielding is the hydrogen content. Since concrete loses at least part of its moisture by diffusion in a dry room, it was decided to measure the moisture diffusivity to determine the deterioration with time of this property of the magnetite shielding. Magnetite concrete spheres three inches in diameter and one inch in diameter were made, as were also some of ordinary concrete. These spheres were first cured in water and then put into desiccators containing P_2O_5. On preliminary tests, $CaCl_2$ was used, but it did not take up the water as rapidly as it diffused from the spheres. The spheres were weighed at suitable intervals of time until there were practically no changes in weight. For the three-inch spheres this required about one month. For the one-inch spheres it was about four days. Typical weight curves are shown in Figs. 4 and 5. They were then placed in a special combustion train in a stainless steel vessel and heated to 950°C, using oil-pumped nitrogen containing some O_2 as a flushing gas, with an H_2SO_4 and P_2O_5 train to collect moisture. From these experiments the total initial weight of hydrogen when collected as water was found to correspond to a water content of approximately ten percent of the total weight of the concrete. This is at least twice as much as is contained in ordinary concrete.

The diffusivity of moisture in these spheres was calculated from the above room temperature weight data as follows: It was assumed that the moisture concentration in the concrete follows the diffusion equation $\nabla^2 M = \alpha^2 dM/dt$, where M is the density of H_2O in grams per cm³ in the concrete, α^2 is the reciprocal of the diffusivity and has dimensions of hours per cm², and t is the time in hours.

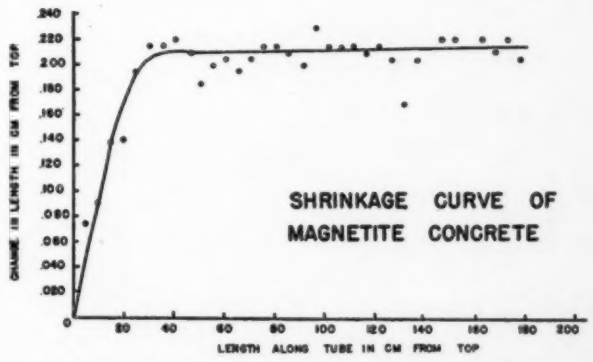

FIG. 3. The shrinkage of a column of magnetite concrete. The ordinate is the change in distance from the top of the column experienced by a point the initial position of which is given by the abscissa. Thus a point initially 10 cm from the top, after setting of the concrete will be about (20 − 0.1) or 19.9 cm from the top. The total shrinkage of a column whose initial length is given by the abscissa will be that shown by the corresponding ordinate.

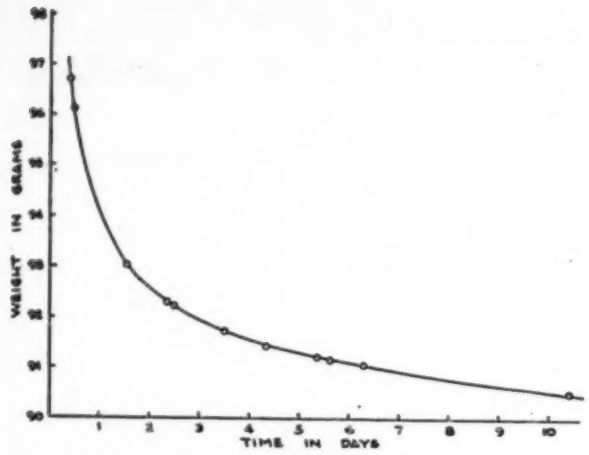

FIG. 4. Total weight of a 1½-inch diameter magnetite concrete sphere No. 10 as a function of the time during which it was left in dry air.

The useful solution to this equation in spherical coordinates is [1,2]

$$M=\sum_{1}^{\infty} A_m \frac{\sin mr}{r} \exp\left[-\frac{m^2}{\alpha^2}t\right].$$

Putting in the boundary conditions that at $t=0$, $M=M_0$ for all r; and that at $r=a$ (the radius of the sphere), $M=0$ for all t, the following result is obtained:

$$M=\sum_{n=1}^{\infty} \frac{2\alpha M_0(-1)^{n+1}\sin(n\pi r/a)}{n\pi r} \exp\left[-\frac{n^2\pi^2}{a^2\alpha^2}t\right].$$

Since the information obtained experimentally is the time dependence of the total weight of the sphere including its moisture, we integrate the above equation throughout the sphere and obtain the following result for the total moisture content T as a function of time:

$$T=\sum_{n=1}^{\infty} \frac{8\alpha^3 M_0}{n^2\pi} \exp\left[-\frac{n^2\pi^2}{a^2\alpha^2}t\right].$$

At large t all terms after the first in this sum are negligible compared to the first. Therefore, the negative derivative of T with respect to t at large times is approximately given by:

$$-\frac{dT}{dt}=\frac{8a\pi M_0}{\alpha^2} \exp\left[-\frac{\pi^2}{a^2\alpha^2}t\right].$$

The logarithm of this expression is then a linear function of the time, with slope proportional to the diffusivity, or

$$\log\left(-\frac{dT}{dt}\right)=\log\frac{8a\pi M_0}{\alpha^2}-\left[\frac{\pi^2}{a^2\alpha^2}t\right].$$

Therefore, to determine the diffusivity, the logarithm of the negative slope of the curve of total weight against time is plotted as a function of t. Typical slope curves are shown in Figs. 6 and 7. From these $1/\alpha^2$ is found to be about 10^{-2} cm²/hr.

Since the concrete in the Carnegie Institute of Technology shielding will be in the form of slabs effectively infinite in extent in two directions and finite with dimension L in the third, the total moisture content of the shielding may be expected to vary with t as:[2]

$$T=T_0(8/\pi^2)\exp[-\pi^2 t/L^2\alpha^2].$$

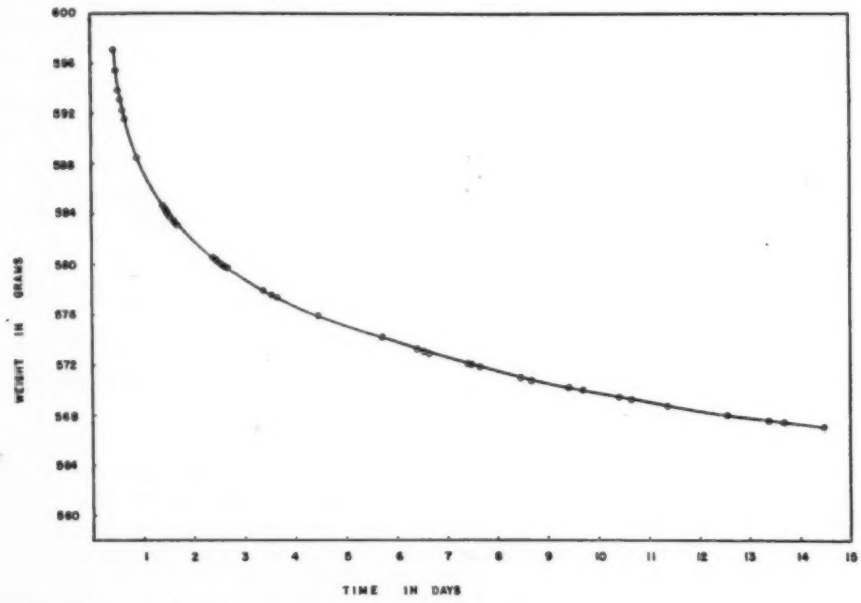

FIG. 5. Total weight of a three-inch diameter magnetite concrete sphere No. 4 as function of the time during which it was left in dry air.

[1] The notation is: $\exp[x]$ means the log base e raised to the power x.
[2] See, for instance, L. R. Ingersoll and O. J. Zobel, *Mathematical Theory of Heat Conduction* (Ginn and Company, New York, 1913).

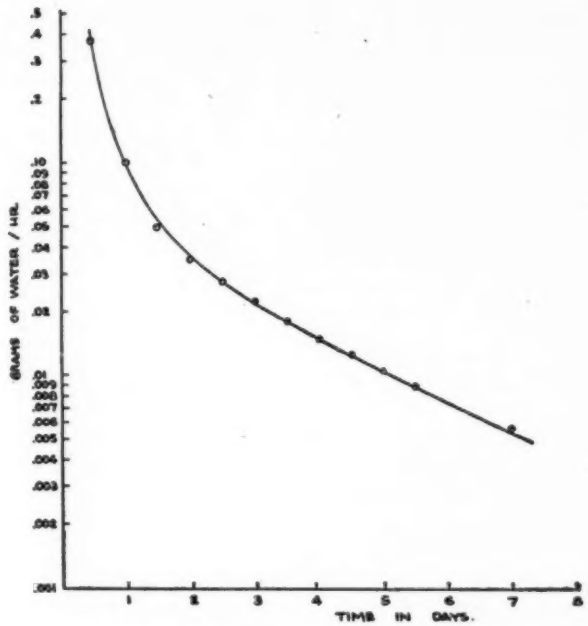

FIG. 6. Slope of weight *vs.* time curve of 1½-inch diameter magnetite concrete sphere No. 10. The slope of this semilogarithmic plot is proportional to the diffusivity of moisture in the concrete.

A convenient expression is obtained for the time when the total moisture content of the shielding falls to five-tenths its value at zero time. This is

$$t_{0.5}=(\alpha^2L^2/\pi^2)\log(16/\pi^2)$$

or

$$t_{0.5}=(\alpha^2L^2/\pi^2)(0.48).$$

For the diffusivities found, $\sim 10^{-2}$ cm²/hr., and for an eight-foot thickness of shield, $t_{0.5}=290{,}000$ hr. for about 33 yr. This result is in fact probably pessimistic, since the moisture content in the air of the cyclotron room will not be zero.

Some commercial coating materials intended to waterproof concrete were applied to concrete spheres, but no measurable differences in the over-all rate of loss of water over that from the uncoated spheres was observed. It is clear, therefore, that since no effect was observed even on three-inch spheres, this coating would be useless on the eight-foot slabs where diffusion times will be several hundred times as long, due to the greater diffusion distance.

MAGNETIC PERMEABILITY

The magnetic permeability of the magnetite concrete was measured by J. E. Goldman of the Westinghouse Research Laboratories. $B-H$ and $\mu-H$ curves are shown in Fig. 8.

RADIATION TESTS

A comparison of magnetite concrete and ordinary concrete was made for their shielding properties for the low energy radiations available in our laboratory, with the help of Mr. James Mates. For these experiments 16-inch diameter hemispheres were made of the two kinds of concrete. Each had a three-inch diameter hemispherical cavity in the center. The source of gamma- and neutron radiation for the experiments was a 40-mc Mesothorium source about three mm in diameter, which was inserted into the three-inch cavity in the center of the concrete sphere with or without a Be jacket around the source. This provides gammas with energies up to 2.62 Mev and, with the Be in place, neutrons up to about 0.85 Mev.

Using a Geiger counter, the gamma-ray intensity at the surface of the ordinary concrete sphere was found

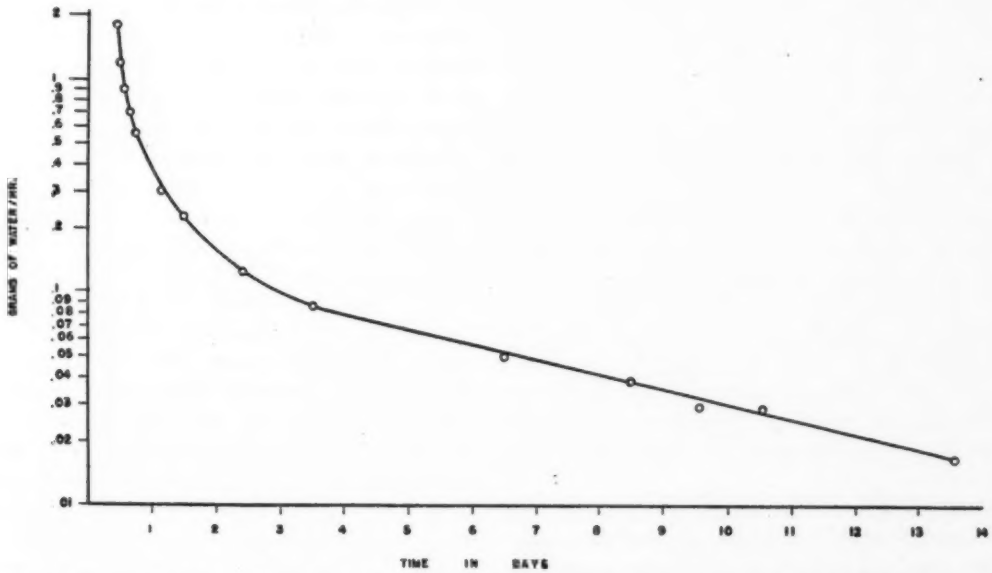

FIG. 7. Slope of weight *vs.* time curve of three-inch diameter magnetite concrete sphere No. 4. The slope of this semilogarithmic plot is proportional to the diffusivity of moisture in the concrete.

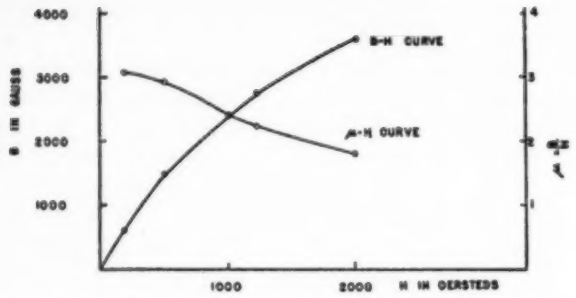

FIG. 8. Flux density and permeability of magnetite concrete as a function of the applied external field.

to be 1.7 times that at the surface of the magnetite concrete sphere. These figures apply to the geometry of the spherical shell. When the concrete spheres were removed and the counter placed in the same geometric relation to the gamma-ray source, the radiation intensity was found to be 6.9 times that received through the magnetite.

A measurement was made of low energy neutrons as detected by a BF_3 counter, connected to a linear amplifier, pulse-height discriminator, and scalar. The Mesothorium source was surrounded with beryllium metal to produce photo-neutrons. In this case, the slow neutron intensity at the surface of the magnetite sphere was found to be one-half that at the surface of the ordinary concrete sphere. However, when neither sphere was in place, but the counter was held at the same distance from the neutron source, the slow neutron intensity was found to be only one-half as much as when the magnetite concrete sphere was in place. This may be explained by the slowing down of the photo-neutrons by the material of the spheres.

To detect only fast neutrons emerging from the spheres, the BF_3 counter was next surrounded with a two-inch layer of paraffin, which in turn was surrounded with a sheet of cadmium. With this detector the ratio of the measured fast neutron intensity at the surface of the magnetite concrete to that at the surface of the ordinary concrete was 1:1.8. With no concrete sphere in place, the intensity was 7.6 times that observed through the magnetite sphere.

An estimate of the "half-thickness" of these concretes for Mesothorium gamma-rays may be made as follows. Assuming a point source of gammas, the intensity in air should fall off with distance as $1/r^2$, while the intensity in concrete should go as $1/r^2 \exp(-r \ln 2/d)$ where d is the thickness of concrete which would reduce the intensity to one-half in the case of an incident plane wave of radiation. The data corresponds to a value for d of 6.9 cm for magnetite concrete and 9.8 cm for ordinary concrete.

A half-thickness for the neutrons detected in this experiment may be obtained in an approximate way similar to that used for gamma-rays. For the magnetite concrete this is 7.3 cm and for ordinary concrete is 10 cm.

It is difficult to extend an interpretation of the above data to the case in which we are most interested, namely, the shielding of a large synchro-cyclotron. However, since the final step in the destruction of radiation by any shielding must be due to reactions between matter and moderate-to-low energy radiation, the above information indicates that the magnetite concrete will be appreciably more effective than ordinary concrete.

COST

The cost of ordinary concrete shielding blocks in place is about \$9.00 per cubic foot and that of magnetite concrete blocks in place is about \$9.60 per cubic foot. The over-all differential cost for removeable block shields made from the two materials may be estimated as follows. For a large synchro-cyclotron the linear length of removable shielding in the form of blocks is, say, about 100 feet. If a ten-foot thickness of ordinary concrete is satisfactory, then on the basis of total *mass* alone, 7.7 feet of magnetite concrete should produce the same shielding. (Actually it should be appreciably better because of the abnormally high water content.) This would represent a saving of $100\times(10-7.7)=230$ square feet of floor space which at \$20.00 per square foot is \$4600.

The cost of the magnetite concrete, assuming a shielding height of 10 feet, would be $7.7\times100\times10\times\$9.60 = \$74{,}000$. The cost of the ordinary concrete would be $10\times100\times10\times\$9.00=\$90{,}000$. Thus, the saving in floor space plus the saving in concrete cost by using the magnetite shielding is approximately \$20,000 for this geometry.

CONCLUSION

Magnetite concrete appears to be useful material for shielding high energy nuclear particle accelerators, even though its cost per cubic foot in place is higher than that for ordinary concrete. The difference is at least balanced by the fact that due to its high density, less floor space is required to produce equivalent shielding.

The strength, setting, and shrinkage properties of magnetite concrete are thoroughly satisfactory. Its moisture content is high, and the rate of loss of moisture by diffusion in ordinary thick shielding geometries is slow enough so that this effect is negligible over a period of several years. For low energy gamma-rays and neutrons, the half-thickness is about seven cm as compared to about ten cm in ordinary concrete. These half-thicknesses are about in the inverse ratio of the densities of the two concretes (1:1.3). Although this data tells nothing of the half-thickness to expect for the very high energy case, it seems reasonable to expect a similar *ratio* of half-thicknesses for the two concretes.

Volume Changes in the Plastic Stages of Simple Compression

P. W. Bridgman
The Physics Laboratories, Harvard University, Cambridge, Massachusetts
(Received July 13, 1949)

A method has been devised by which the volume changes occurring during plastic flow in simple compression are directly measured in a dilatometer during the flow process. The great superiority of such a direct determination over an indirect determination from the alteration of dimensions is pointed out. Results are obtained for three rocks, quartz crystal, and a number of metals, including several grades of steel and iron. The volume change during plastic flow is not equal to the product of mean hydrostatic stress into the ordinary compressibility in the elastic range, but may vary in a much more complicated way. There are in the first place permanent changes of volume retained after release of stress; these have long been known and may be of either sign. In addition to the permanently retained changes there may be changes of volume during the action of stress which may be notably larger than the permanently retained part and which also may be of either sign. The most striking of these is a component of volume *increase* under increasing compressive stress which in the upper range of stress near the fracture point may be larger than the normal component of volume decrease, so that the total volume change is retrograde. This component is recoverable and reversible on release of stress. It would appear, therefore, that in at least some cases the *irreversible* phenomenon of fracture is prepared for in the region immediately below the stress of fracture by the appearance of a *reversible* change of volume of sign the opposite of that due to the elastic action of the stresses.

INTRODUCTION

FOR most practical purposes it is a good enough approximation to assume that volume changes in the plastic range are unimportant. In the actual solution of specific problems in plastic flow this assumption about volume change may be treated in different ways. In the majority of cases it is sufficient to neglect the volume change altogether by imposing such a condition on the strains that the associated volume change vanishes. A second stage of approximation, which neglects strain hardening, treats the volume change as constant during plastic flow and equal to the elastic change under the yield point stresses. The third stage of approximation, which I think represents the most advanced stage at present, takes account of strain hardening and recognizes that the volume may vary during plastic flow because of the variation in stress associated with hardening. The simplest assumption here is that the volume change is proportional to the mean of the three principal stresses, with the same constant of proportionality which holds in the elastic range. This assumption would not be inconsistent with the assumption of isotropy in the strain hardening range, but this assumption is known not to be a good approximation, except for small strains.

Although the factor of volume change is not important in the majority of cases, there are cases where it is important. An example would be the problem of finding the surface separating the plastic from the elastic regions in a massive block of material exposed to stresses above the yield point over parts only of its surface. Another conceivable application would be to the interpretation of seismic waves in the earth. If the effective volume compressibility were different during the process of plastic flow than during static conditions, or if there were anisotropies in the velocity of propagation associated with the direction of plastic flow, conclusions drawn from seismic records might be modified.

Very little has been done in the way of experimental attack on this problem. There is work at the Bureau of Standards by Stang, Greenspan, and Newman[1] on two aluminum alloys and two grades of steel strained in simple tensions up to elongations of 18 percent. The principal strains were measured directly and the results expressed in terms of an effective Poisson's ratio. Most of the measurements were made on thin specimens cut from sheets, so that only two of the three principal strains were measured and the volume changes could not be obtained. The specimens of one grade of steel were circular in section, however, and the volume change was computed from the measured change of length and diameter, on the assumption of isotropy and unaltered Young's modulus on release. In these particular measurements the longitudinal strains were carried only to 1 percent. A large part of the volume change in the plastic range was found to be permanent up to nearly 0.1 percent decrease of density.

The enormous superiority of a direct measurement of the volume change as compared with its indirect determination from measurements of the change of longitudinal and lateral dimensions, as at the Bureau of Standards, is apparent from a simple example. Consider a cylinder of mild steel plastically shortened to 0.85 its initial length by an axial load of 7000 kg/cm². The change of radius under these conditions, assuming no change of volume, differs by only 0.07 percent from that which would be calculated assuming the full elastic change of volume corresponding to this stress. This means that any significant deviations of the change of volume from that expected must be described in terms of measurements within a 0.07 percent range. This is such a difficult problem as to be well nigh hopeless, and the direct attack seems the only one worth considering.

EXPERIMENTAL METHOD

In the following a direct experimental attack was made on this problem by immersing the specimen

[1] Stang, Greenspan, and Newman, J. Research Nat. Bur. Stand. 37, 211–221 (1946).

undergoing plastic deformation in a dilatometer, which is filled with a liquid and provided with a capillary open to the atmosphere in which the liquid meniscus moves in response to changes of volume of the contents of the dilatometer. Simplicity of construction suggested simple linear compression as the type of plastic deformation that could be most easily handled. The apparatus is shown in Fig. 1. The specimen S, surrounded by a liquid in the chamber C, is compressed by the piston P_1 against the bed plate B. In order to compensate for the volume swept out by the piston as it descends compressing S, P_1 is coupled to another piston P_2 of exactly the same cross section, so that as P_1 enters the liquid filled space P_2 is withdrawn by the same amount, and together there is no change of volume and no motion of the meniscus. The adequacy of the apparatus in this respect can be simply checked by displacing the coupled pistons in the absence of a specimen. The motion of the liquid in the capillary is determined by the volume change of the specimen plus a contribution arising from the distortion of the end of the piston and of the chamber C arising from the action of the stresses in the supporting members. The effect of these distortions can be eliminated by using the differential displacement of the meniscus between that given by the plastically deformed specimen and that of a dummy specimen of hardened steel which undergoes only elastic deformation.

The compressive force was applied to the piston P_1 in one of my standard hydraulic pressures, with 3.5 inch piston, actuated by a hand pump having a maximum capacity of 15,000 p.s.i. The pressure was altered in controlled steps by coupling the press to a free piston gauge, the weights of which were varied in appropriate steps. The specimens were almost always 2.5 long and from 1 to 1.5 inches in diameter, depending on the strength of the material. The load was increased in equal steps, usually about 15 in number, until a plastic shortening of the order of 16 percent was reached. Pressure increments were applied on a uniform time schedule, usually one step every 30 seconds. Every increment of load is of course accompanied by temperature effects. In the elastic range these temperature effects were beyond the sensitivity of the apparatus, but in the plastic range, where it is to be expected from the work of Taylor and Quinney[2] that practically all the work of permanent deformation will be converted into heat, the temperature effects in the last and largest stages of plastic deformation become so large as to seriously disturb the course of the readings. In order to eliminate this effect, the maximum load was maintained constant for a long enough interval, usually about 15 or 20 minutes, for the heat of compression to dissipate itself by conduction to other parts of the apparatus, as shown by the cessation of drift in the readings. The load was then released in the same equal steps and on the same time schedule as during the increasing part of the cycle. The possibility of making readings during unloading is an advantage of this method.

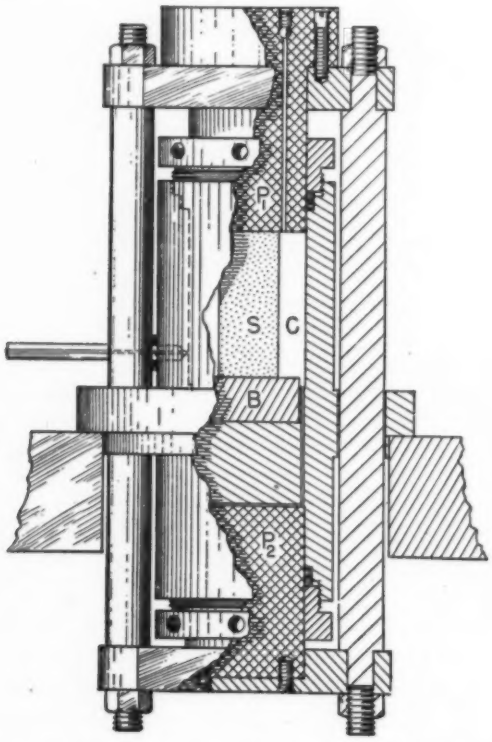

FIG. 1. Dilatometer apparatus for determining the change of volume of the specimen S during simple compression.

Temperature equalization was hastened by stuffing the space between specimen and chamber walls with narrow copper ribbon, such as is sold for scouring dishes in hardware stores. The apparatus was not thermostatted, but the room seldom varied as much as 0.2° during a run. A thermometer was mounted in close thermal contact with the outside of the dilatometer chamber and readings made of temperature drift before and after the run. During the maximum part of the plastic deformation this thermometer indicated a pulse of temperature rise of sometimes as much as 0.5°, but this rapidly dropped back to a permanent temperature rise of not more than 0.1 or 0.2°. Blank runs indicated that uniform temperature changes of as much as this introduced no appreciable error. The liquid filling the chamber and capillary was a mixture of water with a rust inhibitor sold by Sears Roebuck for use in automobile radiators. Water was chosen as the base because of its low thermal expansion.

In much of the preliminary work the capillary thread was mercury, separated by appropriate means from the solution in the chamber. The purpose of the mercury was to avoid error from the aqueous solution dragging out on the walls of the capillary, but the error was found to be inappreciable, and since considerable complication was introduced by the use of two liquids, particularly in getting rid of air, the use of mercury was

[2] G. I. Taylor and H. Quinney, Proc. Roy. Soc. **A134**, 307 (1934).

abandoned in the later experiments. Complete absence of air bubbles in any part of the apparatus is essential. To this end the solution was freed from dissolved air by fresh evacuation before each filling, and the filling itself was conducted with the aid of a vacuum pump. The position of the meniscus in the capillary was adjusted after the apparatus was in place in the press by sucking out excess liquid with the air pump through a fine steel capillary thrust down inside the glass capillary. If there is air in any part of the apparatus the meniscus jumps on applying vacuum to the steel capillary; in this way satisfactory filling could be checked.

In order to function satisfactorily the apparatus must be well made; for this reason the chamber and its supporting rim were turned from the solid piece. The pistons were hardened and ground all over and polished on their cylindrical surfaces. The ends of the specimens were ground to parallelism in the surface grinder. The rubber washers where the pistons enter the chamber are a crucial matter; they must be thin to avoid excessive friction and close fitting enough to avoid perceptible leak. Excessive friction at the packing reveals itself as an initial abnormal motion of the meniscus in the "wrong" direction on reversing the direction of motion of the piston. Part of this is due to elastic stretch in the tie rods coupling the two pistons, which can be minimized by making the rods large enough in diameter, and part is due to a frictional dragging of the rubber packing with the piston, which can be minimized by making the steel washers which confine the rubber a good fit for the piston. By proper attention to details this abnormal reverse motion of the meniscus was practically eliminated, but at first it proved troublesome.

In the elastic range elementary elasticity theory indicates that the volume change, as given by the motion of the meniscus, should be simply proportional to the load and the length of the specimen and independent of the cross section. For an isotropic material the volume change under a principal stress system which has only a single component Z_z along the axis of the cylinder is: $\Delta V/V_0=(\kappa/3)Z_z$, where κ is the ordinary coefficient of cubic compressibility. Substituting the relations $V_0=\pi r^2 l$ and load $=\pi r^2 Z_z$ gives at once

$$\Delta V=(\kappa/3)\cdot l\cdot \text{load}. \qquad (1)$$

As already mentioned, the experiment has to be performed differentially in order to eliminate distortion in the apparatus. In the apparatus as constructed this distortion was comparatively large. When the dummy of hardened steel was used only about 25 percent of the total motion of the meniscus was due to pure volume compression, the balance being due to distortion. This distortion arises almost entirely from change of length of P_1 under the compressive load. The capillary, which was calibrated for uniformity, had a cross section of 0.01 cm². This, with a specimen of hardened steel 2.5 inches long, gave a total motion of the meniscus of approximately 20 cm under the maximum load of 40,000 kg. Of this 20 cm, 5 cm arose from pure volume compression. The position of the meniscus could be read to 0.1 mm, thus making possible, as far as sensitivity of reading goes, a determination of the effective compressibility to a few tenths of a percent. Actually, other irregularities made an accuracy as high as this illusory.

In addition to measurements of the volume from the position of the meniscus the change of length of the specimen was read with an Ames 0.0001-inch dial gauge attached to the piston of the press. With this gauge the beginning of plastic flow could be determined.

The fundamental question at issue was how the plot of ΔV against load continues beyond the plastic yield point; does it experience at once a change of character or does it suffer only slow change? One broad feature in the eventual behavior of the curve can be anticipated because it is known that many substances experience permanent alterations of density after exposure to plastic yield and release of the deforming stresses. The permanent alterations of density were given directly by the difference of position of the meniscus before and after the run. In a number of instances the permanent change of density so determined was checked by direct determination of the density before and after by weighings in air and water.

The simplest anticipation of what to expect is that on the first application of load the curve of ΔV *versus* load beyond the first yield point departs from the linear relation below the yield point by a gradually increasing amount which at the maximum is equal to the permanent change of volume found on release of stress, and that on release of stress the whole curve, except for a correction to be described presently, is displaced by an amount equal to the permanent change of volume, and that it is straight with the same slope as in the initial elastic range. On the second application and release of stress the simplest anticipation is that the curve, corrected as will be indicated, will be straight and have the same slope as in the elastic range. The correction indicated arises from the permanent change of length, since according to formula (1) the change of volume is proportional to load and length. After the first maximum load the length is shortened by about 16 percent, so that on first release and second reapplication the changes of volume to be expected are 16 percent less than at the same load in the initial elastic range. Correction was made for this by multiplying the observed volume changes, after subtracting off the correction for the distortion of the dilatometer obtained from the dummy run, by the ratio of initial to final length.

The simplest anticipation just outlined did not, as a matter of fact, turn out to be realized, but there were departures depending on the individual material. In all cases, and superposed on other complexities, there

was hysteresis, and therefore failure of the complete isotropy assumed in deriving Eq. (1). This means, even for those parts of the curve which are approximately linear, that the constant of proportionality between load and ΔV is no longer simply connected with the coefficient of cubic compressibility, that is, with the volume change under hydrostatic pressure. This coefficient would, under the circumstances, have to be determined by direct experiment in which a hydrostatic pressure is actually applied to the specimen. However one may, if desired, retain the same equation and speak formally of an "effective compressibility" defined by the equation

$$\kappa_{\text{eff}} = 3\Delta V/(l \cdot \text{load}). \tag{2}$$

What the further significance of this effective compressibility is out of its immediate context would have to be found by other sorts of experiment for obviously the present experiments cannot give a complete description of the behavior under all stress systems of material rendered anisotropic by simple compression.

The actual stress system to which the specimens were subjected was not the simple one component Z_z assumed so far in the discussion, but was complicated, after plastic yield had started, by the addition of frictional components on the ends, which manifested themselves as barrelling of the specimen. The magnitude of the barrelling was a function of the material; it was a maximum for copper, for which the plastic increase of diameter was 35 percent less at the ends than at the center, and a minimum for iron, for which it was 21 percent less. Since in the elastic range shearing stresses are accompanied by no change of volume, it is probably safe to assume that under these conditions the frictional stresses on the ends introduced no appreciable change of volume.

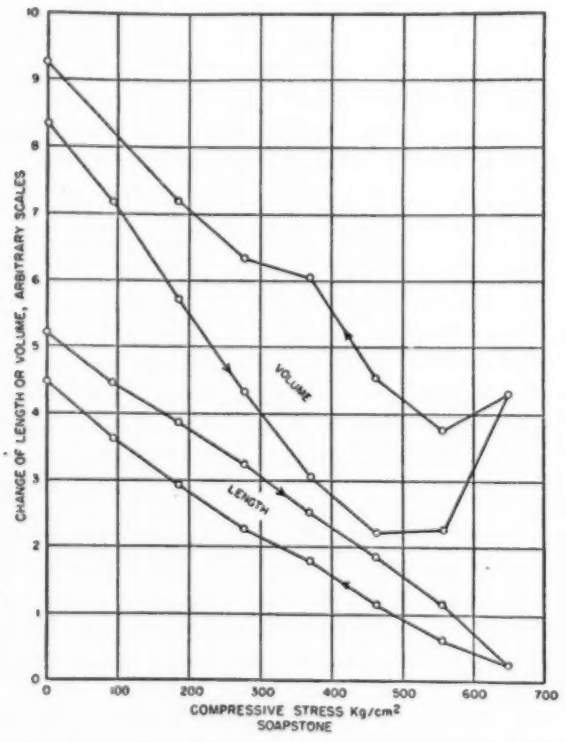

FIG. 2. The changes of length and of volume, both on an arbitrary scale, of soapstone as a function of stress during simple compression.

Some 40 experiments were made in all, of which 12 should be regarded as preliminary. The largest number of measurements were made on iron or steel from various sources, including cast iron, various low carbon steels of commerce, Norway iron, a high carbon steel, and an 18–8 stainless steel. The other metals were copper, brass, and duralumin. In addition, three rocks were tried: soapstone, marble, and diabase. Measurements were also made on two single quartz crystals. The results obtained with the rocks were unexpected and significant, opening up a new point of view with regard to what might be expected in general. Since the unexpected features shown by the rocks seem to be presented to a much less but still appreciable degree by some of the metals, it will probably conduce to clearness to describe the results for the rocks first. I owe all the specimens of rocks to the kindness of Professor Francis Birch, who has had much experience in the preparation of cylindrical specimens of various materials for his geophysical experiments.

EXPERIMENTAL RESULTS

Soapstone

Preliminary experiments with other specimens indicated the very narrow range within which this brittle material may be expected to support permanent deformation without fracture. The final specimen was exposed to two cycles of loading up to a maximum of 650 kg/cm². The first application of load resulted in a permanent shortening of 0.07 percent. On the second application there was further permanent shortening of 0.015 percent, combined with a hysteresis of 0.07 percent. After the first cycle of loading there was a permanent increase of volume of 0.0069 percent, or one tenth the fractional change of length, and after the second cycle an additional permanent volume increase of one-half as much. The specimen had received no externally visible permanent damage at the end of the two cycles. In Fig. 2 the volume change during the first cycle is plotted as a function of compressive stress; the plot for the second cycle is essentially similar. The volume change during increase of load appears as the sum of two effects. The first of these is the normal volume decrease, linear in the load, contributed by the volume compressibility as analyzed in Eq. (1). Superposed on this there is an effect in the opposite direction, that is, a volume increase, which becomes larger so rapidly at the higher loads that it dominates the situation and at the two highest loads the volume increases with increase of compressive load. This increase of

volume can naturally be ascribed to an opening of interstices in the structure as a premonition of the fracture that would occur at a load only slightly beyond the maximum reached. However, the unexpected feature is that this opening of interstices in preparation for fracture has a very large recoverable component, so that in the initial stages of release of load the volume decreases instead of increasing as it would in the elastic range. This recovery proceeds further during release of load so that only a small fraction of the abnormal volume increase at the maximum load is permanently retained on total release of load.

This recoverable volume increase under compressive stress, probably associated with the opening of interstices, is the new feature disclosed by these measurements. Evidences of the same effect are to be looked for in other materials. I think it is natural to expect the effect to be largest in brittle crystalline materials.

Marble

Three specimens of superficially flawless marble from Darby, Vermont, were used. The recoverable volume effects are larger for marble than for soapstone, but on the other hand the balance between permanent plastic deformation and complete fracture is much more delicate and three specimens were used before satisfactory readings were obtained in the region of recoverable volume increase. The relation between volume and load for the third specimen is shown in Fig. 3. The maximum load reached was 510 kg/cm². Application of this load was immediately followed by such rapid creep of the volume readings that the load was at once decreased as rapidly as possible to the next lower step, 500 kg/cm², in order to avoid fracture. Although good readings could not be made in the region of rapid motion, the meniscus was momentarily observed several centimeters beyond the maximum recorded in Fig. 2, corresponding to a recoverable volume increase of perhaps 0.1 percent. An even more extreme case of recoverable volume change was observed in one of the preliminary specimens in which a volume recovery of 20 centimeters of the capillary, or 0.3 percent of the total volume, was observed during the rapid manipulations incident to saving the specimen from catastrophic fracture. Returning now to the third specimen, Fig. 3 shows a permanent volume increase after release of load of 0.04 percent. The specimen was so badly flawed and disintegrated in parts that a second application of load was not attempted. Marble differs from soapstone in that the recoverable volume change during release of load is not spread so uniformly over the entire range of load, but is confined practically entirely to the first 20 percent of release from the maximum. Over the mid-60 percent on releasing load the curve is parallel to the same part of the curve for increasing load, unlike soapstone. The volume compressibility, to be calculated according to Eq. (1), does not agree with the volume compressibility given directly by measurements with hydrostatic pressure. The compressibility so calculated is abnormally high in the first 10 percent of the range, being about 38×10^{-7} (kg/cm² unit), and in the mid-range, where the relation is approximately linear, is abnormally low, being 7.6×10^{-7}, whereas the measurements of Adams and myself[3] suggest a value in the neighborhood of 13.5×10^{-7}. The change of length as a function of load is also shown in Fig. 3. The permanent fractional decrease of length was 0.25 percent, 6 times as great as the permanent fractional increase of volume.

Diabase

This proved to be an extremely brittle material, much more brittle than soapstone or marble. Measurements were made on two specimens. The first specimen fractured at a maximum load of 2490 kg/cm², after practically no warning of impending catastrophe from the length measurements, the last length measurement before fracture differing from a Hooke's law linear rela-

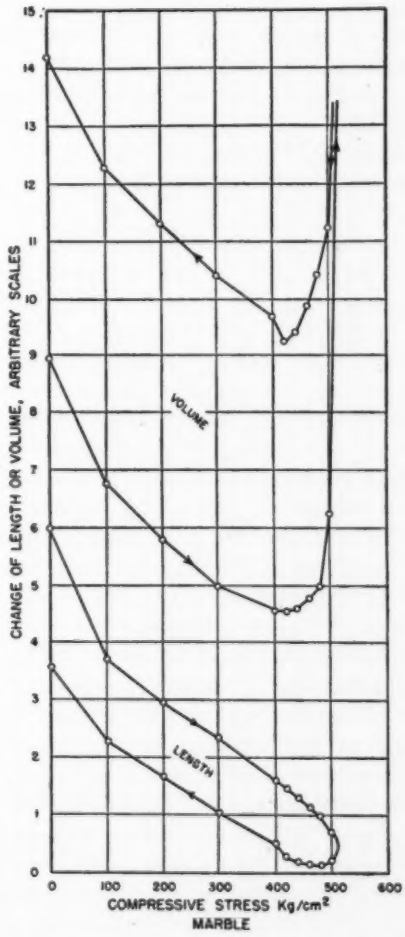

FIG. 3. The changes of length and of volume, both on an arbitrary scale, of marble as a function of stress during simple compression.

[3] L. H. Adams and E. D. Williamson, J. Frank. Inst. 195, 493 (1923); P. W. Bridgman, Am. J. Sci. 7, 96 (1924).

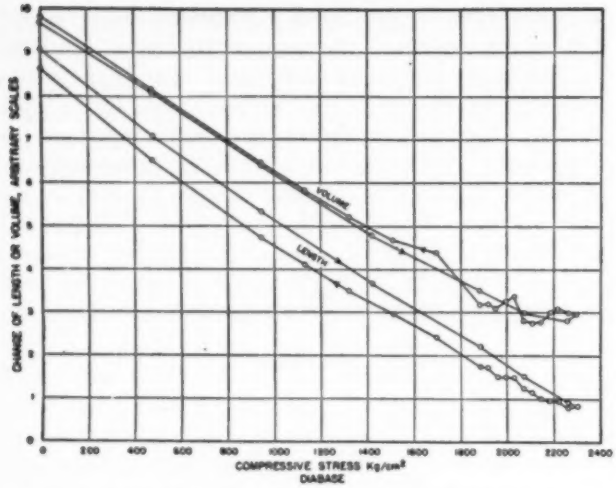

FIG. 4. The changes of length and of volume, both on an arbibitrary scale, of diabase as a function of stress during simple compression.

tion by only 0.01 percent of the length. The volume measurements were much more sensitive, however, perceptible deviation from Hooke's law in the "abnormal" direction having already begun at one half the final load, and at the last reading having progressed so far as to result in a reversal in direction of motion of the meniscus. In the initial linear part of the curve the cubic compressibility calculated according to Eq. (1) was 16×10^{-7} against a value in the general neighborhood of 11×10^{-7} to be expected from direct measurements by Birch.[4] The second specimen was handled more gingerly than the first. Increase of load in the smallest increments, corresponding to 38 kg/cm², was initiated at a somewhat smaller load than before, and load was immediately reversed on the first reversal of motion of the meniscus. The maximum load reached on the first cycle was 2300 kg/cm.² A second cycle was then applied to a maximum of 2090 kg/cm². There was no perceptible permanent change of volume after either of these cycles. A third loading was then applied to the previous maximum of 2090 kg/cm², where the specimen broke with great brittleness after holding the load for a few seconds. The volume changes of the change of length during the first cycle are shown in Fig. 4. During the first loading the "abnormal" component of volume increase is plainly evident in the increase of curvature culminating in final reversal of direction at the last point. This abnormal component of volume increase throws the material into a highly complex state, as shown by the oscillations in the curve on release of load. These oscillations in the volume curve are reflected in less extreme fluctuations in the curve for change of length. The effect of the abnormal volume component gradually disappears on releasing load; after one half load it is no longer evident, and the specimen returns to zero load with no certain permanent effect on the volume. Loading in the second cycle was not carried far enough to give reversal of the volume curve, but the same reverse curvature was found beyond one-half loading on both ascending and descending branches. A new feature on the second cycle was the appearance of hysteresis on the volume curve, amounting at the maximum to 0.00004 of the total volume. This hysteresis was distributed smoothly over the entire extent of the curve, vanishing only with complete release of load.

In all these experiments on the three rocks the distortions beyond the elastic limit were so small that any temperature effects, even assuming that all the work of compression is dissipated as heat, were entirely negligible.

Quartz

Experiments were made on two specimens of single crystal quartz. These I owe to the kindness of Professor Frondel, who selected two flawless crystals from the resources of the University Museum, and to Professor Birch, who had them worked to dimensions in his shop. Both specimens were 0.875 inch in diameter; one was 2.0 and the other 2.5 inches long, the crystal axis being along the length. Load was carried to the beginning of failure, which was manifested by audible snapping, the flaking off of chips around the edges, and the appearance of internal longitudinal cleavage planes arranged in a hexagonal pattern corresponding to the crystal symmetry. The maximum load was 8300 kg/cm². No trace was found of the effect shown by the rocks, but the relation between both length and volume and load remained linear up to the maximum load, and on release there was no appreciable hysteresis and no permanent change of either length or volume. This agrees with what might be expected from other experiments with quartz crystals, for permanent plastic deformation in quartz crystals at room temperature has seldom if ever been realized.

We now turn to a description of the experiments with metals. In assessing the meaning of the results, the suggestions arising from the experiments with rocks are to be kept in mind, namely the entrance of a new volume effect at the upper end of the range of applicable stress, consisting of a component of increasing volume under increasing compressive load, which is recoverable in whole or in part on release of load. This increase of volume is most naturally thought of as due to the opening of interstices of one sort or another under the action of the stress system. These interstices may perhaps be fairly large, as between the grains or around mechanical impurities, or they may be on the much smaller scale of "dislocations" in the lattice. The precise shapes of these interstices and their orientation with respect to the stress system may be expected to vary from material to material, resulting in the appearance of different kinds of anisotropy. In addition to these

[4] Francis Birch and Richard B. Dow, Bull. Geol. Soc. Amer. 47, 1235 (1936).

interstices which increase in number under the action of a stress, it is to be anticipated that there may also be interstices initially present which tend to close and disappear as the compressive stress increases. Altogether, there are possibilities here for many types of behavior, of great complexity.

Mild Steel

Measurements were made on 8 specimens in all. This included 4 specimens of a 1035 steel which were machined to 1 inch in diameter from the residue of a 2-inch bar supplied by the Watertown Arsenal during the war for measurements of plastic distortion in connection with a war contract. This bar was specially selected by Dr. J. H. Hollomon for soundness and isotropy, a condition which was checked by the previous failure of simple compressive tests on 1-inch cubes in different orientations to show any detectible anisotropy. The other 4 specimens of mild steel included two specimens cut from a 1-inch bar of "screw stock" from the stock of the laboratory machine shop, and two specimens from a 1-inch bar of an ordinary commercial "cold rolled" steel.

The cold-rolled steel contained gross imperfections, evidenced at the termination of the run by longitudinal slip lines and extruded seams on the surface. Load was carried to a maximum of 7350 kg/cm² with shortening to 0.86 of the initial length. Measureable plastic yield in length began at 4700 kg/cm². At a load considerably less than this, at 3100 kg/cm², there occurred an abrupt discontinuity in the tangent of the volume curve in the direction of an abnormally high compressibility. The easy explanation of this is that it was due to the closing of imperfections initially present. At the upper end of the range any volume changes in the opposite direction, such as might be suggested by the experiments with rocks, were mostly masked by the temperature changes, but there was a small outstanding residue in this direction. An increased curvature in the initial stages of release was evidence of the same effect. There was no measureable permanent change of volume on conclusion; perhaps the two volume effects cancelled.

The "screw stock," judging by the appearance of the external surface of the yielded specimens, was essentially homogeneous and entirely different in character from the cold rolled. One of the specimens of screw stock was used for the express purpose of getting as much information as possible about the temperature effects during plastic yield. For this purpose the load was increased in a few seconds, immediately after the first appearance of yield, to its maximum value and maintained there for 23 minutes until creep in the volume readings had ceased, indicating the attainment of temperature equilibrium. First yield occurred at 5200 kg/cm²; the maximum was 7200 with shortening to 0.85 of the initial length. The temperature rise to be expected was computed on the basis of direct measurements of the constants of the apparatus. This involved finding the motion of the meniscus when the temperature of the entire apparatus was varied by varying the temperature of a water bath in which it was immersed, and by approximate calculations, involving the weights of the various parts, as to the probable initial distribution of temperature throughout the apparatus. Agreement within 1 percent was found between the measured temperature effect and that computed on the assumption that all the mechanical work of plastic deformation was dissipated as heat. This agreement is, however, fortuitous, the approximations made in the calculations being crude. Taylor and Quinney[2] have found, by experiments designed especially for the purpose, that 85 percent of the work of torsional deformation of a steel bar is dissipated as heat. It cannot be claimed that the present measurements contradict this.

The conventional series of measurements was made on the other specimen of screw stock. Yield point, maximum load, and permanent plastic yield were essentially the same as before. Two cycles of loading were applied; there was a permanent increase of proportional volume after the runs of 0.00014. On the initial application of load there was a break in the tangent of the volume curve at a load 10 percent higher than that of first perceptible yield, in the same abnormal direction as shown by the experiments on rocks, that is, in the direction of a component of increasing volume. At the maximum, this increase was about 50 percent greater

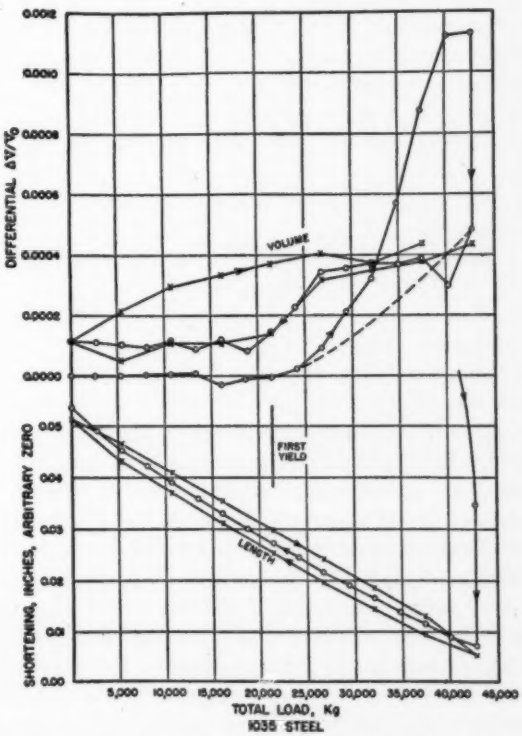

FIG. 5. Results for a 1035 steel. In the upper part of the figure the differential proportional change of volume is shown as a function of total load, and in the lower part the shortening in inches on an initial 2.5-inch length, taken from an arbitrary zero, is shown also as a function of total load.

than the increase of volume permanently retained on release of load. This 50 percent excess is the "recoverable" volume effect, and is distributed more or less uniformly over the entire range, resulting in a too small apparent compressibility on the first release and second cycle of loading. The volume curves after the first maximum were not entirely smooth, but indicated the presence of minor anisotropies. An effect shown by all three curves is a volume compressibility in the upper range of load nearly equal to normal, with a cusp-like decrease at a stress of 2500 kg/cm².

Measurements on the four specimens of 1035 steel gave results agreeing with each other in broad outline but differing in finer detail. The yield point, the maximum load, and the permanent shortening were not essentially different from the screw stock. There was a permanent proportional decrease of density after the runs of approximately 0.0001, given consistently both by the capillary and the weighings in air and water. On the first application of load all the specimens showed, in the general neighborhood of the yield point in length, but sometimes somewhat above and sometimes somewhat below the yield point, a change in direction of the volume curve, indicating the entrance of a component of increasing volume under compressive load.

Figure 5 shows in detail the results for that one of the four specimens for which the results were most complete. Unlike Figs. 2–4, it is the differential $\Delta V/V_0$ which is shown, obtained by calculation from the meniscus readings from which the readings obtained during the dummy run with hardened steel are subtracted off. A differential $\Delta V/V_0$ constant with load means a cubic compressibility, or rather an "effective cubic compressibility," the same as that of hardened steel. The latter is known to be about 1 percent greater than that of pure iron. After the first maximum of load the differential $\Delta V/V_0$'s of Fig. 5 have been corrected by a factor for the permanent change of length, as already explained. The figure shows that on the first application of load the differential $\Delta V/V_0$ remained approximately zero up to the yield point, indicating a cubic compressibility approximately the same as that of pure iron. On passing the yield point, the entrance of a component of increasing volume is rapidly manifest. The true extent of this is at first masked by temperature effects, but on attaining temperature equilibrium a component of permanent volume increase of approximately 0.00005 under the maximum load is indicated. On release of load this component of volume increase is rapidly relinquished until the load of the first yield point is reached; beyond this the component remains practically constant at 0.0001, which is the permanent increase of volume on total release of stress. The "recoverable" component of volume change is here 4 times as large as the permanently retained component, and much larger than for the screw stock. The "effective" compressibility on release is, below the yield point, the same as initially and the same as for pure iron. This does not mean, however, that the initial condition has been regained, for there is a high degree of anisotropy locked up, as shown by the large slope with which the $\Delta V/V_0$ plot starts out on the second application of load. The final volume reached on the second application is essentially the same as that reached on the first application, and the curve of second release practically duplicates that of first release.

It is to be noticed that the hysteresis in the volume relation on the second application of load is in the "abnormal" direction, being in advance of the load rather than lagging behind. Although this sort of hysteresis is unusual, it is not ruled out by thermodynamics, which demands only that work be dissipated in an irreversible cyclic process. This means that a loop must be a lagging loop when its area represents work done during the cycle. Here the coordinates of the loop have the dimensions of volume and force, so that the area does not represent work.

Norway Iron

The specimens were cut from a 5-inch bar in the collection of laboratory relics, which had been obtained by Professor E. H. Hall at least fifty years ago in order to furnish for his experiments a sufficient and reproducible stock of the purest iron then available. It was completely permeated by large scale mechanical imperfections as shown by the seams and slip lines which appeared on the external surface after plastic yield. These imperfections result in a gross behavior unlike that of any other substance. Two specimens were used both 2.5 inches long. The first was 1 inch in diameter; this was too small for the range of the apparatus and only a single cycle of stress was applied to it. The initial yield point was 1570 kg/cm² and the maximum load 4900, where the shortening was to 0.83 the initial length. The abnormal component of volume increase manifested itself almost at once on passing the yield point and increased so rapidly that the volume change was retrograde over nearly one-half the total stress range. Only a small part of the retrograde motion was due to temperature effect. After release of load there was a permenent proportional decrease of density of 0.0025. On release of load the curvature of the volume curve was in the abnormal direction, indicating a higher effective compressibility at the higher stresses. This means that the interstices opened to a certain extent on release of compressive stress, and can be understood if the interstices were flat on the average and oriented across the direction of stress.

The second specimen of Norway iron was 1.25 instead of 1 inch in diameter and could be carried over the normal load range of the apparatus. The first yield occurred at 1680 kg/cm²; load was increased to a maximum of 4600 kg/cm², where the length was reduced to 0.83 initial. It is to be noticed that the strain hardening characteristics of this iron are distinctly different from the steels, strain hardening extending

over a considerably wider range of stress. On release of load a second loading cycle was applied with no further permanent change of volume and very little hysteresis. The proportional permanent change of density was 0.002, consistently by both methods and somewhat less than for the first specimen. This volume increment functioned in the same way as for the first specimen, resulting, after the initial application, in too high an apparent compressibility in the upper stress range. The plot of ΔV *versus* stress on the second cycle consisted of two stretches, each approximately linear, with a knee and change of direction at approximately the stress of initial yield. This would indicate that the anomolous flattening of the interstices begins with increasing stress in the neighborhood of 1700 kg/cm², and plays itself out on release at the same stress.

High Carbon Steel

A single experiment was made on a high carbon steel, annealed drill rod from the laboratory machine shop stock of approximately 1.25 C. The behavior of this was quite different from the low carbon steels. The onset of plastic yield was much more gradual; it began to be perceptible at about 3200 kg/cm². Stress was carried to a maximum of 6900 kg/cm² where the length was reduced to 0.86 initial. On release of stress there was a permanent proportional *increase* of density of 0.00015. Corresponding to this unusual increase of density the character of the curve of volume change versus stress was different. At 3000 kg/cm² there was a slight change in direction corresponding to the expected opening of interstices with increasing stress, but this tendency persisted only to 4000, where there was an abrupt change of direction corresponding to the entry of the opposite effect, or closing of cavities with increasing stress. This dominated the situation above 4000, and was retained on release of load in the permanent increase of density. The volume curve of release of load exhibited several consistent episodes, but these were quite minor in character, and the curve was linear nearly within experimental error.

Cast Iron

Measurements were made on a single specimen of gray cast iron from the stock of the laboratory machine shop. The specimen was 2.5 inches long and 1.25 inch in diameter, turned from a 1.5-inch bar free from obvious imperfections. There was no proper yield point, but deviations from a linear relation between stress and shortening were detectible from the lowest stresses. Stress was pushed to a maximum of 3200 kg/cm², where the permanent shortening was 1.5 percent. After release of load there was a permanent increase of proportional volume of 0.0019. The entry of a component of volume increase was evident on the volume curve as low as 600 kg/cm²; from here it rapidly increased, resulting in retrograde motion above 2200 kg/cm². At the higher stresses this component of volume increase continued to increase with time under constant load, eventually reaching an asymptotic value. This creep is in the opposite direction from that arising from temperature effects, which were probably negligible because of the comparatively small amount of deformation. The maximum creep observed was equivalent to about one tenth the permanent volume change. On release of load the curve of volume versus stress was smooth, but with very marked curvature, corresponding to an effective compressibility rapidly increasing at the low stresses. The effect is in the direction to be explained by the open spaces acting like a more compressible substance coupled to the iron.

Stainless Steel

Measurements were made on a single specimen of "Type 303" from a bar in the laboratory machine shop stock. Type 303 is described as an 18–8 steel, with 0.20 maximum carbon. Plastic yield in length was first perceptible at 3600 kg/cm²; loading was increased to 7240 kg/cm², where the length was decreased to 0.865 initial. On release of load there was a permanent *increase* of proportional density of 0.00012. At no part of the loading or unloading process was there any evidence of the anomalous component of volume increase exhibited by other materials. On the first loading there was a break in the course of the curve of ΔV *versus* load immediately beyond the first yield point in the direction of increasing effective cubic compressibility, indicating a closing of interstices rather than an opening. At the maximum load this additional compression amounted, as well as could be judged, to two or three times the compression permanently retained on release of load. On release, practically all the difference between the maximum and the permanently retained excess compression was relinquished in the first 20 percent of the unloading, the curve being approximately linear in the last 80 percent of its course.

Copper

Measurements were made on four specimens, two of them preliminary before the apparatus was functioning satisfactorily. The specimens were all 2.5 inches long and 1.5 inches in diameter, taken from a 1.5-inch bar of hard drawn copper in the stock of the laboratory machine shop. One of the preliminary specimens was annealed; the other three were left in the hard drawn condition. The plastic shortening of these four specimens varied from 0.90 to 0.84. All four showed a permanent *increase* of proportional density varying from 0.00021 to 0.00049, with a rough correlation between the amount of plastic shortening and increase of density. In this correlation the annealed specimen did not fall out of line with the others.

The results in detail for the fourth specimen (hard drawn), for which the apparatus functioned most satis-

factorily, were as follows. First plastic yield in length was perceptible at a load of 1860 kg/cm²; loading was continued to a maximum of 3050 kg/cm², where the shortening was to 0.870 initial. On release of load the proportional density was increased by 0.00049 according to measurements by capillary and by 0.00047 according to weighing in air and water. On first application of load the curve of volume *versus* load passed smoothly through the yield point without alteration in direction. Practically all the disturbance of this curve occurred in the last step of loading, where 0.8 of the total plastic shortening occurred. The increase of density, once acquired, was permanently retained at a constant value independent of the load during the subsequent unloading and second cycle. This means that the effective cubic compressibility given by Eq. (1) was constant, except during the last step of the first loading, over the entire process of two loadings and two unloadings. The numerical value for this was 7.2×10^{-7} (kg/cm² unit), which checks exactly with my previous value[5] for copper directly determined by applying hydrostatic pressure.

Brass

Three sets of measurements were made, two of them with the preliminary apparatus. The specimens were 1.25 inches in diameter, from a bar of the same diameter of commercial brass from the stock of the laboratory machine shop. These were used "as is," and were presumably hard drawn. All three specimens gave permanent *increases* of density after plastic yield. The two preliminary specimens gave results of little value except for the permanent increase of density. The third specimen yielded first under a load of 3000 kg/cm²; it was carried to a maximum of 4900 kg/cm², where the shortening was to 0.89 initial. The permanent decrease of proportional density was 0.0002 by the capillary and one half as much by weighing. The results for this material were more complicated than for most of the others, doubtless a consequence of the high internal strains which every machinist knows are likely to be locked up in a bar of drawn brass. No disturbance in the ΔV *versus* load curve was evident on the first loading on passing the yield point, and the final equilibrium point lay on a smooth extrapolation from those points at loads low enough not to be disturbed by temperature effects. The curve on first release had a very pronounced S shape with minimum and maximum, and this S shape was retained, but less accentuated, on the second loading and unloading. The simplest description of the behavior is that it is as if there were two components in the volume change arising from the operation of the interstices. One of these is a closing of the pores under the application of load which has a permanently retained part and also another part of approximately equal magnitude which is relinquished in the first quarter of the unloading process. The second component is a recoverable and reversible opening of pores under load, uniformly spread over the entire stress range, which produces too low an effective compressibility as calculated by Eq. (1). The mean effective compressibility, calculated from the second loading cycle, disregarding the upper quarter of the range where the other component of volume change is dominant, is 7.1×10^{-7} against 9.2×10^{-7} (kg/cm² unit) expected from direct measurements under hydrostatic pressure.

Duralumin

Two preliminary measurements were made and one final one. The final specimen was 2.5 inches long and 1.25 inches diameter, cut from a 1.5-inch bar from the laboratory machine shop stock. First yield occurred at 3350 kg/cm². Load was increased to a maximum of 4600 kg/cm², where the length was 0.903 initial. The yield curve was of unusual character; it started with unusual abruptenss and then continued with a nearly linear relation between length and load to the maximum. Any permanent change of density was too small to certainly detect. No change could be established from the capillary, and the weighings gave 2.8080 for the density at room temperature of the virgin specimen, and 2.8079 after deformation. There was an abrupt and large change of slope of the ΔV *versus* load curve on passing the first yield point in the direction to be expected from the anomalous component of increasing volume under increasing compression. This increasing component at the maximum load, estimated by an extrapolation, had risen to the equivalent of a decrease of proportional density of 0.00046. None of this was apparently permanently retained on release of load, but the precise way in which it was relinquished on release of load was not apparent, since the curve consisted of several episodes with at least two points of inflection and one abrupt break in direction near the yield point. The effective cubic compressibility of duralumin calculated by Eq. (1) from the mean of the rising and falling curves, was 11.7×10^{-7} (kg/cm² unit). There is apparently no directly measured value for comparison. The direct value for pure aluminum, however, is 13.4×10^{-7}, suggesting that 11.7 would be smaller than what would be found by direct measurement.

DISCUSSION AND SUMMARY

It has been found that complicated changes of volume accompany the longitudinal plastic yielding of cylindrical specimens under simple compressive stress. It is simpler to describe these volume changes in their own terms than to introduce an effective Poisson's ratio, since even in the ideally simplest case the curve of Poisson's ratio is not simple in the region of large plastic yield. It is found that, superposed on the volume decrease under compressive stress that would be calculated by extending into the plastic range the simple linear relation which holds in the elastic and isotropic

[5] P. W. Bridgman, Proc. Am. Acad. 77, 206 (1949).

range, there are other components of volume change which may vary in a complicated way over the range of stress. These may be components either of volume increase or of decrease—the former would indicate the opening of the interstices and the latter their closing. Both of these effects may be manifested as permanent alterations of density on release of stress.

Of the materials examined in this paper, permanent increases of density were shown by annealed high carbon steel, an 18-8 stainless steel, copper, and hard drawn brass. The opposite effect, a permanent decrease of density, was shown by the three rocks (soapstone, marble and diabase), by two kinds of mild steel, by Norway iron and by gray cast iron. Vanishing volume change was found for quartz crystal, for a cold-rolled steel, and for duralumin. The volume increases of Norway iron and cast iron were comparatively large and doubtless the result of large scale imperfections of structure, and therefore not of particular significance. The component of volume increase shown by mild steel and the rocks probably involves a mechanism which is significant for theories of plastic flow and fracture. This component of volume increase is itself a strong function of stress. For the three rocks it increases so rapidly in the region just below fracture as to dominate the other factors so that the total volume change becomes retrograde. Furthermore, this component of volume increase is largely recoverable and reversible on release of stress. The same effect is also shown by the 1035 steel, although not to so large an extent as to result in retrograde change of volume. Four-fifths of the component of volume increase of this steel is relinquished on release of load and only one-fifth retained as permanent increase of volume. In Duralumin there is a component of volume increase at maximum load amounting to 0.00046, all of which is relinquished on release of load in the region above the initial yield point. In many cases the behavior of the volume on release of load and a subsequent cycle of reloading retains the memory of the initial plastic yield in an elbow on the volume curve at the stress of the initial yield point.

The new picture presented by these experiments is that fracture is prepared for, in at least some cases, by the *reversible* creation by the stress itself of alterations in the structure; when these alterations have proceeded to a critical degree the structure becomes unstable and fracture ensues. Perhaps the simplest way to think of this is as an increase in the number of "dislocations" which are normally present in the lattice. If the lattice under normal conditions tends to assume a certain equilibrium concentration of dislocations, it is natural to suppose that this equilibrium number may be increased with stress. It is probable that the same mechanism operates in simple tension as in simple compression, the energy differences which enter into the conditions of equilibrium being proportional to squares of the stress. It would, however, be more difficult experimentally to detect the effect for tension than for compression. Beside this new effect of a component of increasing volume under increasing compressive stress, some substances, notably copper, show the more naturally to be expected closing of imperfections under compressive stress. This may be retained as a whole or in part as a permanent increase of density on release of stress. There appears to be no reason why the two mechanisms should not operate simultaneously, and this does indeed seem to be the case for a material like brass with complicated behavior.

ACKNOWLEDGMENT

I am indebted to my mechanic, Mr. Charles E. Chase, for the skillful construction of the apparatus and for setting up the experiments.

Impedance of Resonant Transmission Lines and Wave Guides*

W. W. HARMAN
*University of Florida, Gainesville, Florida***
(Received July 5, 1949)

The relation of the Q to the impedance of a resonant transmission line is clarified. Universal curves relating Q and resonant impedance of capacitively terminated transmission-line and wave guide sections are presented and discussed. Their use in cavity resonator design and as a method for measuring resonator shunt resistance is considered.

RESONANT cavities and circuits for many purposes —tuned circuits for amplifiers and oscillators, klystron resonators, wave meters, to name a few—are made in the form of capacitively terminated sections of transmission line or wave guide, usually to facilitate tuning. The Q of such a circuit is easily measured and may be used as a sort of figure of merit for the resonator.[1] For many purposes, however, a parameter of more direct interest is the impedance presented across the terminating capacity at resonance. For resonant cavities in particular this is much more difficult to measure.

The purpose of this paper is to clarify the relationship between resonant impedance and Q, to present universal curves pertaining to this relationship, and to discuss their use in design and in the determination of resonant impedance from a measurement of resonator Q.

There are essentially two methods available for the direct measurement of the shunt resonant resistance in a resonant cavity where the methods suitable for use with unenclosed circuits cannot be applied. One depends on noting the effect on resonant frequency of a perturbation introduced in the capacitive gap, either by changing the spacing over a small portion of the gap area by means of a small piston,[2] or by the introduction of a small amount of dielectric in the gap.[3] Such a method can only be used when the capacitive part of the circuit is accessible; not, for example, when the terminating capacitance is a pair of klystron grids. The other method consists of measuring the interaction between the resonator fields and an electron stream passed through the capacitive gap. In one variation of this a known amount of power is introduced into the resonator at its resonant frequency and the velocity modulation produced in an electron stream passing through the gap is measured from data on the current to a collecting electrode as a function of its voltage[4] or by use of the magnetic spectrograph principle.[5] In another, a known signal, such as shot noise from a temperature-limited cathode, is impressed on the beam and the resulting power in the resonator measured.[6] Neither of these general methods is without its disadvantages and the determination of shunt resistance from the more easily measured resonator Q as described here is in many cases both convenient and accurate.

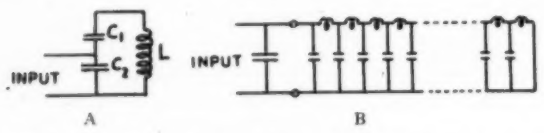

FIG. 1. Similarity between tapped resonant circuit and resonant transmission line.

I. SHUNT RESISTANCE—Q RELATION

In a lumped-constant, parallel $L-C$ circuit, the relation $R=Q\omega_0 C$ holds, ω_0 being the angular frequency at resonance. Here R is *defined* by $R=V^2/2P$ where P is the power loss with a peak voltage V across the capacitance. The fundamental definition of Q may be taken to be the ratio of energy stored to energy loss per radian. Two equivalent definitions involve half-power band width or rate of susceptance change at resonance,

$$Q=\frac{\text{frequency}}{\text{band width}}=\frac{1}{2}R\omega_0\left(\frac{dB}{d\omega}\right)_{\omega=\omega_0}. \tag{1}$$

If, now, the inductance is replaced by a shorted section of transmission line or wave guide with the same impedance appearing across its open terminals, the original $R-Q$ relationship no longer applies. Terman[7] defines an equivalent Q (which is incompatible with the energy definition of Q) to preserve the integrity of the formula. Slater[8] and Ramo and Whinnery[9] prefer

* This paper is a result of work sponsored jointly by the ONR and the Army Signal Corps and by an RCA fellowship in electronics.
** Formerly of Stanford University, California.
[1] For the purpose of this paper the word "resonator" will be interpreted to mean a general resonant circuit whether or not totally enclosed.
[2] W. W. Hansen and R. F. Post, "On the measurement of cavity impedance;" J. App. Phys. **19**, 1059 (1948).
[3] R. L. Sproull and E. G. Linder, "Resonant cavity measurements," Proc. I.R.E. **34**, 305 (1946).
[4] M. B. Adams, "The measurement of klystron resonator shunt resistance by the reflector-voltage method," Stanford Electronics Research Lab. Tech. Report No. 1, ONR Contract N6-onr-251, Task 7 (April 20, 1948).
[5] C. F. Hadley, "Velocity distribution of velocity-modulated electron beams," dissertation for Ph.D. degree, Stanford University (August 1944).
[6] P. Lacy, Stanford Microwave Lab. Report to Sperry Gyroscope Company (1948).
[7] F. E. Terman, *Radio Engineers Handbook* (McGraw-Hill Book Company, Inc., New York, 1943), Section 3, Part 16.
[8] J. C. Slater, "Microwave electronics," Rev. Mod. Phys. **18**, 480–482 (1946).
[9] S. Ramo and J. R. Whinnery, *Fields and Waves in Modern Radio* (John Wiley and Sons, Inc., New York, 1944), Art. 10.04.

to retain the basic definitions of Q and R but imply that some equivalent value of C (different from the C satisfying the resonance condition) will be chosen which will make everything come out all right.

If, however, we are willing to waive the inviolability of this relationship it may be rewritten in such a way that we need introduce no ambiguity into the concept of Q and R nor any divine guidance in the selection of an appropriate C.

It is possible to write

$$R=\zeta Q/\omega_0 C, \tag{2}$$

where ζ is a number between 0 and 1 which might be called the $R-Q$ factor. This factor is a measure of how effectively the electric field in the resonator is concentrated in the capacitance.

It may be noted that this procedure is exactly analogous to the conventional treatment of tapped resonant circuits. The input impedance at resonance of the tapped $L-C$ circuit of Fig. 1 is written

$$R=[C_1/(C_1+C_2)]Q/\omega_0 C_2. \tag{3}$$

There would seem to be no more need for defining equivalent Q's or C's for the resonant transmission line than in the tapped resonant circuit case.

The $R-Q$ factor is simply calculated from the rate of susceptance change expression for Q and the expression for total circuit susceptance of a shorted transmission section terminated in a capacitance,[10]

$$B=\omega C-(1/Z_0)\cot\beta l. \tag{4}$$

II. TRANSMISSION LINES WITH INFINITE CUT-OFF WAVE-LENGTH

In the case of transmission lines with a principal mode—parallel wire, concentric line, conical line, etc. —characteristic impedance is a constant independent of frequency and β is ω/c, whence,

$$\zeta=\frac{\omega_0 CR}{Q}=\frac{2}{1+(2\beta l/\sin 2\beta l)}. \tag{5}$$

This is plotted in Fig. 2.

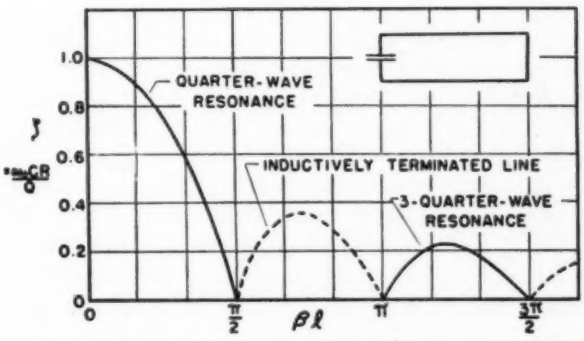

FIG. 2. R-Q factor for principal mode in a resonant transmission line.

The resonator Q is in many cases essentially independent of the length of the line[11] so that such generalizations as the relative shunt resistance of quarter-wave and three-quarter-wave modes and the presence of a maximum shunt resistance in the tunable three-quarter-wave resonator are immediately apparent.

The extent to which use of Fig. 2 is justified in the case of a concentric line resonator such as Fig. 3A might be questioned. Certainly such a resonator cannot be represented exactly by the equivalent circuit 3B because the fields in the vicinity of the gap bear no resemblance to ordinary transmission line fields. An equivalent circuit of the form of Fig. 3C may be a more adequate representation.[12]

With the use of such equivalent circuits it is possible to justify a procedure for estimating the shunt resistance of a concentric-line resonator from a Q measurement. If the tuning curve of wave-length *vs.* length for a resonator be measured, and an equivalent capacitance can be found by trial to make the tuning curve fit the universal tuning curve of Fig. 3D reasonably well over a fairly wide range, then that value of capacitance and the equivalent circuit of Fig. 3B can be used with Fig. 2 to obtain the resistance-Q ratio. For design purposes, information valuable for predicting tuning curves from

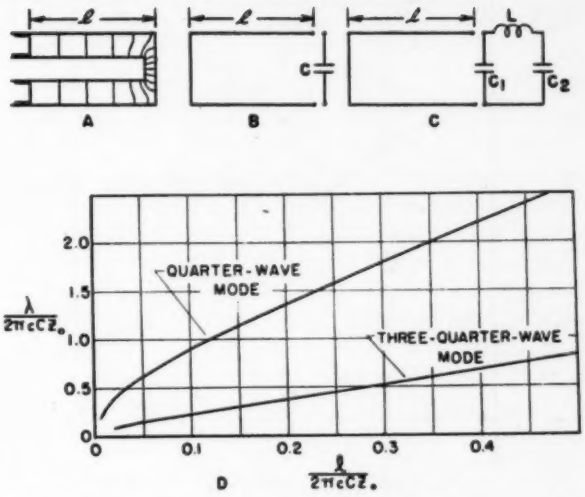

FIG. 3. Universal tuning curve for concentric-line resonator.

[10] More accurately, $Y=j\omega C-(1/Z_0)\coth\gamma l$, where $\gamma=\alpha+j\beta$, α and β being the attenuation and phase constants of the line. The simplified form introduces negligible error unless the line is very lossy or C is very small (βl is nearly an odd number of quarter-wave-lengths).

[11] The Q for principal modes, neglecting end losses and losses associated with the capacity, is given by $\beta/2\alpha$ (see S. I. Schelkunoff, *Electromagnetic Waves* (D. Van Nostrand, Inc., New York, 1943), Art. 7.22 where α and β are the attenuation and phase constants.

[12] Radio Research Laboratory Staff, *Very High Frequency Techniques* (McGraw-Hill Book Company, Inc., New York, 1948), Art. 32-12.

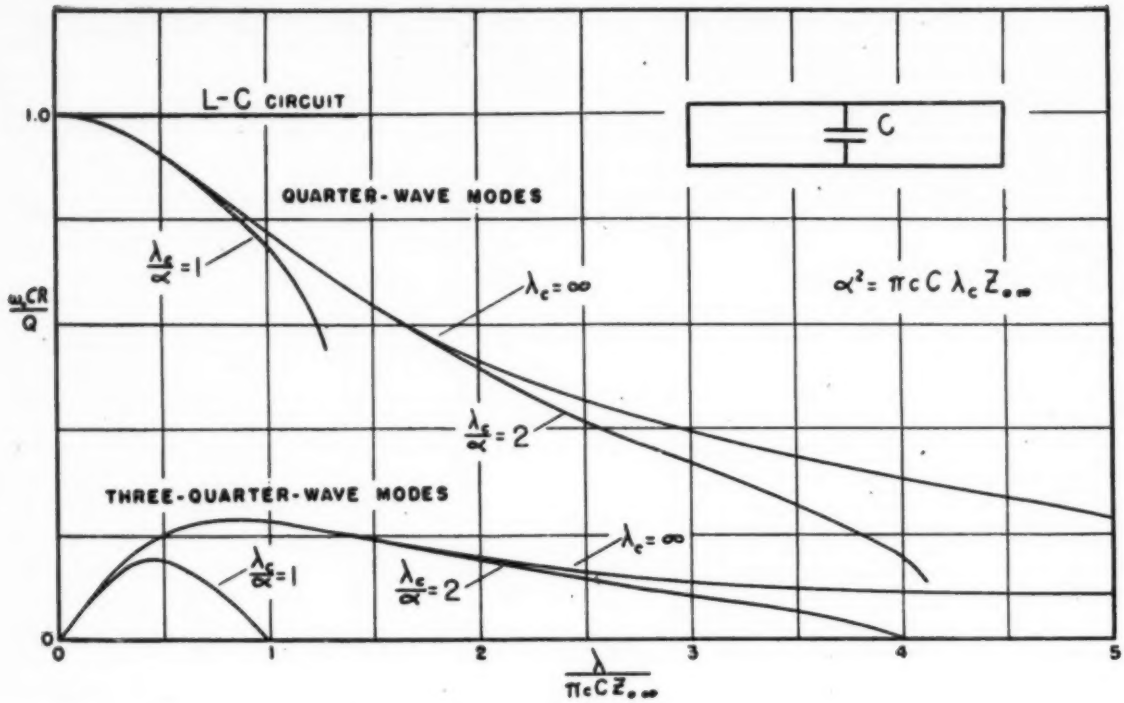

FIG. 4. $R-Q$ factor for general wave guide resonator.

which the equivalent capacitance may be determined is available.[13]

III. TRANSMISSION LINES WITH FINITE CUT-OFF WAVE-LENGTH

In case the transmission line section is a wave guide with a finite cut-off wave-length, the characteristic impedance and phase constant are both functions of frequency, and (5) becomes[14]

$$\zeta \equiv \frac{\omega_0 CR}{Q} = \frac{2[1-(\omega_c^2/\omega^2)]}{1+(2\beta l/\sin 2\beta l)-2(\omega_c^2/\omega^2)}. \tag{6}$$

At frequencies below the cut-off frequency, where Z_0 and the phase constant β are imaginary,

$$\zeta \equiv \frac{\omega_0 CR}{Q} = \frac{2[(\omega_c^2/\omega^2)-1]}{2(\omega_c^2/\omega^2)-1-(2|\beta l|/\sinh 2|\beta l|)}. \tag{7}$$

Equations (6) and (7), combined with Eq. (4) at resonance ($B=0$), lead to Fig. 4, where the $R-Q$ relationship is shown in terms of dimensionless parameters. The characteristic length α is defined by

$$\alpha^2 = \pi c C/\lambda_c Z_{0\infty}, \tag{8}$$

which for the case of the TE_{10} mode in rectangular wave guide becomes

$$\alpha^2 = \pi^2 bC/\epsilon_0. \tag{9}$$

Here c is the velocity of light, $Z_{0\infty}$ is the characteristic impedance at infinite frequency, b is the guide height, and ϵ_0 the dielectric constant of free space. Because of the usual construction of wave guide resonators, having the capacitive gap in the center of the guide section with two symmetrically placed shorting plungers, Fig. 4 is plotted for an equivalent circuit of a shorted transmission line section with a capacity at the center. This is no restriction since this circuit is simply a parallel combination of two circuits similar to that used for Fig. 2.

Similar considerations to those mentioned in connection with concentric line resonators as to validity of the equivalent circuit approximation apply in the wave guide resonator case. If an equivalent capacitance can be found which will make the tuning curve for the simple equivalent circuit approximate that for the actual resonator, this capacitance value can be used with Fig. 4 to obtain the $R-Q$ ratio. In general, it will be found that the simple equivalent circuit is a better approximation in this case than for the concentric-line resonator.

Universal tuning curves for the TE_{10} mode in a rectangular wave guide and similar modes in wave guides of other cross sections are available.[15] So, also,

[13] J. L. Putz, "Tuning curves of coaxial resonators," Stanford Electronics Research Lab. Tech. Report No. 5, ONR Contract N6-onr-251, Task 7 (August 31, 1948).

[14] The discussion here is limited to transverse electric modes and the characteristic impedance is defined on the voltage-current basis (see reference 11, p. 319).

[15] W. W. Harman, "Tunable wave guide cavity resonators for broadband operation of reflex klystrons," Proc. Nat. Electronics Conference 4, 233 (1948).

is information as to λ_c and $Z_{0\infty}$ for ridge wave guide,[16] so the characteristic length α can be easily calculated for this type of guide.

As in the concentric line case, the Q of the wave guide resonator is relatively independent of line length. Ordinary formulas for calculating losses in wave guides are not valid near the guide cut-off frequency, but experimentally the Q is found not to vary radically as the resonant frequency of a wave guide resonator is tuned through the cut-off frequency of the wave guide. For rectangular wave guide, the Q (neglecting end losses and losses associated with the capacitance) is approximately

$$Q \approx (\omega \mu_0 b/2R_s), \tag{10}$$

where R_s is the surface resistivity of the conductor,[17] and μ_0 is the permeability of free space.

[16] S. B. Cohn, "Properties of ridge waveguide," Proc. I.R.E. 35, 783 (1947).

IV. CONCLUSION

The uses of Figs. 2 and 4 are twofold. They should be helpful in resonator design where it is important to obtain the highest value of shunt resistance consistent with other considerations such as mode interference. They are also quite useful in the measurement of shunt resistance where extreme accuracy is not required.

In measurements on a 2-in.$\times\frac{3}{8}$-in. wave guide resonator over a frequency range extending about 25 percent each side of the cut-off, frequency values of the ratio of shunt-resistance to Q, obtained from Fig. 4 (the equivalent capacitance being evaluated by use of universal tuning curves), checked with direct measurements by the perturbation method[2] within experimental error.

[17] See reference 9, Art. 6.07.

Letters to the Editor

Application of Galerkin's Method to Compressible Fluid Flow Problems

CHI-TEH WANG AND R. F. BRODSKY
College of Engineering, New York University, New York, New York
July 18, 1949

IN previous papers,[1-3] one of the present authors has applied the variational method to the compressible fluid flow problems following the Rayleigh-Ritz procedure. The results show surprisingly good agreement between the variational method and the other approximate methods. A study of the results also reveals that the variational method gives good approximate solutions at both high and low Mach numbers and for flows past both thick and thin bodies. The variational method has been applied to steady, non-viscous, irrotational flow past arbitrary bodies without any difficulty. For viscous or rotational flows, analogous problems have yet to be worked out.

In carrying out the variational method, the ratio of the specific heats, γ, has to be such that $\gamma/(\gamma-1)$ is an integer. For simplicity in calculation, $\gamma=2$ was used in the previous calculations. This assumption is shown[3] to increase the final velocities slightly but has practically no effect on the final pressure. Nevertheless, this is a point open to objection. On the other hand, the application of variational method to problems other than non-viscous irrotational flows requires the formulation of new variational principles which is not always easy to accomplish.

The Galerkin method, as it has been applied to elasticity and vibration problems, does not have the above-mentioned difficulties. The Galerkin method is to be carried out as follows. First assume a series of functions including undetermined parameters which satisfy the boundary conditions exactly. For example

$$\phi = \phi_0 + \sum_m \sum_n A_{mn} \phi_{mn},$$

where A_{mn} are the undetermined parameters. Substitute the assumed expression in the differential equation, multiply by ϕ_{mn}, integrate the resulting expression over the domain and equate to zero. If there are s parameters, s algebraic equations are obtained which determine the parameters A_{mn}. A simple proof of the justification of the Galerkin's method is given by Duncan[4] from the consideration of the method of least mean squared error. This proof, however, is valid only for linear problems. A general proof may be found in reference 5.

In applying the Galerkin method to the compressible flow problems, the method can be applied without any modification. The only difficulties are the choosing a function which satisfies the boundary conditions for flow past arbitrary bodies and the method of solution of the resulting simultaneous non-linear equations. Methods to overcome these difficulties have already been discussed in detail in references 1 and 2.

As an example, the problem of compressible flow past a circular cylinder without circulation has been carried out. The fundamental differential equation of a compressible fluid in polar coordinates is as follows:

$$\begin{aligned} L = &\left[a_0^2 + \frac{\gamma-1}{2}\left(U^2 - \phi_r^2 - \frac{\phi_\theta^2}{r^2}\right) - \phi_r^2\right]\phi_{rr} \\ &+ \left[a_0^2 + \frac{\gamma-1}{2}\left(U^2 - \phi_r^2 - \frac{\phi_\theta^2}{r^2}\right) - \frac{\phi_\theta^2}{r^2}\right]\frac{\phi_{\theta\theta}}{r^2} \\ &+ \left[a_0^2 + \frac{\gamma-1}{2}\left(U^2 - \phi_r^2 - \frac{\phi_\theta^2}{r^2}\right) + \frac{\phi_\theta^2}{r^2}\right]\frac{\phi_r}{r} - 2\phi_r\phi_\theta\frac{\phi_{r\theta}}{r^2} = 0, \end{aligned} \tag{1}$$

where ϕ is the velocity potential, a_0 is the velocity of sound at infinity, U is the undisturbed velocity and the subscripts indicate partial differentiation. The boundary conditions are

$$(\phi_r^2 + r^{-2}\phi_\theta^2)^{\frac{1}{2}} = U \text{ at } r = \infty \quad \text{and} \quad \phi_r = 0 \text{ at } r = 1. \tag{2}$$

TABLE I.

Mach No.	A_{11}/a_0 Galerkin		A_{11}/a_0 Variational	q_{max}/U Galerkin		q_{max}/U Variational One Term	q_{max}/U Variational Six Terms	q_{max}/U Rayleigh-Janzen	
M_0	$\gamma=1.405$	$\gamma=2$	$\gamma=2$	$\gamma=1.405$	$\gamma=2$			$\gamma=1.405$	$\gamma=2$
0.1	0.001032	0.001031	0.001031	2.00688	2.00687	2.0069	2.0120	2.01193	2.01197
0.2	0.00859	0.008584	0.008583	2.02867	2.02861	2.0286	2.0524	2.05128	2.05200
0.3	0.03127	0.03119	0.03114	2.06949	2.06930	2.0692	2.1364	2.13141	2.13605
0.4	0.08360	0.08356	0.08307	2.13933	2.13930	2.1385	2.3336	2.28361	2.30271
0.5	0.19878	0.20262	0.1979	2.26504	2.27016	2.2639	—	2.57071	2.63121

The radius of the cylinder is taken to be unity. ϕ may be assumed to be as follows:

$$\phi = U\left(r+\frac{1}{r}\right)\cos\theta + \sum_{m=1}^{\infty}\sum_{n=1}^{\infty} A_{mn}\left[\frac{1}{mr^m} - \frac{1}{(m+2)r^{m+2}}\right]\cos n\theta. \quad (3)$$

Note that expression (3) satisfies the boundary conditions (2) exactly. Then the Galerkin's equations for determining the parameters A_{mn} are:

$$\int_{r=1}^{r=\infty}\int_{\theta=0}^{\theta=2\pi} L\left[\frac{1}{mr^m} - \frac{1}{(m+2)r^{m+2}}\right]\cos n\theta\, dr\, d\theta = 0. \quad (4)$$

Taking one parameter A_{11} only, and carrying out the integration, we obtain

$$A_{11}\{-0.51852a_0^2 + [0.70000-(\gamma-1)0.04446]U^2\} + [0.077006+(\gamma-1)0.19951]UA_{11}^2 + [0.00194+(\gamma-1)0.02346]A_{11}^3 + [0.52778-(\gamma-1)0.000025]U^2 = 0. \quad (5)$$

Solving, at various Mach number of the undisturbed flow M_0, A_{11}/a_0 and the maximum velocity at the surface of the body is tabulated in Table I. The agreement between the results obtained by Galerkin's method and other methods can be seen to be very good.

[1] Chi-Teh Wang, "Variational Method in the Theory of Compressible Fluid," J. Aero. Sci. 15, 675–685 (1948).
[2] Chi-Teh Wang, "Two-Dimensional Subsonic Compressible Flows past Arbitrary Bodies by the Variational Method," report submitted to N.A.C.A., June 1949.
[3] Chi-Teh Wang, "A Variational Method for Transonic Flows with Shock Waves," report submitted to N.A.C.A., June 1949.
[4] W. T. Duncan, "Galerkin's Method in Mechanics and Differential Equations," British A.R.C., R & M No. 1798, August 1937.
[5] I. S. Sokolnikoff, *Mathematical Theory of Elasticity* (McGraw-Hill Book Company, Inc., New York, 1946), pp. 313–316.

Activation Phenomena with Thoria Cathodes

O. A. Weinreich
Bartol Research Foundation of The Franklin Institute, Swarthmore, Pennsylvania
July 11, 1949

THREE states of activation may arbitrarily be distinguished with thoria-coated tungsten cathodes.

(1) The low activation state of a fresh cathode heated to about 1200°C.

(2) The activated state obtained by heating up to about 1700°C.

(3) States of higher activation obtained by (a) flashing to 2600C°, (b) ion bombardment, (c) reverse electron current, (d) exposure to evaporation products from a nearby operating thoria cathode. Procedures (a) and (b) have been reported by the author in an earlier paper.[1] This letter describes the results of additional studies of d.c. phenomena in thoria-coated tungsten filaments. The measurements were made at 1200°K to 1700°K because in this temperature range activation and deactivation phenomena can be studied which escape observation at higher temperatures.

The only reported measurements of state 2 for thoria on tungsten are those of T. E. Hanley,[2] who found a d.c. emission of 0.091 amp/cm² at 1700°K. D. A. Wright[3] reports a d.c. emission of 0.21 amp/cm² at 1700°K for thoria on tantalum. By comparison, the d.c. emissions for state 3 as obtained by any of the procedures (a) through (d) were about 0.7 amp/cm² at this temperature.

In addition to its enhanced emission state 3 is characterized by a high degree of instability. It is rapidly poisoned by oxygen at 10^{-8} mm Hg, it decays rapidly with normal emission, and it is sensitive to the anode material. Of the various anode metals tested thorium seems to be best for maintaining a high activation state. A test diode, still in operation, has run for 4000 hours with a temperature-limited emission current of 0.2 amp/cm² at 1600°K. In these ways state 3 is markedly different from state 2, which has a higher stability and is relatively insensitive to poisoning.[1,4] In its ease of poisoning by oxygen, state 3 is comparable to the activated state of thoriated tungsten filament.

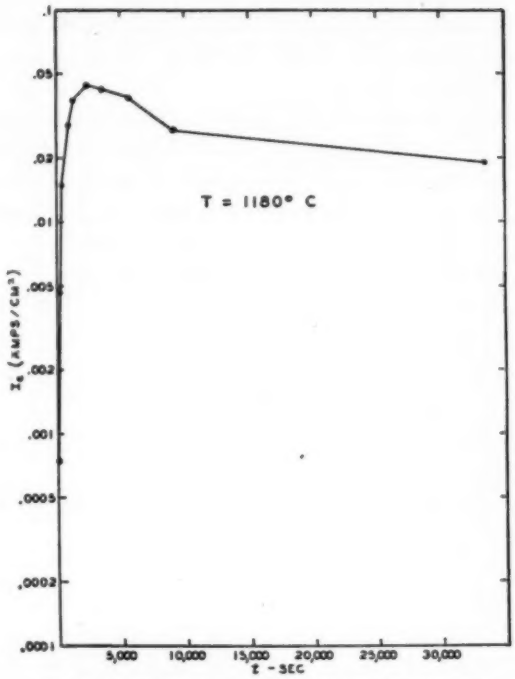

FIG. 1. Activation of a thoria-coated tungsten filament by reverse electron current.

Comparing the results of Richardson plots for the various states, one finds the following values for A (amp/cm² deg²) and φ (ev)

State 1	$A=63$	$\varphi=4.3$
State 2	$A=2.5$	$\varphi=2.5(4)$ (ref. 3)
	$A=2.63$	$\varphi=2.67$ (ref. 2)
State 3	$A=7.9$	$\varphi=2.5(7)$ (ref. 1) (flashing)
	$A=16$	$\varphi=2.6$ (reverse electron current)

(It should be emphasized that the determination of A constants by Richardson plots is subject to errors because of changes in the spectral emissivities which occur during the measurements.) These results show that the d.c. emission in state 3 is higher than that from state 2 because of higher A values, whereas states 2 and 3 give higher d.c. emissions than state 1 because of the lower φ-values. The large decrease in φ from 4.3 ev to 2.6 ev going from state 1 to state 2 is probably due to the formation of impurity centers, which D. A. Wright[4] calculated to be for thoria at a concentration of 10^{18} excess atoms/cm³.

Procedure (c) makes it possible to obtain the highest state of activation at temperatures at which thermal activation is negligible ($T<1600$°K). It has been observed in some cases, that the emission passes through a maximum, and plotting the log of the emission current against the time of reverse electron current drawing, curves of a shape similar to those of I. A. Becker[5] for oxide cathodes were obtained (Fig. 1).

Activation procedure (d) has been used for the activation of a pulsed thoria cathode which worked then as a kind of dispenser cathode, the deactivation being more than compensated probably by adsorption of active material between the pulses. Several tubes containing two thoria-coated tungsten filaments have been made and a high activation state could be reached and maintained for the pulsed emission of the thoria-coated filament if a small d.c. emission was drawn from an auxiliary thoria cathode to the same anode.

A review article on thoria cathodes, including emission measurements, preparation technique of coatings and sintered sleeves, and practical application is being written.

[1] O. Weinreich, Rev. Gen. d'El. 54, 243–256 (1945).
[2] T. E. Hanley, J. App. Phys. 19, 583–589 (1948).
[3] D. A. Wright, Nature 160, 129–130 (1947).
[4] D. A. Wright, Proc. Phys. Soc. B62, 188–203 (1949).
[5] I. A. Becker, Phys. Rev. 34, 1323–1351 (1929).

X-Ray Diffraction Line Broadening and Strain Hardening

D. ROSENTHAL
Department of Engineering, University of California, Los Angeles, California
August 29, 1949

THERE appears to be a substantial body of evidence[1] pointing to the fact that the x-ray diffraction line broadening exhibited by cold-worked polycrystalline metals is due primarily to the variation of the lattice parameter da/a, i.e., to a heterogeneous elastic deformation on a microscopic scale. Since the broadening persists after the specimen has been unloaded the observed phenomenon in effect suggests the presence of *residual microstress*. The latter may be thought of as being produced by the same mechanism as the *residual macrostress*, i.e., by a heterogeneous plastic deformation.[2] This type of deformation is known to exist in polycrystalline metals on the scale of a grain and even crystallite (fraction of grain).[3] However, an inhomogeneous plastic flow alone is not sufficient to produce residual stress. Thus a perfect plastic material with no strain hardening can have no residual stress, since no change in dimensions will occur on unloading. On the other hand, if the strain hardening is independent of deformation, there also will be no residual stress, since the amount of elastic recovery on unloading will be the same for all elements. This condition does not exist ordinarily in a strain-hardening material, but it is probably approached in a stress-relieved mild steel at an early stage of plastic flow (between 0.2 percent and 0.5 percent). It is only when plastic deformation has become large enough to cause sufficient heterogeneity in strain hardening that measurable amounts of residual microstress can be expected. For then the variation in elastic recovery on unloading will be great enough to produce noticeable interaction between individual grains and crystallites. This state of affairs can be followed most easily in uniaxial tension, since the value of the (true) stress S in uniaxial tension is a direct measure of the strain hardening corresponding to a given value of plastic deformation.[4] To be sure the tensile test measures only the average value of S. However, if the distribution of strain hardening around this average is of a Gaussian type with a lower limit at the yield point S_0 of the stress-relieved material, then the r.m.s. (root mean square) deviation will increase proportionally to $S-S_0$, and so also will the r.m.s. deviation of the residual microstress.

That this line of thought is correct is strongly suggested by an earlier work on copper,[5] and a more recent one made at U.C.L.A. on steel. The results of the latter are shown in Fig. 1, where for convenience the abscissas have been made to represent the elastic strain S/E (E=Young's modulus) and the ordinates the r.m.s. deviation of the change of lattice parameter, da/a. The tensile specimen, a mild steel of 0.17 percent, has been treated to yield continuous and sharp diffraction lines in the unstressed condition.[6] It was then pulled to various amounts of plastic deformation ranging from 0 percent to 11.3 percent natural strain. At each step of deformation a back reflection x-ray diagram of the (310) doublets was taken at the same spot of the specimen, using Co unfiltered radiation. The exposure and developing techniques were kept constant to within 3 percent of the indicating instruments. The films were microphotometered* along the diameter that was parallel to the smallest dimension of the target. The traces were then converted to blackening curves and the area above the background density was planimetered at both ends of the diameter. This area is proportional to the integrated diffracted intensity and for an ideally random orientation of crystallites should be a constant independent of the degree of deformation.[6] Under this (ideal) condition the reciprocal of peak intensity multiplied by an appropriate scale factor and corrected for the overlapping of α_1- and α_2- radiation[7] would give the value of r.m.s. deviation of da/a directly. In practice there is always a departure from the ideal randomness, and the integrated intensity is not constant. A computation of the probable error was made, based on the geometry of the exposure technique and the maximum size of crystallites[8] as estimated from the smoothness of the x-ray lines. The computed value was found to be in good agreement with the observed mean deviation of ± 26 percent. The r.m.s. deviation of da/a was then corrected to the same value of the integrated intensity and the results for each side of the diameter of the film plotted individually in Fig. 1 as small circles. A scatter of $da/a = \pm 0.015$ percent may be accounted for by the error in estimating the background intensity. It is believed that through improvement of the experimental technique this error as well as the variation of the integrated intensity can be substantially reduced.

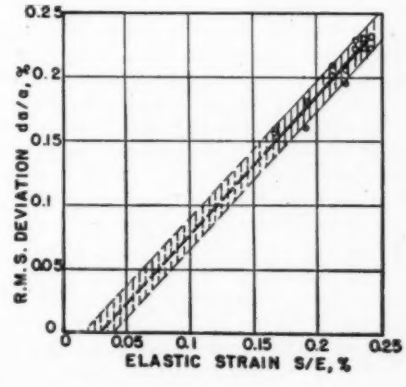

FIG. 1.

The fact that the broadening of lines seems to be indicative of the heterogeneity of strain hardening, rather than strain hardening itself, may be of interest in the interpretation of some of the phenomena accompanying strain hardening, such as, for example, the sharpening of lines without decrease of hardness.[1]

* An Applied Research Laboratory microphotometer was used courtesy of the Physics Department, U.C.L.A.

[1] W. Boas, *An Introduction to the Physics of Metals and Alloys* (John Wiley and Sons, Inc., New York 1947), p. 129.
[2] J. T. Norton and D. Rosenthal, Welding J. **22**, Research Supplement, 65-s. (February, 1943).
[3] C. S. Barrett, *Structure of Metals* (McGraw-Hill Book Company, Inc., New York, 1943), p. 389.
[4] J. H. Hollomon, *The Problem of Fracture* (John Wiley and Sons, Inc., New York, 1946), p. 5.
[5] V. Caglioti and G. Sachs, *Zeits. f. Physik* **74**, 647 (March, 1932).
[6] A. Taylor, *An Introduction to X-Ray Metallography* (Chapman and Hall, London, 1945), Chapter VI.
[7] F. W. Jones, Proc. Roy. Soc., Series A, **166**, 16, No. 924 (May, 1938).
[8] Alexander, Klug, and Kummer, J. App. Phys. **19**, 742 (1948).

Orientation of Single-Crystal Rods of Copper Grown from the Melt*

A. A. PETRAUSKAS AND F. GAUDRY
University of Notre Dame, South Bend, Indiana
August 12, 1949

AS part of a program of measurement of electronic emission from single-crystal surfaces, a large number of single crystals of copper were grown from the melt. These crystals were cylinders ¾ inches in diameter and approximately 5 inches long.

According to the accepted theory of nucleation,[1] the orientation of the cylindrical rods of single crystals grown from a melt should be random provided that the temperature of the molten metal is brought well above its melting point. Figure 1 shows a plot of the axes of copper cylinders plotted on one of the equivalent triangles of a standard projection of a cubic crystal. From the figure, one sees that the orientation of the single crystals analyzed appears to have a random distribution as expected.

The single crystals were grown from the melt in a vertical tubular furnace by the familiar process of controlled solidification.[2] A graphite crucible charged with OFHC copper was brought to a temperature of 1250°C and held there for about a half hour. The molten metal was then lowered through a sharp temperature gradient at a rate of one inch per hour. An atmosphere of dry nitrogen throughout the interior of the combustion tube prevented oxidation of the metal and the crucible. The orientation of the single crystals was determined from back reflection Laue patterns.

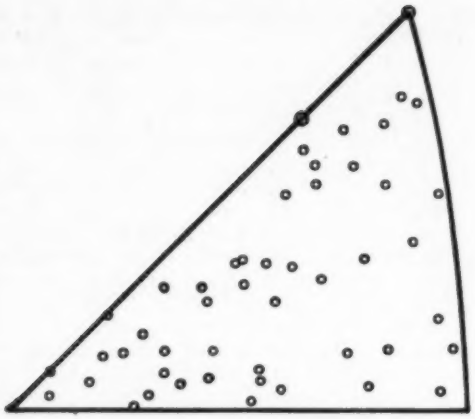

FIG. 1. Unit stereographic triangle of standard projection of cubic crystal containing specimen axes.

Later single crystals of copper of a given orientation were grown from a single-crystal seed having the desired orientation.[3] The seed was planted on the bottom of the crucible. In order to prevent complete melting of the seed, the position of the crucible was adjusted so that only a portion of the seed melted at the beginning of the growing process.

* This work was sponsored by The Research Corporation.

[1] W. P. Davey, *Study of Crystal Structure and its Applications* (McGraw-Hill Book Company, Inc., New York, 1934), first edition, pp. 363–394.

[2] P. W. Bridgman, Proc. Am. Acad. **60**, 305–383 (1925); *ibid.* **63**, 351–355 (1929); F. C. Nix, Rev. Sci. Inst. **9**, 426–427 (1938); S. Siegel, Phys. Rev. **57**, 537–543 (1940).

[3] I. Obreimow and L. Schubnikow, Zeits. f. Physik **25**, 31–36 (1924); P. Kapitza, Proc. Roy. Soc. **A11 9**, 358–386 (1929); C. A. Cinnamon, Rev. Sci. Inst. **5**, 187–190 (1934); M. F. Hosler, Rev. Sci. Inst. **4**, 656–660 (1933).

Fringe Fields of Ferromagnetic Domains

L. MARTON, S. H. LACHENBRUCH, JOHN A. SIMPSON, AND A. VANBRONKHORST

National Bureau of Standards, Washington, D. C.

November 28, 1949

IN previous publications[1–3] descriptions of a new method were given for the mapping of magnetic or electrostatic fields which are otherwise inaccessible to the more conventional types of field measurements. In another publication[4] an attempt was reported also to use an earlier variation of our method, the so-called "electron optical 'schlieren' method" for the exploration of fringe fields of ferromagnetic domains. During a trip to England last year, Dr. E. Orowan pointed out that the patterns shown in the last-mentioned publication are due to "Bitter domains" instead of "Weiss domains."

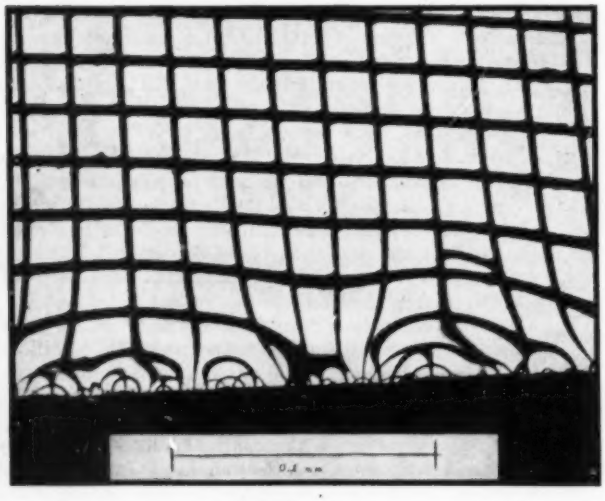

FIG. 1.

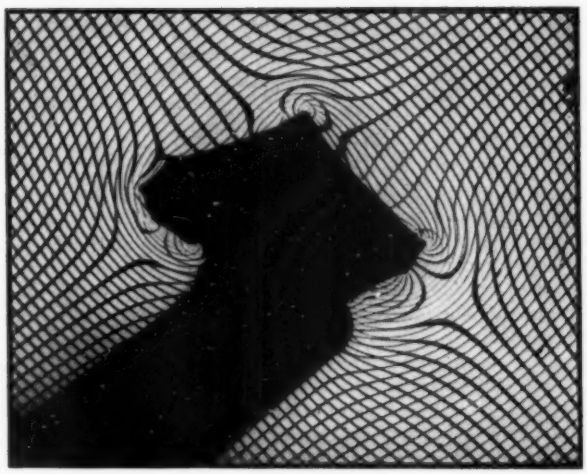

FIG. 2.

Using our improved electron optical mapping method, the experiments were repeated on a cobalt single crystal which was graciously lent to us by Dr. R. M. Bozorth of the Bell Telephone Laboratories. This is the identical crystal which has been described in the recent review of Dr. C. Kittel.[5] For the purposes of observation, a standard magnetic-type electron microscope has been modified to include adjustment and orientation of the sample before the objective lens from the outside without breaking the vacuum. Another modification of the instrument consists of introducing a 1000-mesh/inch electrolytic screen[6] behind the back focus of the objective lens. The mount for that screen permits a rotation of the screen around the optical axis and an axial translation of the screen without breaking the vacuum. A description of these two modifications will appear shortly elsewhere.

A typical result obtained is shown in Fig. 1. It represents the edge of the crystal and the distorted mesh pattern due to the presence of a fringe field along the edge of the crystal. The scale drawn indicates the magnification and the extent of the field.

The interpretation of the patterns thus obtained is not quite complete. In principle, as outlined by L. M. and S. H. L.,[3] in the presence of a field of axial symmetry, such a pattern contains all the information required. Due to the shape of the cobalt crystal, and due to the hexagonal crystal symmetry, the field is certainly very far from being axially symmetrical and, under these circumstances, the missing information has to be supplied by added experiments. This was carried out by taking a set of patterns at different orientations of the crystal, obtained by rotating it around one edge. Calculations are being carried out at present to obtain quantitative data on the value of the field on and in the neighborhood of the surface.

Encouraged by the success of the method, we tried to observe fringe fields from ferroelectric domains, too. Up to now, we have not been successful for the simple reason that the barium titanate crystals used for that purpose charged up strongly in the observing electron beam and the resulting pattern had to be ascribed to the field produced to the accumulated charge rather than to the weak domain field. Figure 2 is shown, however, to indicate what type of patterns are obtained from a small barium titanate crystal supported by a 0.010-in. tungsten wire.

[1] L. Marton, J. App. Phys. **19**, 863 (1948).

[2] L. Marton and S. H. Lachenbruch, J. Research Nat. Bur. Stand. (October, 1949).

[3] L. Marton and S. H. Lachenbruch, J. App. Phys. **20**, 1171 (1949).

[4] L. Marton, Phys. Rev. **73**, 1475 (1948).

[5] Charles Kittel, Rev. Mod. Phys. **21**, 541 (1949).

[6] Obtained from Dr. Law, RCA Manufacturing Company, Lancaster, Pennsylvania.

Author Index to Volume 20

References with (L) are to Letters to the Editor.

Adcock, M. Donald (see Dunbar, Allen S.)—226 (L)
Adler, Fred P. Measurement of the complex conductivity of an ionized gas at microwave frequencies—1115
Adler, F. T., W. M. Sawyer, and John D. Ferry. Propagation of transverse waves in viscoelastic media—1036
Aigrain, Pierre R. and Everard M. Williams. Synthesis of *n*-reactance networks for desired transient response—597
Alessandrini, Eileen I. High temperature furnace for electron diffraction studies of thin films—691
Alexander, Leroy, Elizabeth Kummer, and Harold P. Klug. Dead time and non-linearity characteristics of the Geiger-counter x-ray spectrometer—735
Austin, A. E. (see Schwartz, C. M.)—202
Averbach, B. L. and B. E. Warren. Interpretation of x-ray patterns of cold-worked metal—885 (L)
—— The effect of cold work in metals on powder pattern intensities—1066

Backus, Robert C. (see Williams, Robley C.)—98
—— **and Robley C. Williams.** Small spherical particles of exceptionally uniform size—224 (L)
Baker, Richard F. and Daniel G. Pease. Improved sectioning technique for electron microscopy—480 (L)
Ballou, J. W. and J. C. Smith. Dynamic measurements of polymer physical properties—493
Barnes, R. Bowling (see Burton, Charles J.)—462
—— **and Charles J. Burton.** Visual methods for studying ultrasonic phenomena—286
Barrett, C. S. Book review—723
Bear, Richard S. (see Bolduan, Orvil E. A.)—983
Beatty, J. R. and J. M. Davies. Time and stress effects in the behavior of rubber at low temperature—533
Beatty, Suzanne van Dijke. Table of interplanar spacings for different target materials for the back reflection region —415 (L)
Beck, Paul A. Comments on "Grain growth in octachloropropane"—231 (L)
—— Formation of recrystallization nuclei—633 (L)
—— Some factors affecting the rate of precipitation hardening in Cu-Be alloys—666
Begovich, Nicholas A. High frequency total emission loading in diodes—457
Benfield, A. E. Effect of uplift and denudation on underground temperatures—66
Benner, Arthur H. Phase lead for a.c. servo mechanisms—268
Benzer, S. High inverse voltage germanium rectifiers—804
Beyer, R. T. (see Krumhansl, J. A.)—432, 582
Bikerman, J. J. Effect of surface roughness on rolling friction—971
Birkhoff, Garrett and Thomas E. Caywood. Fluid flow patterns—646
Birks, L. S. (see Wilkinson, P. G.)—1168
Birnbaum, George and Jacques Franeau. Measurement of the dielectric constant and loss of solids and liquids by a cavity perturbation method—817 (L)
Blachman, Nelson M. Demodulation of an F-M carrier and random noise by a limiter and discriminator—38
—— Demodulation of a frequency-modulated carrier and random noise by a discriminator—976
Bleakney, W. (see Weimer, D. K.)—418 (L)
Bolduan, Orvil E. A. and Richard S. Bear. Effective use of collimating apertures in small-angle x-ray diffraction carriers—983
Booth, A. D. Enumeration of Fourier phase permutations using electronic analog machines—388
Bott, R. and R. J. Duffin. Impedance synthesis without use of transformers—816 (L)
Boyer, Raymond F. Compatibility, efficiency and permanence of plasticizers—540
Bracewell, R. N. and K. Weekes. Ionospheric absorption —724 (L)
Breazeale, Francis and John Whisnant. Apparatus to depict the load-elongation diagram of yarn at five cycles per second—621
Brentano, J. C. M. Method for the quantitative evaluation of x-ray patterns from mixed powders adapted to the demands of quantitative analysis—1215
Brewer, G. R. (see Malter, L.)—918
Bridgman, P. W. Volume changes in the plastic stages of simple compression—1241
Brillouin, L. The scattering cross section of spheres for electromagnetic waves—1110
—— The traveling-wave tube (discussion of waves for large amplitudes)—1196
Brodsky, R. F. (see Wang, Chi-Teh)—1255
Brown, Alexander. X-ray diffraction studies of the stretching and relaxing of polyethylene—552
Brown, S. Leroy and Chester M. McKinney. Use of a mechanical harmonic synthesizer in electrical network analysis—316
Brown, S. Leroy and James M. Sharp. Use of a mechanical harmonic synthesizer in electric wave filter analysis—578
Bueche, A. M. (see Debye, P.)—518
Burton, Charles J. (see Barnes, R. Bowling)—286
—— (see Schneider, William C.)—48
—— **and R. Bowling Barnes.** Visual method for demonstrating the path of ultrasonic waves through thin plates of material—462
Burwell, J. T. and C. D. Strang. Incremental friction coefficient—a non-hydrodynamic component of boundary lubrication—79
Bush, O. B., R. B. Vandegrift, and T. E. Hanley. Use of titanium and zirconium nitrides as a conducting element in thoria cathodes—295 (L)

Cady, W. M. (see Marlow, D. G.)—771
Caywood, Thomas E. (see Birkhoff, Garrett)—646
Chandler, C. H. An investigation of dielectric rod as wave guide—1188
Cheng, P. T. (see McCrone, W. C.)—230 (L)
Christ, C. L. (see McLachlan, Dan, Jr.)—829
Chu, E. L. and W. W. Hansen. Disk-loaded wave guides —280
Clark, J. C. Flash radiography applied to ordnance problems —363
Clark, Orrin H. and Ernest M. Lyman. Note on some plastic flow effects in steel—884 (L)
Cohn, S. B. Analysis of the metal-strip delay structure for microwave lenses—257; addendum—1011
Colino, A. Notes on the excitation of electromagnetic waves in cylindrical metallic wave guides—576
Conant, F. S., G. L. Hall, and G. R. Thurman. Relationship between Gough-Joule coefficients and moduli of vulcanized rubbers—526
Conley, Patrick. Antennas and open-wire lines. Part III: Image-line measurements—1022
Cooley, J. P. (see Wantuch, E.)—112
Copeland, Paul L. and Delbert N. Eggenberger. Electron transit time in space-charge limited current between coaxial cylinders—1148

Courant, E. D. Resonance effect in the synchrotron—611
Crede, J. H. and J. P. Martin. Magnetic characteristics of an oriented 50 percent nickel-iron alloy—966
Creutz, E. (see Falk, C. E.)—1183
—— **and K. Downes.** Magnetite concrete for radiation shielding—1236
Cyr, R. R. (see Schaaf, S. A.)—860

Danforth, W. E. and D. L. Goldwater. Resistance of oxide cathode coatings for high values of pulsed emission—163
Davies, John M. Aerodynamics of golf balls—821
—— (see Beatty, J. R.)—533
Debye, P. and A. M. Bueche. Scattering by an inhomogeneous solid—518
Dedrick, J. H. and A. Gerds. A study of the mechanism of sintering of metallic particles—1042
Dodge, C. H. (see Tangren, R. F.)—637
Dorn, John E. Stress-strain rate relations for anisotropic plastic flow—15
Downes, K. (see Creutz, E.)—1236
Drucker, D. C. An analysis of the mechanics of metal cutting—1013
Druesne, M. A. A. (see Prichard, A. C.)—1011 (L)
Duffin, R. J. (see Bott, R.)—816 (L)
Dunbar, Allen S. and M. Donald Adcock. Measurement of gain of electromagnetic horns—266 (L)

Eggenberger, Delbert N. (see Copeland, Paul L.)—1148
Eisenstein, A. Some properties of the Ba_2SiO_4 oxide cathode interface—776
El-Fandy, M. G. Dust—an active meteorological factor in the atmosphere of Northern Africa—660
Ellis, S. G. (see Hillier, James)—700
Elsasser, Walter M. Attenuation in a dielectric circular rod —1193
English, William N. (see Moore, Donald Baker)—370
—— **and Leonard B. Loeb.** Point-to-plane corona onsets—707
Enright, D. P., L. R. Sonders, and W. A. Weyl. Surface polarization and wettability of inorganic substances by water—1011 (L)
Estermann, I. and E. D. Kane. Torsion balance for measuring forces in low density gas flows—608

Falk, C. E. and E. Creutz. The attenuation of neutrons of various energies in water—1183
Fan, H. Y. Thermionic emission from sintered cathode of thoria and tungsten mixture—682
Fankuchen, I. (See Miller, E.)—531
Feaster, G. R. Pulse emission decay phenomenon in oxide-coated cathodes—415 (L)
Ferry, John D. (see Adler, F. T.)—1036
—— (see Smith, Thor L.)—144
Field, Michael and M. Eugene Merchant. Reflection method of determining preferred orientation on the Geiger-counter spectrometer—741
Finklenburg, Wolfgang. High current carbon arc and its mechanism—468
Fletcher, C. H. (see Weimer, D. K.)—418 (L)
Found, C. G. (see Oleson, N. L.)—416 (L)
Franeau, Jacques (see Birnbaum, George)—817 (L)
Fusfeld, Herbert I. New interpretation of the *n*-power law in plastic deformation—1052
Fuson, Nelson. Effect of current magnitude upon the behavior of a superconducting bolometer in its transition region—59

Gaudry, F. (see Petrauskas, A. A.)—1257 (L)
Geisler, A. H. (see Newkirk, J. B.)—816 (L)
Gemant, Andrew. Ionization of paraffin wax by beta-radiation—887
Gerds, A. (see Dedrick, J. H.)—1042
Germer, L. H. and F. E. Haworth. Erosion of electrical contacts on make—1085
Gilmore, G. D. (see Spencer, R. S.)—502
Goldman, J. E. The influence of atomic order on the magnetic properties—1131
Goldwater, D. L. (see Danforth, W. E.)—163
—— (see Haddad, R. E.—886 (L), 1130 (L)
Goodman, Lawrence E. (see Mindlin, Raymond D.)—89
Gordon, Paul. High temperature precision x-ray camera. Some measurements of the thermal coefficients of expansion of beryllium—908
Gordon, W. E. (see Hamlin, E. W.)—248
Greig, J. H. (see Wantuch, E.)—112
Grube, W. L. Effect of "multiple grounds" on electron microscope images—125 (L)
Guth, E. (see Ivey, Donald G.)—486
—— (see Witte, R. S.)—481

Haddad, R. E., D. L. Goldwater, and F. H. Morgan. Zirconium carbide as a thermionic emitter—886 (L)
—— Thermionic emitting properties of two refractories —1130 (L)
Hainer, R. M. (see King, Gilbert W.)—559
Hall, Cecil E. Method of measuring spherical aberration of an electron microscope objective—631 (L)
Hall, G. L. (see Conant, F. S.)—526
Hall, R. N. The application of non-integral Legendre functions to potential problems—925
Hamlin, E. W., P. A. Seay, and W. E. Gordon. New solution to the problem of vertical angle-of-arrival of radio waves—248
Hanley, T. E. (see Bush, O. B.)—295 (L)
Hannay, N. B., D. MacNair, and Addison H. White. Semi-conducting properties in oxide cathodes—669
Hansen, W. W. (see Chu, E. L.)—280
Harman, W. W. Impedance of resonant transmission lines and wave guides—1252
Harrison, Shirley. Aberration phenomenon in electrostatic lenses—412 (L)
Hartley, R. V. L. Note on "The mixing properties of non-linear condensers"—819 (L)
Haworth, F. E. (see Germer, L. H.)—1085
Hay, D. R. (see Woonton, G. A.)—71
Hebb, M. H., C. W. Horton, and F. B. Jones. On the design of networks for constant time delay—616
Heidenreich, R. D. Electron microscope and diffraction study of metal crystal textures by means of thin sections —993
Heinmets, F. Modification of silica replica technique for study of biological membranes and application of rotary condensation in electron microscopy—384
Hillier, James and S. G. Ellis. Illuminating system of the electron microscope—700
Hillier, K. W., H. Kolsky, and J. P. Lewis. Method of measuring dynamic mechanical properties of rubber-like materials—227 (L)
Holm, Else, Ragnar Holm, and Erle I. Shobert II. Theory of hardness and measurements applicable to contact problems—319
Holm, Ragnar. Vaporization of the cathode in the electric arc—715
—— (see Holm, Else)—319
Horton, C. W. (see Hebb, M. H.)—616
—— (see Morrison, H. L.)—1027
Hsiao, C. C. (see Sauer, J. A.)—507
Hudson, Douglas Rennie. Density and packing in an aggregate of mixed spheres—154
Hull, Gordon Ferrie, Jr. Book review—126
Hull, Harry H. A method for studying the distribution and sign of static charges on solid materials—1157

Ivey, Donald G., B. A. Mrowca, and E. Guth. Propagation of ultrasonic bulk waves in high polymers—486
Izard, Emmette F. (see Kolb, Harry J.)—564, 571

Jaffe, L. D. Phase distribution in two-phase solids—1206
Johnson, James R. Photo-density method of determining the relative penetration of diffused sodium 24 tracer into glass—129; erratum—819 (L)
Jones, F. B. (see Hebb, M. H.)—616

Kane, E. D. (see Estermann, I.)—608
Kaye, Wilbur. An electron microscope technique for the study of polymeric molecules—1209
Kê, T'ing-Sui. Grain boundary model and the mechanism of viscous intercrystalline slip—274
—— Grain boundary relaxation and the mechanism of embrittlement of copper by bismuth—1226
Keller, Herbert B. and Joseph B. Keller. Reflection and transmission of electromagnetic waves by a spherical shell —393
Keller, Joseph B. (see Keller, Herbert B.)—393
Kelso, John M. Note on the maximum height of reflection of a radio wave in a curved ionosphere layer—632 (L)
King, Gilbert W., R. M. Hainer, and H. O. McMahon. Infra-red absorption spectra of some polymers at liquid-helium temperatures—559
King, Ronold. Antennas and open-wire lines. Part I. Theory and summary of measurements—832
Klug, Harold P. (see Alexander, Leroy)—735
Knipp, Julian K. On the velocity-dependent characteristics of high frequency tubes—425
Kolb, Harry J. and Emmette F. Izard. Dilatometric studies of high polymers. I. Second-order transition temperature—564; II. Crystallization of aromatic polyesters—571
Kolsky, H. (see Hillier, K. W.)—227 (L)
Krumhansl, J. A. and R. T. Beyer. Barkhausen noise and magnetic amplifiers. I. Theory of magnetic amplifiers—432; II. Analysis of the noise—582
Kuczynski, G. C. Study of the sintering of glass—1160
Kuhlthau, A. R. Air friction on rapidly moving surfaces—217
Kummer, Elizabeth (see Alexander, Leroy)—735

Lachenbruch, S. H. (see Marton, L.)—1171, 1258 (L)
Lehovec, K. New method of capacity measurement on dry disk rectifiers—123 (L)
Levenson, Morris E. Harmonic and subharmonic response for the Duffing equation—1045
Levinstein, Henry. Growth and structure of thin metallic films—306
Lewis, C. R. (see Strang, C. D.)—1164
Lewis, J. P. (see Hillier, K. W.)—227 (L)
Ling, D. P. (see Germer, L. H.) Appendix A. Effect of steady value current upon erosion—1108
Loeb, Leonard B. (see English, William N.)—707
Loosjes, R. and H. J. Vink. Electron emission and conduction mechanism of oxide-coated cathodes—884 (L)
Ludeke, Carl A. Electro-mechanical device for solving non-linear differential equations—600
—— Method of equivalent linearization for non-linear oscillatory systems with large non-linearity—694
Lund, Louis H. and George H. Vineyard. Inter-particle interference effects in the small-angle x-ray scattering from fine powders—593
Lyman, Ernest M. (see Clark, Orrin H.)—884 (L)

Mack, Charles. Coefficient of anomalous viscosity—225 (L)
MacNair, D. (see Hannay, N B.)—669
Mahlman, G. W. Work functions and conductivity of oxide-coated cathodes—197
Malter, L. and G. R. Brewer. Microwave Q measurements in the presence of series losses—918
Manning, L. A., O. G. Villard, Jr., and A. M. Peterson. Radio Doppler investigation of meteoric heights and velocities—475
Marboe, Evelyn C. and W. A. Weyl. Method for studying the forces between metals and ionic substances—124 (L)
Marin, J. (see Sauer, J. A.)—507
Mark, H. (see Miller, E.)—531
Marlow, D. G., C. R. Nisewanger, and W. M. Cady. Method for the instantaneous measurement of velocity and temperature in high speed air flow—771
Martin, D. L. (see Newkirk, J. B.)—816 (L)
Martin, J. P. (see Crede, J. H.)—966
Marton, L. and S. H. Lachenbruch. Electron optical mapping of electromagnetic fields—1171
——, S. H. Lachenbruch, John A. Simpson, and A. Van-Bronkhorst—1258 (L)
Masket, A. Victor. Measurement of forces resisting armor penetration—132
Mason, S. J. Comment on Dr. Vazsonyi's paper "A generalization of Nyquist's stability criteria"—867
Mason, W. P. and H. J. McSkimin. Errata: Energy losses of sound waves in metals due to scattering and diffusion—228 (L)
May, K. R. An improved spinning top homogeneous spray apparatus—932
McCaa, D. G. (see Prichard, A. C.)—1011 (L)
McCracken, Leslie G. Note on the ionospheric absorption problem—229 (L)
McCrone, W. C. and P. T. Cheng. Grain growth in octachloropropane—230 (L)
McCutcheon, Don M. Cathodic vacuum etching of metals—414 (L)
McKinney, Chester M. (see Brown, S. Leroy)—316
McLachlan, Dan, Jr. Determination of relative phases of Fourier coefficients from x-ray diffraction data—295 (L); erratum—1011
—— **and C. L. Christ.** Projection of crystal structure factors on the reciprocal lattice—829
McMahon, H. O. (see King, Gilbert W.)—559
McReynolds, Andrew W. Effects of stress and deformation on the Martensite transformation—896 (L)
McSkimin, H. J. (see Mason, W. P.)—228 (L)
Merchant, M. Eugene (see Field, Michael)—741
Metson, G. H. Papers by Hadrian Stahl—1130 (L)
Michels, Walter C. and Sally Wilford. The physical properties of titanium. I. Emissivity and resistivity of the commercial metal—1223
Middleton, David. On theoretical signal-to-noise ratios in F-M receivers: a comparison with amplitude modulation—334; errata—724
Miles, J. W. On the diffraction of an electromagnetic wave through a plane screen—760
Miller, E., I. Fankuchen, and H. Mark. Polymerization in the solid state—531
Miller, Theodore. Magnetically controlled wave guide attenuators—878
Millman, George H. and Richard C. Raymond. Absorption of microwaves in gases—413 (L)
Mindlin, Raymond D. Mathematical theory of photo-viscoelasticity—206
—— **and Lawrence E. Goodman.** Optical equations of three-dimensional photoelasticity—89
Moore, A. D. Fields from fluid flow mappers—790
Moore, Donald Baker and William N. English. Point-to-plane impulse corona—370
Morduchow, Morris. On surface-fitting in three variables —390
Morgan, F. H. (see Haddad, R. E.)—886 (L), 1130 (L)
Morgan, Samuel P., Jr. Effect of surface roughness on eddy current losses at microwave frequencies—352

Morrison, H. L., F. T. Rogers, Jr., and C. W. Horton. Convection currents in porous media—1027
Mottlau, A. Y. A technique for the preparation of grease or solid samples dispersed in grease-like media for examination with the electron microscope—1055
Mrowca, B. A. (see Ivey, Donald G.)—486
—— (see Witte, R. S.)—481
Muckenhoupt, Carl F. Distribution of temperature and current in cylindrical bodies—939
Munk, M. M. On supersonic flow patterns—302
Muraour, Henri. Note on "Qualitative experimental verification of the change of burning rate of rocket powders with radiation path length"—819 (L)

Newkirk, J. B., A. H. Geisler, and D. L. Martin. Ordering reaction in Co-Pt alloys—816 (L)
Nisewanger, C. R. (see Marlow, D. G.)—771
Nolle, A. W. Comment on "A method of measuring dynamic mechanical properties of rubber-like materials"—277 (L)
—— Electric-field modulation of ultrasonic signals in liquids—589

Okress, E. C. Potential functions for a thermionic vacuum tube—850
Okubo, H. Bending of a thin circular plate of an aeolotropic material under uniform lateral load (supported edge)—1151
—— On the torsion of a prismatic cylinder with a star-shaped section—1155
Oleson, N. L. and C. G. Found. Running striations and multiple electron temperatures—416 (L)

Pal, A. B. Stabilization of breakdown voltage and measurement of some critical currents in a glow tube—451
Papas, Charles H. On the infinitely long cylindrical antenna—437
Pease, Daniel G. (see Baker, Richard F.)—480 (L)
Pell, E. M. (see Tomboulian, D. H.)—263
Penner, S. S. Flow through a rocket nozzle with and without vibrational equilibrium—445
—— Reply to Muraour's letter to the editor—819 (L)
Pepper, Paul M. Coexistence relations of $n+1$ phases in n-component systems—754
Peterson, A. M. (see Manning, L. A.)—475
Petrauskas, A. A. and F. Gaudry. Orientation of single-crystal rods of copper grown from the melt—1257 (L)
Petzold, R. F. (see Singer, S. J.)—816 (L)
Pierce, J. R. Increasing space charge waves—1060
Popov, E. P. Bending of beams with creep—251
Prager, William. Recent developments in the mathematical theory of plasticity—235
Prichard, A. C., M. A. A. Druesne, and D. G. McCaa. Increase in Q-value and reduction of aging of quartz crystal blanks—1011 (L)
Prim, R. C. III. Note on the substitution principle for steady gas flow—448
Protzman, Thomas F. Transition temperatures of methyl methacrylate polymers at ultrasonic frequencies—627

Ragazzini, John R. and Lotfi A. Zadeh. Probability criterion for the design of servo mechanisms—141
Ramberg, E. G. Aberration correction with electron mirrors—183
—— Phase contrast in electron microscope images—441
Raymond, Richard C. (see Millman, George H.)—413 (L)
—— (see Webb, Wayne)—330
—— **and Wayne Webb.** Radiation resistances of loaded antennas—328
Redheffer, R. M. Microwave antennas and dielectric surfaces—397
Rogers, F. T., Jr. (see Morrison, H. L.)—1027
Rohrbaugh, J. H. (see Wantuch, E.)—112
Rosen, Philip. Propagation of electromagnetic waves in a tube containing a coaxial d.c. discharge—868
Rosenthal, D. X-ray diffraction line broadening and strain hardening—1257 (L)

Sauer, J. A., J. Marin, and C. C. Hsiao. Creep and damping properties of polystyrene—507
Saunders, R. A. and D. C. Smith. Infra-red spectra and structure of hevea and gutta elastomers—953
Sawyer, W. M. (see Adler, F. T.)—1036
Schaaf, S. A. and R. R. Cyr. Time constants for vacuum gauge systems—860
Scherzer, O. Theoretical resolution limit of the electron microscope—20
Schlitt, Helmut. Investigations of a bearing for small angular deflections without any friction and with negligible restoring torque—297
Schneider, William C. and Charles J. Burton. Determination of the elastic constants of solids by ultrasonic methods—48
Schnurmann, Robert. Thermoelectric experiments with extreme-pressure lubricants—376
Schremp, Frederic W. (see Smith, Thor L.)—144
Schulz, L. G. A direct method of determining preferred orientation of a flat reflection sample using a Geiger counter x-ray spectrometer—1030
—— Determination of preferred orientation in flat transmission samples using a Geiger counter x-ray spectrometer—1033
Schumacher, William C. "Preliminary study of a physical basis of bird navigation"—123 (L)
Schwartz, C. M., A. E. Austin, and P. M. Weber. Positive-replica technique for electron microscopy—202
Schwertz, F. A. The structure of porous materials from gas penetration rates—1070
Scott, G. David. Spherical particles for electron microscopy—417 (L)
Seay, P. A. (see Hamlin, E. W.)—248
Seemann, Herman E. Comments on "Electronic radiography and microradiography"—231 (L)
Seifert, H. S. (see Tangren, R. F.)—637
Sharp, James M. (see Brown, S. Leroy)—578
Shmoys, J. (see Wantuch, E.)—112
Shobert, Erle I., II (see Holm, Else)—319
Simpson, John A. (see Marton, L.)—1258 (L)
Singer, S. J. and R. F. Petzold. Improvement in the shadow-cast replica technique—816 (L)
Smith, Cyril Stanley. On blowing bubbles for Bragg's dynamic crystal model—631 (L)
Smith, D. C. (see Saunders, R. A.)—953
Smith, Donald P. The role of rifting in cold-work and a possible measure of plastic deformation—1186
Smith, J. C. (see Ballou, J. W.)—493
Smith, P. D. P. Tensor field equations in a region of variable refractive index—633 (L)
—— Comments on biconical antennas—633 (L)
—— Ground plane field of the wide-angle conical dipole—636 (L)
Smith, Thor L., John D. Ferry, and Frederic W. Schremp. Measurements of the mechanical properties of polymer solutions by electromagnetic transducers—144
Smoluchowski, R. and R. W. Turner. Influence of magnetic field on recrystallization—745
Smythe, W. R. On the flow of a perfect fluid between two plates from a circular inlet channel—224 (L)
Sonders, L. R. (see Enright, D. P.)—1011 (L)
Spencer, R. S. and G. D. Gilmore. Equation of state for polystyrene—502
Spencer, Roy C. Discussion of "Geometrical factors affecting x-ray spectrometer maxima"—413 (L)

Stahl, H. A. Structure of extremely thin layers evaporated in kinetic vacuum systems—1
—— Thermal behavior of evaporated layer vacuum devices —8; erratum—724
Steinitz, Robert. Magnetic properties of iron compacts in relation to sintering temperature—712
Straiton, A. W. Extension of MacFarlane's method of deducing refractive index from radio observations—228 (L)
Strang, C. D. (see Burwell, J. T.)—79
—— **and C. R. Lewis.** On the magnitude of the mechanical component of solid friction—1164
Straumanis, M. E. Precision determination of lattice constants by the powder and rotating crystal methods and applications—726
Sulzer, Peter G. Sweep frequency ionosphere equipment—187
Symonds, P. S. Determination of stresses in plastic regions in problems of plane flow—107

Tai, C. T. Study of the e.m.f. method—717
—— Application of a variational principle to biconical antennas—1076
Tangren, R. F., C. H. Dodge, and H. S. Seifert. Compressibility effects in two-phase flow—637
Tasny-Tschiassny, L. Triangulation of a two-dimensional continuum for the purpose of the approximate solution of second-order partial differential equations—419
Thurman, G. R. (see Conant, F. S.)—526
Tomboulian, D. H. and E. M. Pell. Response of certain inorganic phosphors to far ultraviolet radiation—263
Tomiyasu, K. Antennas and open-wire lines. Part II: Measurements on two-wire lines—892
Turnbull, D. Subcooling of liquid metals—817 (L)
Turner, R. W. (see Smoluchowski, R.)—745
Tyndall, E. P. T. (see Wert, C. A.)—587

VanBronkhorst, A. (see Marton, L.)—1258 (L)
Vandegrift, R. B. (see Bush, O. B.)—295 (L)
Vazsonyi, A. Generalization of Nyquist's stability criteria —863
Victoreen, John A. The calculation of x-ray mass absorption coefficients—1141
Villard, O. G., Jr. (see Manning, L. A.)—475
Vineyard, George H. (see Lund, Louis H.)—593
Vink, H. J. (see Loosjes, R.)—884 (L)
Vogan, E. L. (see Woonton, G. A.)—71

Walkinshaw, W. Notes on "Wave guides for slow waves" —634 (L)
Wang, Chi-Teh and R. F. Brodsky. Application of Galerkin's method to compressible fluid flow problems—1255
Wantuch, E., J. H. Rohrbaugh, J. P. Cooley, J. H. Greig, and J. Shmoys. Erratum: Transmission properties of materials in the millimeter wave region—112
Warren, B. E. Method for measuring the total power of small-angle x-ray scattering—96
—— (see Averbach, B. L.)—885 (L), 1066
Watson, John H. L. Morphology of carbon black particles in shadow-cast specimens—747
Wax, Nelson. Some properties of tubular electron beams—242
Webb, Wayne (see Raymond, Richard C.)—328
—— **and Richard C. Raymond.** Current distributions on some simple antennas—330
Weber, P. M. (see Schwartz, C. M.)—202
Weekes, K. (see Bracewell, R. N.)—724 (L)
Weimer, D. K., C. H. Fletcher, and W. Bleakney. Transonic flow in a shock tube—418 (L)
Weinbaum, Sidney and H. L. Wheeler, Jr. Heat transfer in sweat-cooled porous metals—113
Weinreich, O. A. Activation phenomena with thoria cathodes —1256 (L)
Wert, Charles A. Internal friction of zinc single crystals—29
—— Precipitation from solid solution of C and N in α-iron —943
—— **and E. P. T. Tyndall.** Elasticity of zinc crystals—587
Weyl, W. A. (see Enright, D. P.)—1011 (L)
—— (see Marboe, Evelyn C.)—124 (L)
Wheeler, H. L., Jr. (see Weinbaum, Sidney)—113
Whisnant, John (see Breazeale, Francis)—621
White, Addison H. Application of thermodynamics to chemical problems involving the oxide cathode—856
—— (see Hannay, N. B.)—669
Wilford, Sally (see Michels, Walter C.)—1223
Wilkinson, P. G. and L. S. Birks. Properties of gold deposited at liquid air temperature—1168
Williams, Everard M. (see Aigrain, Pierre R.)—597
Williams, Robley C. (see Backus, Robert C.)—224 (L)
—— **and Robert C. Backus.** Electron-micrographic structure of shadow-cast films and surfaces—98
Winslow, W. M. Electrically induced fibration of suspensions—1137
Witte, R. S., B. A. Mrowca, and E. Guth. Propagation of audiofrequency sound in high polymers—481
Woonton, G. A., D. R. Hay, and E. L. Vogan. Experimental investigation of formulas for the prediction of horn radiator patterns—71

Yudowitch, K. L. Particle size determination by soft x-ray scattering—174
—— Collimation error in small angle x-ray scattering—1232

Zadeh, Lotfi A. (see Ragazzini, John R.)—141
Zener, Clarence. Theory of growth of spherical precipitates from solid solution—950

Subject Index to Volume 20

References with (L) are to Letters to the Editor.

Aberration correction with electron mirrors, E. G. Ramberg—183

Aberration phenomenon in electrostatic lenses, Shirley Harrison—412 (L)

Absorption of microwaves in gases, George H. Millman and Richard C. Raymond—413 (L)

Activation phenomena with thoria cathodes, O. A. Weinreich—1256 (L)

Aerodynamics of golf balls, John M. Davies—821

Africa, Northern, Dust—an active meteorological factor in the atmosphere of, M. G. El-Fandy—660

Air flow, high speed, Method for the instantaneous measurement of velocity and temperature in, D. G. Marlow, C. R. Nisewanger, and W. M. Cady—771

Air friction on rapidly moving surfaces—A. R. Kuhlthau—217

Amplitude modulation, Theoretical signal-to-noise ratios in F-M receivers: a comparison with amplitude modulation, David Middleton—334; errata—724 (L)

Analysis of the mechanics of metal cutting, D. C. Drucker—1013

Analysis of the metal-strip delay structure for microwave lenses, S. B. Cohn—257; addendum—1011 (L)

Angle-of-arrival, vertical, of radio waves, New solution to the problem of, E. W. Hamlin, P. A. Seay, and W. E. Gordon—248

Anisotropic plastic flow, Stress-strain rate relations for, John E. Dorn—15

Antenna, Infinitely long cylindrical, Charles H. Papas—437

Antennas, Biconical, P. D. P. Smith—633 (L)

Antennas, biconical, Application of a variational principle to, C. T. Tai—1076

Antennas, loaded, Radiation resistances of, Richard C. Raymond and Wayne Webb—328

Antennas, Microwave, and dielectric surfaces, R. M. Redheffer—397

Antennas and open-wire lines. Part I. Theory and summary of measurements, Ronold King—832

—— Part II. Measurements on two-wire lines, K. Tomiyasu—892

—— Part III. Image-line measurements, Patrick Conley—1022

Antennas, simple, Current distributions on, Wayne Webb and Richard C. Raymond—330

Apparatus to depict the load-elongation diagram of yarn at five cycles per second, Francis Breazeale and John Whisnant—621

Application of Galerkin's method to compressible fluid flow problems, Chi-Teh Wang and R. F. Brodsky—1255

Application of non-integral Legendre functions to potential problems, R. N. Hall—925

Application of thermodynamics to chemical problems involving the oxide cathode, Addison H. White—856

Application of a variational principle to biconical antennas, C. T. Tai—1076

Armor penetration, Measurement of forces resisting, A. Victor Masket—132

Atomic order, Influence of, on the magnetic properties, J. E. Goldman—1131

Attenuation in a dielectric circular rod, Walter M. Elsasser—1193

Attenuation of neutrons of various energies in water, C. E. Falk and E. Creutz—1183

Audiofrequency sound in high polymers, Propagation of, R. S. Witte, B. A. Mrowca, and E. Guth—481

Barkhausen noise and magnetic amplifiers. I. Theory of magnetic amplifiers, J. A. Krumhansl and R. T. Beyer—432

—— II. Analysis of the noise, J. A. Krumhansl and R. T. Beyer—582

Ba_2SiO_2 oxide cathode interface, Some properties of, A. Eisenstein—776

Beams, Bending of, with creep, E. P. Popov—251

Bearing, Investigations of a, for small angular deflections without any friction and with negligible restoring torque, Helmut Schlitt—297

Bending of beams with creep, E. P. Popov—251

Bending of a thin circular plate of an aeolotropic material under uniform lateral load (supported edge), H. Ōkubo—1151

Beryllium, High temperature precision x-ray camera. Some measurements of the thermal coefficients of expansion of, Paul Gordon—908

Beta-radiation, Ionization of paraffin wax by, Andrew Gemant—887

Biconical antennas, P. D. P. Smith—633 (L)

Biological membranes, Modification of silica replica technique for study of, and application of rotary condensation in electron microscopy, F. Heinmets—384

Bird navigation, Preliminary study of a physical basis of, William C. Schumacher—123 (L)

Blowing bubbles for Bragg's dynamic crystal model, Cyril Stanley Smith—631 (L)

Bolometer, Effect of current magnitude upon the behavior of a superconducting bolometer in its transition region, Nelson Fuson—59

Boundary lubrication, Incremental friction coefficient—a non-hydrodynamic component of, J. T. Burwell and C. D. Strang—79

Boundary model, Grain, and the mechanism of viscous intercrystalline slip, T'ing-Sui Kê—274

Bragg's dynamic crystal model, Blowing bubbles for, Cyril Stanley Smith—631 (L)

Bubbles, Blowing bubbles for Bragg's dynamic crystal model, Cyril Stanley Smith—631 (L)

Calculation of x-ray mass absorption coefficients, John A. Victoreen—1141

Carbon arc, High current, and its mechanism, Wolfgang Finkelnburg—468

Carbon black particles, Morphology of, in shadow-cast specimens, John H. L. Watson—747

Cathode, sintered, of thoria and tungsten mixture, Thermionic emission from, H. Y. Fan—682

Cathode, Vaporization of, in the electric arc, Ragnar Holm—715

Cathode, oxide-coated, Pulse emission decay phenomenon in, G. R. Feaster—415 (L)

Cathodes, oxide-coated, Work functions and conductivity of, G. W. Mahlman—197

Cathodes, thoria, Activation phenomena with, O. A. Weinreich—1256 (L)

Cathodes, thoria, Use of titanium and zirconium nitrides as a conducting element in, O. B. Bush, R. B. Vandegrift, and T. E. Hanley—295 (L)

Cathodic vacuum etching of metals, Don M. McCutcheon—414 (L)

Coefficient of anomalous viscosity, Charles Mack—225 (L)

Coexistence relations of $n+1$ phases in n-component systems, Paul M. Pepper—754

Cold work, Role of rifting in, and a possible measure of plastic deformation, Donald P. Smith—1186

Collimating apertures, Effective use of, in small-angle x-ray diffraction carriers, Orvil E. A. Bolduan and Richard S. Bear—983
Collimation error in small angle x-ray scattering, K. L. Yudowitch—1232
Comment on "A method of measuring dynamic mechanical properties of rubber-like materials," A. W. Nolle—227 (L)
Comments on "Electronic radiography and microradiography," Herman E. Seemann—231 (L)
Comments on "Grain growth in octachloropropane," Paul A. Beck—231 (L)
Compatibility, efficiency and permanence of plasticizers, Raymond F. Boyer—540
Compressibility effects in two-phase flow, R. F. Tangren, C. H. Dodge, and H. S. Seifert—637
Compression, simple, Volume changes in the plastic stages of, P. W. Bridgman—1241
Concrete, Magnetite, for radiation shielding, E. Creutz and K. Downes—1236
Contact problems, Theory of hardness and measurements applicable to, Else Holm, Ragnar Holm, and Erle I. Shobert II—319
Convection currents in porous media, H. L. Morrison, F. T. Rogers, Jr., and C. W. Horton—1027
Copper, Grain boundary relaxation and the mechanism of embrittlement of copper by bismuth, T'ing-Sui Kê—1226
Copper, Orientation of single-crystal rods of copper grown from the melt, A. A. Petrauskas and F. Gaudry—1257 (L)
Co-Pt alloys, Ordering reaction in, J. B. Newkirk, A. H. Geisler, and D. L. Martin—816 (L)
Corona onsets, Point-to-plane, William N. English and Leonard B. Loeb—707
Corona, Point-to-plane impulse corona, Donald Baker Moore and William N. English—370
Creep, Bending of beams with, E. P. Popov—251
Creep and damping properties of polystyrene, J. A. Sauer, J. Marin, and C. C. Hsiao—507
Crystal structure factors, Projection of, on the reciprocal lattice, Dan McLachlan, Jr., and C. L. Christ—829
Crystals, zinc single, Internal friction of, Charles A. Wert —29
Cu-Be alloys, Factors affecting the rate of precipitation hardening in, Paul A. Beck—666
Current distributions on some simple antennas, Wayne Webb and Richard C. Raymond—330
Cylinder, prismatic, Torsion of a, with a star-shaped section, H. Ōkubo—1155
Cylinders, coaxial, Electron transit time in space charged limited current between, Paul L. Copeland and Delbert N. Eggenberger—1148
Cylindrical bodies, Distribution of temperature and current in, Carl F. Muckenhoupt—939

Dead time and non-linearity characteristics of the Geiger-counter x-ray spectrometer, Leroy Alexander, Elizabeth Kummer, and Harold P. Klug—735
Demodulation of an F-M carrier and random noise by a limiter and discriminator, Nelson M. Blachman—38
Demodulation of a frequency-modulated carrier and random noise by a discriminator, Nelson M. Blachman—976
Density and packing in an aggregate of mixed spheres, Douglas Rennie Hudson—154
Design of networks for constant time delay, M. H. Hebb, C. W. Horton, and F. B. Jones—616
Determination of the elastic constants of solids by ultrasonic methods, William C. Schneider and Charles J. Burton—48
Determination of preferred orientation in flat transmission samples using a Geiger counter x-ray spectrometer, L. G. Schulz—1033
Determination of relative phases of Fourier coefficients from x-ray diffraction data, Dan McLachlan, Jr.—295 (L); erratum—1011 (L)
Determination of stresses in plastic regions in problems of plane flow, P. S. Symonds—107
Dielectric circular rod, Attenuation in a, Walter M. Elsasser —1193
Dielectric constant and loss of solids and liquids by a cavity perturbation method, Measurement of, George Birnbaum and Jacques Franeau—817 (L)
Dielectric rod, Investigation of, as wave guide, C. H. Chandler—1188
Dielectric surfaces, Microwave antennas and, R. M. Redheffer—397
Differential equations, non-linear, Electro-mechanical device for solving, Carl A. Ludeke—600
Diffraction of an electromagnetic wave through a plane screen, J. W. Miles—760
Dilatometric studies of high polymers. I. Second-order transition temperature. II. Crystallization of aromatic polyesters, Harry J. Kolb and Emmette F. Izard—564, 571
Diodes, High frequency total emission loading in, Nicholas A. Begovich—457
Dipole, Ground plane field of the wide angle conical dipole, P. D. P. Smith—636 (L)
Direct method of determining preferred orientation of a flat reflection sample using a Geiger-counter x-ray spectrometer, L. G. Schulz—1030
Disk-loaded wave guides, E. L. Chu and W. W. Hansen—280
Distribution of temperature and current in cylindrical bodies, Carl F. Muckenhoupt—939
Doppler, Radio Doppler investigation of meteoric heights and velocities, L. A. Manning, O. G. Villard, Jr., and A. M. Peterson—475
Duffing equation, Harmonic and subharmonic response for the, Morris E. Levenson—1045
Dust—an active meteorological factor in the atmosphere of Northern Africa, M. G. El-Fandy—660
Dynamic measurements of polymer physical properties, J. W. Ballou and J. C. Smith—493

Effect of cold work in metals on powder pattern intensities, B. L. Averbach and B. E. Warren—1066
Effect of current magnitude upon the behavior of a superconducting bolometer in its transition region, Nelson Fuson—59
Effect of "multiple grounds" on electron microscope images, W. L. Grube—125 (L)
Effect of surface roughness on eddy current losses at microwave frequencies, Samuel P. Morgan, Jr.—352
Effect of surface roughness on rolling friction, J. J. Bikerman—971
Effect of uplift and denudation on underground temperatures, A. E. Benfield—66
Effective use of collimating apertures in small-angle x-ray diffraction carriers, Orvil E. A. Bolduan and Richard S. Bear—983
Effects of stress and deformation on the Martensite transformation, Andrew W. McReynolds—896
Elastic constants of solids, Determination of, by ultrasonic methods, William C. Schneider and Charles J. Burton—48
Elasticity of zinc crystals, C. A. Wert and E. P. T. Tyndall —587
Elastomers, hevea and gutta, infra-red spectra and structure of, R. A. Saunders and D. C. Smith—953
Electrical contacts, Erosion of, on make, L. H. Germer and F. E. Haworth—1085
Electrically induced fibration of suspensions, W. M. Winslow —1137
Electric-field modulation of ultrasonic signals in liquids, A. W. Nolle—589

Electromagnetic fields, Electron optical mapping of, L. Marton and S. H. Lachenbruch—1171
Electromagnetic wave, Diffraction of, through a plane screen, J. W. Miles—760
Electromagnetic waves, Excitation of, in cylindrical metallic wave guides, A. Colino—576
Electromagnetic waves, Propagation of, in a tube containing a coaxial d. c. discharge, Philip Rosen—868
Electromagnetic waves, Reflection and transmission of, by a spherical shell, Herbert B. Keller and Joseph B. Keller—393
Electromagnetic waves, Scattering cross section of spheres for, L. Brillouin—1110
Electro-mechanical device for solving non-linear differential equations, Carl A. Ludeke—600
Electron beams, tubular, Some properties of, Nelson Wax—242
Electron diffraction studies of thin films, High temperature furnace for, Eileen I. Alessandrini—691
Electron emission and conduction mechanism of oxide-coated cathodes, R. Loosjes and H. J. Vink—884 (L)
Electron-micrographic structure of shadow-cast films and surfaces, Robley C. Williams and Robert C. Backus—98
Electron microscope and diffraction study of metal crystal textures by means of thin sections, R. D. Heidenreich—993
Electron microscope, Illuminating system of, James Hillier and S. G. Ellis—700
Electron microscope images, Effect of "multiple grounds" on, W. L. Grube—125 (L)
Electron microscope images, Phase contrast in, E. G. Ramberg—441
Electron microscope objective, Method of measuring spherical aberration of, Cecil E. Hall—631 (L)
Electron microscope, Technique for the preparation of grease or solid samples dispersed in grease-like media for examination with the, A. Y. Mottlau—1055
Electron microscope technique for the study of polymeric molecules, Wilbur Kaye—1209
Electron microscope, Theoretical resolution limit of the, O. Scherzer—20
Electron microscopy, Improved sectioning technique for, Richard F. Baker and Daniel G. Pease—480 (L)
Electron microscopy, Modification of silica replica technique for study of biological membranes and application of rotary condensation in, F. Heinmets—384
Electron microscopy, Positive-replica technique for, C. M. Schwartz, A. E. Austin, and P. M. Weber—202
Electron microscopy, Spherical particles for, G. David Scott—417 (L)
Electron mirrors, Aberration correction with, E. G. Ramberg—183
Electron optical mapping of electromagnetic fields, L. Marton and S. H. Lachenbruch—1171
Electron optical mapping of fringe fields of ferromagnetic domains, L. Marton, S. H. Lachenbruch, John A. Simpson, and A. VanBronkhorst—1258
Electron temperatures, multiple, Running striations and, N. L. Oleson and C. G. Found—416 (L)
Electron transit time in space charged limited current between coaxial cylinders, Paul L. Copeland and Delbert N. Eggenberger—1148
Electronic radiography and microradiography, Comments on, Herman E. Seemann—231 (L)
e.m.f. method, Study of, C. T. Tai—717
Energy losses of sound waves in metals due to scattering and diffusion, W. P. Mason and H. J. McSkimin, errata—228 (L)
Enumeration of Fourier phase permutations using electronic analog machines, A. D. Booth—388
Equation of state for polystyrene, R. S. Spencer and G. D. Gilmore—502
Erosion of electrical contacts on make, L. H. Germer and F. E. Haworth—1085
Excitation of electromagnetic waves in cylindrical metallic wave guides, A. Colino—576
Experimental investigation of formulas for the prediction of horn radiator patterns, G. A. Woonton, D. R. Hay, and E. L. Vogan—71
Extension of MacFarlane's method of deducing refractive index from radio observations, A. W. Straiton—228 (L)

Factors affecting the rate of precipitation hardening in Cu-Be alloys, Paul A. Beck—666
Ferromagnetic domains, fringe fields of, L. Marton, S. H. Lachenbruch, John A. Simpson, and A. VanBronkhorst—1258 (L)
Fibration of suspensions, Electrically induced, W. M. Winslow—1137
Fields from fluid flow mappers, A. D. Moore—790
Flash radiography applied to ordnance problems, J. C. Clark—363
Flow, Fluid flow patterns, Garrett Birkhoff and Thomas E. Caywood—646
Flow of a perfect fluid between two plates from a circular inlet channel, W. R. Smythe—224 (L)
Flow through a rocket nozzle with and without vibrational equilibrium, S. S. Penner—445
Flow, two-phase, Compressibility effects in, R. F. Tangren, C. H. Dodge, and H. S. Seifert—637
Fluid flow mappers, Fields from, A. D. Moore—790
Fluid flow patterns, Garrett Birkhoff and Thomas E. Caywood—646
Fluid flow problems, compressible, Application of Galerkin's method to, Chi-Teh Wang and R. F. Brodsky—1255
Fluid, perfect, Flow of a, between two plates from a circular inlet channel, W. R. Smythe—224 (L)
F-M carrier, Demodulation of, and random noise by a limiter and discriminator, Nelson M. Blachman—38
F-M receivers, Theoretical signal-to-noise ratios in: a comparison with amplitude modulation, David Middleton—334; errata—724
Formation of recrystallization nuclei, Paul A. Beck—633 (L)
Fourier coefficients, Determination of relative phases of, from x-ray diffraction data, Dan McLachlan, Jr.—295 (L); erratum—1011
Fourier phase permutations, Enumeration of, using electronic analog machines, A. D. Booth—388
Friction, Air, on rapidly moving surfaces—A. R. Kuhlthau—217
Friction coefficient, Incremental—a non-hydrodynamic component of boundary lubrication, J. T. Burwell and C. D. Strang—79
Friction, solid, Magnitude of the mechanical component of, C. D. Strang and C. R. Lewis—1164
Fringe fields of ferromagnetic domains, L. Marton, S. H. Lachenbruch, John A. Simpson, and A. VanBronkhorst—1258
Furnace, High temperature, for electron diffraction studies of thin films, Eileen I. Alessandrini—691

Galerkin's method, Application of, to compressible fluid flow problems, Chi-Teh Wang and R. F. Brodsky—1255
Gas flow, steady, Substitution principle for, R. C. Prim III—448
Gas flows, low density, Torsion balance for measuring forces in, I. Estermann and E. D. Kane—608
Gases, Absorption of microwaves in, George H. Millman and Richard C. Raymond—413 (L)
Geiger-counter spectrometer, Reflection method of determining preferred orientation on, Michael Field and M. Eugene Merchant—741

Geiger-counter x-ray spectrometer, Dead time and non-linearity characteristics of, Leroy Alexander, Elizabeth Kummer, and Harold P. Klug—735
Geiger-counter x-ray spectrometer, Determination of preferred orientation in flat transmission samples using a, L. G. Schulz—1033
Geiger-counter x-ray spectrometer, Direct method of determining preferred orientation of a flat refection sample using a, L. G. Schulz—1030
Generalization of Nyquist's stability criteria, A Vazsonyi—863
—— Comment on, S. J. Mason—867
Geometrical factors affecting x-ray spectrometer maxima, Roy C. Spencer—413 (L)
Glass, Photo-density method of determining the relative penetration of diffused sodium 24 tracer into, James R. Johnson—129; erratum—819 (L)
Glass, Study of the sintering of, G. C. Kuczynski—1160
Glow tube, Stabilization of breakdown voltage and measurement of some critical currents in a, A. B. Pal—451
Gold, Properties of, deposited at liquid air temperature, P. G. Wilkinson and L. S. Birks—1168
Golf balls, Aerodynamics of, John M. Davies—821
Grain boundary model and the mechanism of viscous intercrystalline slip, T'ing-Sui Kê—274
Grain boundary relaxation and the mechanism of embrittlement of copper by bismuth, T'ing-Sui Kê—1226
Grain growth in octachloropropane, W. C. McCrone and P. T. Cheng—230 (L)
—— Paul A. Beck—231 (L)
Grease, Technique for the preparation of grease or solid samples dispersed in grease-like media for examination with the electron microscope, A. Y. Mottlau—1055
Ground plane field of the wide angle conical dipole, P. D. P. Smith—636 (L)
Growth and structure of thin metallic films, Henry Levinstein—306

Hardness, Theory of, and measurements applicable to contact problems, Else Holm, Ragnar Holm, and Erle I. Shobert II—319
Harmonic and subharmonic response for the Duffing equation, Morris E. Levenson—1045
Heat transfer in sweat-cooled porous metals, Sidney Weinbaum and H. L. Wheeler, Jr.—113
Hevea and gutta elastomers, Infra-red spectra and structure of, R. A. Saunders and D. C. Smith—953
High current carbon arc and its mechanism, Wolfgang Finkelnburg—468
High frequency total emission loading in diodes, Nicholas A. Begovich—457
High frequency tubes, On the velocity-dependent characteristics of, Julian K. Knipp—425
High inverse voltage germanium rectifiers, S. Benzer—804
High polymers, Dilatometric studies of. I. Second-order transition temperature. II. Crystallization of aromatic polyesters, Harry J. Kolb and Emmette F. Izard—564, 571
High polymers, Propagation of audiofrequency sound in, R. S. Witte, B. A. Mrowca, and E. Guth—481
High polymers, Propagation of ultrasonic bulk waves in, Donald G. Ivey, B. A. Mrowca, and E. Guth—486
High temperature furnace for electron diffraction studies of thin films, Eileen I. Alessandrini—691
High temperature precision x-ray camera. Some measurements of the thermal coefficients of expansion of beryllium, Paul Gordon—908
Horn radiator patterns, Experimental investigation of formulas for the prediction of, G. A. Woonton, D. R. Hay, and E. L. Vogan—71
Horns, electromagnetic, Measurement of gain of, Allen S. Dunbar and M. Donald Adcock—226 (L)
Illuminating system of the electron microscope, James Hillier and S. G. Ellis—700
Impedance of resonant transmission lines and wave guides, W. W. Harman—1252
Impedance synthesis without use of transformers, R. Bott and R. J. Duffin—816 (L)
Improved sectioning technique for electron microscopy, Richard F. Baker and Daniel G. Pease—480 (L)
Improved spinning top homogeneous spray apparatus, K. R. May—932
Improvement in the shadow-cast replica technique, S. J. Singer and R. F. Petzold—816 (L)
Increase in Q-value and reduction of aging of quartz crystal blanks, A. C. Prichard, M. A. A. Druesne, and D. G. McCaa—1011 (L)
Increasing space charge waves, J. R. Pierce—1060
Incremental friction coefficient—a non-hydrodynamic component of boundary lubrication, J. T. Burwell and C. D. Strang—79
Infinitely long cylindrical antenna, Charles H. Papas—437
Influence of atomic order on the magnetic properties, J. E. Goldman—1131
Influence of magnetic field on recrystallization, R. Smoluchowski and R. W. Turner—745
Infra-red absorption spectra of some polymers at liquid-helium temperatures, Gilbert W. King, R. M. Hainer, and H. O. McMahon—559
Infra-red spectra and structure of hevea and gutta elastomers, R. A. Saunders and D. C. Smith—953
Intercrystalline slip, viscous, Grain boundary model and the mechanism of, T'ing-Sui Kê—274
Internal friction of zinc single crystals, Charles A. Wert—29
Inter-particle interference effects in the small angle x-ray scattering from fine powders, Louis H. Lund and George H. Vineyard—593
Interplanar spacings, Table of, for different target materials for the back reflection region, Suzanne van Dijke Beatty—415 (L)
Interpretation of x-ray patterns of cold-worked metal, B. L. Averbach and B. E. Warren—885 (L)
Investigation of dielectric rod as wave guide, C. H. Chandler—1188
Investigations of a bearing for small angular deflections without any friction and with negligible restoring torque, Helmut Schlitt—297
Ionic substances, Method for studying the forces between metals and, Evelyn C. Marboe and W. A. Weyl—124 (L)
Ionization of paraffin wax by beta-radiation, Andrew Gemant—887
Ionized gas, Measurement of the complex conductivity of an, at microwave frequencies, Fred P. Adler—1115
Ionosphere, Maximum height of reflection of a radio wave in a curved ionosphere layer, John M. Kelso—632 (L)
Ionosphere, Sweep frequency ionosphere equipment, Peter G. Sulzer—187
Ionospheric absorption, R. N. Bracewell and K. Weekes—724 (L)
Ionospheric absorption problem, Note on the, Leslie G. McCracken—229 (L)
Iron compacts, Magnetic properties of, in relation to sintering temperature, Robert Steinitz—712

Lattice constants, Precision determination of, by the powder and rotating crystal methods and applications, M. E. Straumanis—726
Legendre functions, non-integral, Application of, to potential problems, R. N. Hall—925
Lenses, electrostatic, Aberration phenomenon in, Shirley Harrison—412 (L)
Loading in diodes, High frequency total emission, Nicholas A. Begovich—457

Lubricants, extreme-pressure, Thermoelectric experiments with, Robert Schnurmann—376

MacFarlane's method of deducing refractive index from radio observations, Extension of, A. W. Straiton—228 (L)
Machines, Enumeration of Fourier phase permutations using electronic analog machines, A. D. Booth—388
Magnetic amplifiers, Theory of. Barkhausen noise and magnetic amplifiers. I, J. A. Krumhansl and R. T. Beyer—432
——, Barkhausen noise and. II. Analysis of the noise, J. A. Krumhansl and R. T. Beyer—582
Magnetic characteristics of an oriented 50 percent nickel-iron alloy, J. H. Crede and J. P. Martin—966
Magnetic field, Influence of, on recrystallization, R. Smoluchowski and R. W. Turner—745
Magnetic properties of iron compacts in relation to sintering temperature, Robert Steinitz—712
Magnetically controlled wave guide attenuators, Theodore Miller—878
Magnetite concrete for radiation shielding, E. Creutz and K. Downes—1236
Magnitude of the mechanical component of solid friction, C. D. Strang and C. R. Lewis—1164
Mappers, fluid flow, Fields from, A. D. Moore—790
Mapping, Electron optical, of fringe fields of ferromagnetic domains, L. Marton, S. H. Lachenbruch, John A. Simpson, and A. VanBronkhorst—1258
Martensite transformation, Effects of stress and deformation on the, Andrew W. McReynolds—896
Mathematical theory of photo-viscoelasticity, Raymond D. Mindlin—206
Mathematical theory of plasticity, Recent developments in, William Prager—235
Maximum height of reflection of a radio wave in a curved ionosphere layer, John M. Kelso—632 (L)
Measurement of the complex conductivity of an ionized gas at microwave frequencies, Fred P. Adler—1115
Measurement of the dielectric constant and loss of solids and liquids by a cavity perturbation method, George Birnbaum and Jacques Franeau—817 (L)
Measurement of forces resisting armor penetration, A. Victor Masket—132
Measurement of gain of electromagnetic horns, Allen S. Dunbar and M. Donald Adcock—226 (L)
Measurements of the mechanical properties of polymer solutions by electromagnetic transducers, Thor L. Smith, John D. Ferry, and Frederic W. Schremp—144
Metal, cold-worked, Interpretation of x-ray patterns of, B. L. Averbach and B. E. Warren—885 (L)
Metal crystal textures, Electron microscope and diffraction study of, by means of thin sections, R. D. Heidenreich—993
Metal cutting, Analysis of the mechanics of, D. C. Drucker—1013
Metallic films, thin, Growth and structure of, Henry Levinstein—306
Metallic particles, Study of the mechanism of sintering of, J. H. Dedrick and A. Gerds—1042
Metals, Cathodic vacuum etching of, Don M. McCutcheon—414 (L)
Metals, Effect of cold work in, on powder pattern intensities, B. L. Averbach and B. E. Warren—1066
Metals, Energy losses of sound waves in, due to scattering and diffusion, W. P. Mason and H. J. McSkimin, errata—228 (L)
Metals and ionic substances, Method for studying the forces between, Evelyn C. Marboe and W. A. Weyl—124 (L)
Metals, liquid, Subcooling of, D. Turnbull—817 (L)
Metals, sweat-cooled porous, Heat transfer in, Sidney Weinbaum and H. L. Wheeler, Jr.—113
Metal-strip delay structure for microwave lenses, Analysis of, S. B. Cohn—257; addendum—1011
Meteoric heights and velocities, Radio Doppler investigation of, L. A. Manning, O. G. Villard, Jr., and A. M. Peterson—475
Meteorological factor, Dust—an active meteorological factor in the atmosphere of Northern Africa, M. G. El-Fandy—660
Method of equivalent linearization for non-linear oscillatory systems with large non-linearity, Carl A. Ludeke—694
Method for the instantaneous measurement of velocity and temperature in high speed air flow, D. G. Marlow, C. R. Nisewanger, and W. M. Cady—771
Method of measuring dynamic mechanical properties of rubber-like materials, K. W. Hillier, H. Kolsky, and J. P. Lewis—227 (L)
—— A. W. Nolle—227 (L)
Method of measuring spherical aberration of an electron microscope objective, Cecil E. Hall—631 (L)
Method for measuring the total power of small-angle x-ray scattering, B. E. Warren—96
Method for the quantitative evaluation of x-ray patterns from mixed powders adapted to the demands of quantitative analysis, J. C. M. Brentano—1215
Method for studying the distribution and sign of static charges on solid materials, Harry H. Hull—1157
Method for studying the forces between metals and ionic substances, Evelyn C. Marboe and W. A. Weyl—124 (L)
Methyl methacrylate polymers, Transition temperatures of, at ultrasonic frequencies, Thomas F. Protzman—627
Microradiography, Comments on electronic radiography and, Herman E. Seemann—231 (L)
Microwave antennas and dielectric surfaces, R. M. Redheffer—397
Microwave frequencies, Effect of surface roughness on eddy current losses at, Samuel P. Morgan, Jr.—352
Microwave lenses, Analysis of the metal-strip delay structure for, S. B. Cohn—257; addendum—1011
Microwave Q measurements in the presence of series losses, L. Malter and G. R. Brewer—918
Microwaves in gases, Absorption of, George H. Millman and Richard C. Raymond—413 (L)
Millimeter wave region, Transmission properties of materials in, E. Wantuch, J. H. Rohrbaugh, J. P. Cooley, J. H. Greig, and J. Shmoys, erratum—112
Mixing properties of non-linear condensers, Note on, R. V. L. Hartley—819 (L)
Modification of silica replica technique for study of biological membranes and application of rotary condensation in electron microscopy, F. Heinmets—384
Morphology of carbon black particles in shadow-cast specimens, John H. L. Watson—747

n-component systems, Coexistence relations of $n+1$ phases in, Paul M. Pepper—754
Network analysis, electrical, Use of a mechanical harmonic synthesizer in, S. Leroy Brown and Chester M. McKinney—316
Networks for constant time delay, Design of, M. H. Hebb, C. W. Horton, and F. B. Jones—616
Neutrons of various energies, Attenuation of, in water, C. E. Falk and E. Creutz—1183
New interpretation of the n-power law in plastic deformation, Herbert I. Fusfeld—1052
New method of capacity measurement on dry disk rectifiers, K. Lehovec—123 (L)
New solution to the problem of vertical angle-of-arrival of radio waves, E. W. Hamlin, P. A. Seay, and W. E. Gordon—248
Nickel-iron alloy, oriented 50 percent, Magnetic characteristics of, J. H. Crede and J. P. Martin—966

Non-linear condensers, Note on mixing properties of, R. V. L. Hartley—819 (L)
Non-linear oscillatory systems with large non-linearity, Method of equivalent linearization for, Carl A. Ludeke—694
Note on the ionospheric absorption problem, Leslie G. McCracken—229 (L)
Note on "The mixing properties of non-linear condensers," R. V. L. Hartley—819 (L)
Note on "Qualitative experimental verification of the change of burning rate of rocket powders with radiation path length," Henri Muraour—819 (L)
—— S. S. Penner—819 (L)
n-power law, New interpretation of, in plastic deformation, Herbert I. Fusfeld—1052
n-reactance networks, Synthesis of, for desired transient response, Pierre R. Aigrain and Everard M. Williams—597
Nyquist's stability criteria, Generalization of, A. Vazsonyi—863
—— Comment on, S. J. Mason—867

Octachloropropane, Grain growth in, W. C. McCrone and P. T. Cheng—230 (L)
—— Paul A. Beck—231 (L)
Optical equations of three-dimensional photoelasticity, Raymond D. Mindlin and Lawrence E. Goodman—89
Ordering reaction in Co-Pt alloys, J. B. Newkirk, A. H. Geisler, and D. L. Martin—816 (L)
Ordnance problems, Flash radiography applied to, J. C. Clark—363
Orientation of single-crystal rods of copper grown from the melt, A. A. Petrauskas and F. Gaudry—1257
Oxide cathode, Application of thermodynaamics to chemical problems involving the, Addison H. White—856
Oxide cathode coatings, Resistance of, for high values of pulsed emission, W. E. Danforth and D. L. Goldwater—163
Oxide cathode, Some properties of the Ba_2SiO_4 oxide cathode interface, A. Eisenstein—776
Oxide cathodes, Semiconducting properties in, N. B. Hannay, D. MacNair, and Addison H. White—669
Oxide-coated cathodes, Electron emission and conduction mechanism of, R. Loosjes and H. J. Vink—884 (L)
Oxide-coated cathodes, Work functions and conductivity of, G. W. Mahlman—197

Papers by Hadrian Stahl, G. H. Metson—1130 (L)
Paraffin wax, Ionization of, by beta-radiation, Andrew Gemant—887
Particle size determination by soft x-ray scattering, K. L. Yudowitch—174
Particles, spherical, Small, of exceptionally uniform size, Robert C. Backus and Robley C. Williams—224 (L)
Phase contrast in electron microscope images, E. G. Ramberg—441
Phase distribution in two-phase solids, L. D. Jaffe—1206
Phase lead for a.c. servo mechanisms, Arthur H. Benner—268
Phosphors, Response of certain inorganic phosphors to far ultraviolet radiation, D. H. Tomboulian and E. M. Pell—263
Photo-density method of determining the relative penetration of diffused sodium 24 tracer into glass, James R. Johnson—129; erratum—819 (L)
Photoelasticity, three-dimensional, Optical equations of, Raymond D. Mindlin and Lawrence E. Goodman—89
Photo-viscoelasticity, Mathematical theory of, Raymond D. Mindlin—206
Physical properties of titanium. I—Emissivity and resistivity of the commercial metal, Walter C. Michels and Sally Wilford—1223
Plane flow, problems of, Determination of stresses in plastic regions in, P. S. Symonds—107
Plastic deformation, New interpretation of the *n*-power law in, Herbert I. Fusfeld—1052
Plastic deformation, Role of rifting in cold-work and a possible measure of, Donald P. Smith—1186
Plastic flow, anisotropic, Stress-strain rate relations for, John E. Dorn—15
Plastic flow effects in steel, Orrin H. Clark and Ernest M. Lyman—884 (L)
Plastic regions in problems of plane flow, Determination of stresses in, P. S. Symonds—107
Plasticity, mathematical theory of, Recent developments in, William Prager—235
Plasticizers, Compatibility, efficiency and permanence of, Raymond F. Boyer—540
Plate, Bending of a thin circular plate of an aeolotropic material under uniform lateral load (supported edge), H. Ōkubo—1151
Point-to-plane corona onsets, William N. English and Leonard B. Loeb—707
Point-to-plane impulse corona, Donald Baker Moore and William N. English—370
Polyesters, aromatic, Crystallization of, Harry J. Kolb and Emmette F. Izard—571
Polyethylene, X-ray diffraction studies of the stretching and relaxing of, Alexander Brown—552
Polymer physical properties, Dynamic measurements of, J. W. Ballou and J. C. Smith—493
Polymer solutions, mechanical properties of, Measurements of, by electromagnetic transducers, Thor L. Smith, John D. Ferry, and Frederic W. Schremp—144
Polymeric molecules, Electron microscope technique for the study of, Wilbur Kaye—1209
Polymerization in the solid state, E. Miller, I. Fankuchen, and H. Mark—531
Polymers, Infra-red absorption spectra of some polymers at liquid-helium temperatures, Gilbert W. King, R. M. Heiner, and H. O. McMahon—559
Polymers, methyl methacrylate, Transition temperatures of, at ultrasonic frequencies, Thomas F. Protzman—627
Polystyrene, Creep and damping properties of, J. A. Sauer, J. Marin, and C. C. Hsiao—507
Polystyrene, Equation of state for, R. S. Spencer and G. D. Gilmore—502
Porous materials, Structure of, from gas penetration rates, F. A. Schwertz—1070
Positive-replica technique for electron microscopy, C. M. Schwartz, A. E. Austin, and P. M. Weber—202
Potential functions for a thermionic vacuum tube, E. C. Okress—850
Precipitation hardening in Cu-Be alloys, Factors affecting the rate of, Paul A. Beck—666
Precipitation from solid solutions of C and N in α-iron, Charles A. Wert—943
Precision determination of lattice constants by the powder and rotating crystal methods and applications, M. E. Straumanis—726
Preliminary study of a physical basis of bird navigation, William C. Schumacher—123 (L)
Probability criterion for the design of servo mechanisms, John R. Ragazzini and Lotfi A. Zadeh—141
Projection of crystal structure factors on the reciprocal lattice, Dan McLachlan, Jr. and C. L. Christ—829
Propagation of audiofrequency sound in high polymers, R. S. Witte, B. A. Mrowca, and E. Guth—481
Propagation of electromagnetic waves in a tube containing a coaxial d. c. discharge, Philip Rosen—868
Propagation of transverse waves in viscoelastic media, F. T. Adler, W. M. Sawyer, and John D. Ferry—1036

Propagation of ultrasonic bulk waves in high polymers, Donald G. Ivey, B. A. Mrowca, and E. Guth—486
Properties of gold deposited at liquid air temperature, P. G. Wilkinson and L. S. Birks—1168
Pulse emission decay phenomenon in oxide-coated cathodes, G. R. Feaster—415 (L)

Quartz crystal blanks, Increase in Q-value and reduction of aging of, A. C. Prichard, M. A. A. Druesne, and D. G. McCaa—1011 (L)

Radiation resistances of loaded antennas, Richard C. Raymond and Wayne Webb—328
Radiation shielding, Magnetite concrete for, E. Creutz and K. Downes—1236
Radio Doppler investigation of meteoric heights and velocities, L. A. Manning, O. G. Villard, Jr., and A. M. Peterson—475
Radio wave, Maximum height of reflection of, in a curved ionosphere layer, John M. Kelso—632 (L)
Radio waves, New solution to the problem of vertical angle-of-arrival of, E. W. Hamlin, P. A. Seay, and W. E. Gordon—248
Radiography, Flash, applied to ordnance problems, J. C. Clark—363
Recent developments in the mathematical theory of plasticity, William Prager—235
Recrystallization, Influence of magnetic field on, R. Smoluchowski and R. W. Turner—745
Recrystallization nuclei, Formation of, Paul A. Beck—633 (L)
Rectifiers, dry disk, New method of capacity measurement on, K. Lehovec—123 (L)
Rectifiers, High inverse voltage germanium rectifiers, S. Benzer—804
Reflection method of determining preferred orientation on the Geiger-counter spectrometer, Michael Field and M. Eugene Merchant—741
Reflection and transmission of electromagnetic waves by a spherical shell, Herbert B. Keller and Joseph B. Keller—393
Refractive index, Extension of MacFarlane's method of deducing refractive index from radio observations, A. W. Straiton—228 (L)
Refractories, two, Thermionic emitting properties of, R. E. Haddad, D. L. Goldwater, and F. H. Morgan—1130 (L)
Relationship between Gough-Joule coefficients and moduli of vulcanized rubbers, F. S. Conant, G. L. Hall, and G. R. Thurman—526
Resistance of oxide cathode coatings for high values of pulsed emission, W. E. Danforth and D. L. Goldwater—163
Resolution limit, Theoretical, of the electron microscope, O. Scherzer—20
Resonance effect in the synchrotron, E. D. Courant—611
Response of certain inorganic phosphors to far ultraviolet radiation, D. H. Tomboulian and E. M. Pell—263
Rifting, Role of, in cold-work and a possible measure of plastic deformation, Donald P. Smith—1186
Rocket nozzle, Flow through a, with and without vibrational equilibrium, S. S. Penner—445
Rocket powders, Note on "Qualitative experimental verification of the change of burning rate of rocket powders with radiation path length," Henri Muraour—819 (L)
—— S. S. Penner—819 (L)
Role of rifting in cold-work and a possible measure of plastic deformation, Donald P. Smith—1186
Rolling friction, Effect of surface roughness on, J. J. Bikerman—971
Rubber, Time and stress effects in the behavior of rubber at low temperature, J. R. Beatty and J. M. Davies—533
Rubber-like materials, Method of measuring dynamic mechanical properties of, K. W. Hillier, H. Kolsky, and J. P. Lewis—227 (L)
—— A. W. Nolle—227 (L)
Rubbers, vulcanized, Relationship between Gough-Joule coefficients and moduli of, F. S. Conant, G. L. Hall, and G. R. Thurman—526
Running striations and multiple electron temperatures, N. L. Oleson and C. G. Found—416 (L)

Scattering cross section of spheres for electromagnetic waves, L. Brillouin—1110
Scattering by an inhomogeneous solid, P. Debye and A. M. Bueche—518
Second-order partial differential equations, Triangulation of a two-dimensional continuum for the purpose of the approximate solution of, L. Tasny-Tschiassny—419
Sectioning technique, Improved, for electron microscopy, Richard F. Baker and Daniel G. Pease—480 (L)
Semiconducting properties in oxide cathodes, N. B. Hannay, D. MacNair, and Addison H. White—669
Servo mechanisms, a.c., Phase lead for, Arthur H. Benner—268
Servo mechanisms, design of, Probability criterion for, John R. Ragazzini and Lotfi A. Zadeh—141
Shadow-cast films and surfaces, Electron-micrographic structure of, Robley C. Williams and Robert C. Backus—98
Shadow-cast replica technique, Improvement in, S. J. Singer and R. F. Petzold—816 (L)
Shadow-cast specimens, Morphology of carbon black particles in, John H. L. Watson—747
Shell, spherical, Reflection and transmission of electromagnetic waves by a, Herbert B. Keller and Joseph B. Keller—393
Shock tube, Transonic flow in a, D. K. Weimer, C. H. Fletcher, and W. Bleakney—418 (L)
Silica replica technique, Modification of, for study of biological membranes and application of rotary condensation in electron microscopy, F. Heinmets—384
Sintering of glass, Study of, G. C. Kuczynski—1160
Sintering of metallic particles, Study of the mechanism of, J. H. Dedrick and A. Gerds—1042
Sixth Annual Pittsburgh Conference on x-ray and electron diffraction—725
Small spherical particles of exceptionally uniform size, Robert C. Backus and Robley C. Williams—224 (L)
Sodium 24 tracer, Photo-density method of determining the relative penetration of diffused sodium 24 tracer into glass, James R. Johnson—129; erratum—819 (L)
Solid state, Polymerization in the, E. Miller, I. Fankuchen, and H. Mark—531
Some properties of the Ba_2SiO_4 oxide cathode interface, A. Eisenstein—776
Some properties of tubular electron beams, Nelson Wax—242 (L)
Sound waves, Energy losses of, in metals due to scattering and diffusion, W. P. Mason and H. J. McSkimin, errata—228
Spheres, mixed, Density and packing in an aggregate of, Douglas Rennie Hudson—154
Spherical particles for electron microscopy, G. David Scott—417 (L)
Spherical precipitates, Theory of growth of, from solid solution, Clarence Zener—950
Spray apparatus, Improved spinning top homogeneous spray apparatus, K. R. May—932
Stabilization of breakdown voltage and measurement of some critical currents in a glow tube, A. B. Pal—451
Stahl, Papers by Hadrian Stahl, G. H. Metson—1130 (L)
Static charges on solid materials, Method for studying the distribution and sign of, Harry H. Hull—1157

Steel, Note on some plastic flow effects in, Orrin H. Clark and Ernest M. Lyman—884 (L)
Stresses in plastic regions in problems of plane flow, Determination of, P. S. Symonds—107
Stress-strain rate relations for anisotropic plastic flow, John E. Dorn—15
Structure of extremely thin layers evaporated in kinetic vacuum systems, H. A. Stahl—1
Structure of porous materials from gas penetration rates, F. A. Schwertz—1070
Study of the e.m.f. method, C. T. Tai—717
Study of the mechanism of sintering of metallic particles, J. H. Dedrick and A. Gerds—1042
Study of the sintering of glass, G. C. Kuczynski—1160
Subcooling of liquid metals, D. Turnbull—817 (L)
Substitution principle for steady gas flow, R. C. Prim III—448
Supersonic flow patterns, M. M. Munk—302
Surface polarization and wettability of inorganic substances by water, D. P. Enright, L. R. Sonders, and W. A. Weyl—1011 (L)
Surface roughness, Effect of, on eddy current losses at microwave frequencies, Samuel P. Morgan, Jr.—352
Surface-fitting in three variables, Morris Morduchow—390
Surfaces, rapidly moving, Air friction on, A. R. Kulthau—217
Sweep frequency ionosphere equipment, Peter G. Sulzer—187
Synchrotron, Resonance effect in the, E. D. Courant—611
Synthesis of *n*-reactance networks for desired transient response, Pierre R. Aigrain and Everard M. Williams—597
Synthesizer, mechanical harmonic, Use of, in electric wave filter analysis, S. Leroy Brown and James M. Sharp—578
Synthesizer, mechanical harmonic, Use of, in electrical network analysis, S. Leroy Brown and Chester M. McKinney—316

Table of interplanar spacings for different target materials for the back reflection region, Suzanne van Dijke Beatty—415 (L)
Technique for the preparation of grease or solid samples dispersed in grease-like media for examination with the electron microscope, A. Y. Mottlau—1055
Temperatures, underground, Effect of uplift and denudation on, A. E. Benfield—66
Tensor field equations in a region of variable refractive index, P. D. P. Smith—633 (L)
Theoretical resolution limit of the electron microscope, O. Scherzer—20
Theoretical signal-to-noise ratios in f-m receivers: a comparison with amplitude modulation, David Middleton—334; errata—724 (L)
Theory of growth of spherical precipitates from solid solution, Clarence Zener—950
Theory of hardness and measurements applicable to contact problems, Else Holm, Ragnar Holm, and Erle I. Shobert II—319
Thermal behavior of evaporated layer vacuum devices, H. A. Stahl—8; erratum—724 (L)
Thermionic emission from sintered cathode of thoria and tungsten mixture, H. Y. Fan—682
Thermionic emitter, Zirconium carbide as a, R. E. Haddad, D. L. Goldwater, and F. H. Morgan—886 (L)
Thermionic emitting properties of two refractories, R. E. Haddad, D. L. Goldwater, and F. H. Morgan—1130 (L)
Thermodynamics, Application of, to chemical problems involving the oxide cathode, Addison H. White—856
Thermoelectric experiments with extreme-pressure lubricants, Robert Schnurmann—376
Thin films peeled from Teflon, C. K. Jones—1257 (L)
Thoria cathodes, Activation phenomena with, O. A. Weinreich—1256 (L)
Time constants for vacuum gauge systems, S. A. Schaaf and R. R. Cyr—860
Time and stress effects in the behavior of rubber at low temperature, J. R. Beatty and J. M. Davies—533
Titanium, Physical properties of. I—Emissivity and resistivity of the commercial metal, Walter C. Michels and Sally Wilford—1223
Titanium, Use of titanium and zirconium nitrides as a conducting element in thoria cathodes, O. B. Bush, R. B. Vandegrift, and T. E. Hanley—295 (L)
Torsion balance for measuring forces in low density gas flows, I. Estermann and E. D. Kane—608
Torsion of a prismatic cylinder with a star-shaped section, H. Ōkubo—1155
Transducers, electromagnetic, Measurements of the mechanical properties of polymer solutions by, Thor L. Smith, John D. Ferry, and Frederic W. Schremp—144
Transition temperatures of methyl methacrylate polymers at ultrasonic frequencies, Thomas F. Protzman—627
Transmission properties of materials in the millimeter wave region, E. Wantuch, J. H. Rohrbaugh, J. P. Cooley, J. H. Greig, and J. Shmoys, erratum—112
Transonic flow in a shock tube, D. K. Weimer, C. H. Fletcher, and W. Bleakney—418 (L)
Traveling-wave tube (Discussion of waves for large amplitudes), L. Brillouin—1110
Triangulation of a two-dimensional continuum for the purpose of the approximate solution of second-order partial differential equations, L. Tasny-Tschiassny—419

Ultrasonic bulk waves in high polymers, Propagation of, Donald G. Ivey, B. A. Mrowca, and E. Guth—486
Ultrasonic methods, Determination of the elastic constants of solids by, William C. Schneider and Charles J. Burton—48
Ultrasonic phenomena, Visual methods for studying, R. Bowling Barnes and Charles J. Burton—286
Ultrasonic signals in liquids, Electric-field modulation of, A. W. Nolle—589
Ultrasonic waves through thin plates of material, Visual method for demonstrating the path of, Charles J. Burton and R. Bowling Barnes—462
Ultraviolet radiation, far, Response of certain inorganic phosphors to, D. H. Tomboulian and E. M. Pell—263
Uplift and denudation, Effect of, on underground temperatures, A. E. Benfield—66
Use of a mechanical harmonic synthesizer in electric wave filter analysis, S. Leroy Brown and James M. Sharp—578
Use of a mechanical harmonic synthesizer in electrical network analysis, S. Leroy Brown and Chester M. McKinney—316
Use of titanium and zirconium nitrides as a conducting element in thoria cathodes, O. B. Bush, R. B. Vandegrift, and T. E. Hanley—295 (L)

Vacuum devices, evaporated layer, Thermal behavior of, H. A. Stahl—8; erratum—724 (L)
Vacuum gage systems, Time constants for, S. A. Schaaf and R. R. Cyr—860
Vacuum systems, kinetic, Structure of extremely thin layers evaporated in, H. A. Stahl—1
Vacuum tube, thermionic, Potential functions for a, E. C. Okress—850
Vaporization of the cathode in the electric arc, Ragnar Holm—715
Velocity-dependent characteristics of high frequency tubes, Julian K. Knipp—425
Vibrational equilibrium, Flow through a rocket nozzle with and without, S. S. Penner—445
Viscoelastic media, Propagation of transverse waves in, F. T. Adler, W. M. Sawyer, and John D. Ferry—1036

Viscosity, anomalous, Coefficient of, Charles Mack—225 (L)
Visual method for demonstrating the path of ultrasonic waves through thin plates of material, Charles J. Burton and R. Bowling Barnes—462
Visual methods for studying ultrasonic phenomena, R. Bowling Barnes and Charles J. Burton—286
Volume changes in the plastic stages of simple compression, P. W. Bridgman—1241

Water, Attenuation of neutrons of various energies in, C. E. Falk and E. Creutz—1183
Water, Surface polarization and wettability of inorganic substances by, D. P. Enright, L. R. Sonders, and W. A. Weyl—1011 (L)
Wave filter analysis, electric, Use of a mechanical harmonic synthesizer in, S. Leroy Brown and James M. Sharp—578
Wave guide attenuators, Magnetically controlled, Theodore Miller—878
Wave guide, Investigation of dielectric rod as wave guide, C. H. Chandler—1188
Wave guides, cylindrical metallic, Excitation of electromagnetic waves in, A. Colino—576
Wave guides, Disk-loaded, E. L. Chu and W. W. Hansen—280
Wave guides, Impedance of resonant transmission lines and, W. W. Harman—1252
Wave guides for slow waves, W. Walkinshaw—634 (L)
Waves, Increasing space-charge waves, J. R. Pierce—1060
Waves, Traveling-wave tube (Discussion of waves for large amplitudes), L. Brillouin—1196
Wettability of inorganic substances by water, Surface polarization and, D. P. Enright, L. R. Sonders, and W. A. Weyl—1011 (L)
Work functions and conductivity of oxide-coated cathodes, G. W. Mahlman—197

X-ray camera, High temperature precision. Some measurements of the thermal coefficients of expansion of beryllium, Paul Gordon—908
X-ray diffraction carriers, small-angle, Effective use of collimating apertures in, Orvil E. A. Bolduan and Richard S. Bear—983
X-ray diffraction data, Determination of relative phases of Fourier coefficients from, Dan McLachlan, Jr.—295 (L); erratum—1011 (L)
X-ray diffraction line broadening and strain hardening, D. Rosenthal—1257 (L)
X-ray diffraction studies on the stretching and relaxing of polyethylene, Alexander Brown—552
X-ray and electron diffraction, Sixth Annual Pittsburgh Conference on—725
X-ray, Geometrical factors affecting x-ray spectrometer maxima, Roy C. Spencer—413 (L)
X-ray mass absorption coefficients, Calculation of, John A. Victoreen—1141
X-ray patterns of cold-worked metal, Interpretation of, B. L. Averbach and B. E. Warren—885 (L)
X-ray patterns, Method for the quantitative evaluation of, from mixed powders adapted to the demands of quantitative analysis, J. C. M. Brentano—1215
X-ray scattering, small angle, Collimation error in, K. L. Yudowitch—1232
X-ray scattering, small angle, from fine powders, Interparticle interference effects in, Louis H. Lund and George H. Vineyard—593
X-ray scattering, small-angle, Method for measuring the total power of, B. E. Warren—96
X-ray scattering, soft, Particle size determination by, K. L. Yudowitch—174
X-ray spectrometer, Determination of preferred orientation in flat transmission samples using a Geiger-counter x-ray spectrometer, L. G. Schulz—1033
X-ray spectrometer, Direct method of determining preferred orientation of a flat reflection sample using a Geiger-counter x-ray spectrometer, L. G. Schulz—1030

Yarn, Apparatus to depict the load-elongation diagram of yarn at five cycles per second, Francis Breazeale and John Whisnant—621

Zinc crystals, Elasticity of, C. A. Wirt and E. P. T. Tyndall—587
Zinc single crystals, Internal friction of, Charles A. Wert—29
Zirconium carbide as a thermionic emitter, R. E. Haddad, D. L. Goldwater, and F. H. Morgan—886 (L)
Zirconium, Use of titanium and zirconium nitrides as a conducting element in thoria cathodes, O. B. Bush, R. B. Vandegrift, and T. E. Hanley—295 (L)

For CONTINUOUS Recording of

For CONTINUOUS Recording of Small Voltages and Currents

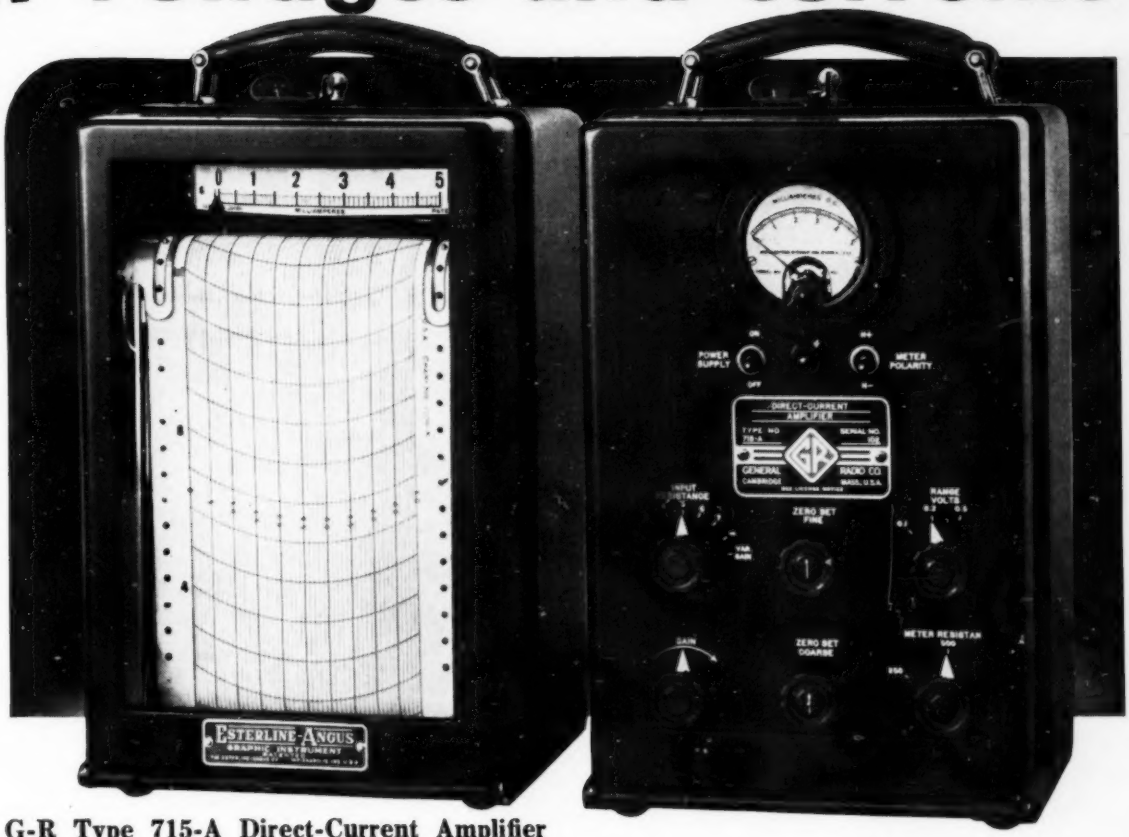

• **The G-R Type 715-A Direct-Current Amplifier** was designed particularly for operation with the Esterline-Angus 5-milliampere recorder to be used as a calibrated recording voltmeter. With appropriate selection of built-in input resistances the combination also is a recording milliammeter or microammeter.

The amplifier can be used in automatic process control circuits where its output operates relays to control the device which feeds the input of the amplifier. It may be operated from frequency meters, sound and vibration measuring equipment, photoelectric cells, resistance strain gauges, resistance thermometers and other similar devices.

The Type 715-A D-C Amplifier has high gain, operates from an a-c line, is very simple to use, requires practically no attention, can be used for very long periods for continuous recording, is exceptionally free from effects of line voltage variation, and has a wide range of built-in input voltage and resistance combinations.

Full-scale output has been made 5 milliamperes to operate the 5 m-a recorder. This full-scale output can be obtained on calibrated ranges from input voltages of 0.1, 0.2, 0.5 and 1.0 volt. The input resistance can be varied between 100 ohms and 10 megohms in powers of 10 by means of a panel switch.

The amplifier is supplied either in a cast metal case to match the Esterline-Angus recorder, or in a walnut cabinet.

SPECIFICATIONS

RANGE: Four switch selected calibrated ranges supplying 5 m-a linear output in recorder circuit for input voltages of 0.1, 0.2, 0.5, and 1.0 volt.

ACCURACY: Approximately 1% as a calibrated voltmeter.

INPUT: From 100 ohms to 10 megohms, in powers of 10, to adjust input resistance and permit use of instrument as calibrated millivoltmeter or microammeter. Short- and open-circuit positions on selector switch. For over one volt input variable gain control provided to adjust voltage to desired value. Input resistance is then about 150,000 ohms.

GRID CURRENT: In input circuit is less than 0.002 microampere.

OUTPUT CIRCUIT: Designed to operate 5 m-a meter on panel, or Esterline-Angus 5 m-a recorder. Provided with compensating resistance to match external device to normal resistance of 1,000 ohms.

TYPE 715-AE D-C AMPLIFIER
(Metal Case) $345.00

TYPE 715-AM D-C AMPLIFIER
(Walnut Cabinet) $300.00

GENERAL RADIO COMPANY Cambridge 39, Massachusetts

90 West St., New York 6 920 S. Michigan Ave., Chicago 5 1000 N. Seward St., Los Angeles 38

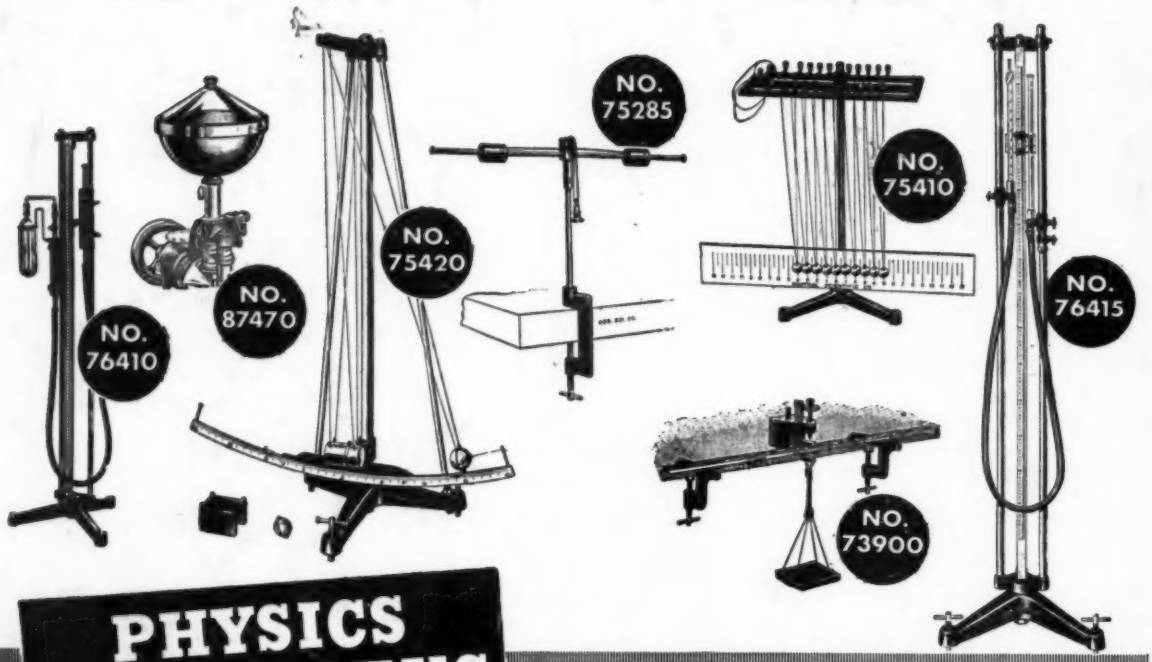

PHYSICS APPARATUS . . . AGAIN AVAILABLE

During the war years many pieces of Cenco manufactured physics apparatus were temporarily discontinued to make way for high-priority government projects. Following the war, because of the scarcity of materials, production was still hampered. Today, the majority of these items are again available from Cenco warehouse stocks.

Instructors in physics will be pleasantly surprised by the prompt delivery that can be made on most of the physics apparatus listed in our general catalog J-141. Typical among the important items now in production or stock are the following catalog numbers: 71245 Alpha Ray Track Apparatus; 73900 Elasticity of Flexure Apparatus; 74720 Rectifier; 74725 Impedance Apparatus; 75275 Inertia Balance; 75280 Radius of Gyration Apparatus; 75285 Rotational Inertia Apparatus; 75410 Collision Balls; 75415 Laws of Motion; 75420 Impact Apparatus; 82060 and 82065 Tangent Galvanometers; 82148 Projection Galvanometer; 83405 Slide Wire Bridge; 83230 Wheatstone Bridge; 87470 Soap Film Interference Apparatus; 87380 Von Nardroff Color Mixer; 76410 and 76415 Boyles Law Apparatus; 78465 Magnetometer and many other similar items,

We welcome your inquiries and orders for Cenco's numerous physics specialties.

CENCO

CENTRAL SCIENTIFIC COMPANY

Scientific Instruments • Laboratory Supplies

1700 IRVING PARK ROAD, CHICAGO 13

NEW YORK BOSTON SAN FRANCISCO NEWARK LOS ANGELES TORONTO MONTREAL

LANCASTER PRESS, INC., LANCASTER, PA.